Mathematical Problems in Engineering

Dynamics and Control of Complex and Switched Systems

Guest Editors: Honglei Xu, Yi Zhang, Jianxiong Ye, and Stanisław Migorski

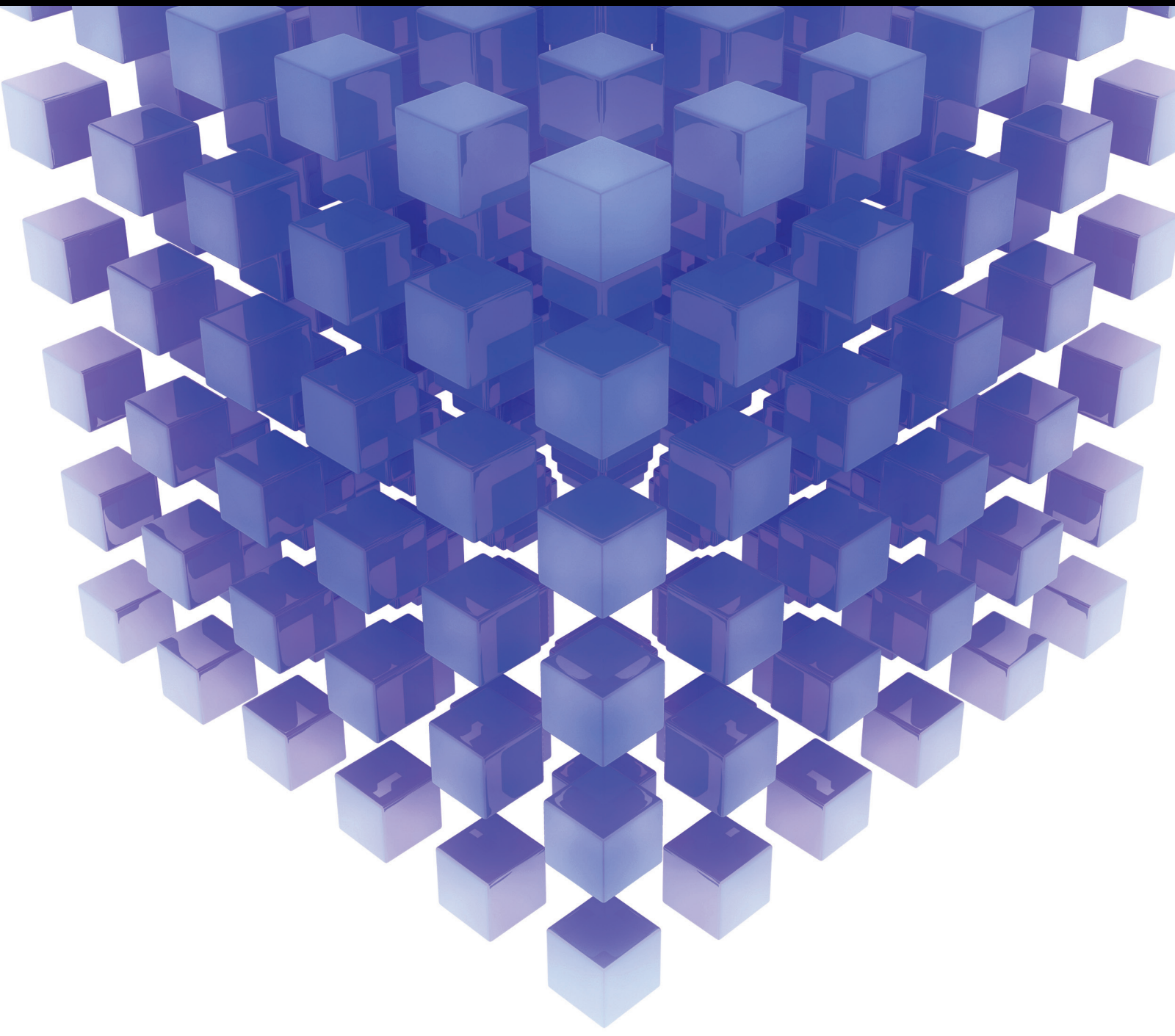

Dynamics and Control of Complex and Switched Systems

Mathematical Problems in Engineering

Dynamics and Control of Complex and Switched Systems

Guest Editors: Honglei Xu, Yi Zhang, Jianxiong Ye, and Stanislaw Migorski

Copyright © 2015 Hindawi Publishing Corporation. All rights reserved.

This is a special issue published in "Mathematical Problems in Engineering." All articles are open access articles distributed under the Creative Commons Attribution License, which permits unrestricted use, distribution, and reproduction in any medium, provided the original work is properly cited.

Editorial Board

Mohamed Abd El Aziz, Egypt
Farid Abed-Meraim, France
Silvia Abrahão, Spain
Paolo Addesso, Italy
Claudia Adduce, Italy
Ramesh Agarwal, USA
Juan C. Agüero, Australia
Ricardo Aguilar-López, Mexico
Tarek Ahmed-Ali, France
Hamid Akbarzadeh, Canada
Muhammad N. Akram, Norway
Mohammad-Reza Alam, USA
Salvatore Alfonzetti, Italy
Francisco Alhama, Spain
Juan A. Almendral, Spain
Lionel Amodeo, France
Igor Andrianov, Germany
Sebastian Anita, Romania
Renata Archetti, Italy
Felice Arena, Italy
Sabri Arik, Turkey
Fumihiro Ashida, Japan
Hassan Askari, Canada
Mohsen Asle Zaeem, USA
Francesco Aymerich, Italy
Seungik Baek, USA
Khaled Bahlali, France
Laurent Bako, France
Stefan Balint, Romania
Alfonso Banos, Spain
Roberto Baratti, Italy
Martino Bardi, Italy
Azeddine Beghdadi, France
Abdel-Hakim Bendada, Canada
Ivano Benedetti, Italy
Elena Benvenuti, Italy
Jamal Berakdar, Germany
Enrique Berjano, Spain
Jean-Charles Beugnot, France
Simone Bianco, Italy
David Bigaud, France
Jonathan N. Blakely, USA
Paul Bogdan, USA
Daniela Boso, Italy
Abdel-Ouahab Boudraa, France
Francesco Braghin, Italy
Michael J. Brennan, UK
Maurizio Brocchini, Italy
Julien Bruchon, France
Javier Buldu', Spain
Tito Busani, USA
P. Cacciola, UK
Salvatore Caddemi, Italy
Jose E. Capilla, Spain
Ana Carpio, Spain
Miguel E. Cerrolaza, Spain
Mohammed Chadli, France
Gregory Chagnon, France
Ching-Ter Chang, Taiwan
M. J. Chappell, UK
Kacem Chehdi, France
Chunlin Chen, China
Xinkai Chen, Japan
Francisco Chicano, Spain
Hung-Yuan Chung, Taiwan
Joaquim Ciurana, Spain
John D. Clayton, USA
Carlo Cosentino, Italy
Paolo Crippa, Italy
Erik Cuevas, Mexico
Peter Dabnichki, Australia
Luca D'Acierno, Italy
Weizhong Dai, USA
Purushothaman Damodaran, USA
Farhang Daneshmand, Canada
Fabio De Angelis, Italy
Stefano de Miranda, Italy
Filippo de Monte, Italy
Xavier Delorme, France
Luca Deseri, USA
Yannis Dimakopoulos, Greece
Zhengtao Ding, UK
Ralph B. Dinwiddie, USA
Mohamed Djemai, France
Alexandre B. Dolgui, France
George S. Dulikravich, USA
Bogdan Dumitrescu, Finland
Horst Ecker, Austria
Ahmed El Hajjaji, France
Fouad Erchiqui, Canada
Anders Eriksson, Sweden
Giovanni Falsone, Italy
Hua Fan, China
Yann Favennec, France
Giuseppe Fedele, Italy
Roberto Fedele, Italy
Jacques Ferland, Canada
Jose R. Fernandez, Spain
Simme Douwe Flapper, Netherlands
Thierry Floquet, France
Eric Florentin, France
Francesco Franco, Italy
Tomonari Furukawa, USA
Mohamed Gadala, Canada
Matteo Gaeta, Italy
Zoran Gajic, USA
Ciprian G. Gal, USA
Ugo Galvanetto, Italy
Akemi Gálvez, Spain
Rita Gamberini, Italy
Maria Gandarias, Spain
Arman Ganji, Canada
Xin-Lin Gao, USA
Zhong-Ke Gao, China
Giovanni Garcea, Italy
Fernando García, Spain
Laura Gardini, Italy
Alessandro Gasparetto, Italy
Vincenzo Gattulli, Italy
Oleg V. Gendelman, Israel
Mergen H. Ghayesh, Australia
Anna M. Gil-Lafuente, Spain
Hector Gómez, Spain
Rama S. R. Gorla, USA
Oded Gottlieb, Israel
Antoine Grall, France
Jason Gu, Canada
Quang Phuc Ha, Australia
Ofer Hadar, Israel
Masoud Hajarian, Iran
Frédéric Hamelin, France
Zhen-Lai Han, China
Thomas Hanne, Switzerland
Takashi Hasuike, Japan
Xiao-Qiao He, China

M.I. Herreros, Spain
Vincent Hilaire, France
Eckhard Hitzer, Japan
Jaromir Horacek, Czech Republic
Muneo Hori, Japan
András Horváth, Italy
Gordon Huang, Canada
Sajid Hussain, Canada
Asier Ibeas, Spain
Giacomo Innocenti, Italy
Emilio Insfran, Spain
Nazrul Islam, USA
Payman Jalali, Finland
Reza Jazar, Australia
Khalide Jbilou, France
Linni Jian, China
Bin Jiang, China
Zhongping Jiang, USA
Ningde Jin, China
Grand R. Joldes, Australia
Joaquim Joao Judice, Portugal
Tadeusz Kaczorek, Poland
Tamas Kalmar-Nagy, Hungary
Tomasz Kapitaniak, Poland
Haranath Kar, India
Konstantinos Karamanos, Belgium
C. M. Khalique, South Africa
Do Wan Kim, Korea
Nam-Il Kim, Korea
Oleg Kirillov, Germany
Manfred Krafczyk, Germany
Frederic Kratz, France
Jurgen Kurths, Germany
Kyandoghere Kyamakya, Austria
Davide La Torre, Italy
Risto Lahdelma, Finland
Hak-Keung Lam, UK
Antonino Laudani, Italy
Aime' Lay-Ekuakille, Italy
Marek Lefik, Poland
Yaguo Lei, China
Thibault Lemaire, France
Stefano Lenci, Italy
Roman Lewandowski, Poland
Qing Q. Liang, Australia
Panos Liatsis, UK
Peide Liu, China
Peter Liu, Taiwan
Wanquan Liu, Australia
Yan-Jun Liu, China
Jean J. Loiseau, France
Paolo Lonetti, Italy
Luis M. López-Ochoa, Spain
Vassilios C. Loukopoulos, Greece
Valentin Lychagin, Norway
Fazal M. Mahomed, South Africa
Y. T. Makkawi, UK
Noureddine Manamanni, France
Didier Maquin, France
Paolo Maria Mariano, Italy
Benoit Marx, France
Ge'rard A. Maugin, France
Driss Mehdi, France
Roderick Melnik, Canada
Pasquale Memmolo, Italy
Xiangyu Meng, Canada
Jose Merodio, Spain
Luciano Mescia, Italy
Laurent Mevel, France
Y. Mikhlin, Ukraine
Aki Mikkola, Finland
Hiroyuki Mino, Japan
Pablo Mira, Spain
Vito Mocella, Italy
Roberto Montanini, Italy
Gisele Mophou, France
Rafael Morales, Spain
Aziz Moukrim, France
Emiliano Mucchi, Italy
Domenico Mundo, Italy
Jose J. Muñoz, Spain
Giuseppe Muscolino, Italy
Marco Mussetta, Italy
Hakim Naceur, France
Hassane Naji, France
Dong Ngoduy, UK
Tatsushi Nishi, Japan
Ben T. Nohara, Japan
Mohammed Nouari, France
Mustapha Nourelfath, Canada
Sotiris K. Ntouyas, Greece
Roger Ohayon, France
Mitsuhiro Okayasu, Japan
Javier Ortega-Garcia, Spain
Alejandro Ortega-Moñux, Spain
Naohisa Otsuka, Japan
Erika Ottaviano, Italy
Alkiviadis Paipetis, Greece
Alessandro Palmeri, UK
Anna Pandolfi, Italy
Elena Panteley, France
Manuel Pastor, Spain
Pubudu N. Pathirana, Australia
Francesco Pellicano, Italy
Haipeng Peng, China
Mingshu Peng, China
Zhike Peng, China
Marzio Pennisi, Italy
Matjaz Perc, Slovenia
Francesco Pesavento, Italy
Maria do Rosário Pinho, Portugal
Antonina Pirrotta, Italy
Vicent Pla, Spain
Javier Plaza, Spain
Jean-Christophe Ponsart, France
Mauro Pontani, Italy
Stanislav Potapenko, Canada
Sergio Preidikman, USA
Christopher Pretty, New Zealand
Carsten Proppe, Germany
Luca Pugi, Italy
Yuming Qin, China
Dane Quinn, USA
Jose Ragot, France
Kumbakonam Ramamani Rajagopal, USA
Gianluca Ranzi, Australia
Sivaguru Ravindran, USA
Alessandro Reali, Italy
Oscar Reinoso, Spain
Nidhal Rezg, France
Ricardo Riaza, Spain
Gerasimos Rigatos, Greece
José Rodellar, Spain
Rosana Rodriguez-Lopez, Spain
Ignacio Rojas, Spain
Carla Roque, Portugal
Aline Roumy, France
Debasish Roy, India
Rubén Ruiz García, Spain
Antonio Ruiz-Cortes, Spain
Ivan D. Rukhlenko, Australia
Mazen Saad, France
Kishin Sadarangani, Spain
Mehrdad Saif, Canada

Miguel A. Salido, Spain
Roque J. Saltarén, Spain
Francisco J. Salvador, Spain
Alessandro Salvini, Italy
Maura Sandri, Italy
Miguel A. F. Sanjuan, Spain
Juan F. San-Juan, Spain
Roberta Santoro, Italy
Ilmar Ferreira Santos, Denmark
José A. Sanz-Herrera, Spain
Nickolas S. Sapidis, Greece
Evangelos J. Sapountzakis, Greece
Andrey V. Savkin, Australia
Valery Sbitnev, Russia
Thomas Schuster, Germany
M. Seaid, UK
Lotfi Senhadji, France
Joan Serra-Sagrista, Spain
Leonid Shaikhet, Ukraine
Hassan M. Shanechi, USA
Sanjay K. Sharma, India
Bo Shen, Germany
Babak Shotorban, USA
Zhan Shu, UK
Dan Simon, USA
Luciano Simoni, Italy
Christos H. Skiadas, Greece
Michael Small, Australia
Francesco Soldovieri, Italy
Raffaele Solimene, Italy
Ruben Specogna, Italy
Sri Sridharan, USA
Ivanka Stamova, USA
Yakov Strelniker, Israel
Sergey A. Suslov, Australia
Thomas Svensson, Sweden
Andrzej Swierniak, Poland
Yang Tang, Germany
Sergio Teggi, Italy
Alexander Timokha, Norway
Rafael Toledo, Spain
Gisella Tomasini, Italy
Francesco Tornabene, Italy
Antonio Tornambe, Italy
Fernando Torres, Spain
Fabio Tramontana, Italy
Sébastien Tremblay, Canada
I. N. Trendafilova, UK
George Tsiatas, Greece
Antonios. Tsourdos, UK
Vladimir Turetsky, Israel
Mustafa Tutar, Spain
Efstratios Tzirtzilakis, Greece
Filippo Ubertini, Italy
Francesco Ubertini, Italy
Hassan Ugail, UK
Giuseppe Vairo, Italy
Kuppalapalle Vajravelu, USA
Robertt A. Valente, Portugal
Pandian Vasant, Malaysia
Miguel E. Vázquez-Méndez, Spain
Josep Vehi, Spain
Kalyana C. Veluvolu, Korea
Fons J. Verbeek, Netherlands
Franck J. Vernerey, USA
Georgios Veronis, USA
Anna Vila, Spain
Rafael J. Villanueva, Spain
U. E. Vincent, UK
Mirko Viroli, Italy
Michael Vynnycky, Sweden
Junwu Wang, China
Shuming Wang, Singapore
Yan-Wu Wang, China
Yongqi Wang, Germany
Desheng D. Wu, Canada
Yuqiang Wu, China
Guangming Xie, China
Xuejun Xie, China
Gen Qi Xu, China
Hang Xu, China
Xinggang Yan, UK
Luis J. Yebra, Spain
Peng-Yeng Yin, Taiwan
Ibrahim Zeid, USA
Huaguang Zhang, China
Qingling Zhang, China
Jian Guo Zhou, UK
Quanxin Zhu, China
Mustapha Zidi, France
Alessandro Zona, Italy

Contents

Dynamics and Control of Complex and Switched Systems, Honglei Xu, Yi Zhang, Jianxiong Ye, and Stanisław Migorski
Volume 2015, Article ID 782467, 2 pages

Infinity Period Dynamic Control of a Kind of Channel's Price and Brand Investment: A Differential Game Method, Kaihong Wang, Li Cheng, and Chuan Ding
Volume 2015, Article ID 721970, 10 pages

Developing a Robust Strategy Map in Balanced Scorecard Model Using Scenario Planning, Mostafa Jafari, Kamran Shahanaghi, and Majid Tootooni
Volume 2015, Article ID 102606, 9 pages

Stability of a Class of Stochastic Nonlinear Systems with Markovian Switching, Xiaohua Liu and Wuquan Li
Volume 2015, Article ID 292794, 7 pages

Study on the Dynamics of Local Pressure Boosting Pneumatic System, Yan Shi, Guanwei Jia, Maolin Cai, and Weiqing Xu
Volume 2015, Article ID 849047, 11 pages

Research on Adaptive Dual-Mode Switch Control Strategy for Vehicle Maglev Flywheel Battery, Hui Gao, Ying-Jun Wu, and Jing-Jin Shen
Volume 2015, Article ID 327347, 9 pages

Construction and Application Research of Isomap-RVM Credit Assessment Model, Guangrong Tong and Siwei Li
Volume 2015, Article ID 197258, 7 pages

Virtual Clutch Controller for Clutch-to-Clutch Shifts in Planetary-Type Automatic Transmission, Yunjiang Cheng, Peng Dong, Shuai Yang, and Xiangyang Xu
Volume 2015, Article ID 213162, 16 pages

The Study of a Mathematical Model in Information Acquisition and Disclosure, Ce Huang
Volume 2015, Article ID 491328, 8 pages

A Multiobjective Genetic Algorithm Based on a Discrete Selection Procedure, Qiang Long, Changzhi Wu, Xiangyu Wang, Lin Jiang, and Jueyou Li
Volume 2015, Article ID 349781, 17 pages

A Lower Extremity Exoskeleton: Human-Machine Coupled Modeling, Robust Control Design, Simulation, and Overload-Carrying Experiment, Qing Guo, Songjing Li, and Dan Jiang
Volume 2015, Article ID 905761, 15 pages

Hindawi Publishing Corporation
Mathematical Problems in Engineering
Volume 2015, Article ID 782467, 2 pages
http://dx.doi.org/10.1155/2015/782467

Editorial

Dynamics and Control of Complex and Switched Systems

Honglei Xu,[1] Yi Zhang,[2] Jianxiong Ye,[3] and Stanisław Migorski[4]

[1]*Department of Mathematics and Statistics, Curtin University, Perth, Australia*
[2]*Department of Mathematics, China University of Petroleum (Beijing), Beijing, China*
[3]*School of Mathematics and Computer Science, Fujian Normal University, Fuzhou, China*
[4]*Faculty of Mathematics and Computer Science, Jagiellonian University, Krakow, Poland*

Correspondence should be addressed to Honglei Xu; h.xu@curtin.edu.au

Received 16 August 2015; Accepted 16 August 2015

Copyright © 2015 Honglei Xu et al. This is an open access article distributed under the Creative Commons Attribution License, which permits unrestricted use, distribution, and reproduction in any medium, provided the original work is properly cited.

Hybrid systems are a class of complex systems involving both continuous systems and a set of discrete events. They exhibit complex phenomena as the continuous systems and the discrete events coexist and interact with each other. There are many hybrid systems that arise in a variety of disciplines. For example, in the manufacturing industry, components are fed into a machine following a specified procedure. The process of the machine is continuous, while the startup of the machine is a discrete event. Thus, the overall system is clearly a hybrid system. As an important class of hybrid systems, switched systems can model the hierarchy and switching structures of a complex system. Engineering examples can be found in chemical processes, air traffic management systems, and computer communications systems, and so forth. However, till now theory and methodologies of switched systems, in particular, involving complicated structure characteristics, still need to be investigated further.

In "Stability of a Class of Stochastic Nonlinear Systems with Markovian Switching," output feedback stabilization of stochastic nonlinear systems with Markovian switching has been investigated using the backstepping design method and homogeneous domination technique. In "Research on Adaptive Dual-Mode Switch Control Strategy for Vehicle Maglev Flywheel Battery," dual-mode adaptive hybrid control has been presented based on H_∞ control and unbalance displacement feed-forward compensation control. Furthermore, a real-time switch controller has been designed as well. In "Study on the Dynamics of Local Pressure Boosting Pneumatic System," dynamics of local pressure boosting pneumatic systems has been studied by modelling them as switched systems. Moreover, optimization problems of the local pressure boosting system have been solved as well. In "A Lower Extremity Exoskeleton: Human-Machine Coupled Modeling, Robust Control Design, Simulation, and Overload-Carrying Experiment," a robust H_∞ control method and a switched control algorithm have been developed for hydraulic actuators in human-machine coordinated motion. It shows that the proposed robust controller can improve the robust stability and performance under the structural and parametric uncertainty disturbances. In "A Multiobjective Genetic Algorithm Based on a Discrete Selection Procedure," a multiobjective genetic algorithm has been studied and applied to identify optimal solutions with better elitism and diversity metrics. In "Infinity Period Dynamic Control of a Kind of Channel's Price and Brand Investment: A Differential Game Method," infinity period dynamic control of distribution channels has been considered using a differential game approach. It includes four differential dynamic control models: coordinated static games, uncoordinated static games, Stackelberg games with controlled manufacture, and Stackelberg games with controlled retailers. In "Developing a Robust Strategy Map in Balanced Scorecard Model Using Scenario Planning," a strategy map-based method has been developed for environmental scenarios and a new method has also been proposed to decide the robustness degree of the strategy map for every scenario's contingency. In "Virtual Clutch Controller for Clutch-to-Clutch Shifts in Planetary-Type Automatic Transmission," an equivalent method has been proposed to control automatic transmission like dual clutch transmission by adopting the torque ratios

of oncoming clutch and offgoing clutch of each gear. In "Construction and Application Research of isomap-RVM Credit Assessment Model," cutting-edge algorithms, applied isometric feature mapping, and relevance vector machine (RVM) have been studied to classify assessment and further improve the accuracy of credit assessment methods. In "The Study of a Mathematical Model in Information Acquisition and Disclosure," a mathematical model with a decision-maker and an expert has been analysed to obtain the expert's information acquisition and disclosure strategy.

The aim of this special issue is to report the recent research progress and advances on all issues and topics related to complex and switched systems and their applications. We hope that this special issue will be beneficial to scientists, researchers, and practitioners in all disciplines, particularly in various application areas.

Acknowledgments

We would like to thank the authors who submitted their papers for publication in this special issue. We also thank our reviewers for their careful and critical evaluation of the manuscripts. Finally, we appreciate the support from the National Natural Science Foundation of China (11171079), the Natural Science Foundation of Hubei Province of China (2014CFB141), and HUST Independent Innovation Research Fund (GF and Natural Science).

Honglei Xu
Yi Zhang
Jianxiong Ye
Stanisław Migorski

Hindawi Publishing Corporation
Mathematical Problems in Engineering
Volume 2015, Article ID 721970, 10 pages
http://dx.doi.org/10.1155/2015/721970

Research Article

Infinity Period Dynamic Control of a Kind of Channel's Price and Brand Investment: A Differential Game Method

Kaihong Wang,[1] Li Cheng,[2] and Chuan Ding[1]

[1]*School of Economic Mathematics, Southwestern University of Finance and Economics, Chengdu 610074, China*
[2]*Research Center for Social Work Development, Southwestern University of Finance and Economics, Chengdu 610074, China*

Correspondence should be addressed to Kaihong Wang; wangkaihong@swufe.edu.cn

Received 22 November 2014; Accepted 20 January 2015

Academic Editor: Honglei Xu

Copyright © 2015 Kaihong Wang et al. This is an open access article distributed under the Creative Commons Attribution License, which permits unrestricted use, distribution, and reproduction in any medium, provided the original work is properly cited.

The infinity period dynamic control problem of distribution channel was studied with differential game approach. Four differential dynamic control models of coordinated channel game, uncoordinated static game, Stackelberg game with manufacture controlled, and Stackelberg game with n retailers controlled were constructed. Some results applied dynamic optimization theory made with Hamilton function. The conclusions are as follows. (1) Optimization brand investment controlled by manufacture has nothing to do with time. (2) Retail price was the most minimum when channel was integrated. (3) Manufacture's profits of uncoordinated static game and Stackelberg game with manufacture controlled were more than Stackelberg game with n retailers controlled. (4) Retailer's profits of Stackelberg game with n retailers controlled were less than Stackelberg game with manufacture controlled. (5) Channel's total profits of Stackelberg game with n retailers controlled were the most minimum.

1. Literature Review and Research Purpose

1.1. Literature Review. Channel members of distribution channel have different target; the channel conflict is likely to happen; therefore, we cannot achieve the pareto optimal decision without channel coordination mechanism. Whether channel manufacturer should vertically integrate (coordination) the manufacturer or sell products by ordinary manufacturer have become the center of attention. Distribution channel decision is mainly focused on two aspects. The first aspect mainly is an analysis of five kinds of channel structure by some marketing experts, on behalf of Desiraju and Moorthy [1] (as shown in Figure 1); the second aspect mainly is channel coordination problem, whose research has a long history. Baligh and Richartz argued that channels should be integrated to achieve internal coordination [2]. But there are some deficiencies in their research, one is not considering the market power of manufacturers and intermediaries, another is ignoring the product differentiation or substitution degree.

In particular, after being searched by McGuire and Staelin [3], channel competition and coordination have become the focus. Jeul and Shugan [4] had researched a question about channel coordination consisting of one manufacturer and a retailer. They considered that, except incentive channel members properly, coordination could become their instinctive behavior. Simultaneously, vertical integration was not the only way to maximize channel profit, which could also come true by agreement, channel latent rules, profit sharing, and quality discount to realize coordination. McGuire and Staelin [3] considered that channel consisted of manufacturer and competitive retailers, and both of them could attend Stackelberg leading game. At this time, vertical integration is not optimal. However, McGuire and Staelin [3] still did not consider the problem of differentiated product. Coughlan [5] researched the issue of vertical integration differentiated product oligarch market, choosing the product price and market channel to maximize the profit; vertical integration had more competitive advantages in price than independent management of members. They also achieved some empirical in semiconductor industry. Xu et al. [6] proposed both single contracts and joint contracts to achieve coordination; they found that the coordinating revenue sharing contract and two-part tariff contract in the supply chain with risk neutral agents were still useful to coordinate the supply chain

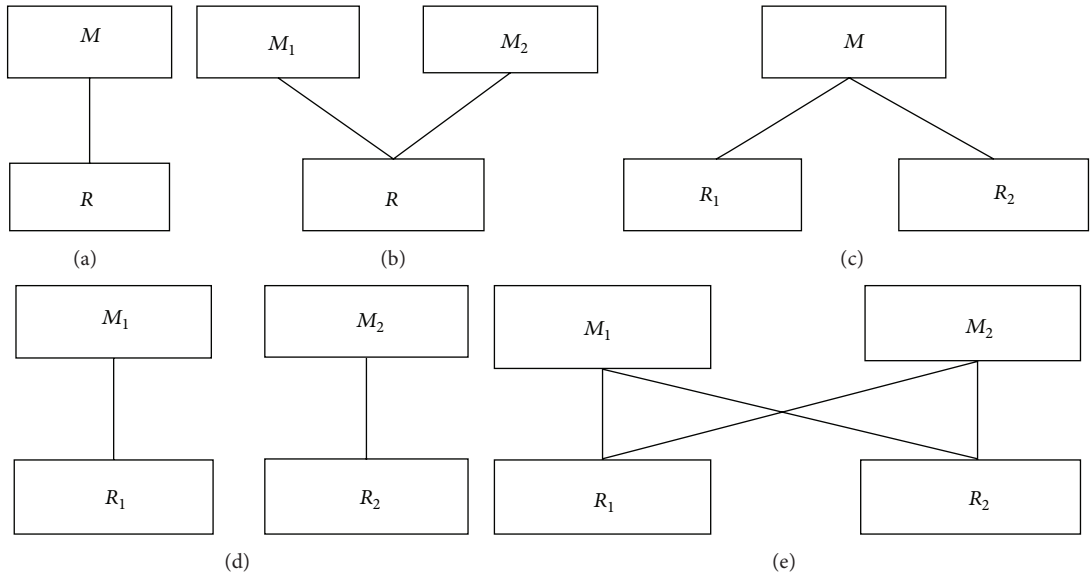

Figure 1: Five channel structures.

taking into account the degree of risk aversion of fashion retailer. They demonstrated that only revenue sharing with two-part tariff contract could coordinate the fashion supply chain. The optimal conditions for contract parameters to achieve channel coordination were determined. Ding et al. [7] constructed four models based on different range of the result fairness preference's coefficient. They thought if there was no coordination mechanism, then the channel coordination could not be achieved in both types (the narrow self-interest and the competitive preference). And channel coordination could be achieved in the types of the avoiding unfair preference and the social welfare preferences, when a fair preference coefficient and other parameters satisfied certain conditions. Ding et al. [8] presented a quantity discount mechanism based on a result fairness preference for achieving channel coordination. They thought that as long as the degree of attention of retailer to manufacturer's profit and the fairness preference coefficients of retailers satisfied certain conditions, channel coordination could be achieved by setting a simple wholesale price and fixed costs. Ding et al. [9] adopted a behavior game method to analyze and forecast channel members' decision behavior based on result fairness preference and reciprocal fairness preference by embedding a fair preference theory in channel research of coordination.

The researches above were mainly about the channel of one manufacturer with one or several middlemen and did not mention the channel of several manufacturers with one retailer, not to speak of channel with various manufacturers and retailers. Altintas et al. [10] studied a multiperiod model, with a buyer facing stochastic end-item demand and a supplier offering an all-units quantity discount to them, studied the supplier's profit as a function of their offered quantity-discount scheme (accommodating the buyer's optimal policy), and discovered a new phenomenon that was distinct and structurally different from the well-known bullwhip effect. Song et al. [11] examined the effect of market segments, consumer choice, and the acceptance of direct online channels on firm performance and the whole system's profit. The analysis indicated that the addition of direct online channel did not necessarily harm the incumbent retailers. A channel coordination zone was proposed. Wang et al. [12] presented a useful and practical procurement approach using the joint replenishment and channel coordination (JR-CC) policy in a two-echelon supply chain considering the coordination cost.

But these studies were mainly static decision of channel members; some scholars had studied the channel members' decision from the dynamic perspective. For example, Zhao et al. [13] assumed that coordination could increase the sales by accumulating the reputation of the supply chain. A differential game model was established with the logistics service supply chain that consists of one service integrator and one supplier. And the results made the benefits of the cost sharing contract in increasing the profits of both players and the whole supply chain explicit, which meant that the cost sharing contract was an effective coordination mechanism in the long-term relationship of the members in a logistics service supply chain. Li et al. [14] considered a decentralized two-period supply chain in which a manufacturer produced a product and sold it through a retailer facing a price-dependent demand. They obtained revenue sharing contracts that could coordinate the dynamic supply chain.

In practice, the channel member may be loss-averse; Chen et al. [15] studied channel coordination with a loss-averse retailer that orders from a risk-neutral supplier via option contracts. This study considered sales-effort dependent demand to extend the model of Wang and Webster [16]. In this area, there were many rich results; due to limited space, we omitted these results and mainly focused

on the multiperiod dynamic channel decision. Jiang et al. [17] investigated decision and coordination in a supply-chain-wide system consisting of a manufacturer, a third-party logistics (3PL) provider, and two competing retailers. They discussed the dominant retailer model where one retailer was a price leader, and the other was a price follower, three contracts: a spanning revenue sharing contract, a quantity discount contract and a two-part tariffs contract were devised to effectively coordinate the decentralized system involving the 3PL provider. Yin et al. [18] considered one manufacturer and multiple suppliers to determine production, prices, and inventory simultaneously with uncertain demands, they aimed at providing an optimal discount policy derived from Stackelberg equilibrium to coordinate a manufacturer and multiple suppliers. The optimal discount coordination mechanism helps the manufacturer to select suppliers in order to maintain long-term relationship with the contracted suppliers under demand uncertainty.

The above researches were based on symmetric information, from the perspective of asymmetric information; Rajiv [19] regarded that coordination level could be improved through channel franchise arrangement. He researched products distribution of manufacturers by service and price of middlemen and considered that member coordination could not be improved by controlling and ascendancy of channel members. Benjamin and Tracy [20] thought that demand condition was the private information of middlemen, who would be in push of sale by promotion. But effort level was also the private information which was not easy to be observed. And manufacturer was also unaware that whether sales volume was associated with the effort level of middlemen. Moral risk model was built based on the information asymmetry. Zissis et al. [21] derived analytical expressions of the quantity discounts that minimize the manufacturer's costs when the retailer had private information. Furthermore, they showed that perfect coordination was possible even under asymmetric information. The results showed that retail competition contributes to manufacturer and improves channel efficiency of the decentralized supply chain. When the retailers were more risk averse, the channel efficiency becomes much lower. Luo et al. [22] researched decentralized supply chain incentive mechanism, which was actually selling race. Tian et al. [23] analyzed with two manufacturers and a retailer of principal-agent problems in the distribution system. In this system, two manufacturers were principal and retailers were agent; the results showed that the manufacturers in noncoordinative competition were damaged, especially the damage to manufacturers was higher with the substitution of their products increasing, and the retailer was benefited more in the situation. Chen et al. [24] studied from the perspective of distribution channel alliance coordination, discussed the formation mechanism of distribution channel alliance interests, and put forward the mechanism of subsidy income change of the game. When manufacturers did not know distributors type, if marketing alliance was unprofitable to manufacturers, they would not choose channel alliance. If its profits would be improved, they were willing to enter into alliance with the distributor.

1.2. Research Purpose. In Section 1.1, we reviewed the research status from the two dimensions (the number of channel members and whether the information was symmetrical or not). However, these studies had two defects.

First, it was a pity that these studies were single stage decision of the channel member, or a static decision. In fact, we found that the current sales were affected by the current sales decisions and also affected by the channel members of past marketing decisions. For example, the manufacturer brand advertising will affect the sales of the product for a long time and has a cumulative effect to the manufacturer's product reputation (goodwill). So this was a long-term dynamic relationship; it needs be studied with a "control theory" and "differential game."

Second, Pradeep and Jain [25], Jørgensen and Zaccour [26], Martín-Herrán and Taboubi [27], and Martín-Herrán and Taboubi [28] used this theory to study simple channels (in Figure 1(a)). Martín-Herrán and Taboubi [29] studied in Figure 1(b) with this theory. In practice, the manufacturer's products through a number of retailers to sell to consumers; therefore, in Figure 1(c) is a common channel structure. We need to study this channel structure (Figure 1(c)) from the perspective of long-term dynamic.

In this paper, according to the two defects, we used the theory of "control" and "differential game" to study another distribution channel structure (Figure 1(c))—a manufacturer and n retailers. Our researches showed that (1) optimization brand investment controlled by manufacture has nothing to do with time. (2) Retail price was the most minimum when channel was integrated. (3) Manufacture's profits of uncoordinated static game and Stackelberg game with manufacture controlled were more than Stackelberg game with n retailers controlled. (4) Retailer's profits of Stackelberg game with n retailers controlled were less than Stackelberg game with manufacture controlled. (5) Channel's total profits of Stackelberg game with n retailers controlled were the most minimum.

2. Symbols, Concepts, and Basic Assumptions

Due to the competition of the market, the layer number of channels is decreasing gradually and many industry patterns distribute products by the pattern of manufacturers-retailers-customers. So in this paper, the channel system is made up of manufacturers, retailers, and customers and is three-level distribution channel management system, so this paper focuses on the simple channel system of manufacturers and retailers.

For convenience analysis, we give the following symbols, assumptions, and a brief illustration of some concept.

Assumptions 1. Channel consists of a manufacturer and n retailers.

Assumptions 2. Time $t \in [0, +\infty)$; manufacturer controls the marginal profits $m_M(t)$ and brand investment $B_M(t)$ (such as advertising, public relations, effort, etc.), retailers control their margins profit $m_i(t)$ as well as investment $B_i(t)$ in order to increase sales (such as in-store promotions and sales

efforts, etc.), $i = 1, 2, \ldots, n$. The retail price of retailer $p_i(t)$ is the sum of the marginal profits of manufacturer $m_M(t)$ and marginal profit of retailers $m_i(t)$. Consider

$$p_i(t) = m_M(t) + m_i(t), \quad i = 1, 2, \ldots, n. \tag{1}$$

Assumptions 3. Market demand function for retailers is [26, 27]

$$q_i(t) = B_i(t)\left[a - bp_i(t)\right]\sqrt{G(t)}. \tag{2}$$

$a > 0$, $b > 0$ is constant and $i = 1, 2, \ldots, n$, $G(t)$ is the stock of band goodwill of products at time $t \in [0, +\infty)$. In this paper, we use $q_i(t) = B_i(t)[a - bp_i(t)]\sqrt{G(t)}$, which reflects the retailer's market demand which is proportional to the sales of their investment $B_i(t)$, and the price $p_i(t)$ and demand response and reputation have the same direction change. $\sqrt{G(t)}$ indicate that reputation $G(t)$ is diminishing to demand and also suggests that retailers are only concerned with the present demand. In time t, $t \in [0, +\infty)$, his marketing investment $m_i(t)$ affects only sales at time t, $t \in [0, +\infty)$ and does not affect the reputation of products. And manufacturer is more concerned about the reputation of the brand, so brand investment of manufacturer $B_M(t)$ does not directly affect demand; by reputation $G(t)$ indirectly affects demand.

Assumptions 4. From the Assumptions 3, manufacturer's brand investment $B_M(t)$ affects the demand by reputation $G(t)$ indirectly, and reputation $G(t)$ has the characteristic of natural attenuation. Let it according to the index law decay over time, as $e^{-\delta t}$ attenuation, in which δ is the attenuation coefficient, so the change of the reputation can be described by the Nerlove-Arrow equation:

$$\frac{dG(t)}{dt} = B_M(t) - \delta G(t), \qquad G(0) = G_0 > 0. \tag{3}$$

Assumptions 5. In practice, cost function needs to meet the marginal cost increases; according to references [25–29], we assume that the cost of manufacturer's brand investment is $(1/2)c_M B_M(t)^2$. The investment costs of retailers $B_i(t)$ are $(1/2)c_i B_i(t)^2$, $i = 1, 2, \ldots, n$. Because the cost of different channel members is not same, the cost functions c_M, c_i ($i = 1, 2, \ldots, n$) are also not identical. Square cost function in the form guarantees that the first-order conditions are greater than zero and the second order condition is greater than zero.

3. Manufacturer Integration (Shorthand for T) Distribution Channel

In channel, manufacturer can integrate the whole channel to get more channel profit, so this section analyzes manufacturer integrated situation and the latter analyzes noncoordination game.

According to the previous assumptions and (1), (2), and (3), manufacturer's discount profits in time t, $t \in [0, +\infty)$ are

$$\pi_M = \int_0^{+\infty} e^{-rt} m_M(t) \sum_{i=1}^{n} \left[B_i(t)\left(a - bp_i(t)\right)\sqrt{G(t)}\right] - \frac{1}{2} c_M B_M(t)^2 \, dt. \tag{4}$$

At t, $t \in [0, +\infty)$, retailer i's all discount profits is as follows:

$$\pi_i = \int_0^{+\infty} e^{-rt} m_i(t) \sum_{i=1}^{n} \left[B_i(t)\left(a - bp_i(t)\right)\sqrt{G(t)}\right] - \frac{1}{2} c_i B_i(t)^2 \, dt, \quad i = 1, 2, \ldots, n, \tag{5}$$

where in (4)-(5) e^{-rt} and r are the discount factor and discount rate, respectively.

If the channel needs to be integrated, different scholars have different ways of integration. This paper comes to a manufacturer and n retailers. So manufacturer and retailers adopt integration marginal profit as follows: $m^i(t) = m_M(t) + m_i(t)$, $i = 1, 2, \ldots, n$. The integrated decision variables are $m^i(t)$, $B_M(t)$, $B_i(t)$. So we get the total channel profit after integration:

$$\pi^T = \int_0^{+\infty} e^{-rt} \sum_{i=1}^{n} m^i(t) \left[B_i(t)\left(a - bp_i(t)\right)\sqrt{G(t)}\right] - \frac{1}{2} \sum_{i=1}^{n} c_i B_i(t)^2 \, dt. \tag{6}$$

Because the margin profit $m^i(t)$ and $B_i(t)$ is not in the dynamic equation (3), so, in (6), two first-order conditions about $m^i(t)$ and $B_i(t)$, respectively, are

$$\frac{\partial \pi^T}{\partial m^i(t)} = a - 2bm^i(t) = 0, \quad i = 1, 2, \ldots, n, \tag{7}$$

$$\frac{\partial \pi^T}{\partial B^i(t)} = m^i(t)\left(a - bm^i(t)\right)\sqrt{G(t)} - c_i B_i(t) = 0, \quad i = 1, 2, \ldots, n. \tag{8}$$

Due to the symmetry (7), we can get

$$m^i(t) = \frac{a}{2b}, \quad i = 1, 2, \ldots, n. \tag{9}$$

Equation (9) is taken into (8):

$$B_i^{T*} = \frac{a^2}{4bc_i}\sqrt{G^{T*}(t)}, \quad i = 1, 2, \ldots, n. \tag{10}$$

To achieve maximum value of (6), we also need the first-order conditions about $B_M(t)$ in (6). Because $B_M(t)$ is implicity in $G(t)$, we can not derive the partial derivatives directly. Due to the particularity of the integral, we need integral firstly

and then derive partial derivatives. The following is to find out optimal $B_M^{T*}(t)$.

At present, the theory methods have two kinds. One is to construct Hamilton-Jacobi-Bellman (HJB) equation. Another is to construct the Hamilton function. In the paper, we construct the Hamilton function to solve the optimal $B_M^{T*}(t)$ (see [28–31]).

Now we build the present value Hamilton function to find the optimal $B_M^{T*}(t)$. According to [28–32], the present value of the Hamilton function in (6) is

$$H_C^T = \sum_{i=1}^{n} m^i(t) B_i(t) (a - bp_i(t)) \sqrt{G(t)} - \frac{1}{2}\sum_{i=1}^{n} c_i B_i(t)^2 + \lambda [B_M(t) - \delta G(t)]. \tag{11}$$

So the fixed present value Hamilton functions is

$$H^T = \sum_{i=1}^{n} m^i(t) \left(B_i(t) (a - bp_i(t)) \sqrt{G(t)}\right) - \frac{1}{2}\sum_{i=1}^{n} c_i B_i(t)^2 + h [B_M(t) - G(t)]. \tag{12}$$

$h = \lambda e^{rt}$; put (9) and (10) into (12):

$$H_C^T = \sum_{i=1}^{n} \frac{a^4}{32b^2 c_i} G^{T*} - \frac{1}{2} c_M B_M(t)^2 + h [B_M(t) - \delta G(t)]. \tag{13}$$

According to the principle of the modified maximum. There are the following necessary conditions for optimal solution.

(1) State equation and the initial conditions:

$$\frac{dG(t)}{dt} = B_M(t) - \delta G(t), \quad G(0) = G_0 > 0. \tag{14}$$

(2) Multiplier equation:

$$\frac{\partial h}{\partial t} = rh - \frac{\partial H^T}{\partial G} = rh + h\delta - \sum_{i=1}^{n} \frac{a^4}{32b^2 c_i}. \tag{15}$$

(3) The optimal equation:

$$\frac{\partial H^T}{\partial t} = -c_M B_M(t) + h = 0. \tag{16}$$

(4) Cross-sectional conditions:

$$h(+\infty) e^{-r\infty} = \lambda(+\infty) = 0. \tag{17}$$

Jointing (14), (15), (16), and (17), we may calculate $B_M^{T*}(t)$, $G^{T*}(t)$. Through the analysis of the above, we get Proposition 1.

Proposition 1. *In the integration of distribution channel, the optimal margins profit, the manufacturer's optimal brand investments, sales of the optimal investment, and optimal reputation are, respectively,*

$$m^i(t) = \frac{a}{2b}, \quad i = 1, 2, \ldots, n,$$

$$B_i^{T*}(t) = \frac{a^2}{4bc_i} \sqrt{G^{T*}(t)}, \quad i = 1, 2, \ldots, n, \tag{18}$$

$$B_M^{T*}(t) = \sum_{i=1}^{n} \frac{a^4}{32b^2 (r+\delta) c_M c_i},$$

$$G^{T*}(t) = \left[G_0 - \sum_{i=1}^{n} \frac{a^4}{32b^2 (r+\delta) \delta c_M c_i}\right] e^{-\delta t} + \sum_{i=1}^{n} \frac{a^4}{32b^2 (r+\delta) \delta c_M c_i}. \tag{19}$$

From Proposition 1, we find that the reputation of products has nothing to do with the integrated optimal marginal profit and the time. The retailer's marketing investment increases as the increasing of product reputation, but the speed of increase is more and more small. Manufacturer's brand investment has nothing to do with the time. The reputation in (19) will be compared later.

4. The Analysis of the Multistage Dynamic Noncooperative Game about the Distribution Channel between Manufacturers and Retailers

In the previous section, we analyze the channel coordination. The following is the analysis of the noncoordination. In practice, for channel members, the relation of dynamic noncoordination is more common. There are static game (shorthand for N), Stackelberg game led by manufacturers (shorthand for MS), and Stackelberg game led by retailers (shorthand for RS). Now, analyze, respectively, as follows.

4.1. The Analysis of the Static Multistage Game between Manufacturer and Retailers. In this channel relationship, manufacturer and n retailers make their decisions at the same time, for maximizing their own profits. Therefore, we only need to find the first-order conditions of (4) and (5), respectively. Similar to the previous section, we analyze $m_M(t), m_i(t)$, and $B_i(t)$; they do not appear in the dynamic state equation (3), so, in (4), the first-order condition about $m_M(t)$ is

$$\frac{\partial \pi_M}{\partial m_M(t)} = \sum_{i=1}^{n} [B_i(t) (a - 2bm_M(t) - bm_i(t))] = 0. \tag{20}$$

And the solution is

$$m_M^{N*}(t) = \frac{a \sum_{i=1}^{n} B_i(t) - b \sum_{i=1}^{n} B_i(t) m_i(t)}{2b \sum_{i=1}^{n} B_i(t)}. \tag{21}$$

Similarly, in (5), the first-order condition about $m_i(t)$, $B_i(t)$ is

$$\frac{\partial \pi_i}{\partial m_i(t)} = a - 2bm_i(t) - bM_i(t) = 0, \quad i = 1, 2, \ldots, n, \tag{22}$$

$$\frac{\partial \pi_i}{\partial B_i(t)} = m_i(t)\left[a - bp_i(t)\right]\sqrt{G(t)} - c_i B_i(t) = 0, \quad i = 1, 2, \ldots, n. \tag{23}$$

Substituting (21) into (22):

$$a\sum_{i=1}^{n} B_i(t) - 4bm_i(t)\sum_{i=1}^{n} B_i(t) + b\sum_{i=1}^{n} B_i(t)\, m_i(t) = 0, \quad i = 1, 2, \ldots, n. \tag{24}$$

The optimal solution is $m_i^{N*}(t) = m_M^{N*}(t) = a/3b$; thus the solution of (23) is

$$B_i^{N*}(t) = \frac{a^2}{9bc_i}\sqrt{G(t)}, \quad i = 1, 2, \ldots, n. \tag{25}$$

Then we construct Hamilton function for the best B_M^{N*}. The Hamiltonian function of (4) is

$$H^N = G(t)\sum_{i=1}^{n}\frac{a^4}{81b^2c_i} - \frac{1}{2}c_M B_M(t)^2 + \lambda\left[B_M(t) - \delta G(t)\right]. \tag{26}$$

With the method of Section 2, B_M^{N*}, $G^{N*}(t)$ can be obtained as follows. (To avoid duplication, details are omitted; please refer to [26–28, 30]).

So the optimal solution meets the necessary conditions:

$$B_M^{N*} = \sum_{i=1}^{n}\frac{a^4}{81b^2(r+\delta)c_M c_i},$$
$$G^{N*}t = \left(G_0 - \sum_{i=1}^{n}\frac{a^4}{81b^2(r+\delta)c_M c_i}\right)e^{-\delta t} + \sum_{i=1}^{n}\frac{a^4}{81b^2(r+\delta)c_M c_i}. \tag{27}$$

So, there is Proposition 2.

Proposition 2. *In the distribution channel, when channel members make decisions at the same time, the best margins profits, manufacturer's best brand investments, retailers' best-selling investments, and the best reputation are, respectively,*

$$m_i^{N*}(t) = m_M^{N*}(t) = \frac{a}{3b}, \quad i = 1, 2, \ldots, n, \tag{28}$$

$$B_i^{N*}(t) = \frac{a^2}{9bc_i}\sqrt{G(t)}, \quad i = 1, 2, \ldots, n, \tag{29}$$

$$B_M^{N*} = \sum_{i=1}^{n}\frac{a^4}{81b^2(r+\delta)c_M c_i}, \tag{30}$$

$$G^{N*}(t) = \left(G_0 - \sum_{i=1}^{n}\frac{a^4}{81b^2(r+\delta)c_M c_i}\right)e^{-\delta t} + \sum_{i=1}^{n}\frac{a^4}{81b^2(r+\delta)c_M c_i}. \tag{31}$$

4.2. The Multistage Game Analysis of Stackelberg Game Led by Manufacturers (Shorthand for MS). In practice, manufacturer may be in a dominant position, such as GREE electric appliances and Sony. This kind of game relation is the Stackelberg game manufacturer dominated. Manufacturer decides first and retailers then carry on the optimal decision according to manufacturer's choice. By backward induction, we find the subgame perfect Nash equilibrium.

In the second phase, the retailers make optimal decision. And in (5), the first-order condition is (22) and (23). So from (22) and (23) we can obtain the two reaction functions about $m_i(t)$, $B_i(t)$, $i = 1, 2, \ldots, n$:

$$m_i(t) = \frac{a - bm_M(t)}{2b}, \quad i = 1, 2, \ldots, n,$$
$$B_i(t) = \frac{\left(a - bm_M(t)\right)^2}{4bc_i}\sqrt{G(t)}, \quad i = 1, 2, \ldots, n. \tag{32}$$

Back to the first stage of the game, substituting (32) into the manufacturer's profit function,

$$\pi_M = \int_0^{+\infty} e^{-rt} m_M(t)\left(a - bm_M(t)\right)^3 G(t)\sum_{i=1}^{n}\frac{1}{8bc_i} - \frac{1}{2}c_M B_M(t)^2\, dt. \tag{33}$$

And the first-order condition about $m_M(t)$ is $m_M^{MS*}(t) = a/4b$. For (33), the first-order condition is $m_M^{MS}(t) = a/4b$; we also construct Hamilton function [19, 20]:

$$H^{MS} = \frac{27a^4}{2048b^2}G(t)\sum_{i=1}^{n}\frac{1}{c_i} - \frac{1}{2}c_M B_M(t)^2 + \lambda\left[B_M(t) - \delta G(t)\right]. \tag{34}$$

Then, the best $m_M^{\mathrm{MS}*}(t)$ and $G^{\mathrm{MS}*}(t)$ are

$$B_M^{\mathrm{MS}*}(t) = \sum_{i=1}^{n} \frac{27a^4}{2048b^2(r+\delta)c_M c_i},$$
$$G^{\mathrm{MS}*}t = \left(G_0 - \sum_{i=1}^{n} \frac{27a^4}{2048b^2(r+\delta)\delta c_M c_i}\right) e^{-\delta t} + \sum_{i=1}^{n} \frac{27a^4}{2048b^2(r+\delta)\delta c_M c_i}. \quad (35)$$

And there is the following Proposition 3.

Proposition 3. *In the Stackelberg game with manufacture dominated, the best margins profit, manufacturer's best brand investments, retailers' best-selling investments, and the best reputation are, respectively (the subgame perfect Nash equilibrium),*

$$m_M^{MS*}(t) = \frac{a}{4b}, \qquad m_i^{MS*}(t) = \frac{3a}{8b}, \quad i = 1, 2, \ldots, n, \quad (36)$$
$$B_i^{MS*}(t) = \sum_{i=1}^{n} \frac{9a^2}{64bc_i} \sqrt{G^{MS*}(t)}, \quad (37)$$
$$B_M^{MS*} = \sum_{i=1}^{n} \frac{27a^4}{2048b^2(r+\delta)c_M c_i}, \quad (38)$$
$$G^{MS*}(t) = \left(G_0 - \sum_{i=1}^{n} \frac{27a^4}{2048b^2(r+\delta)\delta c_M c_i}\right) e^{-\delta t} + \sum_{i=1}^{n} \frac{27a^4}{2048b^2(r+\delta)\delta c_M c_i}. \quad (39)$$

4.3. The Multistage Game Analysis of the Stackelberg Game Led by Retailers (Shorthand for RS). In Section 4.2, we analyzed the Stackelberg game led by manufacturer. In reality, some major retailers control channels, especially some major retail stores which quickly fill the city and have strong bargaining power. So the research of Stackelberg game dominated by retailer has a practical significance.

Although they are two different game models, the analysis is consistent; in the first stage of the game, n retailers choose their optimal marginal profit and optimal marketing investment according to the profit function. And in the second stage, manufacturer determines the optimal margins profit and the optimal brand investment. Similar to Section 4.2, we can find the subgame perfect Nash equilibrium of the Stackelberg game led by retailers, which is given by Proposition 4.

Proposition 4. *In the Stackelberg game retailers dominate; the best margins profit, manufacturers' best brand investments, retailers' best-selling investments, and the best reputation are, respectively (the subgame perfect Nash equilibrium),*

$$m_M^{rS*}(t) = \frac{a}{4b}, \qquad m_i^{RS*}(t) = \frac{a}{2b}, \quad i = 1, 2, \ldots, n, \quad (40)$$
$$B_i^{rS*}(t) = \sum_{i=1}^{n} \frac{a^2}{8bc_i} \sqrt{G^{RS*}(t)}, \quad (41)$$
$$B_M^{RS*} = \sum_{i=1}^{n} \frac{a^4}{128b^2(r+\delta)c_M c_i}, \quad (42)$$
$$G^{RS*}(t) = \left(G_0 - \sum_{i=1}^{n} \frac{a^4}{128b^2(r+\delta)\delta c_M c_i}\right) e^{-\delta t} + \sum_{i=1}^{n} \frac{a^4}{128b^2(r+\delta)\delta c_M c_i}. \quad (43)$$

5. Comparative Analysis of Four Types of Game Model and Its Results

In the previous Sections 2, 3, and 4, we have analyzed four game types. And in this section, we care about the result and comparative static analysis mainly from the perspective of consumers, manufacturers, and retailers. For consumers, we only consider retail price. For manufacturer and retailers, we need to analyze their margins profit, manufacturer's brand investments, reputation, retailers' sales investment, and the changes with time.

5.1. Comparative Analysis of Optimal Decision of Channel Members. For the retail prices, according to Assumptions 2, $p_i(t) = m_M(t) + m_i(t)$, $i = 1, 2, \ldots, n$; (9), (28), (36), and (40) are substituted, respectively,

$$p_i^{T*}(t) = \frac{a}{2b}, \qquad p_i^{N*}(t) = \frac{2a}{3b},$$
$$p_i^{\mathrm{MS}*}(t) = \frac{5a}{8b}, \qquad p_i^{\mathrm{RS}*}(t) = \frac{3a}{4b}, \quad i = 1, 2, \ldots, n. \quad (44)$$

So for a customer, there is the following Conclusion 1.

Conclusion 1. Among the coordination game, the noncoordination static game, Stackelberg game led by manufacturer, and Stackelberg game led by n retailers, the best sale price meets

$$p_i^{\mathrm{RS}*}(t) > p_i^{N*}(t) > p_i^{\mathrm{MS}*}(t) > p_i^{T*}(t), \quad i = 1, 2, \ldots, n. \quad (45)$$

Conclusion 1 shows that for consumers, they want channel integration, or channel partners, because the price is the lowest, which coincide with the practice. When n retailers dominate the channels, the retailers have the right to speak and they will set a higher retail price to gain more profit.

Then we analyze the relationship between the manufacturer's optimal decisions. The margins profit in coordinative

game cannot be separated, so we only compare the rest. From (28), (36), and (40), there is Conclusion 2 clearly.

Conclusion 2. Among the noncoordination static game, Stackelberg game led by manufacturer, and Stackelberg game led by n retailers, the manufacturer's optimal profit margins meet

$$m_M^{\mathrm{RS}*}(t) < m_M^{N*}(t) < m_M^{\mathrm{MS}*}(t). \tag{46}$$

It can be seen from this relationship that the manufacturer has a definite right to speak when it is a leading enterprise, and it will naturally increase its margins profit in order to obtain higher profits. But in the channel relationships led by retailers, it is at a subordinate position and then the worst. Conclusion 2 can be obtained easily by comparing (17), (30), (38), and (42).

Conclusion 3. Among the coordination game, the noncoordination static game, Stackelberg game led by manufacturers, and Stackelberg game led by n retailers, the manufacturer's optimal brand investment meets

$$B_M^{\mathrm{RS}*}(t) < B_M^{N*}(t) < B_M^{\mathrm{MS}*}(t) < B_M^{T*}(t). \tag{47}$$

In Conclusion 3, although the manufacturer's brand investment is a function of time, we found optimal brand investment in the four cases has nothing to do with the time; all are constant. Furthermore, comparing the goodwill of the manufacturer, observing (19), (31), (39), and (43), we will find that the optimal reputation expressions of the four conditions have completely symmetrical structure. So, for comparing them, we only need to compare the coefficient; we can obtain Conclusion 4 below.

Conclusion 4. Among the noncoordination static game, Stackelberg game led by manufacturer, and Stackelberg game led by n retailers, the manufacturer's optimal reputation at time t meets

$$G^{\mathrm{RS}*}(t) < G^{N*}(t) < G^{\mathrm{MS}*}(t) < G^{T*}(t); \tag{48}$$

when $t \to +\infty$, the steady state meets

$$G^{\mathrm{RS}*}(+\infty) < G^{N*}(+\infty) < G^{\mathrm{MS}*}(+\infty) < G^{T*}(+\infty). \tag{49}$$

Conclusion 4 shows that the reputation of the four kinds of channel relationship increase or decrease as time; we need to analyze the positive and negative of the coefficient of $e^{\delta t}$ in the expression. But in either case they will converge to their steady state. And from the inequality relation we can see that its reputation is maximum during channel integration.

Then, we analyze n retailers' optimal decision relationship, and we can find Conclusion 5.

Conclusion 5. Among the noncoordination static game, Stackelberg game led by manufacturer, and Stackelberg game led by n retailers, the retailer's optimal margins profit meet

$$m_i^{N*}(t) < m_i^{\mathrm{MS}*}(t) < m_i^{\mathrm{RS}*}(t), \quad i = 1, 2, \ldots, n. \tag{50}$$

For comparing the retailers' optimal investment, let $B_i^*(t) \triangleq g(\cdot)(a^2/bc_i)\sqrt{G^*(t)}$; when $G^*(t)$ meets $G^{\mathrm{RS}*}(t) < G^{N*}(t) < G^{\mathrm{MS}*}(t) < G^{T*}(t)$, corresponding coefficient $g(\cdot)$ does not meet the corresponding relationship. Pradeep and Jain $a_i = 1, r = 0.1$ in [25]. Guiomar and Taboubi took $\delta = 0.5$, $G_0 = 1$ in [29]. In this paper, we take $a = b = 1$, $c_M = c_i = 1$, $r = 0.5$, $\delta = 1$, $G_0 = 1$, $n = 10$, $B_i^{\mathrm{RS}*}(t)$, $B_i^{N*}(t)$, $B_i^{\mathrm{MS}*}(t)$, $B_i^{T*}(t)$ as follows:

$$B_i^{\mathrm{RS}*}(t) = \frac{1}{8}\sqrt{\frac{91}{96}e^{-t} + \frac{5}{96}}, \quad B_i^{N*}(t) = \frac{1}{9}\sqrt{\frac{223}{243}e^{-t} + \frac{20}{243}},$$
$$B_i^{\mathrm{MS}*}(t) = \frac{9}{64}\sqrt{\frac{467}{512}e^{-t} + \frac{45}{512}}, \quad B_i^{T*}(t) = \frac{1}{4}\sqrt{\frac{19}{24}e^{-t} + \frac{5}{24}}. \tag{51}$$

We can see that $B_i^{T*}(t) > B_i^{\mathrm{MS}*}(t) > B_i^{\mathrm{RS}*}(t)$, $B_i^{T*}(t) > B_i^{\mathrm{MS}*}(t) > B_i^{N*}(t)$, but the relationship between $B_i^{\mathrm{RS}*}(t)$ and $B_i^{N*}(t)$ has a tipping point t^0. When $0 \le t < t^0$, it holds that $B_i^{\mathrm{RS}*}(t) > B_i^{N*}(t)$; when $t^0 < t < +\infty$, it holds that $B_i^{\mathrm{RS}*}(t) < B_i^{N*}(t)$; when $t = t^0$, it holds that $B_i^{\mathrm{RS}*}(t) = B_i^{N*}(t)$. It is easy to get $t^0 = \ln(17.2)$. Therefore, there is Conclusion 6.

Conclusion 6. Among the coordination game, noncoordination static game, Stackelberg game led by manufacturers, and Stackelberg game led by n retailers, the retailer's optimal marketing investment meets

(1) $B_i^{T*}(t) > B_i^{\mathrm{MS}*}(t) > B_i^{\mathrm{RS}*}(t)$, $B_i^{T*}(t) > B_i^{\mathrm{MS}*}(t) > B_i^{N*}(t)$;

(2) when $0 \le t < \ln(17.2)$, it holds that $B_i^{\mathrm{RS}*}(t) > B_i^{N*}(t)$, when $\ln(17.2) \le t < +\infty$, it holds that $B_i^{\mathrm{RS}*}(t) < B_i^{N*}(t)$, and when $t = \ln(17.2)$, it holds that $B_i^{\mathrm{RS}*}(t) = B_i^{N*}(t)$.

5.2. Comparative Analysis of Optimal Profit of Channel Members. In Section 4, when calculating the optimal decision variables, there was no calculation of the optimal profit of channel members, mainly because the specific values of constant a, b, c_M, c_i, r, δ, G_0, n were not given. Because the constant values do not affect the conclusion, Chen et al. take $a_i = 1, r = 0.1$ in [24]; Guiomar and Taboubi take $\delta_i = 0.5$, $G_0 = 1$ in [29]. In this paper, $a = b = 1$. $c_M = c_i = 1$, $r = 0.5$, $\delta = 1$, $G_0 = 1$, $n = 10$, and it can be integral to calculate the optimal profit of channel members in four kinds of conditions; see Table 1 (calculation process slightly).

From Table 1, the following results hold.

Conclusion 7. Among the coordination game, noncoordination static game, Stackelberg game led by manufacturer, and Stackelberg game led by n retailers, the optimal profits meet

(1) $\pi_M^{N*} > \sum_1^n \pi_i^{N*}$, $\pi_M^{\mathrm{MS}*} > \sum_1^n \pi_i^{\mathrm{MS}*}$, $\pi_M^{\mathrm{RS}*} < \sum_1^n \pi_i^{\mathrm{RS}*}$;

(2) channel total profits meets $\pi_{\mathrm{total}}^{T*} > \pi_{\mathrm{total}}^{\mathrm{MS}*} > \pi_{\mathrm{total}}^{N*} > \pi_{\mathrm{total}}^{\mathrm{RS}*}$;

Table 1: The optimal profit of 4 channel game relations.

	Channel integration (T)	Static game (N)	Stackelberg game led by manufacturers (MS)	Stackelberg game led by retailers (RS)
Manufacturers' profits		0.089	0.0956	0.0548
The ith retailer's profits		0.00479	0.00775	0.00575
Retailers total profits		0.0479	0.0775	0.0575
Channel total profits	0.2517	0.1369	0.1731	0.1123

(3) for manufacturers $\pi_M^{MS*} > \pi_M^{N*} > \pi_M^{RS*}$;

(4) for retailers $\pi_i^{MS*} > \pi_i^{N*} > \pi_i^{RS*}$.

In Conclusion 7 (1), we can find that in a noncoordination static game and in a Stackelberg game led by manufacturer, the profits of manufacturer are greater than the profits in the Stackelberg game led by n retailers; while in a Stackelberg game led by retailers, the profits of manufacturer are less than the profits in a Stackelberg game led by n retailers. And (2) shows that the maximum channel total profit can be gained when the channel is integrated, which is the pareto optimal state. At the same time, we also found that the channel total profits are the smallest when retailers dominate. From (3) and (4), while retailers can dominate the whole channel, the optimal profit to each retailer is not optimal.

6. Conclusion

This paper studies the optimal decision problems of distribution channel of one manufacturer and n retailers. Only from the perspective of channel types, the models in this paper are the promotion of Xu et al. [6], Martín-Herrán and Taboubi [27], and Jørgensen and Zaccour [26]. This paper sets up four game models including the coordination game, noncoordination static game, Stackelberg game led by manufacturers, and Stackelberg game led by n retailers. Results show that, for consumers, they hope that channel is integration or channel partners because of the lowest price. When n retailers dominate the channel, retailers have voice and they will set higher retail prices to gain more profit; when the manufacturer is a leading enterprise, he has a certain discourse and he will naturally improve its marginal profit in order to obtain higher profits. But in the channel relationships led by retailers, it is at a subordinate position, then the worst. Although the manufacturer's brand investment is a function of time, we find that optimal brand investment in the four cases has nothing to do with the time, all are constant. Intuitively, a product brand investment should be increasing over time, but the rate of increasement is slower and slower, reaching a steady state value, which may be related to model building. It can be seen that in a noncoordination static game and in a Stackelberg game led by manufacturer, the profits of manufacturer are greater than the profits in the Stackelberg game led by n retailers; while in a Stackelberg game led by retailers, the profits of manufacturer are less than the profits in a Stackelberg game led by n retailers. And the maximum channel total profit can be gained when the channel is integrated, which is the pareto optimal state. At the same time, we also found that the channel total profits is the smallest when retailers dominate. That is to say, while retailers can dominate the whole channel, the optimal profit to each retailer is not optimal.

Some problems in this paper need studying continually, for example,

(1) in modeling, the status of n retailers is equal, but in practice a fraction of retailers may be in a dominant position, as in a consumer market, Wal-Mart, and Carrefour, a number of other smaller retailers are a subordinate position;

(2) this paper uses the demand function $q_i(t) = B_i(t)[a - bp_i(t)]\sqrt{G(t)}$. Currently demand function is in a variety of forms and different expressions may differ, so classification research is needed;

(3) channel structures also need generalizing, such as n manufacturers and n retailers. However, mathematics model may be very complex.

Conflict of Interests

The authors declare that there is no conflict of interests regarding the publication of this paper.

Acknowledgments

The authors are particularly grateful to the associate editor and reviewers for thoughtful, valuable discussions and suggestions. The authors thank the financial support by Humanities and Social Science Project of Ministry of Education of China (14XJCZH001), Soft Science Research Project of Sichuan Province (2014ZR0027), Philosophy and Social Science Projects in Sichuan Province (SC14A030), and the Fundamental Research Funds for the Central Universities (JBK1507114, JBK130401), One of the authors also thank their students Huan Zhou and Weida Zhou's contribution to this paper.

References

[1] R. Desiraju and S. Moorthy, "Managing a distribution channel under asymmetric information with performance requirements," *Management Science*, vol. 43, no. 12, pp. 1628–1644, 1997.

[2] H. Baligh and L. E. Richartz, *Vertical Market Structures*, Allyn and Bacon, Boston, Mass, USA, 1967.

[3] T. W. McGuire and R. Staelin, "Channel efficiency, incentive compatibility, transfer pricing and market structure: an equilibrium analysis of channel relationships," in *Research in Marketing*, L. P. Bucklin and J. M. Carman, Eds., vol. 8, JAI Press, Greenwich, Conn, USA, 1986.

[4] A. P. Jeul and S. M. Shugan, "Managing channel profits," *Marketing Science*, vol. 2, pp. 239–272, 1983.

[5] A. T. Coughlan, "Competition and cooperation in marketing channel choice: theory and application," *Marketing Science*, vol. 4, pp. 110–129, 1985.

[6] M. L. Xu, Q. Wang, and L. H. Ouyang, "Coordinating contracts for two-stage fashion supply chain with risk-averse retailer and price-dependent demand," *Mathematical Problems in Engineering*, vol. 2013, Article ID 259164, 12 pages, 2013.

[7] C. Ding, K. H. Wang, and R. Ran, "Marketing channel coordination mechanism based on fairness preference," *Journal of Management Sciences in China*, vol. 16, pp. 80–94, 2013.

[8] C. Ding, K. H. Wang, and S. Y. Lai, "Channel coordination mechanism with retailer having fairness preference-an improved quantity discount mechanism," *Journal of Industrial and Management Optimization*, vol. 9, pp. 967–982, 2013.

[9] C. Ding, K. H. Wang, and X. Y. Huang, "Channels coordination game model based on result fairness preference and reciprocal fairness preference: a behavior game forecasting and analysis method," *Journal of Applied Mathematics*, vol. 2014, Article ID 321958, 11 pages, 2014.

[10] N. Altintas, F. Erhun, and S. Tayur, "Quantity discounts under demand uncertainty," *Management Science*, vol. 54, no. 4, pp. 777–792, 2008.

[11] W. Song, R. Wang, Y. Fu, and X. Peng, "Consumer choice, firm performance and channel coordination in a dual-channel distribution system," *American Journal of Operations Research*, vol. 4, no. 4, pp. 217–227, 2014.

[12] L. Wang, H. Qu, S. Liu, and C. Chen, "Optimizing the joint replenishment and channel coordination problem under supply chain environment using a simple and effective differential evolution algorithm," *Discrete Dynamics in Nature and Society*, vol. 2014, Article ID 709856, 12 pages, 2014.

[13] H. F. Zhao, B. Lin, W. Q. Mao, and Y. Ye, "Differential game analyses of logistics service supply chain coordination by cost sharing contract," *Journal of Applied Mathematics*, vol. 2014, Article ID 842409, 10 pages, 2014.

[14] T. Li, S. P. Sethi, and X. He, "Dynamic pricing, production, and channel coordination with stochastic learning," *Production and Operations Management*, vol. 121, pp. 245–275, 2015.

[15] X. Chen, G. Hao, and L. Li, "Channel coordination with a loss-averse retailer and option contracts," *International Journal of Production Economics*, vol. 150, pp. 52–57, 2014.

[16] X. Wang and S. Webster, "Channel coordination for a supply chain with a risk-neutral manufacturer and a loss-averse retailer," *Decision Sciences*, vol. 38, no. 3, pp. 361–389, 2007.

[17] L. Jiang, Y. Wang, and X. Yan, "Decision and coordination in a competing retail channel involving a third-party logistics provider," *Computers and Industrial Engineering*, vol. 76, pp. 109–121, 2014.

[18] S. S. Yin, T. Nishi, and I. E. Grossmann, "Optimal quantity discount coordination for supply chain optimization with one manufacturer and multiple suppliers under demand uncertainty," *The International Journal of Advanced Manufacturing Technology*, vol. 76, no. 5, pp. 1173–1184, 2015.

[19] L. Rajiv, "Improving channel coordination through franchising," *Marketing Science*, vol. 9, pp. 299–318, 1990.

[20] F. B. Benjamin and R. L. Tracy, "Optimal retail contracts with asymmetric information and moral hazard," *Rand Journal of Economics*, vol. 5, pp. 284–296, 1994.

[21] D. Zissis, G. Ioannou, and A. Burnetas, "Supply chain coordination under discrete information asymmetries and quantity discounts," *Omega—International Journal of Management Science*, vol. 53, pp. 21–29, 2015.

[22] D. T. Luo, W. J. Zhong, X. Q. Zhang, and H. C. Shen, "Side payment incentive of a decentralized supply chain mechanism," *Journal of System Engineering Research*, vol. 16, pp. 236–240, 2001.

[23] H. P. Tian, Y. J. Guo, and Y. D. Yang, "The principal agent problem of multi principals and the principal may cooperate in the distribution system," *The Application of the Theory of System Engineering Methods*, vol. 13, pp. 567–574, 2004.

[24] J. Chen, F. H. Wang, and C. P. Zhao, "The formation mechanism of the marketing channel alliance based on the information asymmetric game," *Journal of Shanghai Jiao Tong University*, vol. 39, pp. 357–366, 2005.

[25] K. C. Pradeep and D. Jain, "A dynamic model of channel member strategies for marketing expenditures," *Marketing Science*, vol. 11, pp. 168–188, 1992.

[26] S. Jørgensen and G. Zaccour, "Channel coordination over time: incentive equilibria and credibility," *Journal of Economic Dynamics and Control*, vol. 27, pp. 801–822, 2003.

[27] G. Martín-Herrán and S. Taboubi, "Stackelberg leadership in a marketing channel," *International Game Theory Review*, vol. 3, no. 1, pp. 13–26, 2001.

[28] G. Martín-Herrán and S. Taboubi, "Price coordination in distribution channels: a dynamic perspective," *European Journal of Operational Research*, vol. 240, no. 2, pp. 401–414, 2015.

[29] G. Martín-Herrán and S. Taboubi, "Shelf-space allocation and advertising decisions in the marketing channel:a differential game approach," *International Game Theory Review*, vol. 7, pp. 313–330, 2005.

[30] Q. R. Pan, *Economic Management Dynamic System Optimization*, vol. 3, University of Science and Technology of China Press, 1993.

[31] J. Z. Yuan, Y. Zhang, and Y. Tong, *The Economic Foundation of Control Theory and Its Applications*, Higher Education Press, Beijing, China, 2004.

[32] Z. Y. Jiang, *Dynamic Optimization*, The Commercial Press, Beijing, China, 2003.

Hindawi Publishing Corporation
Mathematical Problems in Engineering
Volume 2015, Article ID 102606, 9 pages
http://dx.doi.org/10.1155/2015/102606

Research Article

Developing a Robust Strategy Map in Balanced Scorecard Model Using Scenario Planning

Mostafa Jafari, Kamran Shahanaghi, and Majid Tootooni

Department of Industrial Engineering, Iran University of Science & Technology, Tehran 16846-13114, Iran

Correspondence should be addressed to Majid Tootooni; m_tootooni@iust.ac.ir

Received 14 November 2014; Revised 22 February 2015; Accepted 27 February 2015

Academic Editor: Jianxiong Ye

Copyright © 2015 Mostafa Jafari et al. This is an open access article distributed under the Creative Commons Attribution License, which permits unrestricted use, distribution, and reproduction in any medium, provided the original work is properly cited.

The key to successful strategy implementation in an organization is for people in the organization to understand it, which requires the establishment of complicated but vital processes whereby the intangible assets are converted into tangible outputs. In this regard, a strategy map is a useful tool that helps execute this difficult task. However, such maps are typically developed based on ambiguous cause-effect relationships that result from the extrapolation of past data and flawed links with possible futures. However, if the strategy map is a mere reflection of the status quo but not future conditions and does not embrace real-world uncertainties, it will endanger the organization since it posits that the current situation will continue. In order to compensate for this deficiency, the environmental scenarios affecting an organization were identified in the present study. Then the strategy map was developed in the form of a scenario-based balanced scorecard. Besides, the effect of environmental changes on the components of the strategy map was investigated using the strategy maps illustrated over time together with the corresponding cash flow vectors. Subsequently, a method was proposed to calculate the degree of robustness of every component of the strategy map for the contingency of every scenario. Finally, the results were applied to a post office.

1. Introduction

Balanced scorecard (BSC) is a strong tool used in performance assessment by many successful organizations in the world. BSC converts organizational mission and strategies into goals and criteria that are categorized into four dimensions including learning and growth, internal business processes, customer, and financial aspects. Currently, BSC is the only management system that can incorporate strategies into performance and budget in order to answer the existing challenges. In a report published by Organization for Economic Co-operation and Development (OECD) in 2005 on performance assessment and management systems and operational budgeting in public organizations, it was noted that most of the public organizations tended to launch BSC management systems to establish performance management assessment systems.

Strategy map constitutes the foundation of BSC. According to Kaplan and Norton, successful implementation of BSC is based on the exact illustration of cause-effect relations among strategic goals of the organization in its different aspects. Strategy map is a tool that establishes connections among organizational strategies and among the processes and systems that contribute to strategy implementation. It provides the organization and its employees with a straightforward, transparent view so that they know how their jobs and activities would eventually adhere to the comprehensive organizational goals and coordinate their activities.

The burgeoning complexities and increasing changes in technology as well as the changing institutions and environment are the challenges that face businesses continuously. When managers are exposed to challenges of the business environment, their ability to make effective decisions is vital for organizational survival. Considering the measuring of strategic goals, there is often a misconception about the relationships among goals. This misconception lies in that there are uncertainties of the nature of a lack of knowledge about the strength of relations and interactions among components in BSC and strategy map. Since past performance data are used in developing strategy maps in BSC model, the possible future and prospective scenarios are ignored.

The concept of robust strategy map is used in the present study in order to provide for the management of environmental uncertainties based on BSC model. Once environmental uncertainties are addressed in an organization and a strategy map is developed for it, the organization may be better prepared to deal with strategic uncertainties in the long run. In the present study, the environmental scenarios are identified first in order to obtain a robust, resilient strategy map in dealing with environmental uncertainties. Subsequently, net present value (NPV) technique is used to determine the value of every hyperpath on the strategy map in each scenario. Finally, the compatibility of every hyperpath is computed by considering all scenarios in terms of their contingencies. Then the optimal combination of hyperpath choices is determined by considering all scenarios.

This report is designed as follows: the second section reviews the literature on BSC-based performance assessment, strategy map, and scenario-based planning. Then the key theoretical concepts are elaborated on. The methodology and research framework are explained and illustrated schematically in the third section. The proposed methodology is implemented in Iran Post Company, and the obtained results are reported in the fourth section. The last section of this paper is designed to draw conclusions and recommend directions for future studies.

This paper is organized as follows. Section 2 reviews the relevant literature. Our methodology is developed in Section 3. Section 4 is dedicated to a case study in the Iranian Post Company and the numerical results. Finally, Section 5 concludes the paper.

2. Literature Review

2.1. Balanced Scorecard (BSC). BSC was introduced by Kaplan and Norton. It comprises four aspects of growth and learning, internal business processes, customer, and financial dimension. It is a strategic approach and organizational performance management system that can be used to implement perspectives and strategies. This model is considered as a transition from business-unit strategies to a set of relations among criteria, which provides a mechanism to achieve goal-related feedback along with long-term strategic goals. Strategy map is another strong tool introduced by Kaplan and Norton [1]. Organizations use strategy maps to explain the relations among intangible assets and value creation with great precision and transparency. In other words, strategy map is a tool to implement strategy and create a macropicture of the relationships among performance goals of the organization. The main deficiencies of BSC include a lack of time dimension between cause and effect in the strategy map, insufficient relationships among strategy, and operations and excessive concentration on the organizations' inside.

Although the development and utilization of strategy maps can bear advantages, some researchers emphasized their deficiencies [2, 3]. An important concern is that reliance on the relational cause-effect model presented in the strategy map may not be sufficient to reflect the evolutionary trend of strategy over time [4]. Reliance on a static strategy map in the medium term and in the long run would entail the assumption that not only the organization and its strategy remain stable, but also the competitors continue their previous behavior. Besides, once it is assumed that strategy maps have predictability characteristics, a validation question is raised about how the analysis of past data can be a basis for the prediction of future situation.

First of all, strategy maps do not consider the potential time lag in relation to performance indicators. Second, future conditions will change so that the relations that were valid in the past may not be valid in future. Thus, the organization risks designing a map that focuses on the development of linear set of performance indicators irrespective of the potential changes in future [4].

2.2. Scenario Planning. As a useful tool, scenarios help organizations prepare for possible futures and make them more resilient and creative [5]. A scenario refers to the plot of a performance, a line of motion picture, or a TV broadcast [6]. Scenario planning is often used by managers to embody their subjective models for future in order to make better decisions [7]. Scenarios are used to predict the key factors in technology planning, forecast, strategic analysis, and futurology.

Systematic use of scenarios was started after World War II to clarify thinking about future. United States defense system used scenarios as a method of military planning in the 1950s [6, 8–10]. Afterwards, scenario methodology was extensively employed for social prediction, analysis of public policies, and decision-making in the 1960s. The process of scenario construction exerted a strong effect on thought and decision-making process and was considered as the harbinger of public debates [11].

Porter defined scenario as an internal display of what may happen in future, rather than a prediction but an output of possible future [12]. According to Schwartz, scenario analysis is a tool to organize peoples' understanding of future when their decision will be effective [13].

Scenarios can be used to prepare the organization for what may turn out in future. Scenario planning is a qualitative, systematic method to illustrate the possible conditions in future [14]. Using scenario planning, the involved individuals create coherent stories that develop based on the current trends and future perspectives outside the organization [15]. Schwartz contends that two or three scenarios are usually considered [13]. One scenario can be an extrapolation of the status quo (maintaining the current situation). The second can be a description of a bright future that will lead to favorable conditions because the organization is ready to embrace it. The third scenario can depict a pessimistic scenario (e.g., a fragmentation or discontinuity that causes failure due to a lack of organizational readiness).

When scenarios are created, managers can take measures to reduce the risks induced by major uncertainties using the identified opportunities and by keeping the risk within an acceptable limit [15].

2.3. Scenario Planning and Strategy Map. What is evident in most studies on strategy map is the intraorganizational tendency in designing the strategy map. Nevertheless,

extraorganizational parameters that affect organizational performance are overlooked. When the strategy map is developed with an intraorganizational view, the organization will be less prepared to deal with environmental changes in future. Incorporating into the intraorganizational view the impact of possible futures and future trends affecting the organization would provide a comprehensive and favorable combination. Thus, a robust strategy map may be developed by combining the knowledge of environmental uncertainties outside the organization with performance-related intraorganizational knowledge in the BSC model.

As discussed, scenario planning technique is used to display extraorganizational knowledge. A list of potential scenarios affecting the organization can include the knowledge related to environmental uncertainties affecting the organization. The important point here is to combine scenario planning with the strategy map. Buytendijk et al. (2010) conducted a study on the scenario-based strategy map. They developed three scenarios for an organization and a distinctive strategy map for every scenario [16]. Then they compared the strategy maps corresponding to every scenario and determined the strategic goals among them. There were common goals in the strategy maps corresponding to every three scenarios, which they established in the final strategy map as strategic imperatives. Some goals were common in the strategy maps corresponding to two scenarios out of the three, which they maintained in the final strategy map as strategic choices. Finally, they eliminated the goals that existed only in the strategy map corresponding to a single scenario.

2.4. Fuzzy Inference System. Nowadays, researchers use many intelligent techniques such as fuzzy inference system (FIS) and adaptive neuro-fuzzy inference system (ANFIS) as effective tools for modeling engineering systems [17]. Fuzzy inference is considered as the process of mapping a set of input data to a set of output data, which is expressed using fuzzy logic approach. An FIS is a process that formulates human language into if-then rules using fuzzy logic. An FIS usually consists of four major parts including fuzzification, fuzzy rules, fuzzy inference engine, and defuzzification [18]. Scenario planning and strategic planning are cited in the literature as the areas where the above techniques are used.

Moayer et al. (2007) used ANFIS technique to create different scenarios and compensate for the deficiency of experts' linguistic data [19]. Yu and Lo (2009) combined FIS and talent analysis to introduce a new approach to technological strategy planning. By creating a knowledge base, this new approach distinguishes itself from other traditional tools of management decision-making [20]. Molavi and colleagues used multicriteria decision-making and FIS techniques to introduce a quantitative approach to prioritizing strategic enablers of organizational agility [21]. A comparison between FIS and ANFIS techniques in designing an effective information system shows that the results of ANFIS model are more effective due to their integration with neural networks, genetic algorithm, and/or other optimization techniques [22]. In a recent study, Mohanty and Parhi (2014) used ANFIS technique to solve the path planning problem of autonomous mobile robot [17].

One of the shortcomings of the BSC literature is that researchers do not consider the environmental factors in developing the strategy map. In this paper, the environmental factors affecting an organization were identified and their influence on the strategy map is captured. Moreover, the proposed strategy map is developed in the form of a scenario-based balanced scorecard, where the effects of environmental changes on the components of the strategy map are explicitly investigated. To this end, we design a "time-based strategy map" to take into account the time value of strategy map components. The influence of environmental factors on the strategy map components is investigated under different scenarios. Additionally, the degree of robustness of each component of the strategy map in relation to different scenarios is calculated. Subsequently, a method is proposed to calculate the degree of robustness of every component of the strategy map for the contingency of every scenario.

3. Methodology

Nowadays, it is necessary to use performance assessment models consistent with environmental changes due to enormous complexities and increasing changes of organizational environments. As one of the most prevalent models of organizational performance assessment, BSC can adequately adapt to environmental demands. The concept of robust strategy map is used in the present study in order to manage environmental uncertainties based on BSC model. Since past performance data are used to develop strategy maps in BSC model, possible futures and prospective futures are overlooked for the organization. By considering uncertainties of the organizational environment and creating a robust strategy map, one may increase organizational preparedness to deal with the uncertainties in the long run. The main steps taken in implementing the proposed methodology will be illustrated in the form of a conceptual model (see Figure 1). Subsequently, the developmental steps of the proposed model will be explained.

3.1. Developing Organizational Strategy Maps. Organizations tend to use strategy maps in the BSC model in order to create a common understanding of policies and strategies, in which the relationships among key components of the organization and its strategy are visually represented. Every strategy map should include four aspects entitled finance, customer, internal process, and learning & growth. In each aspect, performance objectives should be defined and their causal relationships should be illustrated.

3.2. Partitioning the Strategy Map into Its Components. Once we show cause-effect relations on a strategy map from the lowest perspective (learning and growth) to the topmost perspective (financial), we will have a network of interrelated performance goals. All possible paths on the strategy map begin with one of the learning and growth goals; therefore, every goal on the learning and growth perspective can be considered as the starting point for a set of paths. In other words, the paths that begin with the lowest perspective and

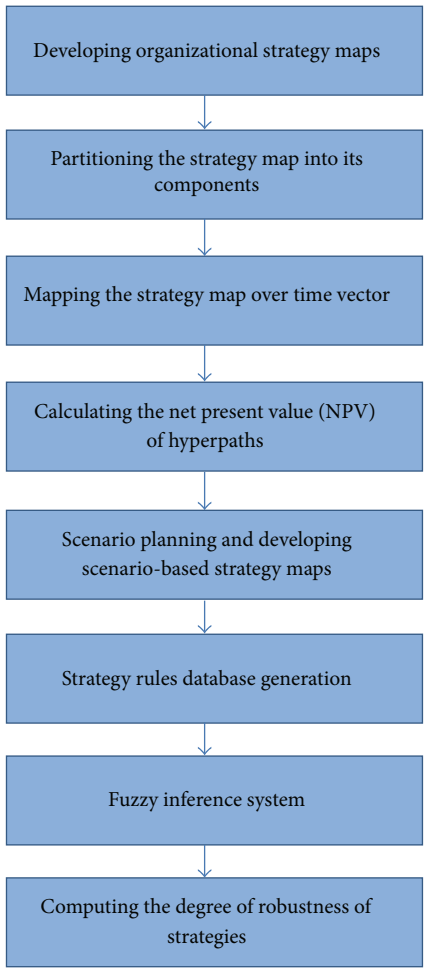

Figure 1: Proposed methodology.

work toward the topmost perspective on the strategy map can be mapped by considering a set of paths. We refer to these sets of paths as hyperpaths that constitute a complete partitioning of the strategy map. It, however, should be noted that hyperpaths overlap so that all of them end in an ultimate goal in the financial perspective. Every hyperpath is a context for strategic value creation in the organization that converts investment in the infrastructural goals to financial results over time. Figure 2 illustrates the portioning of the strategy map into hyperpaths.

3.3. Mapping the Strategy Map over Time Vector. Strategy maps indicate how BSC goals are interrelated and how they contribute to the maximization of the shareholders' profits as a goal in the financial perspective. Since financial goals of the organization in the financial perspective are realized with a time lag, the strategy maps were developed by modeling the time lag in the present study. As higher-order goals of the strategy map occur in future time periods, the cash flows (either cost or revenue) of the organization could be studied on the time vector. Figure 3 shows an example of the time-based strategy map.

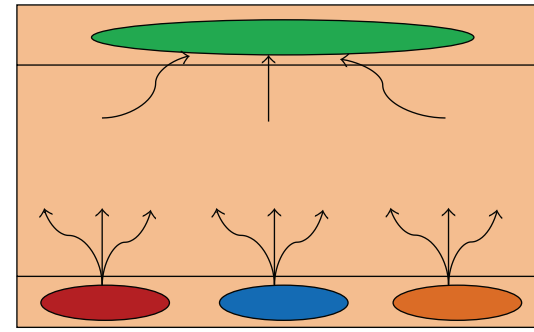

Figure 2: Partitioning the strategy map into hyperpaths.

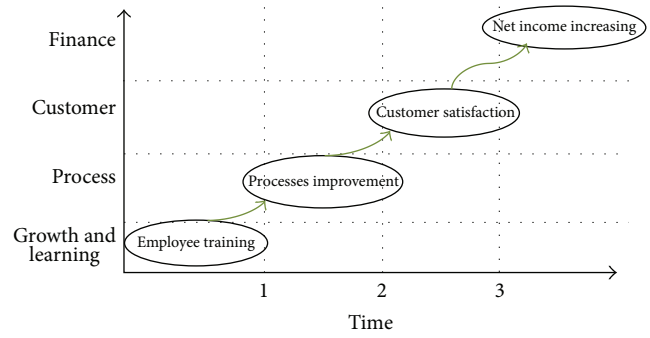

Figure 3: Time-based strategy map.

3.4. Calculating the Net Present Value (NPV) of Hyperpaths. As discussed earlier, an investment in a goal in the BSC learning and growth perspective would lead to an ultimate goal in the financial perspective with a time lag of a few periods. Focus on this time lag clarifies the real value of investment in a hyperpath in the strategy map at present and in future. NPV technique is used to adapt cash flow vector over time periods and transfer it to the present time. In this method, the cash flow (cost or revenue) is discounted at a rate of the day based on the time of occurrence (cost or revenue). In the NPV technique, all costs and revenues are discounted at an adequate rate based on the time of their occurrence. This is done via the following equation [23]:

$$\mathrm{NPV}\,(i, N) = \sum_{t=1}^{N} \frac{\mathrm{FV}_t}{(1+i)^t}, \tag{1}$$

where FV_t is future value in period t, N is the number of periods in the planning horizon and i is annual interest rate.

Period 0 refers to the first year of investment.

Due to uncertainty in estimating future cash flows for every hyperpath, we use interval numbers rather than computing crisp NPV. As explained, every hyperpath can have certain choices. Every choice has a specific cash flow in order to reach higher-order goals; therefore, separate NPVs will be calculated for them. In the next section, we would see that a different NPV is obtained in every hyperpath for different choices. Figure 4 illustrates an example of time-based strategy map with the corresponding cash flow vector.

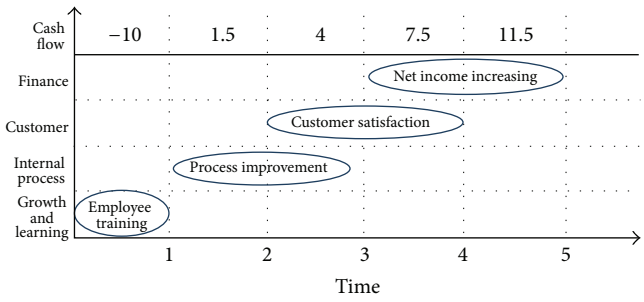

Figure 4: Time-based strategy map and corresponding cash flow over time.

3.5. Scenario Planning and Developing Scenario-Based Strategy Maps. As discussed in Section 2.2, organizations can benefit from the application of scenario analysis to creating the strategy map. The function of scenario analysis is to show how current decisions can affect future results. Scenario analysis can increase the effectiveness of strategy maps. Use of scenario analysis in creating strategy maps can add a contingency and predictive perspective to the standard model of strategy map design.

We employed the scenario analysis technique as proposed in Hanafizadeh et al.'s paper in our methodology [24]. The Hanafizadeh et al. approach has this advantage that each scenario can be described in terms of environmental factors.

When used in the BSC framework, this kind of scenario analysis can assess the value of each organization's strategy in terms of different combination for the environmental factors. The organization strategy itself is a combination of different strategies for different hyperpaths.

3.6. Strategy Rules Database Generation. The values of critical success factors resulting from a strategy should be determined in order to calculate organizational performance for the implementation of a certain strategy. In facing a combination of various values of the stimuli, every strategy reflects certain values of critical success factors for the organization. Specific combinations of environmental stimuli and critical success factors resulting from a strategy implementation can be predicted with regard to the knowledge of experts and decision makers of the organization as well as past data of the organization. FIS can be used to simulate experts' knowledge in predicting future conditions for every strategy, and a knowledge base can be created based on it. Such a knowledge base is able to deduce and express the results of entering new combinations of stimuli values. Consequently, having entered the values of stimuli for every scenario, one can extract the output using the rules established in the knowledge base. In other words, critical success factors derived from strategy implementation is computed after entering the values of every scenario stimuli into such a system. Finally, the organizational performance is obtained for the environmental conditions after the strategy implementation. Experts use linguistic variables to express their idea and knowledge. For example, the value of every linguistic variable can be determined using the set {very small, small, medium, large, and very large}.

Table 1: Hyperpaths strategies.

Hyperpaths	Hyperpaths strategies
A	(1) Providing the organization experts with specialty training (2) Recruiting experts with a high educational profile
B	(1) Creating a comprehensive, Web-based system for all software used in the organization (2) Using different software systems for different organizational sections
C	(1) Promoting management culture in the organization through appointing competent managers (2) Increasing managerial skills in the current managers

3.7. Fuzzy Inference System (FIS). The FIS knowledge base comprises a set of rules extracted from every strategy. Every scenario is defined based on a certain combination of environmental stimuli and is finally expressed with fuzzy numbers. In this system, every scenario is entered into the knowledge base as a separate entry. Then the values of critical success factors are obtained based on FIS engine if-then rules. Finally, organizational performance is calculated via the sum total of their weights.

3.8. Computing the Degree of Robustness of Strategies. The higher the NPV of a strategy per occurrence of all strategies, the more attractive and robust it is. In fact, a strategy that has a better NPV in more contingent scenarios is more acceptable and more robust.

The output obtained from the implementation of FIS is used to compute the degree of the robustness of strategies. If the performance of strategy i under scenario j is shown as R_{ij}, the identical performance of two strategies in two different scenarios does not indicate their identical utility. Rather this figure makes sense when compared with the performance of other strategies in the same scenario. Thus, performance percentage instead of numerical value of performance is used in computing the degree of robustness. The percentage of performance well indicates how much of the whole performance in a scenario is produced by the strategy. Performance percentage is calculated as follows:

$$\%R_{ij} = \frac{R_{ij}}{\sum_i R_{ij}}. \quad (2)$$

The contingency of every scenario is another determining factor that should be addressed in computing the degree of robustness because the identical performance of a strategy in two scenarios with different contingencies means that the strategy will not have identical attractiveness and weight. In other words, the more contingent a scenario is, the higher the weight of strategy performance is. If P_j represents the contingency of scenario j, the following equation is used to

Table 2: Quantitative values of environmental factors under scenarios.

Scenario	Environmental factors					
	Competitors performance		Demand		Alternative services	
	Linguistic	Quantitated	Linguistic	Quantitated	Linguistic	Quantitated
Optimistic	Weak	2	High	7.5	Low	3
Realistic	Mediocre	6	Mean	4	Mean	5
Pessimistic	Strong	8.5	Low	1	High	9

compute the degree of robustness of every strategy for the occurrence of all scenarios [24]:

$$\mathrm{DS} = \sum_{j} \%R_{ij} * P_j. \tag{3}$$

4. Case Study in a Post Company

An Iranian post company was selected to implement the method proposed in the present study. Post services are considered as basic services such as water supply, power, and public education. The postal network conducted through those services is part of the social and economic infrastructure in the country. Considering the importance of and great changes in post services in the developed countries, the post company, selected as the case, suffers serious deficiencies and challenges. The percentage of employment in the post business and the ratio of the number of post offices to the population in Iran are considerably lower than the global average. The diversity, penetration rate, and speed of postal services are below the global standard. In addition to the above deficiencies, changes in post services are necessary due to organizational, legal, and technological factors. It is also necessary to increase productivity and review strategic programs and goals of the post due to the emergence of international competitors, offering postal services in a competitive market and increased role of technology in effective service offering. The above discussion would justify the selection of a post office to implement the proposed method. In this regard, a strategy map was drawn for the selected post company based on the BSC perspectives and cause-effect relations. Then the strategy map was partitioned into its components, hyperpaths, to carry out more exact analyses of financial-economic flows. Every one of the three hyperpaths on the post company strategy map has different choices that are illustrated in Table 1. Every hyperpath will have two choices. Thus, there are eight different combinations ($2 \times 2 \times 2 = 8$) for every scenario.

Like any other organization, post companies are affected by a set of external factors that exert an influence on intraorganizational performance. Table 2 illustrates the quantitative values of environmental factors under every scenario.

The effective stimuli and critical success factors need to be identified in order to determine the exact impact of every external factor on organizational performance. By studying the relationships between these two types of factors for every strategy, a knowledge base can be designed to display organizational performance under every strategy. Table 3 illustrates the strategy rules database designed for the post company.

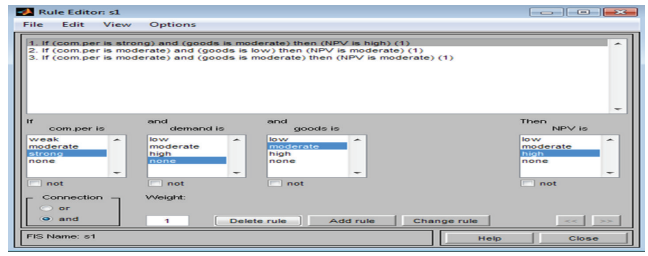

Figure 5: Knowledge base of $A_1B_1C_1$ strategy.

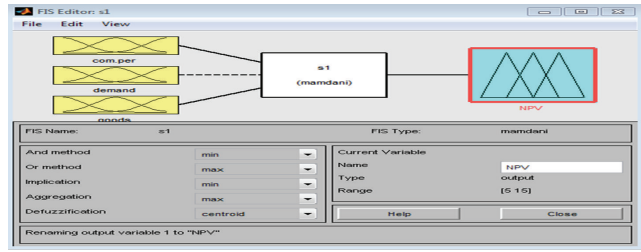

Figure 6: Inputs & outputs in MATLAB.

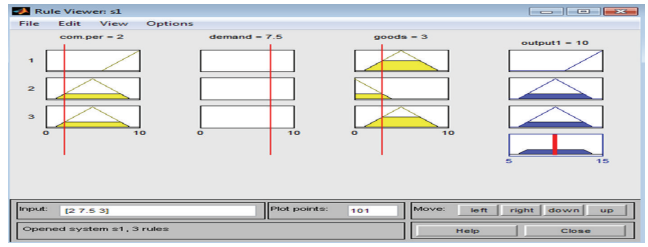

Figure 7: Output of $A_1B_1C_1$ strategy under optimistic scenario.

The data on external stimuli and intraorganizational critical success factors were inserted into the MATLAB software as inputs and outputs, respectively, to develop a fuzzy rules database. Figures 5–7 illustrate the process of the creation of the database in MATLAB software.

Now, the performance of the post company can be predicted based on the developed knowledge base and the occurrence of different environmental scenarios. To this end, every scenario should be defined in terms of environmental factors. The fuzzy inference engine, designed for every strategy, receives every scenario as an input and then displays the output (NPV) in the form of organizational performance in Table 4.

Table 3: Knowledge base of strategies.

	Environmental factors				Organization profitability				
					Cash flow vector				
	Competitors performance	Demand	Alternative services	NPV	t_4	t_3	t_2	t_1	t_0
$A_1B_1C_1$	Strong		Mean	8.4	13	11	6	4	−7
	Mediocre		Low	11.8	14	9	7	2	−8
	Mediocre		Mean	8.7	14	11	5	3	−7
	Strong		High	7.11	13	11	5	4	−9
	Weak		Mean	11.2	12	9	7	2	−8
	Weak		Low	13	12	9	7	2	−10
$A_1B_1C_2$	Mediocre	Mean		10.44	14	10	6	3	−7
	Weak	Mean		11.4	13	10	6	4	−9
	Weak	Low		7.2	13	11	7	3	−7
	Strong	Low		7	12	10	5	3	−8
	Weak	High		13	14	9	5	2	−8
$A_1B_2C_1$	Weak	Mean	High	8	12	11	5	4	−8
	Mediocre	Mean	Low	10	13	11	7	4	−8
	Strong	Low	High	7	12	10	7	3	−7
	Weak	High	Low	13	13	11	6	4	−7
$A_1B_2C_2$		Low	Mean	7.8	14	9	7	2	−8
		Mean	High	8.8	14	11	5	3	−7
		Low	High	7.01	13	11	5	4	−9
		High	Low	12.8	12	9	7	2	−8
$A_2B_1C_1$	Strong	Low	High	7.01	12	9	7	2	−10
	Mediocre	Mean	High	9	14	10	6	3	−7
	Mediocre	Low	Mean	8	13	10	6	4	−9
	Weak	High	Low	13	13	11	7	3	−7
$A_2B_1C_2$		High	Mean	10	12	10	5	3	−8
		Mean	Mean	8.5	14	9	5	2	−8
		High	Low	11	12	11	5	4	−8
		Low	High	7.02	13	11	7	4	−8
$A_2B_2C_1$	Strong	Low		7.4	12	10	7	3	−7
	Weak	High		12.78	14	9	6	3	−8
	Weak	Low		8	12	11	7	2	−7
	Strong	Mean		8.98	13	10	5	2	−7
$A_2B_2C_2$	Weak		Low	10	14	9	7	2	−9
	Mediocre		Mean	8.5	14	10	7	2	−8
	Strong		High	7	13	9	5	4	−9
	Strong		Low	8.2	13	11	5	2	−10

Table 4: Strategies' NPVs under three scenarios.

Scenario	Strategy							
	$A_1B_1C_1$	$A_1B_1C_2$	$A_1B_2C_1$	$A_1B_2C_2$	$A_2B_1C_1$	$A_2B_1C_2$	$A_2B_2C_1$	$A_2B_2C_2$
Scenario 1	12.1	13.5	13.3	13.3	13.3	10	13.5	10
Scenario 2	7.92	10	10	10	10	6.37	6.74	10
Scenario 3	7.87	6.44	6.44	6.37	6.44	6.37	6.44	6.44

For example, the number 12.1 is the output produced by the inference system based on strategy knowledge base $A_1B_1C_1$ under the first scenario with the input {competitors' performance: strong, alternative goods: average}. In order to compute the degree of robustness, we should first normalize the performance of every strategy, extracted from the system as NPV, under every individual scenario. Then, as shown in Table 5, the degree of robustness of every strategy for all potential scenarios was computed using (3). Finally, $A_1B_2C_1$ was selected as the more robust strategy.

Table 5: Degree of robustness of strategies under three scenarios.

Scenarios		Strategies							
		$A_1B_1C_1$	$A_1B_1C_2$	$A_1B_2C_1$	$A_1B_2C_2$	$A_2B_1C_1$	$A_2B_1C_2$	$A_2B_2C_1$	$A_2B_2C_2$
Scenario 1	0.20	0.12	0.14	0.13	0.13	0.13	0.10	0.14	0.10
Scenario 2	0.65	0.11	0.14	0.15	0.14	0.14	0.09	0.09	0.14
Scenario 3	0.15	0.15	0.12	0.12	0.12	0.12	0.12	0.12	0.12
Degree of robustness		0.119	0.132	0.141	0.136	0.137	0.097	0.107	0.130

5. Conclusion

Strategy maps lack the potential to deal with future changes in the organization as they have a retrospective approach. Thus, considering the rapid changes and increasing complexities of organizational environment, it is necessary to consider environmental uncertainties in in the models and outputs of organizational strategic management. Incorporating environmental uncertainties and organizational scenarios in redesigning strategy maps produces a new tool that is most compatible with real environmental conditions in an organization, hence the concept of robust strategy map under uncertain environmental conditions. In the present study, we first determined the choices related to every hyperpath of the strategy map. The combination of these choices constitutes the strategies of the organization. Subsequently, environmental stimuli affecting the organization were identified, and the most important factors were listed. Then fuzzy rules were defined, and the relationships between environmental stimuli and NPV of every strategy were described. A knowledge base was developed. By locating (interpolation and extrapolation) every scenario in the knowledge base, the NPV of every strategy was computed. Finally, the strategies were ranked in terms of their robustness based on the combination of contingency of every scenario and the generated NPV. In other words, the most robust strategy was created by considering all scenarios. Robust strategies have high adaptability in facing environmental changes and good dynamicity over time periods because environmental scenarios are updated continuously.

Conflict of Interests

The authors declare that there is no conflict of interests regarding the publication of this paper.

References

[1] R. S. Kaplan and D. P. Norton, *Strategy Maps: Converting Intangible Assets into Tangible Outcomes*, Harvard Business School Press, Boston, Mass, USA, 2004.

[2] H. Ahn, "Applying the balanced scorecard concept: an experience report," *Long Range Planning*, vol. 34, no. 4, pp. 441–461, 2001.

[3] H. Nørreklit, "The balance on the balanced scorecard—a critical analysis of some of its assumptions," *Management Accounting Research*, vol. 11, no. 1, pp. 65–88, 2000.

[4] R. Othman, "Enhancing the effectiveness of the balanced scorecard with scenario planning," *International Journal of Productivity and Performance Management*, vol. 57, no. 3, pp. 259–266, 2008.

[5] E. Hiltunen, "Scenarios: process and outcome," *Journal of Futures Studies*, vol. 13, no. 3, pp. 151–152, 2009.

[6] F. Roubelat, "Scenario planning as a networking process," *Technological Forecasting and Social Change*, vol. 65, no. 1, pp. 99–112, 2000.

[7] A. Martelli, "Scenario building and scenario planning: state of the art and prospects of evolution," *Futures Research Quarterly*, vol. 17, pp. 57–70, 2001.

[8] P. Durance and M. Godet, "Scenario building: uses and abuses," *Technological Forecasting and Social Change*, vol. 77, no. 9, pp. 1488–1492, 2010.

[9] C. Bezold, "Lessons from using scenarios for strategic foresight," *Technological Forecasting and Social Change*, vol. 77, no. 9, pp. 1513–1518, 2010.

[10] R. Bradfield, G. Wright, G. Burt, G. Cairns, and K. van der Heijden, "The origins and evolution of scenario techniques in long range business planning," *Futures*, vol. 37, no. 8, pp. 795–812, 2005.

[11] J. P. Martino, "A review of selected recent advances in technological forecasting," *Technological Forecasting and Social Change*, vol. 70, no. 8, pp. 719–733, 2003.

[12] M. E. Porter, *Competitive Advantage*, Free Press, New York, NY, USA, 1985.

[13] P. Schwartz, *The Art of the Long View*, Doubleday, New York, NY, USA, 1991.

[14] P. Schoemaker, "Scenario planning: a tool for strategic thinking," *Sloan Management Review*, vol. 36, no. 2, pp. 25–40, 1995.

[15] K. D. Miller and H. G. Waller, "Scenarios, real options and integrated risk management," *Long Range Planning*, vol. 36, no. 1, pp. 93–107, 2003.

[16] F. Buytendijk, T. Hatch, and P. Micheli, "Scenario-based strategy maps," *Business Horizons*, vol. 53, no. 4, pp. 335–347, 2010.

[17] P. K. Mohanty and D. R. Parhi, "Path planning strategy for mobile robot navigation using MANFIS controller," *Advances in Intelligent Systems and Computing*, vol. 247, pp. 353–361, 2014.

[18] N. Saberi and A. Rezaie, "Inference system application in quality analysis for underground water," *Iran Environmental Engineering Journal*, pp. 123–138, 2013.

[19] A. Moayer, P. A. Bahri, and A. Nooraii, "Adaptive neuro-fuzzy inference system for generating scenarios in business strategic planning," in *Proceedings of the IEEE International Conference on Systems, Man and Cybernetics (ISIC '07)*, pp. 109–114, Montreal, Canada, October 2007.

[20] W.-D. Yu and S.-S. Lo, "Patent analysis-based fuzzy inference system for technological strategy planning," *Automation in Construction*, vol. 18, no. 6, pp. 770–776, 2009.

[21] B. Molavi, M. Esmaeilian, and R. Ansari, "Proposing a new approach for prioritization of organizational agility strategies

using FTOPSIS and fuzzy inference system," *IRAN Industrial Management Journal*, vol. 5, no. 1, pp. 123–138, 2014.

[22] B. P. Kaur and H. Aggrarwal, "An optimization of a planning information system using fuzzy inference system and adaptive neuro-fuzzy inference system," *WSEAS Transactions on Information Science and Applications*, vol. 10, no. 8, pp. 249–260, 2013.

[23] M. Y. Khan, *Theory & Problems in Financial Management*, McGraw Hill Higher Education, 1993.

[24] P. Hanafizadeh, M. Rezaei, and A. Ghafouri, "Defining strategic processes in investment companies: an exploration study in Iranian investment companies," *Business Process Management Journal*, vol. 15, no. 1, pp. 20–33, 2009.

Hindawi Publishing Corporation
Mathematical Problems in Engineering
Volume 2015, Article ID 292794, 7 pages
http://dx.doi.org/10.1155/2015/292794

Research Article

Stability of a Class of Stochastic Nonlinear Systems with Markovian Switching

Xiaohua Liu and Wuquan Li

School of Mathematics and Statistics Science, Ludong University, Yantai 264025, China

Correspondence should be addressed to Wuquan Li; sea81@126.com

Received 11 December 2014; Revised 13 August 2015; Accepted 13 August 2015

Academic Editor: Asier Ibeas

Copyright © 2015 X. Liu and W. Li. This is an open access article distributed under the Creative Commons Attribution License, which permits unrestricted use, distribution, and reproduction in any medium, provided the original work is properly cited.

This paper investigates the stability of a class of stochastic nonlinear systems with Markovian switching via output-feedback. Based on the backstepping design method and homogeneous domination technique, an output-feedback controller is constructed to guarantee that the closed-loop system has a unique solution and is almost surely asymptotically stable. The efficiency of the output-feedback controller is demonstrated by a simulation example.

1. Introduction

There are lots of real systems, such as hierarchical control of manufacturing systems, financial engineering, and wireless communications systems, whose structure and parameters may change abruptly. Further, if the occurrence of these events is governed by a Markov chain, these systems are called Markovian jump systems. As one branch of modern control theory, the study of Markovian jump systems has aroused lots of attention with fruitful results achieved for linear case, such as the controllability and observability [1], the stability and stabilization [2–4], H_2 control [5], H_∞ control [6, 7], filtering [8], and model reduction [9]. For semilinear stochastic differential equations with Markovian switching, [10] discusses the stabilization problem; [11] discusses the exponential stability problem for general nonlinear differential equations with Markovian switching. References [12, 13] focus on the controller design for hybrid systems with the global Lipschitz condition or linear growth condition. Based on the backstepping design method developed by [14–17] investigates the control of stochastic systems with Markovian switching.

Considering that the system states are incompletely measurable, the problem of output-feedback control is more important and challenging than that of the state-feedback control in practical applications. Reference [18] addresses the problem of global output-feedback and link position tracking control of robot manipulators despite the fact that only link position measurements are available in the presence of incomplete model information. Reference [19] presents the output-feedback tracking controllers design for an underactuated ship and introduces global nonlinear coordinate changes to transform the ship dynamics to a system affine in the ship velocities to design observers to globally exponentially estimate unmeasured velocities. Reference [20] focuses on the problem of output-feedback tracking control for stochastic Lagrangian systems with the unmeasurable velocity. By using the structural properties of Lagrangian systems, a reduced-order observer is skillfully constructed to estimate the velocity. Inspired by [17], this paper aims to solve the output-feedback stabilization problem for a class of stochastic nonlinear systems with Markovian switching. As demonstrated by [21], due to the fact that these classes of systems' Jacobian linearizations are neither controllable nor feedback linearizable, the existing design tools are hardly applicable.

Compared with the existing results, the contributions of this paper are as follows:

(1) The results in [22] consider the stabilization problem of stochastic nonlinear systems without considering Markovian switching. However, considering that systems may often undergo abrupt disturbances in the practical environment which can be modelled

as Markovian process, thus from both practical and theoretical points of view, the stochastic nonlinear systems model without Markovian switching is somewhat restrictive. This paper considers the Markovian switching version of [22].

(2) Since the drift terms and diffusions terms are all Markovian switching, how to design an effective observer to deal with the unmeasurable states and how to design a control to guarantee that the closed-loop system has a unique solution and is almost surely asymptotically stable are nontrivial work.

The remaining part of this paper is organized as follows. Section 2 offers some preliminary results. The problem investigated is described in Section 3. After that, in Section 4, the output-feedback controller is designed followed by a simulation example to show the effectiveness of the designed controller in Section 5. Finally, the paper is concluded in Section 6.

2. Preliminary Results and Useful Lemmas

The following notations will be used throughout this paper. $\mathbb{R}_+$ denotes the set of all nonnegative real numbers, and $\mathbb{R}^n$ denotes the real n-dimensional space: $\mathbb{R}^{\geq 1}_{\text{odd}} \triangleq \{q \in \mathbb{R} : q \geq 1 \text{ and } q \text{ is a ratio of odd integers}\}$. One has $\overline{x}_i = (x_1, \ldots, x_i)^T$, $\overline{x}_1 = x_1$, and $\overline{x}_n = x$. For a given vector or matrix X, X^T denotes its transpose, $\text{Tr}\{X\}$ denotes its trace when X is square, and $|X|$ is the Euclidean norm of a vector X. $\mathscr{C}^i$ denotes the set of all functions with continuous ith partial derivatives.

Consider the stochastic differential equations with Markovian switching:

$$dx(t) = f(x(t), t, r(t))\,dt + g(x(t), t, r(t))\,d\omega, \quad (1)$$

where $x(t) \in \mathbb{R}^n$ is the state of system; ω is an m-dimensional independent standard Wiener process defined on the complete probability space $(\Omega, \mathscr{F}, \mathscr{F}_t, P)$ with a filtration $\mathscr{F}_t$ satisfying the usual conditions (i.e., it is increasing and right continuous while $\mathscr{F}_0$ contains all P-null sets). Let $r(t)$ be a right-continuous homogeneous Markov process on the probability space taking values in a finite state space $S = \{\mathbf{1}, \mathbf{2}, \ldots, \mathbf{N}\}$ with generator $\Gamma = (\gamma_{\mathbf{pq}})_{\mathbf{N}\times\mathbf{N}}$ given by

$$P_{\mathbf{pq}}(t) = P\{r(t+s) = \mathbf{q} \mid r(s) = \mathbf{p}\} = \begin{cases} \gamma_{\mathbf{pq}} t + o(t) & \text{if } \mathbf{p} \neq \mathbf{q} \\ 1 + \gamma_{\mathbf{pp}} t + o(t) & \text{if } \mathbf{p} = \mathbf{q} \end{cases} \quad (2)$$

for any $s, t \geq 0$. Here $\gamma_{\mathbf{pq}} > 0$ is the transition rate from $\mathbf{p}$ to $\mathbf{q}$ if $\mathbf{p} \neq \mathbf{q}$ while

$$\gamma_{\mathbf{pp}} = -\sum_{\mathbf{q}=1, \mathbf{q}\neq\mathbf{p}}^{N} \gamma_{\mathbf{pq}}. \quad (3)$$

We assume that the Markov process $r(t)$ is independent of the Wiener process $w(t)$. The Borel measurable functions $f : \mathbb{R}^n \times \mathbb{R}_+ \times S \to \mathbb{R}^n$ and $g : \mathbb{R}^n \times \mathbb{R}_+ \times S \to \mathbb{R}^{n\times p}$ are locally Lipschitz in $x \in \mathbb{R}^n$ for all $t \geq 0$.

For $V(x, t, r(t)) \in C^{2,1}(\mathbb{R}^n \times \mathbb{R}_+ \times S; \mathbb{R}_+)$, introduce the infinitesimal generator by

$$\begin{aligned} &\mathscr{L}V(x, t, \mathbf{p}) \\ &\quad = V_t(x, t, \mathbf{p}) + V_x(x, t, \mathbf{p}) f(x, t, \mathbf{p}) \\ &\qquad + \frac{1}{2}\text{Tr}\left[g^T(x, t, \mathbf{p}) V_{xx}(x, t, \mathbf{p}) g(x, t, \mathbf{p})\right] + \text{II}V, \end{aligned} \quad (4)$$

where $\text{II}V = \sum_{\mathbf{q}=1}^{N} \gamma_{\mathbf{pq}} V(x, t, \mathbf{q})$, $V_t(x, t, \mathbf{p}) = \partial V(x, t, \mathbf{p})/\partial t$, $V_x(x, t, \mathbf{p}) = (\partial V(x, t, \mathbf{p})/\partial x_1, \ldots, \partial V(x, t, \mathbf{p})/\partial x_n)$, and $V_{xx}(x, t, \mathbf{p}) = (\partial^2 V(x, t, \mathbf{p})/\partial x_{\mathbf{p}} \partial x_{\mathbf{q}})_{n\times n}$.

Definition 1 (see [14]). A stochastic process $x(t)$ is said to be bounded in probability if the random variable $|x(t)|$ is bounded in probability uniformly in t; that is,

$$\lim_{c\to\infty} \sup_{t>t_0} P\{|x(t)| > c\} = 0. \quad (5)$$

Lemma 2 (see [12]). *For any $l > 0$, define the first exit time η_l as*

$$\eta_l = \inf\{t : t \geq t_0, |x(t)| \geq l\}. \quad (6)$$

Assume that there exist a positive function $V(x, t, r(t)) \in C^{2,1}(\mathbb{R}^n \times \mathbb{R}_+ \times S; \mathbb{R}_+)$ and parameters d and $D \geq 0$ such that

$$\begin{aligned} &EV(x, \eta_l \wedge t, r(\eta_l \wedge t)) \leq De^{d(\eta_l \wedge t - t_0)}, \\ &R \longrightarrow \infty \Longrightarrow V_R = \inf_{t\geq t_0, |x|>R} V(x, t, r(t)) \longrightarrow \infty. \end{aligned} \quad (7)$$

Then for every $x(t_0) = x_0 \in \mathbb{R}^n$ and $r(t_0) = \mathbf{i}_0 \in S$, there exists a solution $x(t) = x(x_0, \mathbf{i}_0; t, r(t))$, unique up to equivalence, of system (1).

Lemma 3 (see [12]). *Let $V(x, t, r(t)) \in C^{2,1}(\mathbb{R}^n \times \mathbb{R}_+ \times S; \mathbb{R}_+)$ and let τ_1, τ_2 be bounded stopping times such that $0 \leq \tau_1 \leq \tau_2$ a.s. If $V(x, t, r(t))$ and $\mathscr{L}V(x, t, r(t))$ are bounded on $t \in [\tau_1, \tau_2]$ a.s., then*

$$\begin{aligned} &E[V(x, \tau_2, r(\tau_2)) - V(x, \tau_1, r(\tau_1))] \\ &\quad = E\int_{\tau_1}^{\tau_2} \mathscr{L}V(x, t, r(t))\,dt. \end{aligned} \quad (8)$$

3. Problem Formulation

Consider the following stochastic nonlinear systems:

$$\begin{aligned} dx_i &= \left(x_{i+1}^{p_i} + f_{i,r(t)}(\overline{x}_i)\right)dt + g_{i,r(t)}^T(\overline{x}_i)\,d\omega, \\ &\qquad i = 1, \ldots, n-1, \\ dx_n &= \left(u^{p_n} + f_{n,r(t)}(\overline{x}_n)\right)dt + g_{n,r(t)}^T(\overline{x}_n)\,d\omega, \\ y &= x_1, \end{aligned} \quad (9)$$

where $x = (x_1, \ldots, x_n)^T \in \mathbb{R}^n$, $u \in \mathbb{R}$, and $y \in \mathbb{R}$ are the system state and control input and output, respectively. $x_2, \ldots, x_n$ are unmeasurable. One has $\overline{x}_i = (x_1, \ldots, x_i)^T$, $i = 1, \ldots, n$. And one has $p_i \in \mathbb{R}^{\geq 1}_{\text{odd}}$, $i = 1, \ldots, n$. The nonlinear functions $f_{i,r(t)} : R^i \times S \to R$ and $g_{i,r(t)} : R^i \times S \to R^r$, $i = 1, \ldots, n$, are assumed to be $\mathscr{C}^1$, vanishing at the origin.

We need the following assumption.

Assumption 4. There are constants $\tau \geq 0$ and $b > 0$ such that

$$\begin{aligned} &\left|f_{i,r(t)}\left(\overline{x}_i\right)\right| \leq b\left(\left|x_1\right|^{(\rho_i+\tau)/\rho_1} + \cdots + \left|x_i\right|^{(\rho_i+\tau)/\rho_i}\right), \\ &\left|g_{i,r(t)}\left(\overline{x}_i\right)\right| \\ &\quad \leq b\left(\left|x_1\right|^{(2\rho_i+\tau)/(2\rho_1)} + \cdots + \left|x_i\right|^{(2\rho_i+\tau)/(2\rho_i)}\right), \end{aligned} \tag{10}$$

where $\rho_1 = 1$ and $\rho_{i+1} = (\rho_i + \tau)/p_i > 0$. Let $\rho_0 = \max_{1\leq i\leq n}\{\rho_i\}$ and $a_i = \rho_0/\rho_i$, $i = 1, \ldots, n$. Meanwhile, one of the following conditions should be satisfied:

Condition (1) $\rho_n + \tau \geq \rho_i$, if $a_i = 1$ or $a_i \geq 2$ for all $i = 1, \ldots, n$.

Condition (2) $\rho_n + \tau \geq 2\rho_i$, otherwise.

Remark 5. When $S = \{\mathbf{1}\}$, $p_i = 1$, and $\tau = 0$, $i = 1, \ldots, n$, Assumption 4 reduces to the natural condition used for output-feedback controller design [14, 15]. Therefore, this assumption is general and reasonable. Condition (1) or condition (2) in Assumption 4 plays an essential role in designing the locally Lipschitz controller, which guarantees the existence and uniqueness of the solution of system (9).

4. Output-Feedback Stabilization of System (9)

By introducing the coordinates

$$\begin{aligned} z_1 &= x_1, \\ z_i &= \frac{x_i}{L^{\iota_i}}, \\ v^{p_n} &= \frac{u^{p_n}}{L^{\iota_n+1}}, \end{aligned} \tag{11}$$

where $\iota_1 = 0$, $\iota_i = (\iota_{i-1} + 1)/p_{i-1}$, and $L > 1$ is a constant to be designed, with (11), system (9) can be written as

$$\begin{aligned} dz_i &= \left(Lz_{i+1}^{p_i} + \frac{f_{i,r(t)}\left(\overline{x}_i\right)}{L^{\iota_i}}\right)dt + \frac{g_{i,r(t)}^T\left(\overline{x}_i\right)}{L^{\iota_i}}d\omega, \\ &\qquad i = 1, \ldots, n-1, \\ dz_n &= \left(Lv^{p_n} + \frac{f_{n,r(t)}\left(\overline{x}_n\right)}{L^{\iota_n}}\right)dt + \frac{g_{n,r(t)}^T\left(\overline{x}_n\right)}{L^{\iota_n}}d\omega, \\ y &= z_1, \end{aligned} \tag{12}$$

whose nominal nonlinear system is

$$\begin{aligned} dz_i &= z_{i+1}^{p_i}dt, \quad i = 1, \ldots, n-1, \\ dz_n &= v^{p_n}dt, \\ y &= z_1. \end{aligned} \tag{13}$$

The design of output-feedback controller for system (9) is divided into three steps. In Step 1, one supposes that the states are available for measurement, and a state-feedback controller is designed for nominal nonlinear system (13). Then in Step 2, by constructing a reduced-order observer, an output-feedback controller is designed for (13). Finally, by using the homogeneous domination technique, the output-feedback stabilization problem is solved for system (9).

For simplicity, we assume $\tau \in \mathbb{R}^+_{\text{even}} = \{q/d : q \text{ being an even integer and } d \text{ being an odd integer}\}$. Under this assumption, we know that $\rho_i \in \mathbb{R}^+_{\text{odd}}$.

Choose $l \geq 1$ to satisfy $\rho_n + \tau \geq (\rho_i + \tau)/l$ and $\rho_0 \geq (\rho_i + \tau)/l$, $i = 1, \ldots, n$. With Assumption 4, σ is chosen in the following manner:

(a) Choose $\sigma = \rho_0$ if condition (1) of Assumption 4 is satisfied.

(b) σ can be chosen as any $\sigma \in \mathbb{R}^+_{\text{odd}}$ satisfying $\rho_n + \tau \geq \sigma \geq \max_{1\leq i\leq n}\{(\rho_i + \tau)/l, 2\rho_i\}$ if condition (2) of Assumption 4 holds.

Step 1 (state-feedback controller design for nominal nonlinear system (13)). We introduce the following transformation:

$$\begin{aligned} \xi_1 &= z_1^{\sigma/\rho_1}, \\ \xi_k &= z_k^{\sigma/\rho_k} - z_k^{*\sigma/\rho_k}, \quad k = 2, \ldots, n, \\ z_1^* &= 0, \\ z_s^* &= -\xi_{s-1}^{\rho_s/\sigma}\alpha_{s-1}^{\rho_s/\sigma}, \quad s = 2, \ldots, n+1, \end{aligned} \tag{14}$$

where α_i, $1 \leq i \leq n$, are positive constants to be designed later.

By choosing the Lyapunov function

$$\begin{aligned} V_n\left(\overline{z}_n\right) &= \sum_{k=1}^{n}\int_{z_k^*}^{z_k}\left(s^{\sigma/\rho_k} - z_k^{*\sigma/\rho_k}\right)^{(4l\sigma-\tau-\rho_k)/\sigma}ds \\ &\triangleq \sum_{k=1}^{n}W_k, \end{aligned} \tag{15}$$

one has

$$\begin{aligned} \mathscr{L}V_n\left(\overline{z}_n\right) &= \sum_{k=1}^{n-1}\frac{\partial W_k}{\partial z_k}z_{k+1}^{p_k} + \frac{\partial W_n}{\partial z_n}v^{p_n} + \sum_{k=1}^{n}\sum_{i=1}^{k-1}\frac{\partial W_k}{\partial z_i}z_{i+1}^{p_i} \\ &= \sum_{k=1}^{n-1}\frac{\partial W_k}{\partial z_k}\left(z_{k+1}^{p_k} - z_{k+1}^{*p_k}\right) \end{aligned}$$

$$-\sum_{k=1}^{n-1}\frac{\partial W_k}{\partial z_k}\xi_k^{\rho_{k+1}p_k/\sigma}\alpha_k^{\rho_{k+1}p_k/\sigma}+\frac{\partial W_n}{\partial z_n}v^{p_n}+\sum_{k=1}^{n}\sum_{i=1}^{k-1}\frac{\partial W_k}{\partial z_i}\left(\xi_{i+1}-\xi_i\alpha_i\right)^{\rho_{i+1}p_i/\sigma}. \tag{16}$$

Note that

$$\frac{\partial W_k}{\partial z_i}=-\frac{4l\sigma-\tau-\rho_k}{\sigma}\frac{\partial z_k^{*\sigma/\rho_k}}{\partial z_i}\cdot\int_{z_k^*}^{z_k}\left(s^{\sigma/\rho_k}-z_k^{*\sigma/\rho_k}\right)^{((4l-1)\sigma-\tau-\rho_k)/\sigma}ds, \tag{17}$$

$$\frac{\partial W_k}{\partial z_k}=\xi_k^{(4l\sigma-\tau-\rho_k)/\sigma},$$

where $i=1,\ldots,k-1$. By (17) and Young's inequality in [14], one gets

$$\sum_{k=1}^{n-1}\frac{\partial W_k}{\partial z_k}\left(z_{k+1}^{p_k}-z_{k+1}^{*p_k}\right)\le\sum_{k=1}^{n-1}\sum_{i=1}^{k-1}d_{k,i,1}\xi_i^{4l}+\sum_{k=1}^{n-1}b_{k,1}\xi_k^{4l},$$

$$\sum_{k=1}^{n}\sum_{i=1}^{k-1}\frac{\partial W_k}{\partial z_i}\left(\xi_{i+1}-\xi_i\alpha_i\right)^{\rho_{i+1}p_i/\sigma}\le\sum_{k=1}^{n}\sum_{i=1}^{k-1}d_{k,i,2}\xi_i^{4l}+\sum_{k=1}^{n}b_{k,2}\xi_k^{4l}, \tag{18}$$

where $d_{1,i,1}=d_{1,i,2}=0$, $d_{k,i,1}$, $d_{k,i,2}$, $b_{k,1}$ and $b_{k,2}$ are positive constants.

Substituting (18) into (16), one gets

$$\begin{aligned}\mathscr{L}V_n\left(\overline{z}_n\right)=&-\sum_{k=1}^{n-2}\left(\alpha_k^{(\rho_k+\tau)/\sigma}-\sum_{i=k+1}^{n-1}\left(d_{i,k,1}+d_{i,k,1}\right)\right.\\&\left.-b_{k,1}-b_{k,2}\right)\xi_k^{4l}-\left(\alpha_{n-1}^{(\rho_{n-1}+\tau)/\sigma}-d_{n,n-1,2}-b_{n-1,1}\right.\\&\left.-b_{n-1,2}\right)\xi_{n-1}^{4l}+\xi_n^{(4l\sigma-\tau-\rho_n)/\sigma}\left(v^{p_n}-z_{n+1}^{*p_n}\right)\\&-\left(\alpha_n^{(\rho_n+\tau)/\sigma}-b_{n,2}\right)\xi_n^{4l}.\end{aligned} \tag{19}$$

Choosing

$$\alpha_k=\left(1+\sum_{i=k+1}^{n-1}\left(d_{i,k,1}+d_{i,k,1}\right)+b_{k,1}+b_{k,2}\right)^{\sigma/(\rho_k+\tau)},\quad k=1,\ldots,n-2,$$

$$\alpha_{n-1}=\left(1+d_{n,n-1,2}+b_{n-1,1}+b_{n-1,2}\right)^{\sigma/(\rho_{n-1}+\tau)},$$

$$\alpha_n=\left(1+b_{n,2}\right)^{\sigma/(\rho_n+\tau)}, \tag{20}$$

one has

$$\mathscr{L}V_n\left(\overline{z}_n\right)\le-\sum_{k=1}^{n}\xi_k^{4l}+\xi_n^{(4l\sigma-\tau-\rho_n)/\sigma}\left(v^{p_n}-z_{n+1}^{*p_n}\right). \tag{21}$$

Step 2 (output-feedback controller design for nominal nonlinear system (13)). Since $z_2,\ldots,z_n$ are unmeasurable, we construct a homogeneous observer:

$$\begin{aligned}\dot{\eta}_k&=-l_{k-1}\widehat{z}_k^{p_{k-1}},\\\widehat{z}_k&=\left(\eta_k+l_{k-1}\widehat{z}_{k-1}\right)^{\rho_k/\rho_{k-1}},\end{aligned} \tag{22}$$

where l_{k-1} is a constant gain which can be selected by a similar manner in [22], $k=2,\ldots,n$, and $\widehat{z}_1=z_1$. By replacing z_i with $\widehat{z}_i$ in z_{n+1}^*, one obtains the output-feedback controller:

$$\begin{aligned}v\left(\widehat{z}\right)=-\alpha_n\left(\widehat{z}_n^{\sigma/\rho_n}+\alpha_{n-1}\widehat{z}_{n-1}^{\sigma/\rho_{n-1}}+\cdots\right.\\\left.+\alpha_{n-1}\alpha_{n-2}\cdots\alpha_1 z_1^{\sigma/\rho_1}\right)^{\rho_{n+1}/\sigma},\end{aligned} \tag{23}$$

where $\widehat{z}=(z_1,\widehat{z}_2,\ldots,\widehat{z}_n)^T$. Choose

$$\begin{aligned}&U\left(\eta_2,\ldots,\eta_n\right)\\&=\sum_{i=2}^{n}\int_{\gamma_i}^{z_i^{(4l\sigma-\tau-\rho_{i-1})/\rho_i}}\left(s^{\rho_{i-1}/(4l\sigma-\tau-\rho_{i-1})}-\gamma_i\right)ds,\end{aligned} \tag{24}$$

where $\gamma_i=\eta_i+l_{i-1}z_{i-1}$.

The following design procedure proceeds in the similar way as (22)–(35) in [22]. One can obtain

$$\mathscr{L}V\left(z_1,\ldots,z_n,\eta_2,\ldots,\eta_n\right)\le-\frac{1}{2}\left(\sum_{i=1}^{n}\xi_i^{4l}+\sum_{i=2}^{n}e_i^{4l}\right), \tag{25}$$

where $e_i=(z_i^{p_{i-1}}-\widehat{z}_i^{p_{i-1}})^{\sigma/(\rho_i p_{i-1})}$, $i=2,\ldots,n$, and $V(z_1,\ldots,z_n,\eta_2,\ldots,\eta_n)=V_n(z_1,\ldots,z_n)+U(\eta_2,\ldots,\eta_n)$.

The construction of $V(z_1,\ldots,z_n,\eta_2,\ldots,\eta_n)$ indicates that $V(z_1,\ldots,z_n,\eta_2,\ldots,\eta_n)$ is positive definite and proper with respect to $Z=(z_1,\ldots,z_n,\eta_2,\ldots,\eta_n)^T$.

Hence, (25) implies that the closed-loop system described by the compact form

$$\begin{aligned}dZ&=E\left(Z\right)dt\\&=\left(z_2^{p_1},\ldots,z_n^{p_{n-1}},v^{p_n}\left(\widehat{z}\right),f_{n+1},\ldots,f_{2n-1}\right)^T dt\end{aligned} \tag{26}$$

is globally asymptotically stable, where $f_i=-l_{i-n}\widehat{z}_{i-n+1}^{p_{i-n}}$, $i=n+1,\ldots,2n-1$.

By introducing the dilation weight

$$\Delta=\left(\underbrace{\rho_1,\rho_2,\ldots,\rho_n}_{\text{for } z_1,\ldots,z_n},\underbrace{\rho_1,\rho_2,\ldots,\rho_{n-1}}_{\text{for } \eta_2,\ldots,\eta_n}\right), \tag{27}$$

we know that (26) is homogeneous of degree τ.

Step 3 (homogeneous output-feedback controller design for (9)). For system (12), we construct a homogeneous observer:

$$\begin{aligned}\dot{\eta}_k&=-Ll_{k-1}\widehat{z}_k^{p_{k-1}},\\\widehat{z}_k&=\left(\eta_k+l_{k-1}\widehat{z}_{k-1}\right)^{\rho_k/\rho_{k-1}},\end{aligned}\quad k=2,\ldots,n, \tag{28}$$

where $l_1, \ldots, l_{n-1}$ are defined in (22). We use the output-feedback controller with the same structure as (23); specifically,

$$\upsilon(\widehat{z}) = -\alpha_n \left(\widehat{z}_n^{\sigma/\rho_n} + \alpha_{n-1}\widehat{z}_{n-1}^{\sigma/\rho_{n-1}} + \cdots + \alpha_{n-1}\alpha_{n-2}\cdots\alpha_1 z_1^{\sigma/\rho_1}\right)^{\rho_{n+1}/\sigma}. \tag{29}$$

Considering the closed-loop system (12), (28)-(29) can be written as

$$dZ = LE(Z)\,dt + F_{r(t)}(Z)\,dt + G_{r(t)}^T(Z)\,d\omega, \tag{30}$$

where

$$\begin{aligned} F_{r(t)}(Z) &= \left(f_{1,r(t)}(x_1), \frac{f_{2,r(t)}(\overline{x}_2)}{L^{\iota_2}}, \ldots, \frac{f_{n,r(t)}(\overline{x}_n)}{L^{\iota_n}}, 0, \ldots, 0\right)^T, \\ G_{r(t)}(Z) &= \left(g_{1,r(t)}(x_1), \frac{g_{2,r(t)}(\overline{x}_2)}{L^{\iota_2}}, \ldots, \frac{g_{n,r(t)}(\overline{x}_n)}{L^{\iota_n}}, 0, \ldots, 0\right)^T. \end{aligned} \tag{31}$$

Now, we state the main results in this paper.

Theorem 6. *If Assumption 4 holds for the stochastic high-order nonlinear system (9), with (11) and (28), under the output-feedback controller (29) with* $L > L^* = \max\{((c_0 + \widetilde{c}_0)/\underline{c}_0)^{1/\gamma}, 1\}$, *where* c_0, $\widetilde{c}_0$, $\underline{c}_0$, *and* γ *are positive constants, then one has the following:*

(1) *For every* $x(t_0) = x_0 \in \mathbb{R}^n$ *and* $r(t_0) = i_0 \in S$, *the closed-loop system has a solution* $x(t) = x(x_0, i_0; t, r(t))$, *unique up to equivalence.*

(2) *For any* $x_0 \in \mathbb{R}^n$ *and* $i_0 \in S$, *the solution of the closed-loop systems is almost surely asymptotically stable.*

Proof. By the definition of V, we can conclude that

$$V_R = \inf_{t\geq t_0, |Z|>R} V(Z(t)) \longrightarrow \infty \Longleftrightarrow R \longrightarrow \infty. \tag{32}$$

From (21) and (25), considering that $V(Z)$ and $E(Z)$ are homogeneous of degree $4l\sigma-\tau$ and τ, respectively, one obtains

$$\frac{\partial V}{\partial Z}E(Z) \leq -\underline{c}_0 \|Z\|_\Delta^{4l\sigma} \tag{33}$$

for a constant $\underline{c}_0 > 0$.

In view of Assumption 4, $L > 1$, one gets

$$\left|\frac{f_{i,r(t)}(\overline{x}_i)}{L^{\iota_i}}\right| \leq \delta L^{1-\gamma_i}\sum_{j=1}^{i}\left|z_j\right|^{(\rho_i+\tau)/\rho_j} \leq \overline{\delta}L^{1-\gamma_i}\|Z\|_\Delta^{\rho_i+\tau}, \tag{34}$$

where δ, $\overline{\delta}$, and γ_i are positive constants. By (34), noting that $\partial V/\partial Z_i$ is homogeneous of degree $4l\sigma - \tau - r_i$, one arrives at

$$\frac{\partial V}{\partial Z}F_{r(t)}(Z) = \sum_{i=1}^{n}\frac{\partial V}{\partial Z_i}\cdot\frac{f_{i,r(t)}(\overline{x}_i)}{L^{\iota_i}} \leq c_0 L^{1-\gamma_0}\|Z\|_\Delta^{4l\sigma}, \tag{35}$$

where $\gamma_0 = \min\{\gamma_i\}_{1\leq i\leq n}$ and $c_0 > 0$ is a constant.

Similar to (35), we can obtain

$$\frac{1}{2}\operatorname{Tr}\left\{G_{r(t)}\frac{\partial^2 V}{\partial Z^2}G_{r(t)}^T\right\} \leq \widetilde{c}_0 L^{1-\widetilde{\gamma}_0}\|Z\|_\Delta^{4l\sigma}, \tag{36}$$

where $\widetilde{\gamma}_0 > 0$ and $\widetilde{c}_0 > 0$ are constants.

From (33), (35), and (36), noting that $\underline{c}_0$ is independent of c_0 and $\widetilde{c}_0$, for system (30), we have

$$\begin{aligned} \mathscr{L}V|_{(30)} &= L\frac{\partial V}{\partial Z}E(Z) + \frac{\partial V}{\partial Z}F_{r(t)}(Z) \\ &\quad + \frac{1}{2}\operatorname{Tr}\left\{G_{r(t)}\frac{\partial^2 V}{\partial Z^2}G_{r(t)}^T\right\} + \sum_{\mathbf{s}=1}^{N}\gamma_{i\mathbf{s}}V_{\mathbf{s}} \\ &\leq -L\underline{c}_0\|Z\|_\Delta^{4l\sigma} + (c_0 + \widetilde{c}_0)L^{1-\gamma}\|Z\|_\Delta^{4l\sigma} \\ &\quad + \sum_{\mathbf{s}=1}^{N}\gamma_{i\mathbf{s}}V_{\mathbf{s}} \\ &\leq -L\left(\underline{c}_0 - (c_0 + \widetilde{c}_0)L^{-\gamma}\right)\|Z\|_\Delta^{4l\sigma} + \sum_{\mathbf{s}=1}^{N}\gamma_{i\mathbf{s}}V_{\mathbf{s}}, \end{aligned} \tag{37}$$

where $\gamma = \min\{\gamma_0, \widetilde{\gamma}_0\} > 0$. □

From the definition of L, one has $\underline{c}_0 - (c_0 + \widetilde{c}_0)L^{-\gamma} > 0$. By checking the controller design process, one can obtain $\sum_{\mathbf{s}=1}^{N}\gamma_{i\mathbf{s}}V_{\mathbf{s}} = 0$.

For any $l > 0$, define the first exit time:

$$\eta_l = \inf\{t : t \geq t_0,\ |Z| \geq l\}. \tag{38}$$

Let $t_l = \eta_l \wedge t$ for any $t \geq t_0$. $|Z|$ is bounded in the interval $[t_0, t_l]$ a.s., which implies that $V(Z)$ is bounded on $[t_0, t_l]$ a.s. From (37), it can be obtained that $\mathscr{L}V$ is also bounded on $[t_0, t_l]$ a.s.

By Lemma 3, one can get

$$EV(\Lambda(t_l, r(t_l))) \leq EV(\Lambda(t_0, r(t_0))) + \overline{\lambda}(t_l - t_0). \tag{39}$$

By (32), (39), and Lemma 2, conclusion (1) holds.

With (37) and the definition of V, by using Theorem 2.1 in [13], conclusion (2) holds.

Remark 7. The unique features of the approaches proposed in this paper include the following:

(1) This paper is the first result about the output-feedback control of stochastic nonlinear systems with Markovian switching and uncontrollable linearizations.

(2) Since the drift terms and diffusions terms are all Markovian switching, a homogeneous domination approach is developed in this paper, which can effectively deal with the Markovian switching and uncontrollable linearizations simultaneously.

5. A Simulation Example

Consider the following system with two modes. The Markov process $r(t)$ belongs to the space $S = \{1, 2\}$ with generator

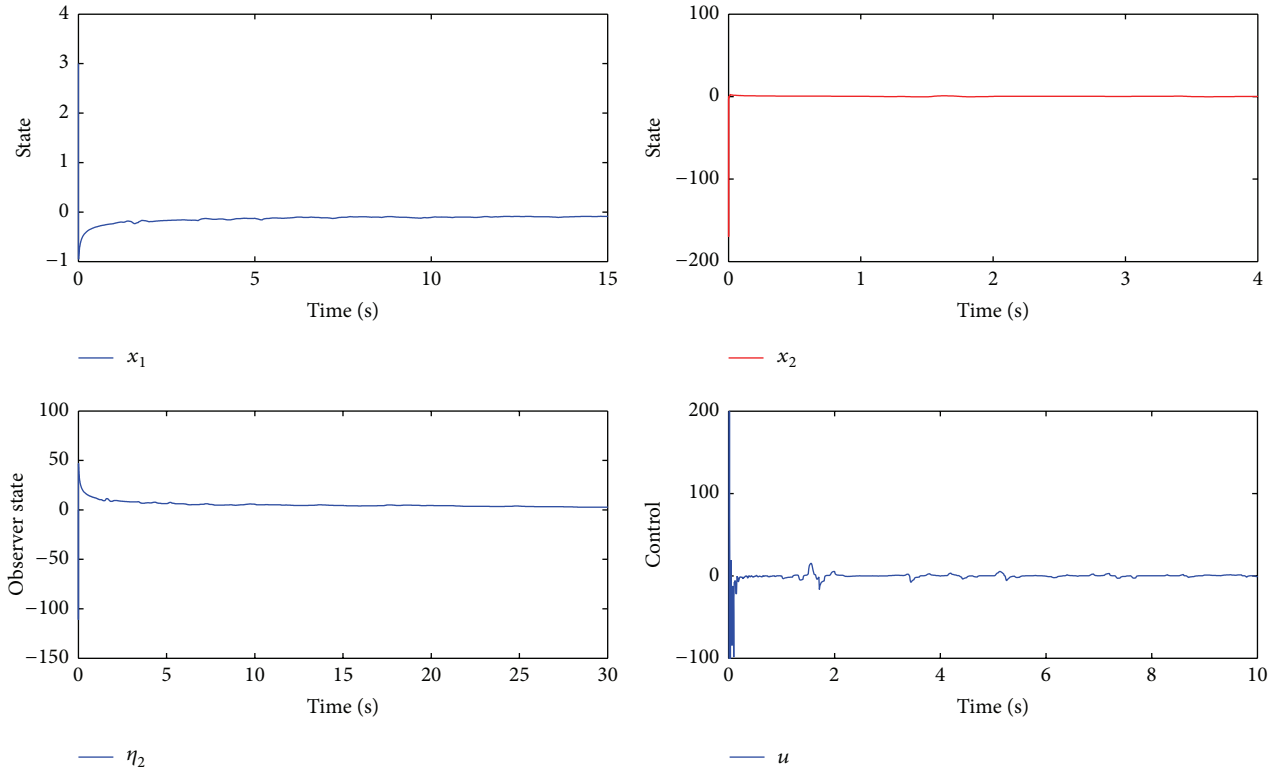

Figure 1: The responses of closed-loop system (40)-(41).

$\Gamma = (\gamma_{pq})_{2\times 2}$ given by $\gamma_{11} = -1$, $\gamma_{12} = 1$, $\gamma_{21} = 2$, and $\gamma_{22} = -2$. One gets $\pi_1 = 2/3$ and $\pi_2 = 1/3$.

The system is described by

$$\begin{aligned} dx_1 &= \left(x_2^3 + f_{1,r(t)}(x_1)\right) dt + g_{1,r(t)}^T(x_1)\, d\omega, \\ dx_2 &= \left(u + f_{2,r(t)}(\bar{x}_2)\right) dt + g_{2,r(t)}^T(\bar{x}_2)\, d\omega, \\ y &= x_1, \end{aligned} \tag{40}$$

where $f_{1,\mathbf{1}}(x_1) = (1/4)x_1^{2/3}(\sin x_1)^3$, $f_{2,\mathbf{1}}(x_1) = (1/4)x_2^3$, $f_{1,2}(\bar{x}_2) = (1/4)x_1^2 \sin x_1$, $f_{2,2}(\bar{x}_2) = (1/3)x_2 \sin^2 x_2$, $g_{1,\mathbf{1}}(x_1) = (1/8)x_1 \sin x_1$, $g_{2,\mathbf{1}}(x_1) = (1/8)x_2^{1/11}(\sin x_2)^2$, $g_{1,2}(\bar{x}_2) = x_1^{4/3} \sin x_1$, and $g_{2,2}(\bar{x}_2) = x_2 \cos^2 x_2$.

Here, without detailed arguments, we only state the final results as follows:

$$\begin{aligned} \dot{\eta}_2 &= -400\left(\eta_2 + 50x_1\right)^{11/3}, \\ u(x_1, \eta_2) &= -226\left(\left(\eta_2 + 50x_1\right)^{11/3} + 2x_1^{11/3}\right)^{35/33}. \end{aligned} \tag{41}$$

In the simulation, one chooses the initial values $x_1(0) = 3$, $x_2(0) = 0.1$, and $\eta_2(0) = -0.01$. Figure 1 gives the responses of (40)-(41), from which the efficiency of the controller is demonstrated. Figure 2 shows the runs of the Markov process $r(t)$.

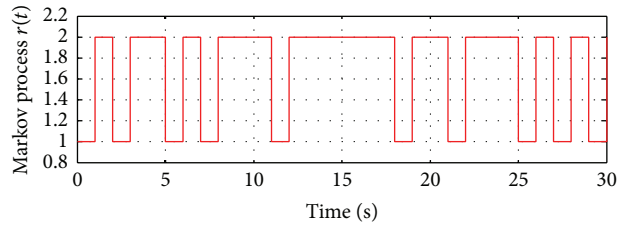

Figure 2: Runs of Markov process $r(t)$.

6. Conclusions

This paper investigates the output-feedback stabilization of stochastic nonlinear systems with Markovian switching for the first time. By using the backstepping design method and homogeneous domination technique, an output-feedback controller is constructed to guarantee that the closed-loop system is almost surely asymptotically stable.

There are some related problems for further consideration, for example, how to generalize the results in this paper to more general stochastic nonlinear systems with plant and parameter uncertainties.

Conflict of Interests

The authors declare that there is no conflict of interests regarding the publication of this paper.

Acknowledgments

This work is supported by the National Natural Science Foundation of China (nos. 61174097 and 61573179) and by Promotive Research Fund for Excellent Young and Middle-Aged Scientists of Shandong Province (no. BS2013DX001).

References

[1] Y. Ji and H. J. Chizeck, "Controllability, stabilizability, and continuous-time Markovian jump linear quadratic control," *IEEE Transactions on Automatic Control*, vol. 35, no. 7, pp. 777–788, 1990.

[2] X. Feng, K. A. Loparo, Y. Ji, and H. J. Chizeck, "Stochastic stability properties of jump linear systems," *IEEE Transactions on Automatic Control*, vol. 37, no. 1, pp. 38–53, 1992.

[3] P. Shi, Y. Xia, G. P. Liu, and D. Rees, "On designing of sliding-mode control for stochastic jump systems," *IEEE Transactions on Automatic Control*, vol. 51, no. 1, pp. 97–103, 2006.

[4] E. K. Boukas, P. Shi, and K. Benjelloun, "On stabilization of uncertain linear systems with jump parameters," *International Journal of Control*, vol. 72, no. 9, pp. 842–850, 1999.

[5] O. L. V. Costa, J. B. R. Do Val, and J. C. Geromel, "Continuous-time state-feedback H_2-control of Markovian jump linear systems via convex analysis," *Automatica*, vol. 35, no. 2, pp. 259–268, 1999.

[6] D. P. de Farias, J. C. Geromel, J. B. R. do Val, and O. L. V. Costa, "Output feedback control of Markov jump linear systems in continuous-time," *IEEE Transactions on Automatic Control*, vol. 45, no. 5, pp. 944–949, 2000.

[7] P. Shi and E. K. Boukas, "H∞-control for Markovian jumping linear systems with parametric uncertainty," *Journal of Optimization Theory and Applications*, vol. 95, no. 1, pp. 75–99, 1997.

[8] S. Xu, T. Chen, and J. Lam, "Robust H_∞ filtering for uncertain Markovian jump systems with mode-dependent time delays," *IEEE Transactions on Automatic Control*, vol. 48, no. 5, pp. 900–907, 2003.

[9] L. Zhang, B. Huang, and J. Lam, "H_∞ model reduction of Markovian jump linear systems," *Systems and Control Letters*, vol. 50, no. 2, pp. 103–118, 2003.

[10] G. K. Basak, A. Bisi, and M. K. Ghosh, "Stability of a random diffusion with linear drift," *Journal of Mathematical Analysis and Applications*, vol. 202, no. 2, pp. 604–622, 1996.

[11] X. Mao, "Stability of stochastic differential equations with Markovian switching," *Stochastic Processes and their Applications*, vol. 79, no. 1, pp. 45–67, 1999.

[12] X. Mao and C. Yuan, *Stochastic Differential Equations with Markovian Switching*, Imperial College Press, 2006.

[13] C. Yuan and X. Mao, "Robust stability and controllability of stochastic differential delay equations with Markovian switching," *Automatica*, vol. 40, no. 3, pp. 343–354, 2004.

[14] M. Krstić and H. Deng, *Stabilization of Uncertain Nonlinear Systems*, Springer, New York, NY, USA, 1998.

[15] X. Yu and X.-J. Xie, "Output feedback regulation of stochastic nonlinear systems with stochastic iISS inverse dynamics," *IEEE Transactions on Automatic Control*, vol. 55, no. 2, pp. 304–320, 2010.

[16] Z.-J. Wu, X.-J. Xie, P. Shi, and Y.-Q. Xia, "Backstepping controller design for a class of stochastic nonlinear systems with Markovian switching," *Automatica*, vol. 45, no. 4, pp. 997–1004, 2009.

[17] Z. J. Wu, J. Yang, and P. Shi, "Adaptive tracking for stochastic nonlinear systems with Markovian switching," *IEEE Transactions on Automatic Control*, vol. 55, no. 9, pp. 2135–2141, 2010.

[18] W. E. Dixon, E. Zergeroglu, and D. M. Dawson, "Global robust output feedback tracking control of robot manipulators," *Robotica*, vol. 22, no. 4, pp. 351–357, 2004.

[19] K. D. Do, Z. P. Jiang, and J. Pan, "Global partial-state feedback and output-feedback tracking controllers for underactuated ships," *Systems & Control Letters*, vol. 54, no. 10, pp. 1015–1036, 2005.

[20] M.-Y. Cui, Z.-J. Wu, X.-J. Xie, and P. Shi, "Modeling and adaptive tracking for a class of stochastic Lagrangian control systems," *Automatica*, vol. 49, no. 3, pp. 770–779, 2013.

[21] C. J. Qian and W. Lin, "A continuous feedback approach to global strong stabilization of nonlinear systems," *IEEE Transactions on Automatic Control*, vol. 46, no. 7, pp. 1061–1079, 2001.

[22] W. Li, X.-J. Xie, and S. Zhang, "Output-feedback stabilization of stochastic high-order nonlinear systems under weaker conditions," *SIAM Journal on Control and Optimization*, vol. 49, no. 3, pp. 1262–1282, 2011.

Hindawi Publishing Corporation
Mathematical Problems in Engineering
Volume 2015, Article ID 849047, 11 pages
http://dx.doi.org/10.1155/2015/849047

Research Article

Study on the Dynamics of Local Pressure Boosting Pneumatic System

Yan Shi, Guanwei Jia, Maolin Cai, and Weiqing Xu

School of Automation Science and Electrical Engineering, Beihang University, Beijing 100191, China

Correspondence should be addressed to Yan Shi; yesoyou@gmail.com

Received 1 October 2014; Revised 25 December 2014; Accepted 11 January 2015

Academic Editor: Stanisław Migorski

Copyright © 2015 Yan Shi et al. This is an open access article distributed under the Creative Commons Attribution License, which permits unrestricted use, distribution, and reproduction in any medium, provided the original work is properly cited.

Local pressure boosting system is a complex and switched system, which is widely used in modern pneumatic systems, to optimize local pressure boosting system; firstly, the basic and the dimensionless mathematical models of the local pressure system were setup. Furthermore, the mathematical models were verified through the experimental study on the local pressure boosting system. Moreover, the influences of the tank's three main parameters on the performance of local pressure boosting system were studied. It can be seen that the pressure wave amplitude is mainly affected by the dimensionless volume of the tank; its influence degree is 95.1%, and it increases when the later one decreases. The pressure loss of the tank is mainly affected by the dimensionless output pressure, and its influence degree is 68.7%, and it decreases rapidly with the increase of the dimensionless output pressure of the tank. Last, the optimization method of the local pressure boosting system was obtained.

1. Introduction

Pressure-boosting technologies have been used in many fields [1–6]. Because of its compact structure, small size, and nonexternal power supply, and so forth, air-driven booster was widely used in locally pressure-boosting occasions of pneumatic system [1–7]. Most common booster was called input pressure reduced pneumatic booster (short for IPR booster), pressure of output air of which was set by adjusting input pressure of the driving-chamber, such as VBA series of booster of SMC Corporation [7]. With the development of energy-saving technologies of pneumatic system, importance of booster has become more and more obvious [8, 9]. However this type of booster has its own shortages, such as its small output flow, when boosting ratio is higher, the shortage becomes more distinct. Furthermore, its energy efficiency is not high, which restricts its application [10, 11].

Recently, main research on pneumatic booster was focused on its characteristics and factors which influence the characteristics of pneumatic booster [12–14]. Moreover, some new structures of pneumatic booster were designed. However, efficiency and flow of pneumatic booster still were not developed sufficiently [11, 15–17].

Therefore, one novel type of booster was proposed, which is called expansion energy used pneumatic booster, short for EEU booster. The wave amplitude of output flow and pressure increases with the increase of the EEU booster's efficiency and power, and that not only affects the working performance of pneumatic actuator, but also seriously shortens the working span of pneumatic components (such as actuator, regulator, and valve).

To reduce the pulse and the loss of output pressure of the EEU booster, in this paper, the local pressure boosting system (consists of the EEU booster, tank, and pipes, etc.) was studied. Firstly, the working principles of the local pressure boosting system and the EEU booster was introduced, the basic and the dimensionless mathematical models of the local pressure system were set up. Furthermore, pressure boosting pneumatic system was studied experimentally to verify the mathematical models. Last, the influences of the tank's main parameters on the performance of pressure boosting system were studied. This research lays a foundation

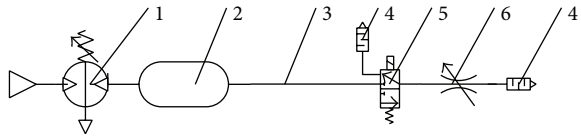

Figure 1: Configuration of local pressure boosting system. 1: EEU booster, 2: air tank, 3: pipeline, 4: silencer, 5: solenoid valve, and 6: throttle valve.

for the optimization and energy saving of the local pressure boosting system.

There are several definitions that should be introduced.

(1) Wave Amplitude Ratio. It is the amplitude ratio of the output pressure wave and the input pressure wave of the research unit, which can be used to directly illustrate the damping of pressure pulse of compressed air.

(2) Influence Degree. When a parameter changes in a range, the difference between the maximum value and the minimum value of a characteristic of the research unit is defined as Influence Degree, which represents the degree of the influence of a parameter on a characteristic of the research unit.

(3) Wave Amplitude Influence Ratio. It is the ratio of "the Influence Degree of one parameter on the Wave Amplitude of the research unit" and "the sum of the Influence Degree of other parameters on the Wave Amplitude of the research unit."

(4) Pressure Loss Influence Ratio. It is the ratio of "the Influence Degree of one parameter on the pressure loss of the research unit" and "the sum of the Influence Degree of other parameters on the pressure loss of the research unit."

2. Working Principle Introduction

2.1. Working Principles of Pressure Boosting System. The structure of local pressure boosting system can be shown in Figure 1.

As is shown in Figure 1, the research local pressure boosting system is mainly constituted of an EEU booster, a tank, pipes, a solenoid valve, and a throttle valve. The compressed air with low pressure is boosted through the EEU booster and flows into the tank, and pressure pulse of compressed air with high pressure is reduced in the tank, and last, the pressure boosted air is emitted to the atmosphere through the solenoid valve, throttle valve, and the silencer.

2.2. Working Principles of EEU Booster. A typical EEU booster, as shown in Figure 2, is composed of a controller, four magnetic switches, two magnetic rings, two solenoid valves, a piston, two driving chambers, two boosting chambers, and four check valves, and so forth. Input flow of the booster is controlled by the controller.

When piston reaches the left travel destination, Solenoid Valve A and Solenoid Valve B change their position, driving chamber B is connected with the atmosphere, compressed air charged from the primary side flows into boosting chamber A and driving chamber A. Compressed air in boosting chamber A and driving chamber A drives the piston to move toward the right; then the pressure of air in boosting chamber B increases, and higher-pressure compressed air in boosting chamber B is not discharged from the second side until the pressure is higher than the pressure in the second side.

When the piston moves near the magnetic switch C, the solenoid valve A changes its position and compressed air charged from the primary side stops to flow into driving chamber A, depending on its expansion, compressed air in driving chamber A keeps driving piston to move, and finally, arrives the right travel destination (viz., near the magnetic switch D); then part of expansion energy of the air is used. The solenoid valve A and the solenoid valve B are controlled by the controller to change their position, air in driving chamber A flows to atmosphere, and air, charged from the primary side, flows into boosting chamber B and driving chamber B; then air in the boosting chamber B and driving chamber B drives the piston to move towards the left, the pressure of air in boosting chamber A ascends, and finally higher-pressure compressed air in boosting chamber A is discharged from the second side.

When the piston moves near the magnetic switch B, the solenoid valve A changes its position and compressed air charged from the primary side stops to flow into driving chamber B; then part of expansion energy of the air is used to drive the piston continue to move, and arrives the left travel destination (viz., near the magnetic switch A). The Solenoid Valve A and the Solenoid Valve B change their position, air in driving chamber B is exhausted to atmosphere. The booster goes around and repeats the process discussed above, higher-pressure compressed air is discharged continuously.

The piston stroke, when the driving chambers stopped to charge air, is defined to be Piston Stroke-set (LL), as shown in Figure 3.

3. Modeling of the Local Pressure Boosting System

3.1. Basic Mathematical Model. To facilitate this research, the following assumptions were made:

(1) The working fluid (air) of the system follows all ideal gas laws.

(2) There is no leakage between the chambers, the area of the piston rod end is too small to be considered, and the effective areas of all intake and exhaust ports are the same.

(3) Supply temperature is equal to atmosphere temperature.

(4) The flow of air moving into and out of the chambers is a stable one-dimensional flow that is equivalent to the flow of air through the nozzle contraction.

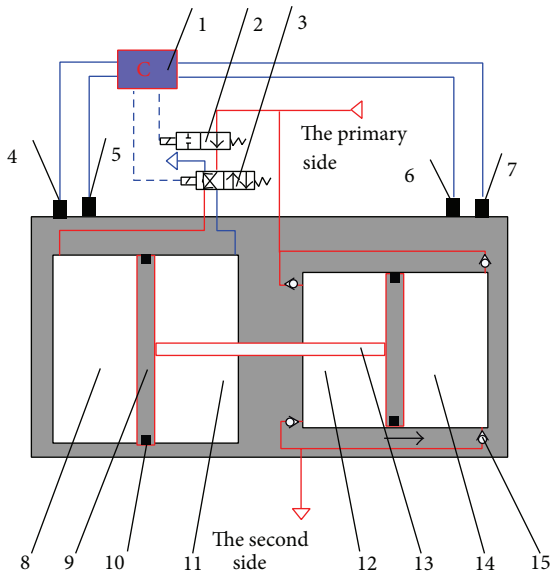

Figure 2: Structure of EEU Booster. 1: Controller, 2: solenoid valve A, 3: solenoid valve B, 4: magnetic switch A, 5: magnetic switch B, 6: magnetic switch C, 7: magnetic switch D, 8: driving chamber A, 9: piston, 10: magnetic ring, 11: driving chamber B, 12: boosting chamber A, 13: piston rod, 14: boosting chamber B, and 15: check valve.

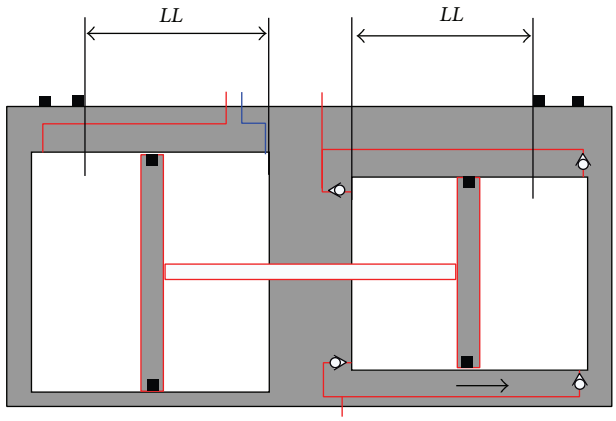

Figure 3: Piston stroke-set of EEU booster.

3.1.1. Energy Equation. Because there is no leakage in either chamber, the chambers do not charge and exhaust air simultaneously. Consequently, the energy equation for the discharge and charge side of each chamber can be illustrated by the following equations:

$$C_v W \frac{d\theta}{dt} = (S \cdot h_c + C_v \cdot G)(\theta_a - \theta) + RG\theta_a - PAu,$$
$$C_v W \frac{d\theta}{dt} = S \cdot h_d (\theta_a - \theta) + RG\theta - PAu. \quad (1)$$

The value of C_v is 718.

3.1.2. Equation of Continuity. From the law of mass conservation, air mass can be given as

$$\frac{dW}{dt} = G. \quad (2)$$

Air mass flow is calculated from the flow equation, which is described later on.

3.1.3. Flow Equation. The input and output pressures of the booster are below the critical pressure; the temperature of the compressed air is above the critical temperature, according to the ratio P_l/P_h, the flow equation for the flow through a restriction can be written as follows:

$$G = \begin{cases} \dfrac{A_e P_h B}{\sqrt{\theta_h}} \varphi(P_h, P_l) & \dfrac{P_l}{P_h} > b \\ \dfrac{A_e P_h D}{\sqrt{\theta_h}} & \dfrac{P_l}{P_h} \le b, \end{cases} \quad (3)$$

where

$$\varphi(P_h, P_l) = \left[\left(\frac{P_l}{P_h} \right)^{2/\kappa} - \left(\frac{P_l}{P_h} \right)^{(\kappa+1)/\kappa} \right],$$
$$B = \sqrt{\frac{2\kappa}{R(\kappa - 1)}}, \quad (4)$$
$$D = \left(\frac{2}{\kappa + 1} \right)^{1/(\kappa-1)} \sqrt{\frac{2\kappa}{R(\kappa + 1)}}.$$

The value of b, which referenced the critical pressure ratio of the throttle valve, is 0.49; the average output flow of the booster is the average value of one period. Consider

$$\overline{G} = \frac{\int_0^T G dt}{T}. \quad (5)$$

3.1.4. Motion Equation. The velocity of the piston is calculated from Newton's second law of motion. In this paper, the friction force model is considered to be the sum of the Coulomb friction and viscous friction. The viscous friction force is considered to be a linear function of piston velocity. The forces on the piston of the booster are shown in Figure 4.

The right side was considered to be the positive direction of the vector. The motion equation of the piston can be given by the following equation:

$$\frac{d^2x}{dt^2} = \begin{cases} \dfrac{1}{M} \left(P_{dA} \cdot A_d - P_{dB} \cdot A_d + P_{bA} \cdot A_b \right. \\ \qquad \left. - P_{bB} \cdot A_b - F_f \right), & x \ne 0, L \\ 0, & x = 0, L, \end{cases} \quad (6)$$

where

$$F_f = \begin{cases} F_s & u = 0 \\ F_c + Cu & u \ne 0. \end{cases} \quad (7)$$

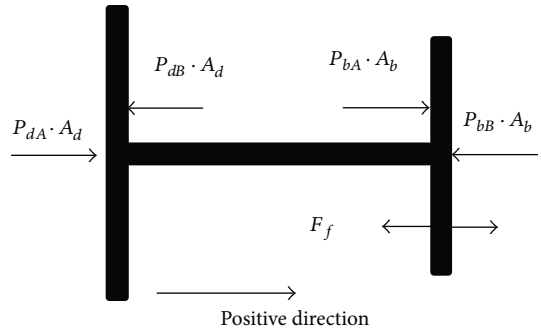

Figure 4: The forces on the piston of the booster.

3.1.5. State Equation. Pressure changes in the air in each chamber can be obtained by deriving the state equation of ideal gases:

$$\frac{dP}{dt} = \frac{1}{V}\left[\frac{PV}{\theta}\cdot\frac{d\theta}{dt} + R\theta G - PAu\right]. \tag{8}$$

3.2. Dimensionless Mathematical Model. The reference values and the dimensionless variables are shown in Table 1. The basic mathematical model can be made dimensionless as described in the following section.

3.2.1. Dimensionless Energy Equation. The dimensionless energy equation for the discharge side and the charge side becomes

$$\begin{aligned} W^*\frac{d\theta^*}{dt^*} &= \frac{S^*}{S_b^* T_{hd}^*}\left(1-\theta^*\right) + (k-1)\left(P^*u^* - G^*\theta^*\right), \\ W^*\frac{d\theta^*}{dt^*} &= \left(\frac{S^*}{S_b^* T_{hc}^*} + G^*\right)\left(1-\theta^*\right) \\ &\quad + (k-1)\left(G^* - P^*A^*u^*\right), \end{aligned} \tag{9}$$

respectively, where the dimensionless parameter T_{hd}^*, which is the dimensionless temperature settling time of the discharge side, is the ratio of the temperature settling time constant, T_{hd}, and the isothermal pressure time constant, T_p [18]. The dimensionless and dimensional time constant can be written as follows:

$$\begin{aligned} T_{hd}^* &= \frac{T_{hd}}{T_P}, \\ T_{hd} &= \frac{C_v W}{S_b h_d}, \\ S_b &= 2A_b + 2L\sqrt{\pi A_b}. \end{aligned} \tag{10}$$

The dimensionless maximum heat transfer area can be calculated by the following equation:

$$S_b^* = \frac{2A_b + 2L\sqrt{\pi A_b}}{A_b} = 2 + 2L\sqrt{\frac{\pi}{A_b}}. \tag{11}$$

For the charge side:

$$\begin{aligned} T_{hc}^* &= \frac{T_{hc}}{T_P}, \\ T_{hc} &= \frac{C_v W}{S_b h_c}. \end{aligned} \tag{12}$$

3.2.2. Dimensionless Equation of Continuity. The dimensionless equation of continuity can be given as the following equation:

$$\frac{dW^*}{dt^*} = G^*. \tag{13}$$

3.2.3. Dimensionless Flow Equation. The dimensionless flow equation for both sides of the chambers becomes

$$G^* = \begin{cases} \dfrac{P_h^* B}{D\sqrt{\theta_h^*}}\sqrt{\left(\dfrac{P_l^*}{P_h^*}\right)^{2/\kappa} - \left(\dfrac{P_l^*}{P_h^*}\right)^{(\kappa+1)/\kappa}} & \dfrac{P_l^*}{P_h^*} > 0.528 \\ \dfrac{P_h^*}{\sqrt{\theta_h^*}} & \dfrac{P_l^*}{P_h^*} \le 0.528. \end{cases} \tag{14}$$

The average output flow of the booster can be given as

$$\overline{G}^* = \frac{W^*}{t^*}. \tag{15}$$

3.2.4. Dimensionless Equation of Motion. The dimensionless equation of motion can be written as follows:

$$\frac{d^2x^*}{d\left(t^*\right)^2} = \begin{cases} \left(\dfrac{1}{T_f^*}\right)^2 \left(P_{dA}^*\cdot A_d^* - P_{dB}^*\cdot A_d^* \right. \\ \qquad \left. + P_{bA}^* - P_{bB}^* - F_f^*\right), & x \ne 0, 1 \\ 0, & x^* = 0, 1. \end{cases} \tag{16}$$

Here, F_f^* is the dimensionless friction force, which can be written as

$$F_f = \begin{cases} F_s^* & u^* = 0 \\ F_c^* + C^*u^* & u^* \ne 0. \end{cases} \tag{17}$$

Here, F_s^* is the dimensionless maximum static friction force, F_c^* is the dimensionless Coulomb friction force, and C^* is the dimensional viscous friction force coefficient. All dimensional parameters can be written as follows:

$$\begin{aligned} F_s^* &= \frac{F_s}{P_s A_b}, \\ F_c^* &= \frac{F_c}{P_s A_b}, \\ C^* &= \frac{C\cdot u_0}{P_s A_b}. \end{aligned} \tag{18}$$

Table 1: Reference values and dimensionless variables.

Variable	Reference value		Dimensionless variable
Time	$T_p = \frac{W_b}{G_{\max}} = \frac{V_b}{A_e DR\sqrt{\theta_a}}$	Time to totally exhaust W_b of air at $G_{\max}$ of air mass flow	$t^* = \frac{t}{T_p}$
Pressure	P_s	Supply pressure	$P^* = \frac{P}{P_s}$
Temperature	θ_a	Atmosphere temperature	$\theta^* = \frac{\theta}{\theta_a}$
Air mass flow	$G_{\max} = \frac{A_e P_s D}{\sqrt{\theta_s}}$	Maximum air mass flow at charge side of boosting chamber	$G^* = \frac{G}{G_{\max}}$
Air mass	$W_b = \frac{P_s V_b}{R\theta_a}$	Maximum air mass in boosting chamber	$W^* = \frac{W}{W_b} = \frac{P^* V^*}{\theta^*}$
Displacement	L	Maximum displacement	$x^* = \frac{x}{L}$
Volume	$V_b = L \cdot A_b$	Maximum volume of boosting chamber B	$V^* = \frac{V}{V_b}$
Area of piston	A_b	Area of piston in boosting chamber	$A^* = \frac{A}{A_b}$
Diameter	d_b	Diameter of piston in boosting chamber	$d^* = \frac{d}{d_b}$

Dimensionless parameter, T_f^*, is defined in the following. T_f^* corresponds to the J-parameter that is used in the current selection method of a pneumatic cylinder [19, 20]. The J-parameter is given by

$$T_f^* = \frac{T_f}{T_p}, \tag{19}$$

$$T_f = \sqrt{\frac{ML}{A_b P_s}}, \tag{20}$$

$$J = \frac{T_p^2 P_s A_d}{LM}. \tag{21}$$

From (19), (20), and (21), the relation between T_f^* and the J-parameter is

$$J = \left(\frac{1}{T_f^*}\right)^2. \tag{22}$$

Because the J-parameter appears as a coefficient of acceleration, it was thought that this parameter related to the inertia of the booster, and it is known as the inertia coefficient. The dimensionless parameter, T_f^*, represents the dimensionless natural period of the booster [21].

The dimensionless Piston Stroke-set (LL^*) is

$$LL^* = \frac{LL}{L}. \tag{23}$$

3.2.5. Dimensionless State Equation. The dimensionless state equation for the discharge side and charge side becomes

$$\frac{dP^*}{dt^*} = \frac{P^*}{\theta^*}\frac{d\theta^*}{dt^*} + \frac{\theta^* G^*}{V^*} - \frac{P^* A^* u^*}{V^*}. \tag{24}$$

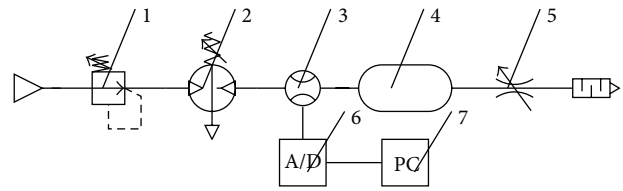

Figure 5: Configuration of experimental apparatus. 1: Regulator, 2: booster, 3: air power meter, 4: tank, 5: throttle valve, 6: data acquisition card, and 7: computer.

4. Experimental Study on the Pressure Boosting System

The dimensionless output flow and dimensionless cycle time can be attained easily and expediently. These parameters were studied experimentally to verify the dimensionless mathematical model that was set up above.

The experimental apparatus shown in Figure 5 consists of a regulator (IR3020-03BC) by SMC, an EEU booster, PLC (S7-220) by Siemens, a flow sensor (APM-450) by Tokyo Meter, a tank, a throttle valve (AS3001F) by SMC, and a data acquisition card (USB-4711A) by Advantech. The EEU booster is composed of two cylinders (CDQ2B100-100D), a floating connector (JAL100-26-150), four magnetic switches (A73), and four check valves (AKH08) by SMC. The adopted flow sensor is an Air Power Meter (integrates a thermal type flow sensor, a semiconductor type pressure sensor, and a thermocouple type temperature sensor), which can measure the pressure, flow, and temperature of compressed air simultaneously. The accuracy of pressure, flow, and temperature is 0.1%, ±1% F.S. and 0.10C, respectively [22, 23].

Table 2: The initial values of the parameters.

Parameter	LL^*	P_o^*	A^*	F_f^*	S_b^*	C^*	T_f^*	T_{hc}^*	T_{hd}^*
Value	0.67	1.33	1	0.008	1	0.0008	0.0167	4.47	2.98

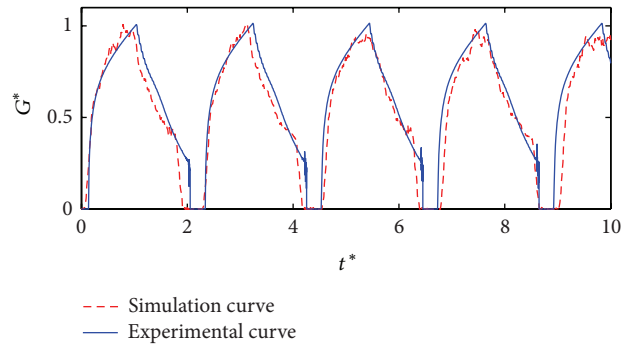

Figure 6: Curves of output flow of boosters.

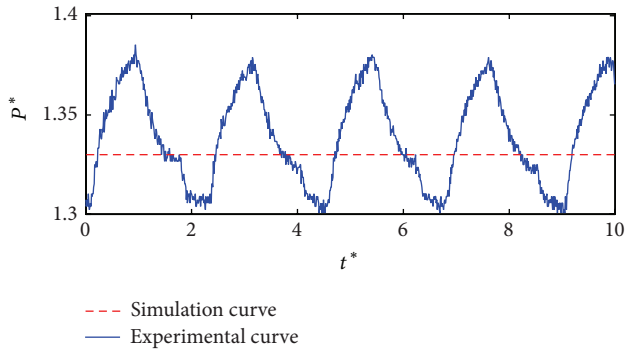

Figure 7: Curves of pressure of air in tank.

In this experiment, we first opened the compressed air source, adjusted the regulator, and set the pressure to the fixed value (0.6 MPa). Next, we adjusted the throttle valve, making sure that air was exhausted from the tank steadily, and the pressure of the air was approximately the fixed value (0.8 MPa). The last stage was data acquisition and preservation.

The values of the nine dimensionless parameters are shown in Table 2. The experiment can be performed according to the method described above. The output flow of the booster, which was obtained by simulation and experimentation, is shown in Figure 6, and the pressure curve of the compressed air in the tank is shown in Figure 7. As the dimensionless output pressure was set to a fixed value (1.33), therefore the simulation curve of pressure of air in tank is a line.

From Figures 9 and 10, it is clear that the simulation results are more consistent with the experimental results, and this verifies the mathematical model above. It should be noted that the effective area of intake and exhaust port is difficult to be determined, so the parameters were adjusted to get the good fit.

The main reasons for the difference between the simulation results and the experimental results are the fluctuation of the supply pressure, leakage between chambers, temperature of the atmosphere, and the fluctuation of pressure of air in tank, which can be seen in Figure 7.

5. Study on the Performance of the Pressure Boosting System

5.1. The Influence of the Dimensionless Volume of the Tank. Assume that the dimensionless output pressure of the tank is 1.33, the dimensionless piston stroke-set of the tank is 0.83, the dimensionless diameter of the outlet of the tank is 1, and the dimensionless volume of the tank is set 1.4, 9.9, 14.2, 21.2, 28.3, 35.4, and 42.4, respectively. The research results are shown in Figure 8.

As shown in Figure 8, the tank has a good inhibiting effect on the output pressure pulse; pressure wave amplitude in the tank increases with the decrease of the dimensionless volume of the tank, and the pressure loss of the tank increase with the decease of the volume of the tank.

5.2. The Influence of the Dimensionless Output Pressure of the Tank. Assume that the dimensionless volume of the tank is 11.33, the dimensionless piston stroke-set of the tank is 0.83, the dimensionless diameter of the outlet of the tank is 1, and the dimensionless output pressure of the tank is set 1.3, 1.29, 1.33, 1.38, 1.42, 1.46, and 1.5, respectively. The research results are shown in Figure 9.

As shown in Figure 9, the pressure wave amplitude in the tank increases slowly with the increase of the dimensionless output pressure of the tank, and the pressure loss of the tank decreases rapidly with the increase of the output pressure of the tank.

5.3. The Influence of the Dimensionless Diameter of the Outlet of the Tank. Assume that the dimensionless volume of the tank is 11.33, the dimensionless piston stroke-set of the tank is 0.83, the dimensionless output pressure of the tank is 1.33, and the dimensionless diameter of the outlet of the tank is set 0.8, 0.9, 1, 1.1, 1.2, and 1.3, respectively, the research results are shown in Figure 10.

As shown in Figure 10, the pressure wave amplitude in the tank rarely has respond to the changes of the dimensionless diameter of the outlet of the tank, and the pressure loss of the tank increase with the increase of the dimensionless diameter of the outlet of the tank.

5.4. The Compare of the Influence of the Three Main Parameters of the Tank. Each parameter can be changed within a certain range for comparison of the influence degree while other

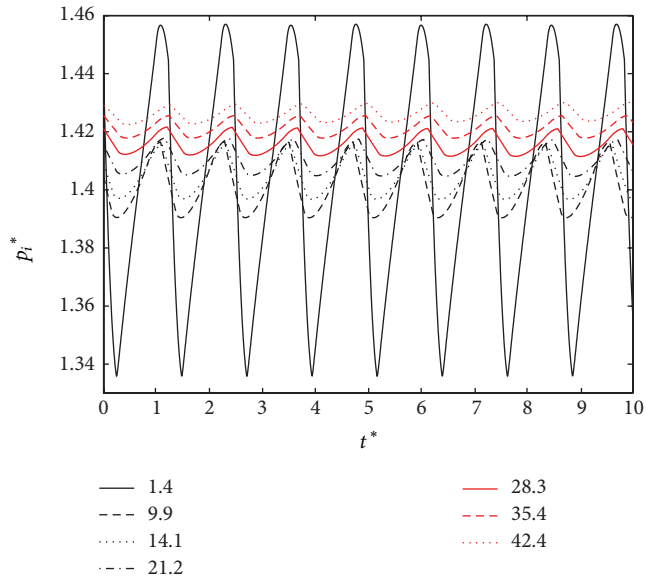

(a) The dimensionless dynamic characteristics of air pressure in the tank

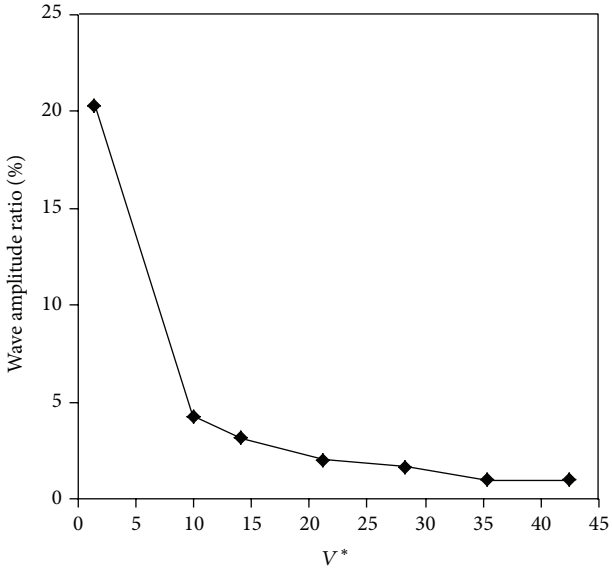

(b) The dimensionless pressure wave amplitude ratio of the tank

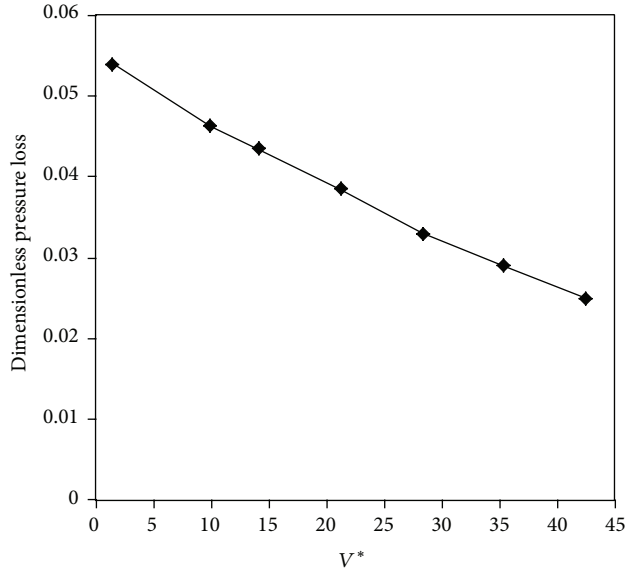

(c) The dimensionless pressure loss in the tank

Figure 8: The influence of the dimensionless volume of the tank.

parameters are kept constant. And the influence degree of the main parameters of the tank on the pressure wave amplitude and the pressure loss influence ratio can be given by the following equations:

$$
\begin{aligned}
p_{\text{wa-total}} &= p_{\text{wa-}V^*} + p_{\text{wa-}p_o^*} + p_{\text{wa-}d_o^*},\\
\text{Dg}_{\text{wa-}V^*} &= \frac{p_{\text{wa-}V^*}}{p_{\text{wa-total}}},\\
\text{Dg}_{\text{wa-}V^*} &= \frac{p_{\text{wa-}p_o^*}}{p_{\text{wa-total}}},\\
\text{Dg}_{\text{wa-}V^*} &= \frac{p_{\text{wa-}d_o^*}}{p_{\text{wa-total}}},\\
p_{\text{pl-total}} &= p_{\text{pl-}V^*} + p_{\text{pl-}p_o^*} + p_{\text{pl-}d_o^*},\\
\text{Dg}_{\text{pl-}V^*} &= \frac{p_{\text{pl-}V^*}}{p_{\text{pl-total}}},\\
\text{Dg}_{\text{pl-}V^*} &= \frac{p_{\text{pl-}p_o^*}}{p_{\text{pl-total}}},\\
\text{Dg}_{\text{pl-}V^*} &= \frac{p_{\text{pl-}d_o^*}}{p_{\text{pl-total}}}.
\end{aligned}
\tag{25}
$$

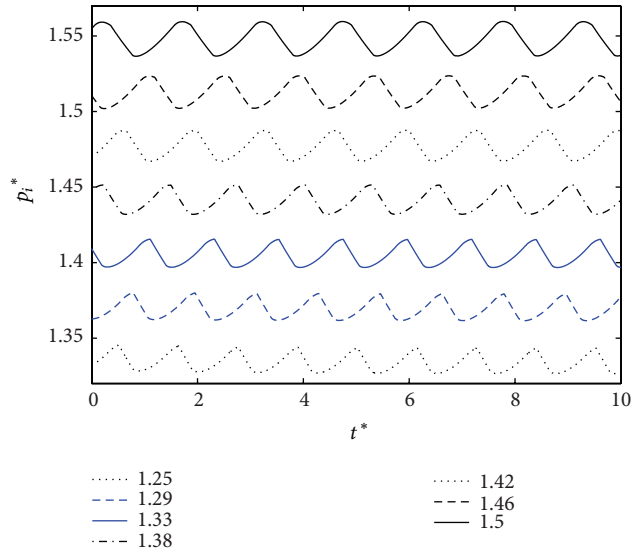

(a) The dimensionless dynamic characteristics of pressure in the tank

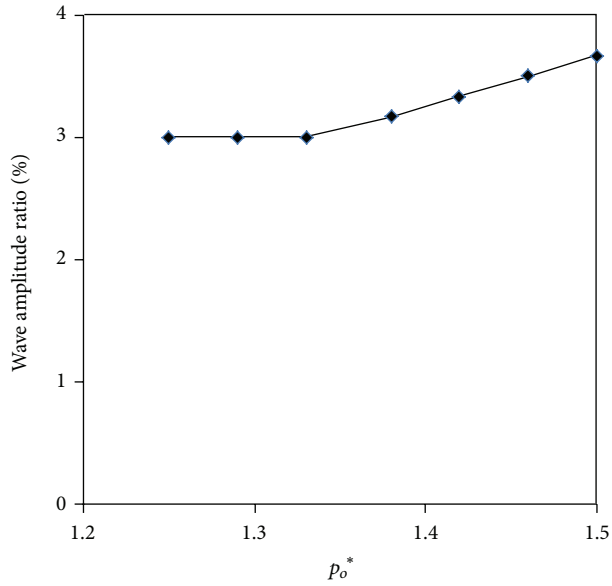

(b) The dimensionless pressure wave amplitude in the tank

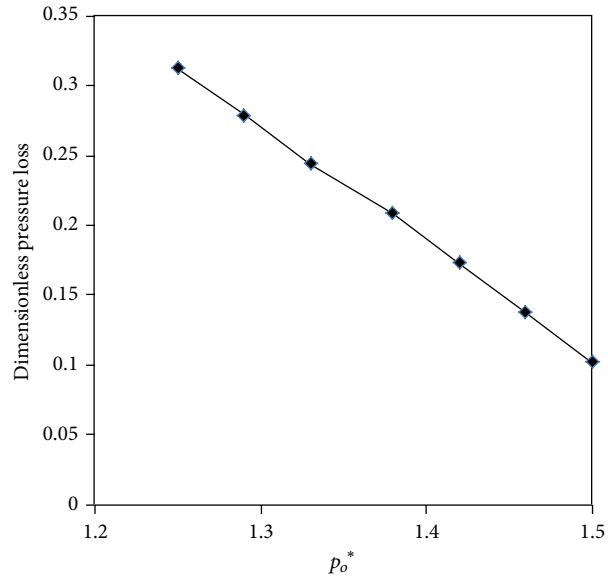

(c) The dimensionless pressure loss in the tank

Figure 9: The influence of the dimensionless output pressure of the tank.

Based on the numerical study, the influence degrees of the dimensionless volume, the dimensionless output pressure, and the dimensionless diameter of the outlet of the tank on the pressure wave amplitude and the pressure loss are shown in Figures 11 and 12.

As shown in Figures 11 and 12, it is clear that

(1) The pressure wave amplitude of the tank is mainly affected by the dimensionless volume of the tank, and its influence degree is 95.1%. And the influences of the dimensionless output pressure and the diameter of the outlet of the tank can be ignored.

(2) The pressure loss of the tank is mainly affected by the dimensionless output pressure and the diameter of the outlet of the tank, and the three parameters' influence degree is 68.7%, 21.8%, and 9.5%.

6. Conclusions

In this paper, a new kind of booster, EEU booster, was proposed, the local pressure boosting system was studied, and the basic mathematical model of the system was developed. Appropriate reference values were selected, the basic mathematical model was transferred to a dimensionless expression,

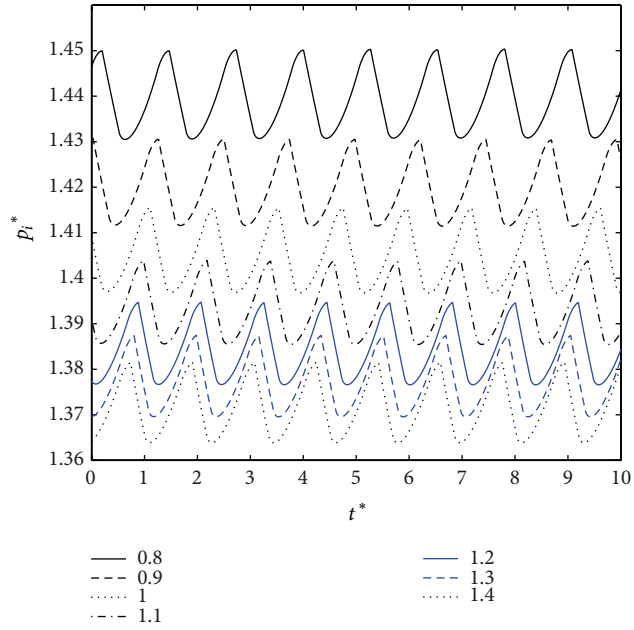

(a) The dimensionless dynamic characteristics of pressure in the tank

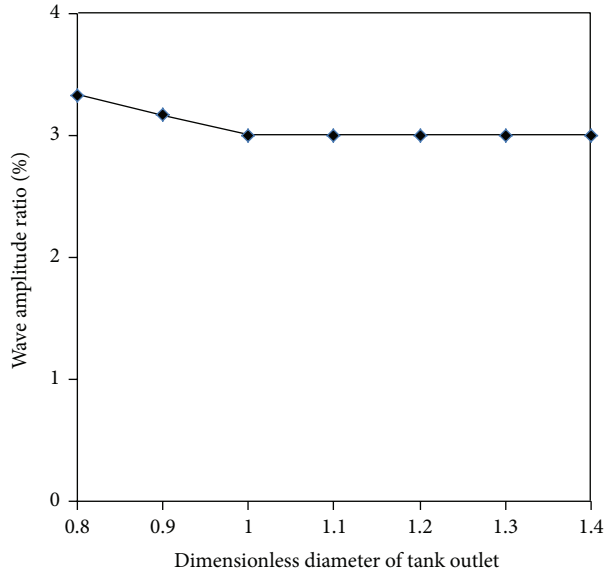

(b) The dimensionless pressure wave amplitude in the tank

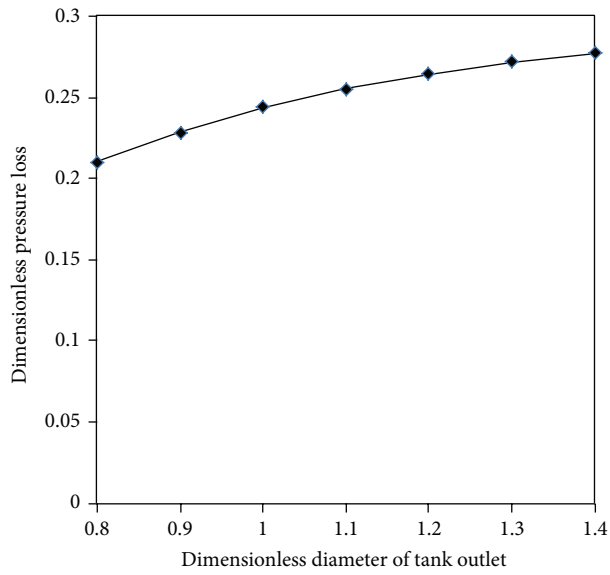

(c) The dimensionless pressure loss in the tank

Figure 10: The influence of the dimensionless diameter of the outlet of the tank.

and the influence of the tank on the working performance of the local pressure boosting system was analyzed through simulation and experimentation. The conclusions are summarized as follows.

(1) Simulation results have better consistency with experimental results, and the mathematical model set up above is correct.

(2) The pressure wave amplitude is mainly affected by the dimensionless volume of the tank, its influence degree is 95.1%, and it increases when the later one decreases. Other parameters' influence on pressure wave amplitude can be ignored.

(3) The pressure loss of the tank is mainly affected by the dimensionless output pressure, and secondly by the diameter of the outlet of the tank, and the three parameters' influence degree is 68.7%, 21.8%, and 9.5%.

(4) The pressure loss of the compressed air decreases with the increase of the volume of the tank and rapidly decreases with the increase of the dimensionless output pressure of the tank and increases with the increase of the dimensionless diameter of the outlet of the tank.

So, aiming at the optimization of the local pressure boosting pneumatic system, we can draw conclusions as follows.

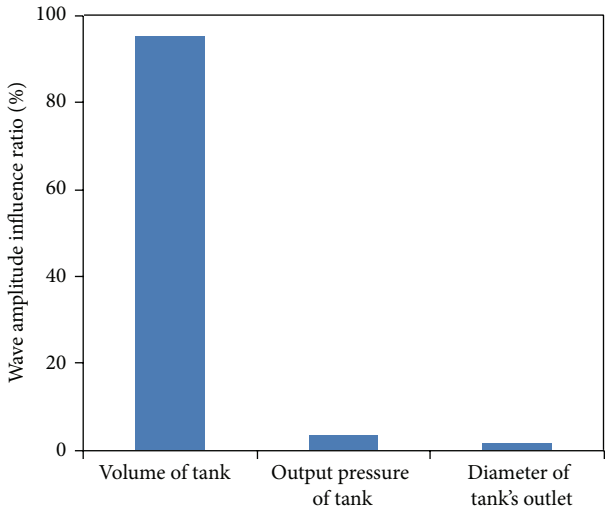

Figure 11: The influence degree of the main parameters of the tank on the pressure wave amplitude.

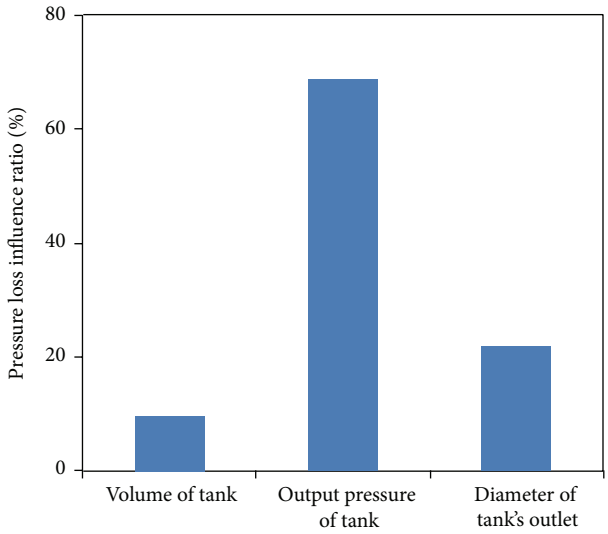

Figure 12: The influence degree of the main parameters of the tank on the pressure loss.

(1) In the case of allowing, increase the volume of the tank as much as possible.

(2) In the case that the industrial site requirements have been satisfied, increase the output pressure in a proper range.

(3) In the case that the booster is working in its best condition, decrease the diameter of the outlet of the tank and decrease the output flow rate of the tank in a proper range.

If those measurements were taken, the pressure wave amplitude in the tank and the pressure loss of the compressed air could both be reduced.

This research lays a foundation for the optimization design and energy saving of the local pressure boosting system.

Nomenclature

A: Area of piston [m^2]
A_e: Effective area of intake and exhaust port [m^2]
C: Viscous friction coefficient [Ns/m]
C_v: Specific heat at constant volume
d: Diameter [m]
Dg: Degree
F_f: Friction force [N]
F_c: Coulomb friction force [N]
F_s: Maximum static friction force [N]
G: Air mass flow [kg/s]
h: Heat transfer coefficient [W/(m^2K)]
L: Stroke [m]
LL: Piston stroke-set [m]
M: Mass of piston [kg]
P: Pressure [Pa]
R: Gas constant
S: Heat transfer area [m^2]
t: Time [s]
T: Time period [s]
u: Velocity [m/s]
V: Volume [m^3]
W: Air mass [kg]
x: Piston displacement [m]
κ: Specific heat ratio
θ: Temperature [K].

Subscripts

a: Atmosphere
d: Driving chamber
b: Boosting chamber
c: Charge side
d: Discharge side
A: Chamber A
B: Chamber B
h: Upstream side
l: Downstream side
o: Output of booster
s: Supply of booster
t: Tank
pl: Pressure loss changes
Wa: Pressure wave amplitude changes
0: Equilibrium conditions.

Superscripts

$*$: Dimensionless.

Conflict of Interests

The authors declare that there is no conflict of interests regarding the publication of this paper.

Acknowledgment

This project is supported by National Natural Science Foundation of China Grant no. (51205008).

References

[1] Z. Li, Y. Zhao, L. Li, and P. Shu, "Mathematical modeling of compression processes in air-driven boosters," *Applied Thermal Engineering*, vol. 27, no. 8-9, pp. 1516–1521, 2007.

[2] H. P. Cheng, C. J. Chen, and P. W. Cheng, "Computational fluid dynamics performance estimation of turbo booster vacuum pump," *Journal of Fluids Engineering*, vol. 125, no. 3, pp. 586–589, 2003.

[3] C. A. M. Brenninkmeijer and P. A. Roberts, "An air-driven pressure booster pump for aircraft-based air sampling," *Journal of Atmospheric and Oceanic Technology*, vol. 11, no. 6, pp. 1664–1671, 1994.

[4] V. E. Minaichev and V. M. Zykov, "Cryo-codensation booster pump," *Instruments and Experimental Techniques*, vol. 17, no. 3, pp. 795–798, 1974.

[5] P. Wang, F. X. Ren, and Y. P. Wang, "Balance characteristic of hydraulic balanced booster plunger pump," *China Petroleum Machinery*, vol. 25, no. 1, pp. 26–28, 1997 (Chinese).

[6] L. J. Budgen, "Developments in the transmission for mechanical booster pumps," *Journal of Vacuum Science and Technology A: Vacuum, Surfaces and Films*, vol. 1, no. 2, pp. 147–149, 1982.

[7] SMC (China) Co, *Modern Practical Pneumatic Technology*, China Machine Press, Beijing, China, 2008, (Chinese).

[8] N. Oneyama, "Pneumatic manufacturer's attempts on energy saving," *Hydraulics and Pneumatics*, vol. 2, no. 3, pp. 372–377, 1996.

[9] Y. Shi, M. Cai, and G. Wang, "Study on air-supplied with different pressure and locally pressure-boosting technology of pneumatic system," *Machine Toll and Hydraulics*, vol. 28, no. 9, pp. 57–59, 2010.

[10] N. Hamaura, T. Fujita, and T. Kagawa, "Characteristics analysis of pneumatic booster," in *Proceedings of the Autumn Symposium on Hydraulics and Pneumatics*, pp. 77–80, 1994, (Japanese).

[11] O. Takeuchi, T. Fujita, and T. Kagawa, "Characteristics analysis of expanding-type booster," in *Proceedings of the Autumn Symposium on Hydraulics and Pneumatics*, pp. 69–72, 1995, (Japanese).

[12] W. Haitao, W. Xiong, and L. Zhonghua, "Research on the dynamic characteristics during boosting charge of gas booster," in *Proceedings of the 5th National Conference on Fluid Power Transmission and Control & Conference on Hydraulic and Pneumatic of Chinese Society of Aeronautics and Astronautics*, pp. 362–366, Beijing, China, October 2008, (Chinese).

[13] Xu. Wang, H. Wang, and W. Xiong, "Study on the characteristics of air driven gas booster based on experiments," in *Proceedings of the 7th International Conference on Fluid Power Transmission and Control*, pp. 608–611, Hangzhou, China, 2009.

[14] S. H. I. Yan and C. A. I. Maolin, "Experimental study on working characteristics of pneumatic booster valve," in *Proceedings of the 7th International Conference on Fluid Power Transmission and Control*, pp. 511–515, Hangzhou, China, 2009.

[15] F. Dong, G. He, Z. Zhang et al., "Design of pneumatic booster pump," *Mechanical Science and Technology*, vol. 27, no. 1, pp. 23–27, 2008 (Chinese).

[16] X. Wang, *Study on New Kind Energy-Saving Gas Booster*, Dalian Maritime University, Dalian, China, 2009, (Chinese).

[17] S. H. I. Yan and C. A. I. Maolin, "Study on efficiency and flow characteristics of two kinds of pneumatic booster valves," in *Proceedings of the International Conference on Computer, Mechatronics, Control and Electronic Engineering*, pp. 45–50, Changchun, China, 2010.

[18] T. Kagawa, "Heat transfer effects on the frequency response of a pneumatic nozzle flapper," *Journal of Dynamic Systems, Measurement and Control*, vol. 107, no. 4, pp. 332–336, 1985.

[19] K. Ando, *Study on Characteristics of Pneumatic Systems for Resistance Welding Machines*, The Japan Welding Engineering Society, 1965, (Japanese).

[20] U. Kadota, "Characteristics of air (13)," *Hydraulics and Pneumatics Design*, vol. 9, no. 2, pp. 109–115, 1971.

[21] K. Tokashiki, *Dynamic Characteristics of Pneumatic Cylinder Systems*, Department of Control Engineering, Tokyo Institute of Technology, Tokyo, Japan, 1999.

[22] M. Cai, K. Kawashima, and T. Kagawa, "Power assessment of flowing compressed air," *Journal of Fluids Engineering*, vol. 128, no. 2, pp. 402–405, 2006.

[23] C. Maolin, F. Tatsuya, K. Kenji, and K. Toshiharu, "Development of pneumatic power meter for energy saving," in *Proceedings of Symposium on Fluid Power System at Spring*, pp. 119–121, Tokyo, Japan, 2003.

Hindawi Publishing Corporation
Mathematical Problems in Engineering
Volume 2015, Article ID 327347, 9 pages
http://dx.doi.org/10.1155/2015/327347

Research Article

Research on Adaptive Dual-Mode Switch Control Strategy for Vehicle Maglev Flywheel Battery

Hui Gao, Ying-Jun Wu, and Jing-Jin Shen

Nanjing University of Posts and Telecommunications, Nanjing 210023, China

Correspondence should be addressed to Hui Gao; gaohui2005@163.com

Received 3 November 2014; Accepted 15 January 2015

Academic Editor: Honglei Xu

Copyright © 2015 Hui Gao et al. This is an open access article distributed under the Creative Commons Attribution License, which permits unrestricted use, distribution, and reproduction in any medium, provided the original work is properly cited.

Because of the jamming signal is real-time changeable and control algorithm cannot timely tracking control flywheel rotor, this paper takes vehicle maglev flywheel battery as the research object. One kind of dual-model control strategy is developed based on the analysis of the vibration response impact of the flywheel battery control system. In view of the complex foundation vibration problems of electric vehicles, the nonlinear dynamic simulation model of vehicle maglev flywheel battery is solved. Through analyzing the nonlinear vibration response characteristics, one kind of dual-mode adaptive hybrid control strategy based on $H\infty$ control and unbalance displacement feed-forward compensation control is presented and a real-time switch controller is designed. The reliable hybrid control is implemented, and the stability in the process of real-time switch is solved. The results of this project can provide important basic theory support for the research of vehicle maglev flywheel battery control system.

1. Introduction

As the future main traffic tools, electric vehicle (EV) is required in the performance of starting, acceleration, and climbing; however, this performance depends largely on the power battery performance [1]. But, the faults of costly, short range and short service life become the bottleneck to restrict EV development scale. Specifically in the process of frequent start-stop or climbing, the chemical battery life is more shorten because of fast and deep discharging [2, 3]. How to eliminate these shortcomings becomes the key EV to be quickly developed.

Maglev flywheel can be applied in EV electric power system, aerospace, and other fields because of having high specific energy, high power, fast charge and discharge, long service life, no waste gas pollution, environment-friendly advantages, and so on [4–6]. In the field of EV, the maglev flywheel either can be as an independent power driving EV [3], or can be used as auxiliary power assisting the motive power batteries work [7, 8]. However, the maglev flywheel control stability will be affected because of existing start-stop, acceleration and deceleration, steering, and road random vibration in the process of the EV driving and even cause instability. So, the efficiency of magnetic suspension flywheel must be reduced.

For the scientific research and practical application of maglev flywheel, a dual-mode adaptive hybrid control strategy is studied based on $H\infty$ control and AILC algorithms, and the state space equation of maglev flywheel was analyzed. To improve the robust stability of flywheel control system and reduce the real-time interference, one $H\infty$ controller based on the state space equation was solved. To reduce maglev flywheel radial run-out, one adaptive iterative learning control theory was deduced and unbalance displacement compensation was implemented. The experimental result shows the dual-model control strategy has better interference capability in maglev flywheel start-up process and has stronger active control ability relative to only PID control. The maglev flywheel based on the dual-model control can help the EV primary battery, improve its discharge characteristics, and help to prolong its service life.

2. Maglev Flywheel Nonlinear Dynamic Model

The below force and movement differential equation of the flywheel are discussed in order to solve the maglev flywheel nonlinear dynamic model. Figure 1 shows the below force of the flywheel.

In Figure 1, O-XYZ is the space coordinate, 1 and 2 are, respectively, the left and right position of the radial magnetic

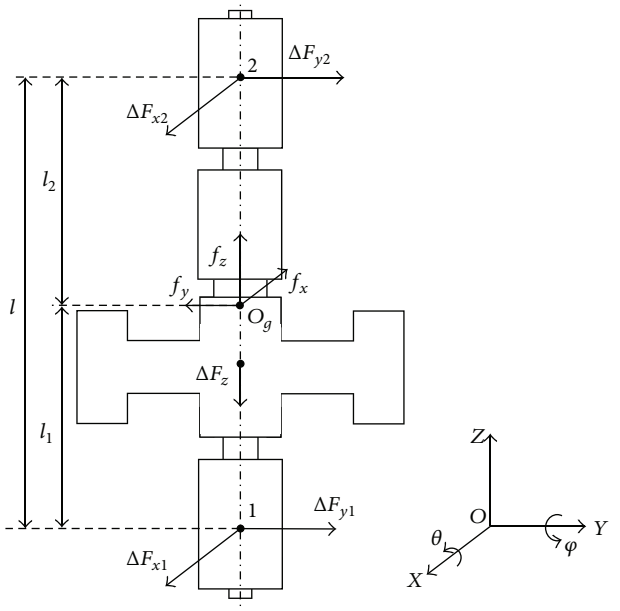

Figure 1: Flywheel below force analysis.

bearing, $O_g\,(x_g, y_g, z_g)$ is the mass center of the flywheel, l is the distance between 1 and 2, l_1 is the distance from the mass center to 1, l_2 is the distance from the mass center to 2, φ and θ are, respectively, the angular displacements around the x-axis and y-axis, ΔF_{x1}, ΔF_{x2}, ΔF_{y1}, ΔF_{y2}, and ΔF_z are the electromagnetic force of the flywheel in the three axes, and f_x, f_y, and f_z are the disturbing force and the unbalance force of the flywheel in the three axes. The flywheel movement differential equations are deduced according to the below force analysis in Figure 1 and the motion laws of particles [9]:

$$\begin{aligned} m\ddot{x}_g &= \Delta F_{x1} + \Delta F_{x2} - f_x, \\ m\ddot{y}_g &= \Delta F_{y1} + \Delta F_{y2} - f_y, \\ I_r\ddot{\varphi} - \omega I_a\dot{\theta} &= \Delta F_{y1}\cdot l_1 - \Delta F_{y2}\cdot l_2, \\ I_r\ddot{\theta} + \omega I_a\dot{\varphi} &= -\Delta F_{x1}\cdot l_1 + \Delta F_{x2}\cdot l_2, \\ m\ddot{z}_g &= \Delta F_z - f_z, \end{aligned} \tag{1}$$

where m is the flywheel quality, I_r and I_a are, respectively, the radial inertia moment and axial inertia moment, and ω is the angular velocity of the flywheel. The motion differential equation of matrix form can be written by [10]

$$\begin{pmatrix} \frac{l_2}{l}m & \frac{l_1}{l}m & 0 & 0 & 0 \\ 0 & 0 & \frac{l_2}{l}m & \frac{l_1}{l}m & 0 \\ 0 & 0 & -\frac{I_r}{l} & \frac{I_r}{l} & 0 \\ -\frac{I_r}{l} & \frac{I_r}{l} & 0 & 0 & 0 \\ 0 & 0 & 0 & 0 & m \end{pmatrix} \begin{pmatrix} \ddot{x}_1 \\ \ddot{x}_2 \\ \ddot{y}_1 \\ \ddot{y}_2 \\ \ddot{z} \end{pmatrix}$$

$$+ \begin{pmatrix} 0 & 0 & 0 & 0 & 0 \\ 0 & 0 & 0 & 0 & 0 \\ \frac{\omega I_a}{l} & -\frac{\omega I_a}{l} & 0 & 0 & 0 \\ 0 & 0 & -\frac{\omega I_a}{l} & \frac{\omega I_a}{l} & 0 \\ 0 & 0 & 0 & 0 & 0 \end{pmatrix} \begin{pmatrix} \dot{x}_1 \\ \dot{x}_2 \\ \dot{y}_1 \\ \dot{y}_2 \\ \dot{z} \end{pmatrix}$$

$$= \begin{pmatrix} k_{xx1} & k_{xx2} & 0 & 0 & 0 \\ 0 & 0 & k_{xy1} & k_{xy2} & 0 \\ 0 & 0 & l_1k_{xy1} & -l_2k_{xy2} & 0 \\ -l_1k_{xx1} & l_2k_{xx2} & 0 & 0 & 0 \\ 0 & 0 & 0 & 0 & k_{xz} \end{pmatrix} \begin{pmatrix} x_1 \\ x_2 \\ y_1 \\ y_2 \\ z \end{pmatrix}$$

$$+ \begin{pmatrix} k_{ix1} & k_{ix2} & 0 & 0 & 0 \\ 0 & 0 & k_{iy1} & k_{iy2} & 0 \\ 0 & 0 & l_1k_{iy1} & -l_2k_{iy2} & 0 \\ -l_1k_{ix1} & l_2k_{ix2} & 0 & 0 & 0 \\ 0 & 0 & 0 & 0 & k_{iz} \end{pmatrix} \begin{pmatrix} i_{cx1} \\ i_{cx2} \\ i_{cy1} \\ i_{cy2} \\ i_{cz} \end{pmatrix}$$

$$+ \begin{pmatrix} 1 & 0 & 0 & 0 & 0 \\ 0 & 1 & 0 & 0 & 0 \\ 0 & 0 & 1 & 0 & 0 \\ 0 & 0 & 0 & 1 & 0 \\ 0 & 0 & 0 & 0 & 1 \end{pmatrix} \begin{pmatrix} f_x \\ f_y \\ 0 \\ 0 \\ f_z \end{pmatrix}, \tag{2}$$

where x_1, x_2, y_1, y_2, and z are the displacements of the flywheel in five freedom degrees, $i_{cx1}, i_{cx2}, i_{cy1}, i_{cy1}$, and i_{cz} are, respectively, the control current corresponding to each freedom degree, k_{xx1}, k_{xx2}, k_{xy1}, k_{xy2}, and k_{xz} are, respectively, the displacement stiffness of each freedom degree, and k_{ix1}, k_{ix2}, k_{iy1}, k_{iy2}, and k_{iz} are, respectively, the current stiffness of each freedom degree.

For the convenience of analysis, type (2) can be expressed by type (3):

$$\mathbf{M}\ddot{\mathbf{x}} + \mathbf{C}\dot{\mathbf{x}} + \mathbf{K}\mathbf{x} = \mathbf{B}\mathbf{i}_\mathbf{c} + \mathbf{I}\mathbf{f}, \tag{3}$$

where $\mathbf{M}$ is the mass matrix, $\mathbf{C}$ is the damping coefficient matrix, $\mathbf{K}$ is the displacement stiffness matrix, $\mathbf{B}$ is the current stiffness matrix, $\mathbf{I}$ is the unit matrix, $\mathbf{x}$ is the displacement vector, $\mathbf{i}_\mathbf{c}$ is the control current vector, and $\mathbf{f}$ is the unbalanced inertial force vector. Type (3) can be rewritten as

$$\ddot{\mathbf{x}} = -\frac{\mathbf{C}}{\mathbf{M}}\dot{\mathbf{x}} - \frac{\mathbf{K}}{\mathbf{M}}\mathbf{x} + \frac{\mathbf{B}}{\mathbf{M}}\mathbf{i}_\mathbf{c} + \frac{\mathbf{I}}{\mathbf{M}}\mathbf{f}. \tag{4}$$

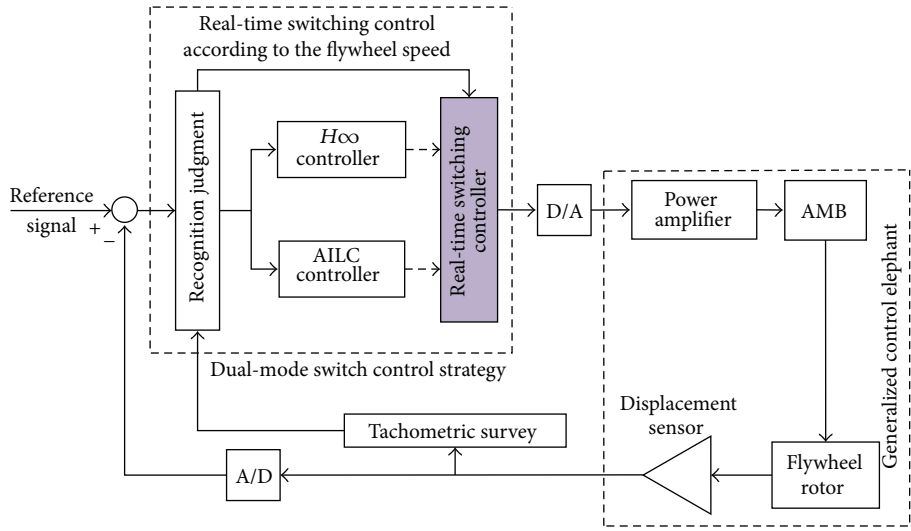

Figure 2: The dual-mode switch control strategy diagram.

The state space of the flywheel system transfer function matrix $G(s)$ is

$$\begin{aligned} \dot{\overline{\mathbf{x}}} &= \mathbf{A}\overline{\mathbf{x}} + \mathbf{B}_1\mathbf{f} + \mathbf{B}_2\mathbf{u}, \\ \mathbf{y} &= \mathbf{C}\overline{\mathbf{x}}, \end{aligned} \tag{5}$$

where $\overline{\mathbf{x}} = [\mathbf{x}\ \ \dot{\mathbf{x}}]^{\mathbf{T}}$ is the state vector, $\mathbf{u} = \mathbf{i_c}$ is the vector control, $\mathbf{y} = \mathbf{x}$ is the measured quantity, namely, the sensor output signal vector of the five freedom degrees. Moreover, type (5) can also be expressed as

$$\mathbf{G}(s) = \begin{bmatrix} G_{11}(s) & G_{12}(s) \\ G_{21}(s) & G_{22}(s) \end{bmatrix} = \left[\begin{array}{c|cc} \mathbf{A} & \mathbf{B}_1 & \mathbf{B}_2 \\ \hline \mathbf{C} & O & O \end{array}\right], \tag{6}$$

where O is the five-order zero matrix; it can be solved out through types (4) and (5):

$$\begin{aligned} \mathbf{A} &= \begin{bmatrix} O & \mathbf{I} \\ -\dfrac{\mathbf{K}}{\mathbf{M}} & -\dfrac{\mathbf{C}}{\mathbf{M}} \end{bmatrix}, \qquad \mathbf{B}_1 = \begin{bmatrix} O \\ \dfrac{\mathbf{I}}{\mathbf{M}} \end{bmatrix}, \\ \mathbf{B}_2 &= \begin{bmatrix} O \\ -\dfrac{\mathbf{I}}{\mathbf{M}} \end{bmatrix}, \qquad \mathbf{C} = [\mathbf{I}\ \ O]. \end{aligned} \tag{7}$$

So far, the nonlinear dynamic model $G(s)$ of the maglev flywheel is solved, and the precise model is provided for the design of the following dual-mode switch controller.

3. Dual-Mode Switch Control Strategy

To improve the control stability and the energy storage density of vehicle maglev flywheel, a dual-mode switch control strategy is study based on $H\infty$ control algorithm and adaptive iterative learning control algorithm. The control strategy is shown in Figure 2. The control strategy includes generalized control elephant and dual-mode switch controller. Among them, the generalized control elephant is composed of power amplifiers, active magnetic bearing (AMB), flywheel rotor, and displacement and the dual-mode switch controller is composed of $H\infty$ controller and unbalance compensation controller.

The basic response is a random signal when EV is driving on the bumpy road or start-stop, acceleration-deceleration, and steering. To reduce the random impact and improve the control robustness, a $H\infty$ controller is solved. Besides, to limit the flywheel radial run-out of the maglev flywheel battery in the charging process and improve the energy storage density of the maglev flywheel, an unbalance displacement feed-forward compensation controller based on adaptive iterative learning control (AILC) algorithm is adopted [10]. The switching work between $H\infty$ control and AILC is implemented by the real-time switching controller by judging the status of the EV and the maglev flywheel.

3.1. $H\infty$ Controller Design. A kind of $H\infty$ control strategy with mixed sensitivity is designed according to the characteristic of the maglev flywheel state space equation; it is shown in Figure 3.

In Figure 3, $\mathbf{K_H}$ is the transfer function matrix of the $H\infty$ controller, $\mathbf{u}$ is the input signal matrix, W_1, W_2, and W_3 are the weighted functions, $\mathbf{G}$ is the state space equation of the maglev flywheel (it contains the power amplifier transfer function G_A, the sensor transfer function G_S, and the control current $\mathbf{i_c}$, and so forth), $\mathbf{y}$ is the sensor output signal vector, $\mathbf{r}$ is the system reference signal vector, and $\mathbf{e}$ is the error signal matrix.

$\mathbf{T_c}$ is the closed transfer function in Figure 3 can be written as [11]

$$\mathbf{T_c} = F_l(\mathbf{G}, \mathbf{K}_H) = \mathbf{G}_{11} + \mathbf{G}_{12}\mathbf{K}_H\left(\mathbf{I} - \mathbf{G}_{22}\mathbf{K}_H\right)^{-1}\mathbf{G}_{21}, \tag{8}$$

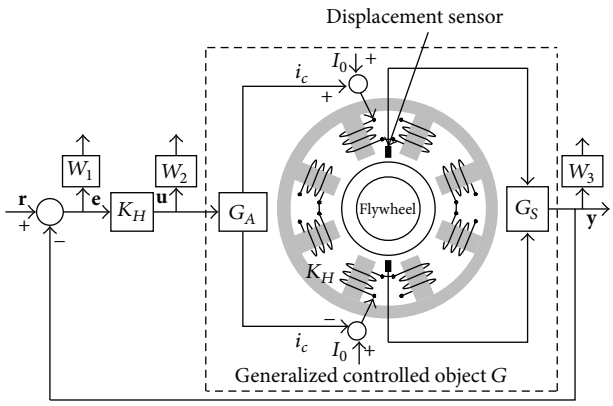

Figure 3: The diagram of $H\infty$ control strategy.

where type (8) is the linear fractional transformation of the $H\infty$ controller $\mathbf{K}_H$. The standard of $H\infty$ control problem is to find a real rational $\mathbf{K}_H$, to make the controlled object $\mathbf{G}$ stable work, and to make the minimal $H\infty$ norm of $\mathbf{T_c}$ in the whole frequency range [12], should be satisfied by

$$\left\|\mathbf{T_c}\right\|_\infty = \sup_\omega \overline{\sigma}\left(\mathbf{T_c}\left(j\omega\right)\right) < \gamma, \tag{9}$$

where $\overline{\sigma}(\mathbf{T_c}(j\omega))$ is the biggest singular value of $\mathbf{T_c}$, "sup" is the supremum of $\overline{\sigma}(\mathbf{T_c}(j\omega))$ in the whole frequency range, and γ is a given positive number.

The corresponding sensitivity and complementary sensitivity matrix functions $\mathbf{S}$ and $\mathbf{T}$ combined with Figure 2 can be deduced:

$$\begin{aligned}\mathbf{S} &= \frac{\mathbf{e}}{\mathbf{r}} = \frac{1}{\mathbf{I} + \mathbf{K}_H(s)\,\mathbf{G}(s)},\\ \mathbf{T} &= \frac{\mathbf{y}}{\mathbf{r}} = \frac{\mathbf{K}_H(s)\,\mathbf{G}(s)}{\mathbf{I} + \mathbf{K}_H(s)\,\mathbf{G}(s)} = \mathbf{I} - \mathbf{S}.\end{aligned} \tag{10}$$

$W_1(s)$ is the weighted function of $\mathbf{S}$; its main purpose is to limit the amplitude of $\mathbf{S}$ in a specified frequency range. $W_3(s)$ is the weighted function of $\mathbf{T}$, whose purpose is to limit the amplitude of $\mathbf{T}$. In addition, the transfer function matrix of the $H\infty$ controller output is

$$\mathbf{R} = \frac{\mathbf{u}}{\mathbf{r}} = \frac{\mathbf{K}_H(s)}{\mathbf{I} + \mathbf{K}_H(s)\,\mathbf{G}(s)}. \tag{11}$$

$\mathbf{R}$ also has a weighted function $W_2(s)$; its main purpose is to limit the $\mathbf{K}_H$ controller output. $W_2(s)$ should be chosen as a relatively small value in order to reduce the compensators and shorten operation cycle.

The structural parameters of the maglev flywheel are calculated and got as $m = 10.8\,\text{kg}$, $k_{ix1} = k_{ix2} = k_{iy1} = k_{iy2} = 954.6\,\text{N/A}$, $k_{iz} = 1543.8\,\text{N/A}$, $k_{xx1} = k_{xx2} = k_{xy1} = k_{xy2} = 1.517 \times 10^6\,\text{N/m}$, and $K_{XZ} = 3.216 \times 10^6\,\text{N/m}$. Based on $H\infty$ controller problem solving limit and MATLAB robust control instructions, the solved parameters are involved in the $\mathbf{G}(s)$ solution procedure, and the weighting functions $W_1(s)$ and $W_3(s)$ are determined, respectively, by

$$\begin{aligned}W_1(s) &= \frac{98}{s+2},\\ W_3(s) &= \frac{1.5s}{s+3200}.\end{aligned} \tag{12}$$

In addition, $W_2(s)$ is selected as 2.0×10^7 through the simulation analysis. Then, the robust performance index (0.4232) is calculated based on the controlled object transfer function matrix $\mathbf{G}$ and the three weighted functions; if the index greater than 1, the three weighted functions need to be selected. Finally, the four radial and one axial discrete transfer functions of the $H\infty$ controller are concluded:

$$\begin{aligned}K_{Hx1} &= K_{Hx2} = K_{Hy1} = K_{Hy2}\\ &= \frac{-21.8z^3 + 15.3z^2 - 25.6z + 21.32}{z^3 - 10.61z^2 + 8.69z - 1.73},\\ K_{Hz} &= \frac{-101.3z^3 + 80.5z^2 + 4.68}{z^3 - 5.87z^2 + 2.32z - 0.21}.\end{aligned} \tag{13}$$

Because the maglev flywheel is axially symmetric distribution in four radial freedom degrees, the four radial discrete transfer functions are the same. In order to make the control cycle consistent with the actual flywheel control system, the simulation sampling frequency is selected as 20000 Hz.

3.2. Feed-Forward Compensation Control Analysis. To reduce the radial run-out of the flywheel and solve the problem of variable speed, the AILC algorithm is adopted as the feed-forward controller to implement vibratory displacement compensation [10]. In Figure 4, the control scheme consists of PID feedback control system, AILC feed-forward compensation controller, and generalized plant. The PID controller can steady the whole system and improve the anti-interference ability, and the action of AILC is to make the learning gain accurately track the expectant orbit. The generalized plant includes power amplifier, electromagnetic coils, and rotor system.

To improve control performance and enhance the convergence rate of the learning law, there are two modifications in AILC. The first one is enhancing the error information action of previous control period and the second one is proposing a novel impacting factor β as the coefficient of the learning gain v_k. β can reduce the effects of learning gain to the control system when rotor speed does not coincide with the learning cycle of AILC. AILC can implement vibratory displacement compensation without any information of the generalized plant, and it will not increase the interference of the feedback controller. Only the expectant signal y_d and the output of the sensor y_k are needed in AILC; here, y_d is 2.5 V witch is defined as the balance position of rotor during static suspension. The error signal between y_d and y_k is iteratively learned, then, the perfect and unknown control signal u_k is obtained as the input signal of the power amplifier.

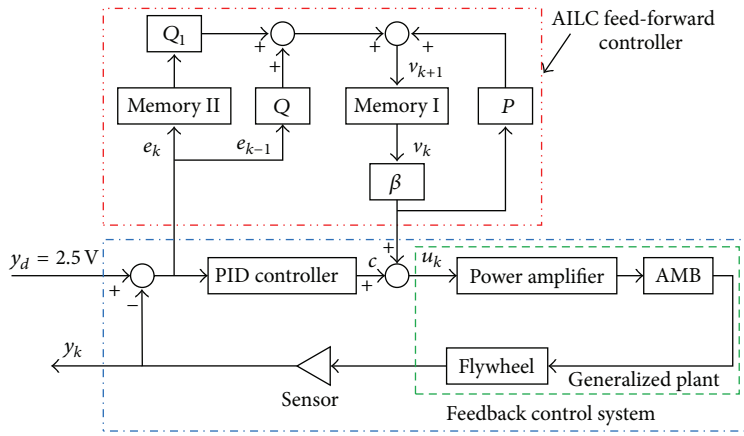

Figure 4: AILC compensation principle of AMB system.

The functions of AILC can be introduced by the iterative formulas in discrete domain. The error formula is given.

The update learning law of AILC is summarized as

$$v_{k+1}(n) = \beta P v_k(n) + Q e_k(n) + Q_1 e_k(n-1). \tag{14}$$

To understand the action of AILC better, the control input signal of generalized plant is written as

$$u_k(n) = c(n) + \beta v_k(n), \tag{15}$$

where $u_k(n)$ is the controller input, $c(n)$ is PID controller output, $v_k(n)$ is the learning gain of AILC, and β is the impacting factor of $v_k(n)$. The last objective is to obtain perfect controller signal u_d when having infinitely iterative learning and then make the error signal become zero. It should be satisfied as [13]

$$\lim_{k\to\infty} u_k(n) = u_d, \qquad \lim_{k\to\infty} e_k(n) = 0. \tag{16}$$

The discrete transfer function of the learning law of (14) can be calculated by

$$\begin{aligned} V_{k+1}(z) &= \beta P V_k(z) + Q E_k(z) + Q_1 E_k(z) z^{-1} \\ &= \beta P V_k(z) + \left(Q + Q_1 z^{-1}\right) E_k(z), \end{aligned} \tag{17}$$

where z^{-1} represents the lag operator in time domain, and it could make the sampled signal lag one period. This is the reason why the former error information is added into the modified learning law of AILC.

The PID controller with incomplete differential part is given in time domain:

$$\begin{aligned} c(t) &= G_P(t) \\ &= K_p\left[e(t) + \frac{1}{T_i}\int_0^t e(t)\,dt + \frac{T_d}{1+T_f}\frac{d(e(t))}{dt}\right]. \end{aligned} \tag{18}$$

The discrete function of (18) is deduced as

$$\begin{aligned} C(z) &= K_p\left[1 + \frac{T_0}{T_i}\frac{1}{1-z^{-1}} + \frac{T_d}{\left(1+T_f\right)T_0}\left(1-z^{-1}\right)\right]E(z). \end{aligned} \tag{19}$$

The z-transform of the control signal function of (15) is deduced by

$$\begin{aligned} U_k(z) &= C(z) + \beta V_k(z) \\ &= k_p\left[1 + \frac{T_0}{T_i}\frac{1}{1-z^{-1}} + \frac{T_d}{\left(1+T_f\right)T_0}\left(1-z^{-1}\right)\right]E(z) \\ &\quad + \beta V_k(z), \end{aligned} \tag{20}$$

where defining

$$\begin{aligned} H(z) &= 1\left(k_p\left[1 + \frac{T_0}{T_i}\frac{1}{1-z^{-1}} + \frac{T_d}{\left(1+T_f\right)T_0}\left(1-z^{-1}\right)\right]\right)^{-1}. \end{aligned} \tag{21}$$

The discrete function of error signal can be obtained as

$$E(z) = \left(U_k(z) - \beta V_k(z)\right) H(z). \tag{22}$$

Putting (22) into (17), it has

$$\begin{aligned} V_{k+1}(z) &= \beta P V_k(z) + \left(Q + Q_1 z^{-1}\right)\left(U_k(z) - \beta V_k(z)\right) H(z) \\ &= \beta\left[P - \left(Q + Q_1 z^{-1}\right) H(z)\right] V_k(z) \\ &\quad + \left(Q + Q_1 z^{-1}\right) H(z) U_k(z). \end{aligned} \tag{23}$$

Equation (24) gives the transformation in limit calculation at the two sides of (23)

$$V_\infty(z) = \lim_{k\to\infty} V_k(z) = \lim_{k\to\infty} \frac{\left(Q + Q_1 z^{-1}\right) H(z) U_k(z)}{1 - \beta\left[P + \left(Q + Q_1 z^{-1}\right) H(z)\right]}. \tag{24}$$

If P and β all are 1, at the same time, the following inequality is satisfied by [14]:

$$\left\|\beta P - \beta[Q + Q_1 z^{-1}] H(z)\right\|_\infty < 1. \tag{25}$$

Equation (24) can be simplified by

$$V_\infty(z) = \lim_{k\to\infty} U_k(z) = U_d(z). \tag{26}$$

That is, the controller signal $u_k(z)$ is replaced by $\beta v_k(z)$ when infinite iteration is operated, and the error signal will become zero. According to (22) and (26), the error signal can be shown as

$$\begin{aligned} \lim_{k\to\infty} E(z) &= H(z)\left[\lim_{k\to\infty} U_k(z) - \beta \lim_{k\to\infty} V_k(z)\right] \\ &= H(z)\left[U_d(z) - \beta V_\infty(z)\right] \\ &= H(z)\left[U_d(z) - \beta U_d(z)\right] = 0. \end{aligned} \tag{27}$$

The convergence of AILC has been demonstrated according to (26) and (27), and a perfect controller signal u_d has been obtained as power amplifier input. Therefore, the AILC algorithm as the feed-forward compensation controller can be adopted in the application of maglev flywheel unbalance vibratory compensation.

According to the start-up time and the variability of the rotor frequency from static suspension to one fixed speed, the equation of β is given as

$$\beta = \left(\frac{f}{f_d}\right)^n, \tag{28}$$

where f is the flywheel frequency, f_d is a given frequency, and the action of n is to reduce the value of β when f is far away from f_d (usually, n is greater than 2). In the start-up process, due to $f \ll f_d$, the value of β should be very small; it can weaken the influence of V_k on the generalized plant. However, β will be close to 1 if $f \approx f_d$; it can enhance the effect of repetitive learning and can make the error signal to converge toward zero.

4. Simulation and Experimental

4.1. Simulation Analysis. First, the stability of $H\infty$ controller is attested through analyzing the singular values relationship between $S(s)$ and $W_1(s)$, as well as between $T(s)$ and $W_3(s)$. The sensitivity and complementary sensitivity function and the corresponding weighted function singular value relations are shown in Figure 5. The curves in Figure 5 are created in the "M" file of MATLAB through some command functions, the transfer functions of $\mathbf{T_c}$, $\mathbf{K}_H$, and $\mathbf{G}(s)$, and so on.

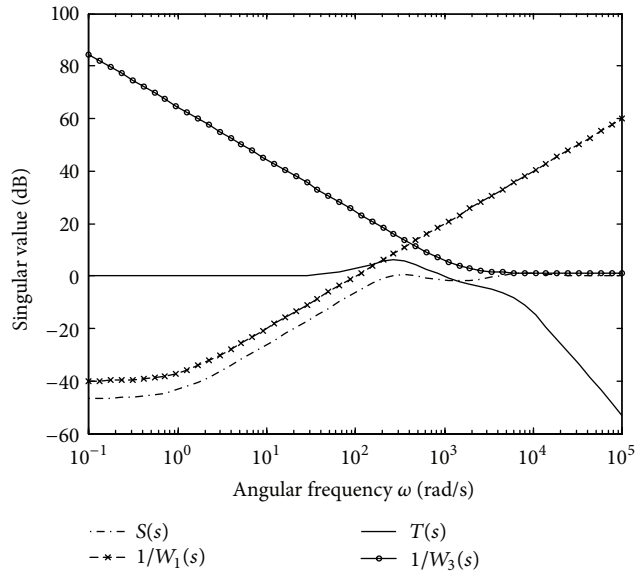

Figure 5: Sensitivity, complementary sensitivity, and the corresponding weighted function singular value relations.

The choice principle of $W_1(s)$ is guaranteeing the anti-interference and tracking ability of the flywheel system, and the smaller the singular value of $S(s)$ is, the better the system tracking ability is. The curve of $S(s)$ should be under the curve of the $1/W_1(s)$; if it does not conform to the demand, the weighted function $W_1(s)$ must be chosen again. The choice principle of $W_3(s)$ is guaranteeing the flywheel system output to recurrence the input, and the smaller the singular value of $T(s)$ is, the smaller the system impact by compound disturbance because of model uncertainty is. The curve of $T(s)$ should also be under the curve of the $1/W_3(s)$; if it does not conform to the demand, the weighted function $W_3(s)$ must be chosen again. Figure 5 shows that the curve of $S(s)$ is under the curve of $1/W_1(s)$, and the curve of $T(s)$ is under the curve of $1/W_3(s)$, which demonstrates that the selection of weighted function in types (14) and (15) can meet the design requirements, and the solved $H\infty$ controller is appropriate.

Second, the simulation parameters of AILC are selected as $f_d = 600$ Hz, $P = 0.995$, $Q = 0.75$, $Q_1 = 0.25$, $n = 0, 1, \ldots, 99$, and the definition of "n" indicates that the AILC algorithm has 100 memory points in one control period. Figure 6 shows the rotor simulation orbits and radial run-out displacements with AILC compensation.

The flywheel has a regular circular trajectory in Figure 6(a) and a sine radial run-out displacement in Figure 6(b) without adding AILC compensation. When the AILC algorithm starts to work at 0.05 s, the circular trajectory is gradual convergence to a point and the amplitude of the radial run-out displacement is obvious attenuation. The curves change simulation result in Figure 6 testifies the AILC algorithm having good displacement compensation effect

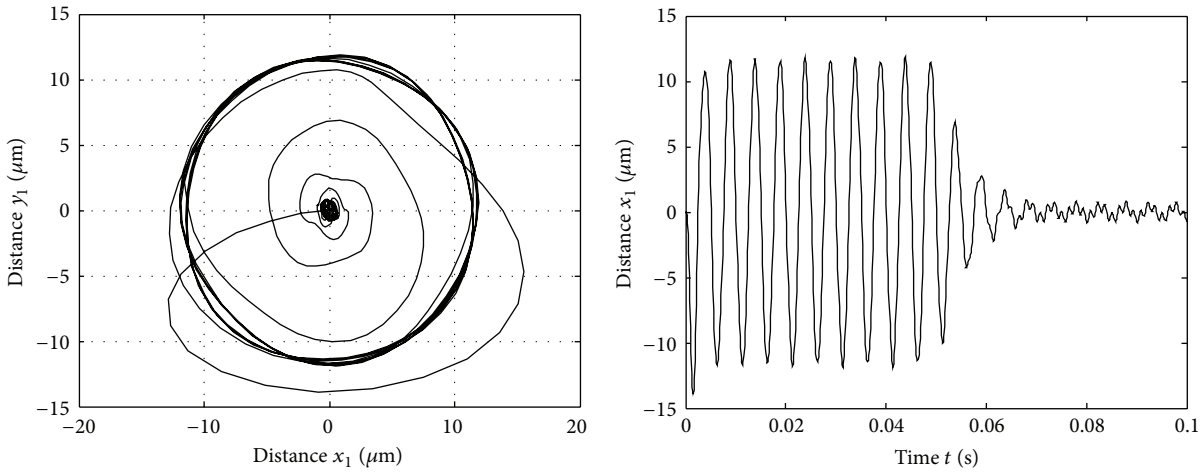

(a) Rotor position orbit

(b) Rotor run-out in axis x_1

FIGURE 6: Flywheel trajectory with AILC compensation.

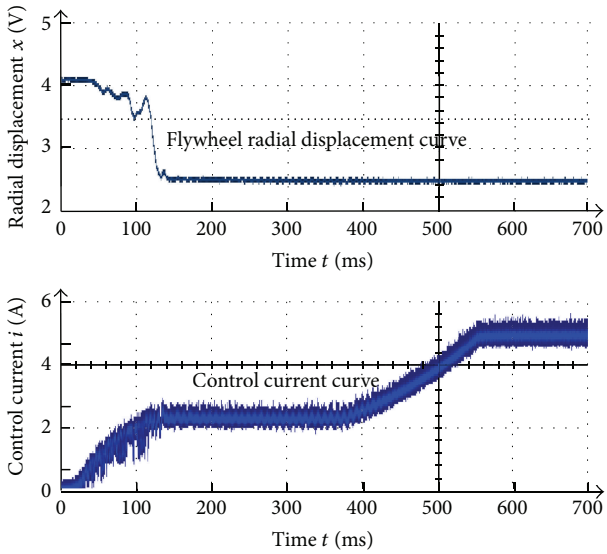

FIGURE 7: Flywheel displacement and control current in start-up process by $H\infty$ control.

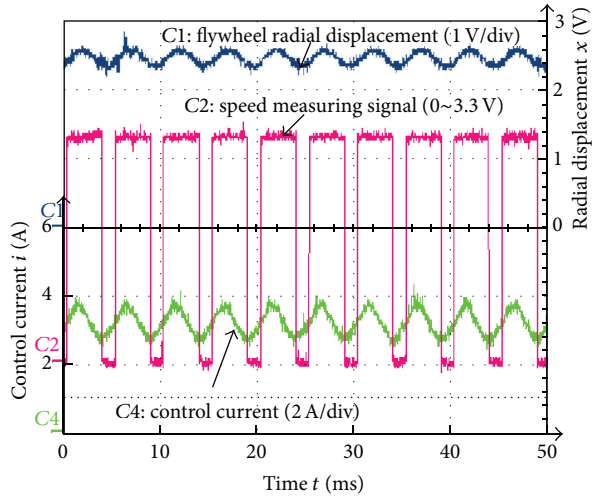

FIGURE 8: Flywheel displacement and control current in rotating process by $H\infty$ control and the speed measuring pulse at 600 Hz.

and ensuring the flywheel to rotate around its collection center.

4.2. Experimental Results. In Figure 7, the radial displacement voltage curve and the control current curve of the flywheel are shown in start-up process by the solved $H\infty$ controller control; the displacement voltage quickly drops to the equilibrium position (2.5 V) from the sensor calibration position (4 V). It illustrates that the $H\infty$ controller has good robust stability and can be used in the control system of vehicle maglev flywheel.

Figure 8 includes the radial displacement curve, the control current curve, and the speed measuring pulse when flywheel normal is rotating by $H\infty$ control and flywheel rotational frequency is 600 Hz. The displacement curve is a sine wave, and it can show the flywheel has mass unbalance. To restrict flywheel radial run-out, the control current also is sine having basic consistent phase with the displacement voltage. The speed measuring pulse has a voltage range from 0 V to 3.3 V; the purpose is to guarantee the pulse be captured by DSP acquisition circuit.

The compensated effect by AILC algorithm at 600 Hz is shown in Figure 9, including the radial displacement curve and the control current curve after compensation. Compared with the radial sine displacement in Figure 8, the radial displacement is balance in the position of 2.5 V, which indicates the flywheel is limited rotating around its geometric center. To limit the radial run-out and increase the active control effect, the control current amplitude is significantly larger than without compensation.

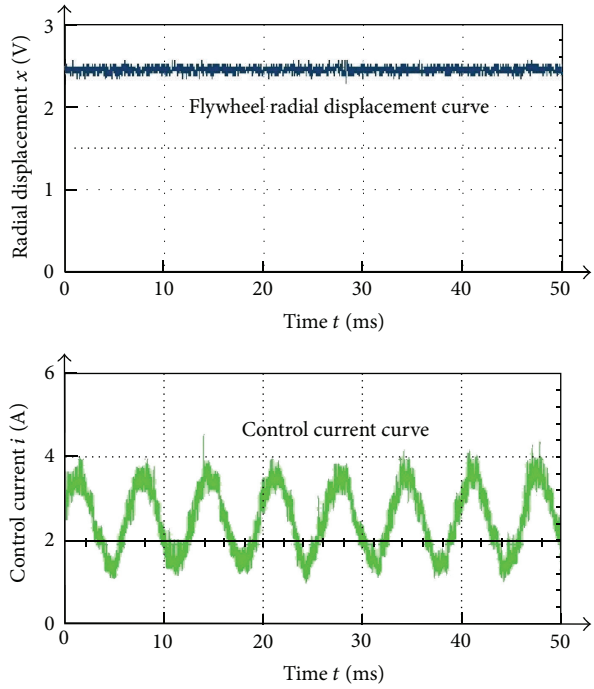

Figure 9: Flywheel displacement and control current in AILC compensation process at 600 Hz.

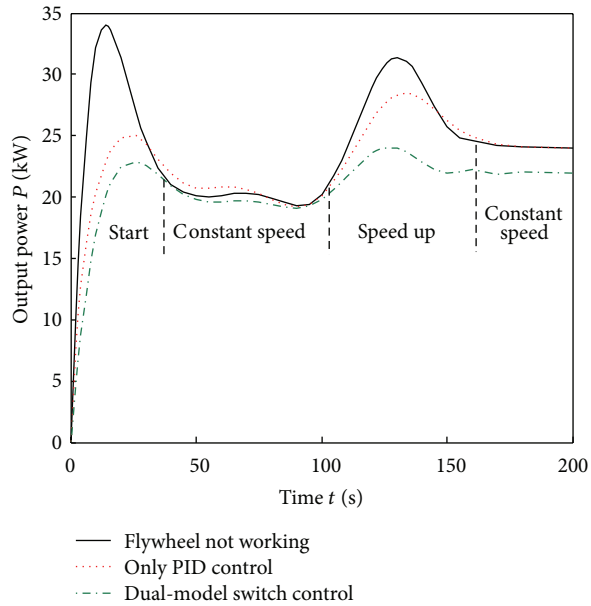

Figure 10: EV primary battery output power in different modes.

Figure 10 gives the output power curves of EV primary battery in three different modes. If flywheel is not working, the output power is about 35 kW when EV starts up; if the flywheel battery is working and only PID controlling, the output power of the primary battery is about 25 kW in EV start-up process; if the dual-model switch control strategy is acting on the flywheel, the output power reduces to 23 kW. The power change shows the flywheel has better auxiliary effect to EV primary battery when it is controlled by the dual-model switch control strategy. Similarly, the output power of EV primary battery is the smallest in the acceleration process when the dual-model switch control strategy controls the flywheel. Moreover, because the flywheel rotate speed is higher when the dual-model switch control strategy is working, EV needs lower motive power when restarting. Therefore, when maglev flywheel participates in discharge and is controlled by dual-model switch control strategy, EV primary battery output power is obviously decreased in the whole driving process, the influence on chemical characteristics of primary battery is reduced because the instantaneous discharge depth is small, and the service life of EV primary battery can be improved.

5. Conclusion

Through analyzing the nonlinear dynamic characteristics and the application on EV, one kind of dual-model control strategy based on $H\infty$ control and AILC algorithms has been studied in this paper, and the state space equation of maglev flywheel was analyzed. To improve the robust stability of flywheel control system and reduce the real-time interference, one $H\infty$ controller based on the state space equation was solved. To reduce maglev flywheel radial run-out, one adaptive iterative learning control theory was deduced, and unbalance displacement compensation was implemented. The experimental result shows the dual-model control strategy has better interference capability in maglev flywheel start-up process and has stronger active control ability relative to only PID control. The maglev flywheel based on the dual-model control can help the EV primary battery, improve its discharge characteristics, help to prolong its service life, and accelerate the development scale of electric vehicles.

Conflict of Interests

The authors declare that they have no conflict of interests regarding this paper.

Acknowledgments

This work is supported by the National Natural Science Foundation of China (51405244), the China Postdoctoral Science Foundation (2014M551634), and the Jiangsu Province Natural Science Foundation of China (BK20140880). The authors would like to thank the editor and the reviewers for their constructive comments and suggestions to improve the quality of the paper.

References

[1] E. Sortomme, *Optimal aggregator bidding strategies for vehicle-to-grid [Ph.D. thesis of Philosophy]*, University of Washington, 2011.

[2] H.-F. Dai, Z.-C. Sun, and X.-Z. Wei, "Technologies to relief un-uniformity of power batteries used in electrical vehicles," *Journal of Automotive Safety and Energy*, vol. 2, no. 1, pp. 62–67, 2011.

[3] B. Bolund, H. Bernhoff, and M. Leijon, "Flywheel energy and power storage systems," *Renewable and Sustainable Energy Reviews*, vol. 11, no. 2, pp. 235–258, 2007.

[4] M. Jiang, J. Salmon, and A. M. Knight, "Design of a permanent magnet synchronous machine for a flywheel energy storage system within a hybrid electric vehicle," in *Proceedings of the IEEE International Electric Machines and Drives Conference (IEMDC '09)*, pp. 1736–1742, May 2009.

[5] J. Abrahamsson, J. de Santiago, and J. G. Oliveira, "Prototype of electric driveline with magnetically levitated double wound motor," in *Proceedings of the 19th International Conference on Electrical Machines (ICEM '10)*, pp. 1–5, September 2010.

[6] M. S. Raymond, M. E. F. Kasarda, and P. E. Allaire, "Windage power loss modeling of a smooth rotor supported by homopolar active magnetic bearings," *Journal of Tribology*, vol. 130, no. 2, pp. 1–8, 2008.

[7] Y.-L. Xu and J.-C. Fang, "Development of low power loss energy storage flywheel," *Transactions of China Electrotechnical Society*, vol. 23, no. 12, pp. 11–16, 2008.

[8] T. A. Aanstoos, J. P. Kajs, W. G. Brinkman et al., "High voltage stator for a flywheel energy storage system," *IEEE Transactions on Magnetics*, vol. 37, no. 1, pp. 242–247, 2001.

[9] H. Qing-kai, *Nonlinear Vibration Analysis and Diagnosis Method for Fault Rotor System* , Science Press, Beijing, China, 2010.

[10] H. Gao, L. Xu, and Y. Zhu, "Unbalance vibratory displacement compensation for active magnetic bearings," *Chinese Journal of Mechanical Engineering*, vol. 26, no. 1, pp. 95–103, 2013.

[11] Z. Gosiewski and A. Mystkowski, "Robust control of active magnetic suspension: analytical and experimental results," *Mechanical Systems and Signal Processing*, vol. 22, no. 6, pp. 1297–1303, 2008.

[12] J.-M. Kim, C.-K. Kim, M.-K. Park, and K.-H. Kim, "A robust control of a magnetic suspension system with a flexible rail," in *Proceedings of the IEEE International Symposium on Industrial Electronics (ISIE '01)*, vol. 2, pp. 1309–1312, Pusan, Republic of Korea, June 2001.

[13] H. G. Chiacchiarini and P. S. Mandolesi, "Unbalanced compensation for active magnetic bearings using ILC," in *Proceedings of the IEEE International Conference on Control Applications*, pp. 58–63, Mexico City, Mexico, September 2001.

[14] C. Bi, D. Wu, Q. Jiang, and Z. Liu, "Automatic learning control for unbalance compensation in active magnetic bearings," *IEEE Transactions on Magnetics*, vol. 41, no. 7, pp. 2270–2280, 2005.

Hindawi Publishing Corporation
Mathematical Problems in Engineering
Volume 2015, Article ID 197258, 7 pages
http://dx.doi.org/10.1155/2015/197258

Research Article

Construction and Application Research of Isomap-RVM Credit Assessment Model

Guangrong Tong and Siwei Li

School of Economics and Management, Wuhan University, Wuhan 430072, China

Correspondence should be addressed to Guangrong Tong; tonggr2014@126.com

Received 5 November 2014; Accepted 10 January 2015

Academic Editor: Honglei Xu

Copyright © 2015 G. Tong and S. Li. This is an open access article distributed under the Creative Commons Attribution License, which permits unrestricted use, distribution, and reproduction in any medium, provided the original work is properly cited.

Credit assessment is the basis and premise of credit risk management systems. Accurate and scientific credit assessment is of great significance to the operational decisions of shareholders, corporate creditors, and management. Building a good and reliable credit assessment model is key to credit assessment. Traditional credit assessment models are constructed using the support vector machine (SVM) combined with certain traditional dimensionality reduction algorithms. When constructing such a model, the dimensionality reduction algorithms are first applied to reduce the dimensions of the samples, so as to prevent the correlation of the samples' characteristic index from being too high. Then, machine learning of the samples will be conducted using the SVM, in order to carry out classification assessment. To further improve the accuracy of credit assessment methods, this paper has introduced more cutting-edge algorithms, applied isometric feature mapping (Isomap) for dimensionality reduction, and used the relevance vector machine (RVM) for credit classification. It has constructed an Isomap-RVM model and used it to conduct financial analysis of China's listed companies. The empirical analysis shows that the credit assessment accuracy of the Isomap-RVM model is significantly higher than that of the Isomap-SVM model and slightly higher than that of the PCA-RVM model. It can correctly identify the credit risks of listed companies.

1. Introduction

By constructing an accurate and reliable credit assessment model, we can conduct an in-depth analysis of the financial data of listed companies and identify the financial risks of such companies. This is of great significance to the operational decisions of shareholders, corporate creditors, and management. Along with the development of large data methods, the theory of applying machine learning methods to construct credit assessment models has become increasingly reliable. Machine learning methods are superior to traditional multivariate discriminant analysis methods and logistic discriminant analysis models, when processing any data subject to less stringent hypothetical restrictions and dealing with nonlinear relationships. At present, commonly used machine learning methods with good data classification results include the neural network (NN) [1] and the support vector machine (SVM). Odom and Sharda [2] built an early warning model for financial crises. They did so by applying the neural network and comparing this model with the Fisher multivariate discriminant analysis model. The research results showed that the artificial neural network has higher prediction accuracy and robustness. However, the neural network has methodological defects, such as slow convergence rate, overfitting, and falling into local minima [3, 4]. Later, Cortes and Vapnik [5] proposed the vector machine method, which is based on the theory of statistical machine learning. This method laid stress on structural risk minimization and is able to effectively overcome the defects of the neural network. Min and Lee [6] applied the SVM to build a financial early warning model for the purpose of corporate bankruptcy prediction. The results showed that the SVM has higher discriminant analysis accuracy than BP neural network, MDA, and logit models. However, SVM has the following main defects: the penalty parameter C must be determined in the model building process, and the selection of kernel function must comply with "Mercer's theorem" [7]. For these reasons, this paper suggests using a relevance vector

machine (RVM) to overcome the defects of SVM. RVM is another efficient supervised learning method proposed by Tipping [8]. By applying this method to conduct machine learning under the Bayesian theory, the model obtained will be sparser than with SVM, and the result probability output can also be obtained. While properly maintaining all the advantages of SVM, this method has reduced the inaccurate assignment of key parameters, broadened the application scope of vector machines, provided a greater degree of freedom, and effectively overcome the defects of SVM [9]. This will help to improve the accuracy of vector machine classification.

In credit risk assessment samples, there tends to be a close correlation between the selected financial risk characteristic indices. High dimensionality and high correlation of the sample characteristic indices may have a strong impact on the accuracy of risk assessment. Therefore, a data dimensionality reduction method is required for the pretreatment of the sample indices, so as to reflect the main features of the data as much as possible and reduce correlation between the characteristic indices. At present, the principal component analysis method (PCA) is one of the most widely used methods [10]. However, as a linear dimensionality reduction method, PCA may not achieve satisfactory dimensionality reduction results when applied to nonlinear data. Therefore, this paper attempts to apply a nonlinear dimensionality reduction method—isometric mapping (Isomap)—to conduct dimensionality reduction pretreatment on the sample data. Isomap is a nonlinear manifold learning algorithm proposed by Tenenbaum et al. [11]. By seeking low-dimensional embedding among high-dimensional manifolds, this algorithm has maintained low-dimensional embedding in the neighborhood structure between high-dimensional manifold data points, while producing excellent robustness and global optimality. Lin et al. [12] used the Isomap-SVM, PCA-SVM, and SVM separately to conduct risk assessment classification of more than one hundred listed Taiwan companies. It proved that Isomap-SVM has the highest prediction accuracy. This research showed that, in the process of nonlinear data classification, Isomap can improve accuracy through reasonable dimensionality reduction. Ribeiro et al. [13] constructed a Semi-Supervised Isomap model with Isomap and SVM. They used the Semi-Supervised Isomap model, SVM, RVM, and KNN separately to conduct bankruptcy prediction of more than one thousand industrial French companies. The results showed that the classification accuracy of Semi-Supervised Isomap model is comparable to SVM and RVM. But in the study they did not propose the idea of constructing a new model by combining Isomap with other machine learning methods such as RVM.

By applying the Isomap method to reduce the dimensions and avoid correlation between sample characteristic indices and by using the RVM to conduct the classification, this paper builds an Isomap-RVM model. It conducts a credit assessment classification analysis of China's listed companies. It then compares this model with the Isomap-SVM and PCA-RVM models and examines Isomap-RVM model discriminant analysis accuracy.

2. Isomap-RVM Model Construction

2.1. RVM Classification Method. Assume a training set of n samples, where its characteristic index part constitutes a vector set $\{\mathbf{x}_i\}$, $i = 1, 2, \ldots, n$; the corresponding output target value of the training set is $\mathbf{t} = [t_1, t_2, \ldots, t_n]^T$, where t_i may only be either 0 or 1, which corresponds to two categories. Like the support vector machine, $\mathbf{x}$ has the following nonlinear function expression:

$$y(\mathbf{x}; \mathbf{w}) = \sum_{i=1}^{n} w_i K(\mathbf{x}, \mathbf{x}_i) + w_0, \tag{1}$$

where $\mathbf{w} = [w_0, w_1, \ldots, w_n]^T$ stands for the weight, while $K(\mathbf{x}, \mathbf{x}_i)$ stands for the kernel function selected. There are four commonly used kernel functions, as follows.

Linear kernel:

$$K(a, b) = a \cdot b. \tag{2}$$

Polynomial kernel:

$$K(a, b) = [(a \cdot b) + 1]^c. \tag{3}$$

Neural kernel:

$$K(a, b) = \tanh(\eta(a \cdot b) - \varsigma). \tag{4}$$

RBF kernel:

$$K(a, b) = \exp\left(-\frac{\|a - b\|^2}{2\sigma^2}\right). \tag{5}$$

In this study, radial basis function (RBF) is adopted. The reason is that, compared with other kernel functions, RBF can be applied to conduct nonlinear mapping without substantially increasing the complexity of the model.

After constructing $y(\mathbf{x}; \mathbf{w})$, the correspondence between $\mathbf{t}$ and $\mathbf{x}$ can be expressed by the following sigmoid function:

$$p(t_i = 1 \mid \mathbf{w}) = \frac{1}{1 + e^{-y(\mathbf{x}_i; \mathbf{w})}}. \tag{6}$$

Then, provided that the weight $\mathbf{w}$ is known, the probability of $\mathbf{t}$ is as follows:

$$p(\mathbf{t} \mid \mathbf{w}) = \prod_{i=1}^{n} \left[\frac{1}{1 + e^{-y(\mathbf{x}_i; \mathbf{w})}}\right]^{t_i} \left[1 - \frac{1}{1 + e^{-y(\mathbf{x}_i; \mathbf{w})}}\right]^{1 - t_i}. \tag{7}$$

After calculating the best weight $\mathbf{w}_M$, substitute $\mathbf{w}_M$ and the sample testing set characteristic index $\mathbf{x}_*$ into (6); we will get the probability of the testing set output target value t_*.

To avoid overlearning due to the fact that most weights are not zero, it can be assumed that $\mathbf{w}$ is subject to a normal distribution:

$$\mathbf{w} \sim N\left(0, \frac{1}{\boldsymbol{\alpha}}\right), \tag{8}$$

where $\boldsymbol{\alpha} = [\alpha_0, \alpha_1, \ldots, \alpha_n]^T$.

The prior probability of weight is expressed as

$$p(\mathbf{w} \mid \boldsymbol{\alpha}) = \prod_{i=0}^{n} (2\pi)^{-1/2} \alpha_i \exp\left(-\frac{\alpha_i w_i^2}{2}\right). \tag{9}$$

The posterior probability $p(\mathbf{w} \mid \mathbf{t}, \boldsymbol{\alpha})$ of weight is expressed as

$$p(\mathbf{w} \mid \mathbf{t}, \boldsymbol{\alpha}) = \frac{p(\mathbf{t} \mid \mathbf{w})\, p(\mathbf{w} \mid \boldsymbol{\alpha})\, p(\boldsymbol{\alpha})}{p(\boldsymbol{\alpha}, \mathbf{t})}. \tag{10}$$

The best weight $\mathbf{w}_M$ is the weight that maximizes the posterior probability $p(\mathbf{w} \mid \mathbf{t}, \boldsymbol{\alpha})$. Provided that $\boldsymbol{\alpha}$ is known, then

$$p(\mathbf{w} \mid \mathbf{t}, \boldsymbol{\alpha}) \propto p(\mathbf{t} \mid \mathbf{w})\, p(\mathbf{w} \mid \boldsymbol{\alpha}). \tag{11}$$

$\mathbf{w}_M$ can be expressed as follows:

$$\begin{aligned} \mathbf{w}_M &= \arg\max_{\mathbf{w}} p(\mathbf{w} \mid \mathbf{t}, \boldsymbol{\alpha}) = \arg\max_{\mathbf{w}} p(\mathbf{t} \mid \mathbf{w})\, p(\mathbf{w} \mid \boldsymbol{\alpha}) \\ &= \arg\max_{\mathbf{w}} \lg\left[p(\mathbf{t} \mid \mathbf{w})\, p(\mathbf{w} \mid \boldsymbol{\alpha})\right]. \end{aligned} \tag{12}$$

Let

$$\begin{aligned} z_i &= \frac{1}{1 + e^{-y(\mathbf{x}_i; \mathbf{w})}}, \\ \mathbf{z} &= \left[z_1, z_2, \ldots, z_n\right]^T. \end{aligned} \tag{13}$$

Then $\lg[p(\mathbf{t} \mid \mathbf{w})p(\mathbf{w} \mid \boldsymbol{\alpha})]$ is expressed as follows:

$$\begin{aligned} \lg\left[p(\mathbf{t} \mid \mathbf{w})\, p(\mathbf{w} \mid \boldsymbol{\alpha})\right] &= \sum_{i=1}^{n} \left[t_i \lg z_i + (1 - t_i) \lg(1 - z_i)\right] \\ &\quad - \frac{\mathbf{w}^T A \mathbf{w}}{2}, \end{aligned} \tag{14}$$

where $A = \mathrm{diag}(\alpha_0, \alpha_1, \ldots, \alpha_n)$.

Use the Newton iteration method to seek $\mathbf{w}_M$ in (14):

$$\begin{aligned} \Delta\mathbf{w} &= -\left\{\nabla_{\mathbf{w}} \nabla_{\mathbf{w}} \lg\left[p(\mathbf{t} \mid \mathbf{w})\, p(\mathbf{w} \mid \boldsymbol{\alpha})\right]\right\}^{-1} \\ &\quad \cdot \left\{\nabla_{\mathbf{w}} \lg\left[p(\mathbf{t} \mid \mathbf{w})\, p(\mathbf{w} \mid \boldsymbol{\alpha})\right]\right\} \\ &= \left(\phi^T B \phi + A\right)\left[\phi^T (\mathbf{t} - \mathbf{z}) - A\mathbf{w}\right], \end{aligned} \tag{15}$$

where $B = \mathrm{diag}\,[z_1(1 - z_1), z_2(1 - z_2), \ldots, z_n(1 - z_n)]$,

$$\phi = \begin{bmatrix} 1 & K(\mathbf{x}_1, \mathbf{x}_1) & K(\mathbf{x}_1, \mathbf{x}_2) & \cdots & K(\mathbf{x}_1, \mathbf{x}_n) \\ 1 & K(\mathbf{x}_2, \mathbf{x}_1) & K(\mathbf{x}_2, \mathbf{x}_2) & \cdots & K(\mathbf{x}_2, \mathbf{x}_n) \\ & & \vdots & & \\ 1 & K(\mathbf{x}_n, \mathbf{x}_1) & K(\mathbf{x}_n, \mathbf{x}_2) & \cdots & K(\mathbf{x}_n, \mathbf{x}_n) \end{bmatrix}. \tag{16}$$

When $\Delta\mathbf{w}$ is obtained, $\mathbf{w}_M$ and $\boldsymbol{\alpha}$ should be updated by formula

$$\begin{aligned} \mathbf{w}_M^{\mathrm{new}} &= \mathbf{w}_M + \Delta\mathbf{w}, \\ \alpha_i^{\mathrm{new}} &= \frac{1 - \alpha_i \left(\left(\phi^T B \phi + A\right)^{-1}\right)_{ii}}{\left(\mathbf{w}_M^{\mathrm{new}}\right)_i^2}. \end{aligned} \tag{17}$$

Substitute the new value back into (15) to calculate $\Delta\mathbf{w}$ over and over again until $\Delta\mathbf{w}$ is reduced to a level that is below a certain limit; then we can substitute $\mathbf{w}_M$ into (6) to calculate the accurate classification probability and determine the sample category based on the classification probability $p(t_i = 1 \mid \mathbf{w})$.

2.2. Dimensionality Reduction Method Based on Isomap Manifold Learning. Isomap is developed on the basis of multidimensional scaling (MDS). It aims at seeking out the low-dimensional coordinates embedded in the high-dimensional space and achieves dimensionality reduction by constructing the shortest path distance matrix for high-dimensional sample data, under the assumption that the intrinsic geometric properties of the sample data remain unchanged [14]. The dimensionality reduction steps are shown below.

Step 1. Construct a neighborhood graph G. With respect to the characteristic index vector set $\{\mathbf{x}_i\}$, $i = 1, 2, \ldots, m$, for a total number of m samples in the training set and the testing set, each original sample $\mathbf{x}_i$ has N characteristic indices $\mathbf{x}_i = (x_{i1}, x_{i2}, \ldots, x_{iN})$. The Euclidean distance $d(\mathbf{x}_i, \mathbf{x}_j)$ between each $\mathbf{x}_i$ and each of the remaining vectors in the vector set can be calculated by the following formula:

$$d\left(\mathbf{x}_i, \mathbf{x}_j\right) = \sqrt{\sum_{k=1}^{N} \left(x_{ik} - x_{jk}\right)^2}. \tag{18}$$

When $\mathbf{x}_j$ is one of the q vectors closest to $\mathbf{x}_i$, they should be deemed as neighboring vectors. Such neighboring $q + 1$ vectors will together constitute an undirected graph G; the connection between $\mathbf{x}_i$ and its neighboring vector will constitute the boundary of graph G, where the boundary value is the distance between any two vectors constituting the boundary.

Step 2. Construct the shortest path distance matrix. Apply Dijkstra's algorithm to calculate the shortest path distance between any two vectors on the neighborhood graph G.

Above all, for any two vectors $\mathbf{x}_i$ and $\mathbf{x}_j$, the boundary value should be directly taken as the distance when they constitute the boundary, or the distance may be assumed to be ∞ when constituting no boundary at all; that is,

$$\begin{aligned} &d_0\left(\mathbf{x}_i, \mathbf{x}_j\right) \\ &\quad = \begin{cases} d\left(\mathbf{x}_i, \mathbf{x}_j\right) & \mathbf{x}_i, \mathbf{x}_j \text{ constitute the boundary} \\ \infty & \text{others.} \end{cases} \end{aligned} \tag{19}$$

Then, find out all the indirect paths between $\mathbf{x}_i$ and $\mathbf{x}_j$ along the boundary, where the path distance should be the sum of boundary values (denoted as $d_1, d_2, \ldots, d_L$); next, compare all the path distances and find the shortest distance $d_G(\mathbf{x}_i, \mathbf{x}_j)$:

$$d_G\left(\mathbf{x}_i, \mathbf{x}_j\right) = \min\left\{d_0\left(\mathbf{x}_i, \mathbf{x}_j\right), d_1, \ldots, d_L\right\}. \tag{20}$$

Use the squared value of the shortest path distance between each pair of vectors in G to create the shortest path distance matrix $D_G = [{d_G}^2(\mathbf{x}_i, \mathbf{x}_j)]_{m \times m}$.

Step 3. Apply a classical MDS algorithm to compress the vector to a d-dimensional vector.

Let

$$\xi_{ij} = \begin{cases} 0 & i \neq j \\ 1 & i = j, \end{cases}$$
$$u_{ij} = \xi_{ij} - \frac{1}{m}, \tag{21}$$
$$U = \left(u_{ij}\right)_{m \times m}.$$

Calculate the matrix τ:

$$\tau = -\frac{UD_G U}{2}. \tag{22}$$

Eigenvectors $u_1, u_2, \ldots, u_d$ corresponding to a maximum of d eigenvalues $(\lambda_1, \lambda_2, \ldots, \lambda_d)$ of τ will constitute the eigenvector matrix $U = [u_1, u_2, \ldots, u_d]$. Then, the dimensionality reduction result X_d is shown as follows:

$$X_d = \operatorname{diag}\left({\lambda_1}^{1/2}, {\lambda_2}^{1/2}, \ldots, {\lambda_d}^{1/2}\right) U^T. \tag{23}$$

The dimensionality reduction error is

$$\mathrm{Er} = 1 - R^2\left(S_G, D_{Xd}\right), \tag{24}$$

where R^2 is the correlation coefficient; $S_G = [d_G(\mathbf{x}_i, \mathbf{x}_j)]_{m \times m}$; D_{Xd} is the Euclidean distance matrix of the vectors in the d-dimensional space.

The reduced dimensionality d may be determined by observing the Er error curve. When there is an inflection point on the error curve or the Er turns to be stable and sufficiently small, the dimensionality used is the optimal dimensionality d.

2.3. Isomap-RVM Model Classification Steps.

Step 1. Conduct normalized pretreatment of the sample data. Normalize different characteristic indices into a $[0, 1]$ interval, maintain the commensurability of different indices during operation, and improve the operation speed. For m samples, the normalization formula for a sample index is

$$\overline{x}_i = \frac{x_i - x_{\min}}{x_{\max} - x_{\min}}, \tag{25}$$

where, $i = 1, 2, \ldots, m$, $\overline{x}_i$ is the value of the normalized characteristic index of the ith sample; x_i is the value of the original characteristic index of the ith sample; $x_{\max}$ and $x_{\min}$ are the maximum and minimum values, respectively, of the characteristic index in all samples.

Step 2. Apply Isomap to reduce the dimensions of the normalized sample data, reduce the correlation between the sample characteristic indices, and improve the sample quality.

Step 3. Train the training set data and apply the genetic algorithm to optimize the kernel width of RVM.

Table 1: Sample size of listed companies.

ST implementation year	2009	2010	2011	2012	2013	Total
ST companies	26	36	13	22	19	116
Non-ST companies	78	108	39	66	57	348

Step 4. Substitute the optimized kernel width, sample training set data, and the characteristic index part of testing set data into RVM for classification and get the final result.

3. Empirical Analysis

3.1. Samples and Indices. Special treatment (ST) is used to signify listed companies that have undergone a financial crisis in China's securities market. In research, ST companies are generally deemed as companies with poor credit standing, while non-ST companies are generally deemed as companies with normal credit standing. A listed company may be declared as an ST company in year t based on the financial report for year $t - 1$; hence using the financial data of year $t - 1$ to predict whether such listed company will be declared as an ST company in year t will overestimate the assessment capability of the model. For this reason, this paper has adopted the financial data of year $t - 2$ to predict whether such listed company will be declared as an ST company in year t. The raw data are derived from the financial index database on CSMAR Chinese listed companies. This paper has selected 116 companies subjected to ST between 2009 and 2013 in this database. Such new ST sample companies exclude those declared as ST companies due to nonfinancial reasons. 348 non-ST sample companies in the same industry for the corresponding year were selected, based on the ratio of 1 : 3. Altogether 464 sample companies were chosen for the empirical analysis. The sample size is shown in Table 1.

Sample category label is expressed as 0 or 1, where 0 means that the sample is an ST sample and 1 means that it is a non-ST sample. The sample characteristic index is derived from the financial index data two years before the corresponding year (i.e., 2007~2011) of each sample. This paper has selected 25 indices as the sample for estimating the characteristic index of a company's credit standing (as shown in Table 2) based on the following 8 aspects of the listed companies: cash flow capacity, return on equity, earning capacity, operating capacity, growth capacity, risk level, short-term solvency, and long-term solvency [15–18].

The 464 samples were randomly grouped into the training set and testing set. This paper classified 320 samples into the training set (accounting for about 69% of the total sample size), including 80 ST companies and 240 non-ST companies. 144 samples were classified into the testing set (accounting for about 31% of the total sample size), including 36 ST companies and 108 non-ST companies.

3.2. Empirical Results. This paper has established three credit assessment models—Isomap-RVM, Isomap-SVM, and PCA-RVM using MATLAB software. The aim is to examine

Table 2: Sample characteristic index.

Type	Variables	Name of index
Cash flow capacity	$X1$	Cash Interest Cover
	$X2$	Ratio of Cash to Operating Revenue
Return on equity	$X3$	Earnings per Share
	$X4$	P/B Ratio
	$X5$	Net Assets per Share
Earning capacity	$X6$	Return on Equity (ROE)
	$X7$	Return on Assets (ROA)
	$X8$	Net Profit Margin of Fixed Assets
Operating capacity	$X9$	Accounts Receivable Turnover
	$X10$	Inventories Turnover
	$X11$	Ratio of Current Assets to Income
	$X12$	Current Assets Turnover
	$X13$	Total Assets Turnover
Growth capacity	$X14$	Capital Preservation & Appreciation Rate
	$X15$	Growth Rate of Fixed Assets
	$X16$	Growth Rate of Total Assets
	$X17$	Growth Rate of Operating Revenue
Risk level	$X18$	Financial Leverage
Short-term solvency	$X19$	Current Ratio
	$X20$	Quick Ratio
	$X21$	Cash Ratio
	$X22$	Ratio of Working Capital to Net Assets
Long-term solvency	$X23$	Ratio of Liabilities to Total Assets
	$X24$	Times Interest Earned
	$X25$	Ratio of Debt to Equity

the classification accuracy of RVM and SVM by comparing Isomap-RVM with Isomap-SVM and to investigate the effect of different dimensionality reduction methods on the classification result by comparing Isomap-RVM with PCA-RVM. Toolboxes IsomapR1 [19] and SB1_Release_110 [20] were used when writing the PCA-RVM and Isomap-RVM; toolboxes IsomapR1 and libsvm-mat-2.89-3 [21] were used when writing the Isomap-SVM. The kernel width of RVM and parameters C and σ of SVM were optimized using the genetic algorithm.

This paper adopted a default value of 7 for the adjacency parameter q of the Isomap algorithm. Substituting this value into the sample data, we can get the residual error curve as shown in Figure 1. Figure 1 shows that the Er error, starting from the dimensionality of 12, begins to become stable from below 0.05. Thus, the reduced dimensionality of 12 was chosen.

After the data had been normalized, it was input into the SPSS, and PCA analysis was conducted. When the main component is extracted up to 12, the accumulating contribution rate will reach 83.968%. Therefore, this paper has selected information covering 85% of the original indices (i.e., the accumulating contribution rate = 85%) to conduct PCA dimensionality reduction and used the Isomap dimensionality reduction model to compare the results.

During the training process, the vector machine kernel parameters for the three models were optimized and acquired using the genetic algorithm (GA), where the RVM kernel width of the Isomap-RVM model was 1.457; the RVM kernel width of the PCA-RVM model was 0.534; and, for the Isomap-SVM model, $C = 3.9174$, $\sigma = 1.7073$.

The prediction results of the credit assessment are determined by the prediction accuracy of the test sample and are often measured by two types of errors. Type I error occurs when mistakenly classifying any ST company as a non-ST company; Type II error occurs when mistakenly classifying any non-ST company as an ST company. The results of prediction on the testing set by the three models are shown in Table 3.

It turned out that Isomap-RVM has the lowest total false rate (i.e., 9.72%), followed by PCA-RVM (10.41%). Isomap-SVM has the highest total false classification rate (i.e., 13.89%). The probability of a Type II error occurring in any of the three models is minimal, which indicates that these three models can all correctly identify any non-ST company and will not classify it as an ST company. This is because non-ST companies have normal financial data and are more easily distinguished than those classified as ST companies due to significant deterioration of financial data. The false classification gap among these three models

Table 3: False results of prediction on the testing set by the three models.

Model	Type I error	Type II error	Total false
Isomap-RVM	12/36 (33.33%)	2/108 (1.85%)	14/144 (9.72%)
Isomap-SVM	17/36 (47.22%)	3/108 (2.78%)	20/144 (13.89%)
PCA-RVM	11/36 (30.56%)	4/108 (3.7%)	15/144 (10.41%)

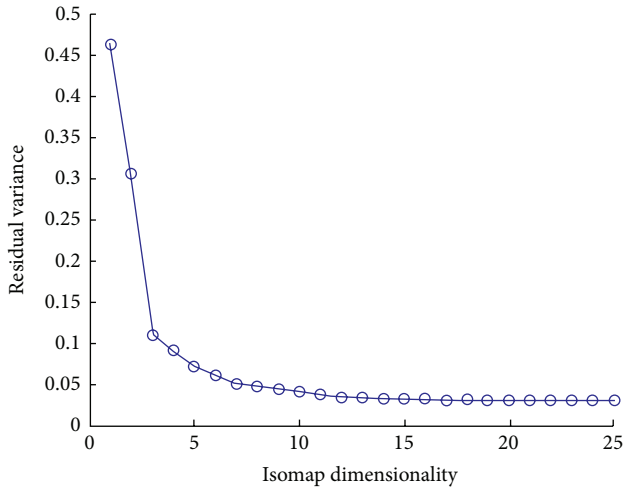

Figure 1: Er error curve.

is mainly manifested by the number of occurrences of Type I error.

By comparing the false results of Isomap-RVM and Isomap-SVM after dimensionality reduction, we can discover that, for the same data, the classification accuracy of the RVM model is significantly higher than that of the SVM model. In particular, the occurrence rate of Type I errors using the SVM method is 13.89% higher than when using RVM. Compared with the RVM model, the SVM model is more likely to classify any ST company as a non-ST company. This will underestimate the risk of financial deterioration of listed companies and may not help the companies and investors effectively circumvent and spread their financial risk.

By comparing the classification results of Isomap-RVM and PCA-RVM, we can discover that the classification accuracy of these two models is quite close. The total false classification rate of Isomap-RVM is lower than that of PCA-RVM, but the Isomap-RVM had one more Type I error occurrence than the PCA-RVM. These results may not indicate that using Isomap instead of PCA to reduce dimensions can better help improve the classification accuracy of the model, but it still shows that, for nonlinear data, Isomap can also be deemed as a reliable dimensionality reduction method for reducing data correlation.

4. Summary and Conclusions

This paper has constructed a credit assessment model—Isomap-RVM. Compared with existing credit assessment models, the methods applied by the new model have the following two major advantages: while inheriting advantages of SVM, RVM has met the Mercer conditions of the kernel function and avoided the penalty parameter selection process; Isomap is suitable for dimensionality reduction of nonlinear samples. Isomap-RVM uses Isomap to reduce the dimensions of the sample so as to reduce the sample correlation and uses RVM to conduct the training and classification prediction so as to create a new machine learning model and achieve better credit assessment results.

The empirical results show that when using the Isomap-RVM model to conduct a credit assessment of listed companies, the accuracy is significantly higher than when using the Isomap-SVM model and slightly higher than when using the PCA-RVM model. In all cases (i.e., total false classification, Type I error, or Type II error), the classification error occurrence rate of the RVM method is lower than that of the SVM method. This demonstrates that the RVM method performs better than the SVM method in terms of credit assessment.

From the perspective of characteristic index dimensionality reduction, the total false classification rate of the RVM method using Isomap to reduce dimensions is lower than that of the RVM method using PCA to reduce dimensions, yet Type I error occurrence rate of the former is higher than that of the latter. The classification accuracy gap between the two methods is minimal. Since the degree of dimensionality reduction effect is related to the sample data structure, the reasons for this result may be that the nonlinear structure of the sample selected in this research is not clear enough. However, the empirical results still show that, just like PCA, Isomap can also reliably achieve data dimensionality reduction and thereby improve the assessment precision of the model.

There are two issues which will require further investigation in subsequent research. Firstly, only China's listed companies were selected as the sample in this research, so the sample data structure lacked diversification. Hence, subsequent research may select company data from other countries for analysis. It may also further analyze the effect on model accuracy when applying the Isomap method and the PCA method to RVM. Secondly, the optimization algorithm for the RVM kernel width is not limited to GA. Other parameter optimization algorithms may be applied to conduct research on how to further improve the assessment accuracy of the model.

Conflict of Interests

The authors declare that there is no conflict of interests regarding the publication of this paper.

References

[1] S. Dutta and S. Shekhar, "Bond rating: a nonconservative application of neural networks," in *Proceedings of the IEEE International Conference on Neural Network*, pp. 443–450, San Diego, Calif, USA, July 1988.

[2] M. D. Odom and R. Sharda, "A neural network model for bankruptcy prediction," in *Proceedings of the International Joint Conference on Neural Prediction Networks (IJCNN '90)*, pp. 163–168, 1990.

[3] K. G. Coleman, T. J. Graettinger, and W. F. Lawrence, "Neural networks for bankruptcy prediction: the power to solve financial problems," *AI Review*, vol. 4, pp. 48–50, 1991.

[4] G. Zhang, M. Y. Hu, B. E. Patuwo, and D. C. Indro, "Artificial neural networks in bankruptcy prediction: general framework and cross-validation analysis," *European Journal of Operational Research*, vol. 116, no. 1, pp. 16–32, 1999.

[5] C. Cortes and V. Vapnik, "Support-vector networks," *Machine Learning*, vol. 20, no. 3, pp. 273–297, 1995.

[6] J. H. Min and Y.-C. Lee, "Bankruptcy prediction using support vector machine with optimal choice of kernel function parameters," *Expert Systems with Applications*, vol. 28, no. 4, pp. 603–614, 2005.

[7] N. Cristianini and J. Shawe-Taylor, *An Introduction to Support Vector Machines*, Cambridge University Press, Cambridge, UK, 2000.

[8] M. E. Tipping, "Sparse Bayesian learning and the relevance vector machine," *Journal of Machine Learning Research*, vol. 1, no. 3, pp. 211–244, 2001.

[9] N. Hazarika and J. G. Taylor, "Predicting bonds using the linear relevance vector machine," in *Neural Networks and the Financial Markets*, Perspectives in Neural Computing, pp. 145–155, Springer, London, UK, 2002.

[10] Y. Chen-Guang and D. Xiao-Bo, "Credit risk assessment in commercial banks based on SVM using PCA," in *Proceedings of International Conference on Machine Learning and Cybernetics*, vol. 2, pp. 1207–1211, IEEE, Kunming, China, July 2008.

[11] J. B. Tenenbaum, V. de Silva, and J. C. Langford, "A global geometric framework for nonlinear dimensionality reduction," *Science*, vol. 290, no. 5500, pp. 2319–2323, 2000.

[12] F. Lin, C.-C. Yeh, and M.-Y. Lee, "The use of hybrid manifold learning and support vector machines in the prediction of business failure," *Knowledge-Based Systems*, vol. 24, no. 1, pp. 95–101, 2011.

[13] B. Ribeiro, A. Vieira, J. Duarte et al., "Learning manifolds for bankruptcy analysis," in *Advances in Neuro-Information Processing*, vol. 5506 of *Lecture Notes in Computer Science*, pp. 723–730, Springer, Berlin, Germany, 2009.

[14] F. Ratle, A. L. Terrettaz, M. Kanevski, P. Esseiva, and O. Ribaux, "Learning manifolds in forensic data," in *Artificial Neural Networks—ICANN 2006*, vol. 4132 of *Lecture Notes in Computer Science*, pp. 894–903, Springer, Berlin, Germany, 2006.

[15] W. H. Beaver, "Financial ratios as predictors of failure empirical research in accounting: selected studies," *Journal of Accounting Research*, vol. 4, supplement, pp. 179–199, 1966.

[16] E. B. Deakin, "A discriminant analysis of predictors of business failure," *Journal of Accounting Research*, vol. 10, no. 1, pp. 167–179, 1972.

[17] D. Martens, L. Bruynseels, B. Baesens, M. Willekens, and J. Vanthienen, "Predicting going concern opinion with data mining," *Decision Support Systems*, vol. 45, no. 4, pp. 765–777, 2008.

[18] J. A. Ohlson, "Financial ratios and the probabilistic prediction of bankruptcy," *Journal of Accounting Research*, vol. 18, no. 1, pp. 109–131, 1980.

[19] http://isomap.stanford.edu.

[20] http://www.relevancevector.com.

[21] http://www.csie.ntu.edu.tw/~cjlin/libsvm.

Hindawi Publishing Corporation
Mathematical Problems in Engineering
Volume 2015, Article ID 213162, 16 pages
http://dx.doi.org/10.1155/2015/213162

Research Article

Virtual Clutch Controller for Clutch-to-Clutch Shifts in Planetary-Type Automatic Transmission

Yunjiang Cheng,[1] Peng Dong,[2] Shuai Yang,[1] and Xiangyang Xu[1]

[1]*School of Transportation Science and Engineering, Beihang University, Beijing 100191, China*
[2]*Chair of Industrial and Automotive Drivetrains, Department of Mechanical Engineering, Ruhr-University Bochum, 44801 Bochum, Germany*

Correspondence should be addressed to Peng Dong; peng.dong@rub.de

Received 14 November 2014; Accepted 20 January 2015

Academic Editor: Honglei Xu

Copyright © 2015 Yunjiang Cheng et al. This is an open access article distributed under the Creative Commons Attribution License, which permits unrestricted use, distribution, and reproduction in any medium, provided the original work is properly cited.

It is known that the shift processes of the four types of clutch-to-clutch shifts can theoretically be divided into two phases which are torque phase and inertia phase, but the execution orders are different. Two virtual clutch controllers are designed with the same eight states which include all control processes for these shifts. An equivalent method is proposed so that AT can be controlled just like DCT by adopting the torque ratios of oncoming clutch and offgoing clutch of each gear. The powertrain system model and the shift controller are established on Matlab/Simulink platform. The clutch-to-clutch shift processes have been studied based on the virtual clutch controller by software-in-the-loop simulations. Some typical problems in the clutch-to-clutch shift control are discussed and several control methods are compared to solve these problems.

1. Introduction

The planetary-type automatic transmission (AT) and the dual clutch transmission (DCT) are two widely equipped stepped automatic transmissions in the automotive industry. They both can accomplish gear shift without power interruption to improve driving comfort. In the early days of AT, the one-way clutches which can automatically disengage if the input torque becomes negative are used to improve the clutch-to-clutch shift quality. However, the use of one-way clutches requires additional shift elements and complicates the structure. Since 21st century, the development of DCT has become a hotspot study in the automotive industry due to the development of faster and more capable transmission control unit (TCU) which makes the precise control of clutch-to-clutch shifts possible. However, due to the high cost of the dual mass fly wheel (DMFW), which is used to isolate engine vibration from the transmission and drive train, and the dual clutch module, the DCT has no obvious advantage of cost compared to AT. In addition, there is one more preselection actuator for the synchronizers of DCT that also complicates the control of gearshift process. On the contrary, the high-performance TCU can also be used in AT to abolish one-way clutches to lower the cost, and the mechanical efficiency of AT can be improved extensively by locking up the torque converter clutch after the launch of vehicle. And these need to be based on the precise clutch-to-clutch shift control technologies.

The control technologies for clutch-to-clutch shifts have been studied by many researches in both AT and DCT. For the researches on AT, the sliding model control is used by Runde [1] and the optimization of gearshift based on a model is studied by Haj-Fraj and Pfeiffer [2], but these methods are difficult to apply in practice; a robust adaptive control scheme with intelligent supervisor is studied by Kim et al. [3]; the hydraulic washout technique based on open loop control is developed by Bai and Moses [4]; the clutch engagement judder and stick-slip during the shift process are studied by Crowther et al. [5]. For the researches on DCT, the engine torque reduction control and transmission output torque control during the inertia phase are used by Goetz [6, 7]; the modeling, simulation, and experimental analysis

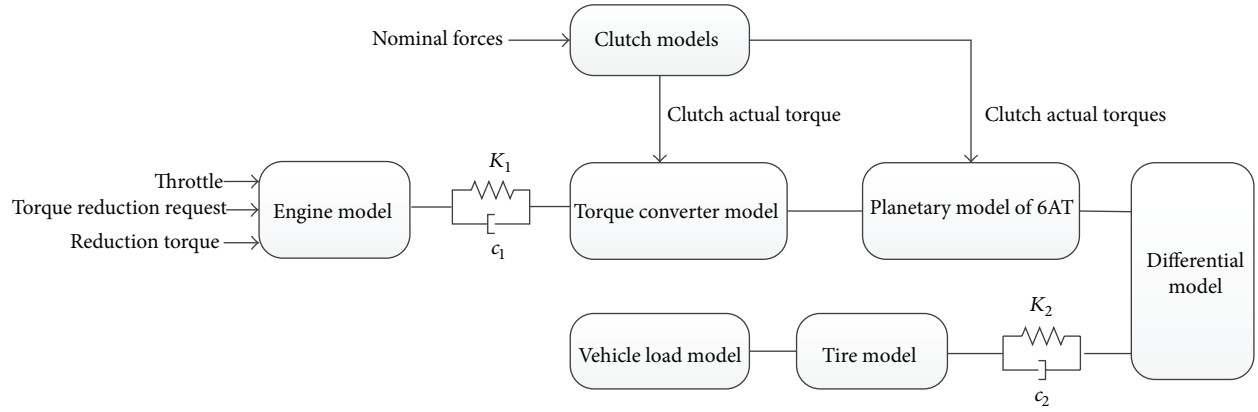

Figure 1: Outline of the powertrain dynamic model.

of clutch-to-clutch shifts have been conducted by Liu [8, 9]; the extensive vibration analysis of shift process has been studied by Walker [10, 11]; the constant output torque control technology based on a power-based integrated powertrain control system has been developed by Bai et al. [12].

There are four types of clutch-to-clutch shifts, that is, power-on upshift, power-on downshift, power-off upshift, and power-off downshift. When the power is transferred from the input side to the output side of the transmission, the shift is called power-on shift; otherwise, the shift is called power-off shift. The shift processes of the four types can theoretically be divided into two phases which are torque phase and inertia phase, but the execution orders are different. The power-on upshift and power-off downshift go through the torque phase before the inertia phase; on the contrary, the power-on downshift and power-off upshift get through the inertia phase before the torque phase.

The clutch-to-clutch shift is also known as a single-transition shift which means only one offgoing clutch needs to be released and one oncoming clutch needs to be engaged. Therefore, the two clutches need to be controlled during the shift. In this paper, the control algorithms of the offgoing clutch and the oncoming clutch are designed with eight states which include all control processes for the four types of clutch-to-clutch shifts. It is known that the principle of clutch-to-clutch shifts in AT is the same to that in DCT. However, the number of clutches in an AT is more than that in a DCT which has only two clutches in most cases, and the clutches are often not at the input side of AT. An equivalent method is proposed to solve the problem. Two "virtual" clutches, that is, virtual oncoming clutch and virtual offgoing clutch, are assumed to exist at the input side of AT by adopting the torque ratios of oncoming clutch and offgoing clutch of each gear.

This paper starts with a brief overview of the dynamic model of the powertrain system. In the next section, the torque ratios of the clutches in 6AT have been derived for the virtual clutch controller. This is then followed by an introduction of the upper controller which manages the shift process of clutch-to-clutch shifts. Then the virtual clutch controller with eight states is proposed in detail. At the end of this paper, the clutch-to-clutch shift processes have been studied based on the virtual clutch controller. Some typical problems in the clutch-to-clutch shift control are discussed, such as clutch tie-up or input speed flare at the end of the torque phase, the torque "hump" during the inertia phase, and the output torque vibration at the end of the inertia phase. And several control methods are compared to solve these problems.

2. The Dynamic Model of the Powertrain System

A brief outline of the dynamic model of the powertrain system is given in this section. In order to study control algorithms for clutch-to-clutch shifts, the powertrain system model should be built appropriately. A low order model can reduce the computational demand, but on the other hand it must be complex enough that it represents the relevant dynamics of the powertrain system. Therefore, a 7-degree-of-freedom (DOF) powertrain model is developed in the research which includes an engine model, seven clutch models, a torque converter model, a planetary model of 6AT, a differential model, a tire model, and a vehicle load model, as shown in Figure 1.

The engine map model is adopted. The experimental data of the mean engine torque is shown in Figure 2. During the clutch-to-clutch shift process, the engine torque may need to be controlled for the synchronization of oncoming clutch speed. Therefore, the model is designed to have the ability for torque reduction control, and the delay of torque response is modeled by a first-order damp element. The engine drag torque is also considered in the model.

The powertrain system contains a torque converter clutch and six multidisc clutches. The piecewise clutch model which contains two sets of equation of motion is adopted to divide the clutch state into slip state and slip state.

The steady-state torque converter model is adopted, and the torque ratio and K-factor data are provided by the component supplier, as shown in Figure 3.

The study object 6AT consisted of two simple minus planetary gear sets and one compound planetary gear set,

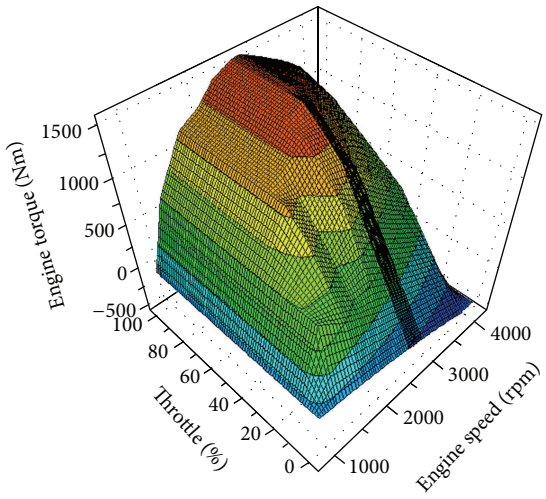

Figure 2: Engine map model.

as shown in Figure 4. The use of shift elements is shown in Table 1. The Lagrange method is an efficient way to describe the dynamic model of planetary gear sets and is adopted.

Equation (1) is the general form of Lagrange equations of the first kind for systems with linear speed constraints [13], and (2) is the form of the linear speed constraint equations:

$$\frac{d}{dt}\left(\frac{\partial L}{\partial \dot{\theta}_j}\right) - \frac{\partial L}{\partial \theta_j} - Q_j + \sum_{i=1}^{S}\lambda_i \frac{\partial f_i}{\partial \theta_j} + \sum_{i=1}^{r} F_i A_{ij} = 0, \quad (j = 1, 2, \ldots, m), \tag{1}$$

$$\sum_{j=1}^{m} A_{ij}(\theta_1, \theta_2, \ldots, \theta_m, t)\,\dot{\theta}_j + b_i(\theta_1, \theta_2, \ldots, \theta_m, t) = 0, \quad (i = 1, 2, \ldots, r), \tag{2}$$

where ∂ is a partial derivative; L is the Lagrange function; θ is the generalized coordinate; Q is the generalized nonpotential force; F and λ are the Lagrange multipliers, also known as the internal forces; m is the number of generalized coordinates; S is the number of constraint equations; and r is the number of linear speed constraint equations.

Under the condition of ideal constraint, four independent speed constraint equations of the system can be obtained, as shown in (3):

$$\begin{aligned} R_{s1}\cdot\dot{\theta}_1 + R_{r1}\cdot\dot{\theta}_3 &= (R_{s1} + R_{r1})\cdot\dot{\theta}_4, \\ R_{s2}\cdot\dot{\theta}_1 + R_{r2}\cdot\dot{\theta}_5 &= (R_{s2} + R_{r2})\cdot\dot{\theta}_3, \\ R_{s3}\cdot\dot{\theta}_6 + R_{r3}\cdot\dot{\theta}_3 &= (R_{s3} + R_{r3})\cdot\dot{\theta}_2, \\ -R_{s3}\cdot\dot{\theta}_6 + R_{r4}\cdot\dot{\theta}_7 &= (R_{r4} - R_{s3})\cdot\dot{\theta}_2, \end{aligned} \tag{3}$$

where R_{si} is the radius of circle passing through the center of the ith sun gear; R_{ri} is the radius of circle passing through the center of the ith ring gear; θ_i is the rotational displacement of the ith shaft, as shown in Figure 4.

According to (1)–(3), the dynamic equations of planetary system of 6AT can be obtained in matrix format, as shown in (4):

$$\mathbf{M}\cdot\boldsymbol{\Omega} = \mathbf{T}. \tag{4}$$

Here,

$$\mathbf{M} = \begin{bmatrix} I_1 & 0 & 0 & 0 & 0 & 0 & 0 & R_{s1} & R_{s2} & 0 & 0 \\ 0 & I_2 & 0 & 0 & 0 & 0 & 0 & 0 & 0 & -R_{s3}-R_{r3} & R_{s3}-R_{r4} \\ 0 & 0 & I_3 & 0 & 0 & 0 & 0 & R_{r1} & -R_{s2}-R_{r2} & R_{r3} & 0 \\ 0 & 0 & 0 & I_4 & 0 & 0 & 0 & -R_{s1}-R_{r1} & 0 & 0 & 0 \\ 0 & 0 & 0 & 0 & I_5 & 0 & 0 & 0 & R_{r2} & 0 & 0 \\ 0 & 0 & 0 & 0 & 0 & I_6 & 0 & 0 & 0 & R_{s3} & -R_{s3} \\ 0 & 0 & 0 & 0 & 0 & 0 & I_7 & 0 & 0 & 0 & R_{r4} \\ R_{s1} & 0 & R_{r1} & -R_{s1}-R_{r1} & 0 & 0 & 0 & 0 & 0 & 0 & 0 \\ R_{s2} & 0 & -R_{s2}-R_{r2} & 0 & R_{r2} & 0 & 0 & 0 & 0 & 0 & 0 \\ 0 & -R_{s3}-R_{r3} & R_{r3} & 0 & 0 & R_{s3} & 0 & 0 & 0 & 0 & 0 \\ 0 & R_{s3}-R_{r4} & 0 & 0 & 0 & -R_{s3} & R_{r4} & 0 & 0 & 0 & 0 \end{bmatrix}, \tag{5}$$

$$\boldsymbol{\Omega} = \begin{bmatrix} \ddot{\theta}_1 & \ddot{\theta}_2 & \ddot{\theta}_3 & \ddot{\theta}_4 & \ddot{\theta}_5 & \ddot{\theta}_6 & \ddot{\theta}_7 & F_1 & F_2 & F_3 & F_4 \end{bmatrix}^T,$$

$$\mathbf{T} = \begin{bmatrix} T_1 - T_{c5a} & T_2 - T_{c3a} & 0 & T_{c5a} + T_{c6a} & T_{c4a} & T_{c2a} + T_{c3a} & T_{c1a} & 0 & 0 & 0 & 0 \end{bmatrix}^T,$$

Table 1: Use of shift elements.

Gear	C1	C2	C3	C4	C5	C6
D1	✗			✗		
D2		✗		✗		
D3			✗	✗		
D4	✗				✗	
D5		✗			✗	
D6			✗		✗	
R1	✗					✗
R2		✗				✗
R3			✗			✗

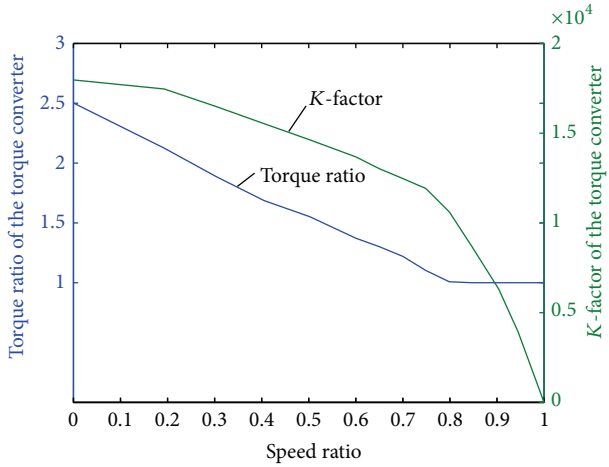

Figure 3: Performance characteristic curve of a torque converter.

where I_i is the inertia of the ith shaft; F_i is the internal forces of planetary gear sets; and T_{cia} is the actual torque of the ith clutch; T_1 is the input torque exerted on the turbine shaft; and T_2 is the load torque exerted on the output shaft of 6AT; see Figure 4.

The differential is modeled to be a simple connecting component to the final drive. The nonrigid characteristic of the drive shafts is considered by a spring-damper element. The tire is modeled according to the slip characteristic which is a curve using the approach published by Wohnhaas et al. [14]. The vehicle load model is established including gradient resistance, aerodynamic drag, and rolling resistance.

3. Torque Ratios of the Clutches in 6AT

It is known that the principle of clutch-to-clutch shifts in AT is the same to that in DCT. However, in most cases, the number of clutches in an AT is more than that in a DCT which has only two clutches, and the clutches are often not at the input side of AT. An equivalent method is proposed to solve the problem. Two "virtual" clutches, that is, virtual oncoming clutch and virtual offgoing clutch, are assumed to exist at the input side of AT by adopting the torque ratios of corresponding clutches of each gear.

There are six clutches for gearshift which are at different positions in 6AT; see Figure 4. Take the 4th drive gear of 6AT to explain this method, as shown in Figure 5. Clutch 1 (C1) and clutch 5 (C5) are engaged in this Figure. A "virtual clutch" (CV) is imagined at the input side of 6AT. In order to facilitate static analysis of the actual torque transferred by a clutch and slip speed of the clutches, assume the system is in an equilibrium state. Under the condition of ideal constraint (i.e., no backlash and no gear teeth compliance), the constraint equations of planetary gear sets are shown in (3). Because C1 and C5 are engaged, (6) can be obtained:

$$\begin{aligned} \dot{\theta}_1 &= \dot{\theta}_4, \\ \dot{\theta}_7 &= 0. \end{aligned} \tag{6}$$

Thus the actual torques of CV, C1, and C5 can be obtained, as shown in the following:

$$\begin{aligned} T_{cva} &= T_1, \\ T_{c1a} &= \left(\frac{R_{r4}}{R_{r3}}\right) \cdot T_1, \\ T_{c5a} &= \left(1 + \frac{R_{s1}}{R_{r1}}\right) \cdot T_1. \end{aligned} \tag{7}$$

Therefore, the torque ratios of C1 and C5 to CV can be obtained, as shown in the following:

$$\begin{aligned} \beta_{c1d4} &= \frac{R_{r4}}{R_{r3}} \\ \beta_{c5d4} &= 1 + \frac{R_{s1}}{R_{r1}}. \end{aligned} \tag{8}$$

Note that β_{cij} is the ith clutch at the jth gear; for example, β_{c5d4} denotes the torque ratio of C5 at the 4th drive gear.

Through speed analysis, the slip ratios of C1 and C5 to CV are reciprocal relationships to the torque ratios, and the slip speed of C1 and C5 can be calculated by (9) and (10). The slip speed of CV can be calculated using the input speed, output speed, and current gear ratio, as shown in (11) as follows:

$$\Delta\dot{\theta}_{c5} = \frac{\Delta\dot{\theta}_{cv}}{\beta_{c5d4}}, \tag{9}$$

$$\Delta\dot{\theta}_{c1} = \frac{\Delta\dot{\theta}_{cv}}{\beta_{c1d4}}, \tag{10}$$

$$\Delta\dot{\theta}_{cv} = \dot{\theta}_1 - \dot{\theta}_2 \cdot i_{d4}, \tag{11}$$

where $\Delta\dot{\theta}_{ci}$ is the slip speed of the ith clutch and i_{d4} is the speed ratio of the 4th drive gear.

In the same way, the torque ratios of six drive gears and three reverse gears can be obtained, as shown in Table 2. By utilizing the torque ratios of the clutches, the 6AT can be controlled like a DCT for only two virtual clutches at the input side of the transmission; that is, an oncoming clutch and an offgoing clutch need to be controlled during each clutch-to-clutch shift process. The differences are that the target slip speed of virtual clutch needs to be calculated by

Table 2: Torque ratios of the six clutches at each gear.

β_{cij}	D1	D2	D3	D4	D5	D6	R1	R2	R3
C1	$\left(1+\frac{R_{r2}}{R_{s2}}\right)\frac{R_{r4}}{R_{r3}}$			$\frac{R_{r4}}{R_{r3}}$			$-\frac{R_{r1}R_{r4}}{R_{s1}R_{r3}}$		
C2		$\left(1+\frac{R_{r2}}{R_{s2}}\right)\frac{R_{s3}}{R_{r3}}$			$\frac{R_{s3}}{R_{r3}}$			$-\frac{R_{r1}R_{s3}}{R_{s1}R_{r3}}$	
C3			$-\left(1+\frac{R_{r2}}{R_{s2}}\right)\frac{R_{s3}}{R_{r3}}$			$-\frac{R_{s3}}{R_{r3}}$			$\frac{R_{r1}R_{s3}}{R_{s1}R_{r3}}$
C4	$\frac{R_{r2}}{R_{s2}}$	$\frac{R_{r2}}{R_{s2}}$	$\frac{R_{r2}}{R_{s2}}$						
C5				$1+\frac{R_{s1}}{R_{r1}}$	$1+\frac{R_{s1}}{R_{r1}}$	$1+\frac{R_{s1}}{R_{r1}}$			
C6							$-1-\frac{R_{r1}}{R_{s1}}$	$-1-\frac{R_{r1}}{R_{s1}}$	$-1-\frac{R_{r1}}{R_{s1}}$

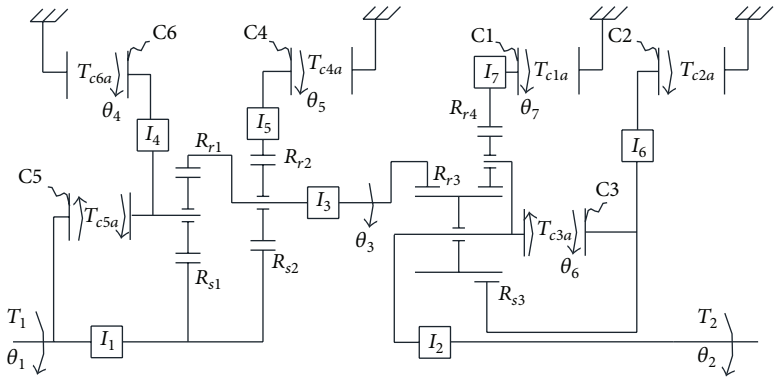

Figure 4: Structure of planetary system of 6AT.

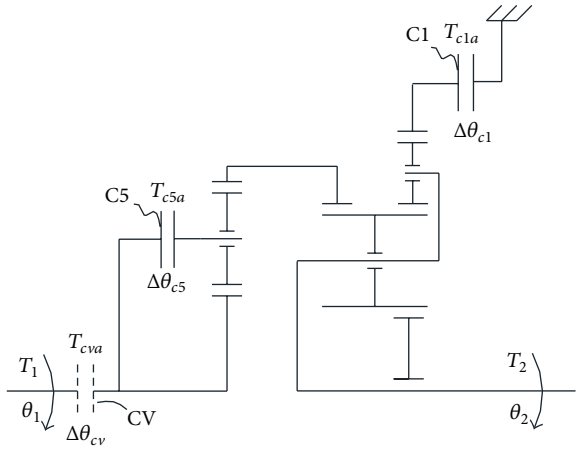

Figure 5: Structure of the 4th drive gear of 6AT.

multiplying the target slip speed of "real clutch" by the torque ratio of real clutch at the current gear before the controller, and the demand torque of real clutch needs to be calculated by multiplying the demand torque of virtual clutch by the torque ratio of real clutch at the current gear after the controller, as shown in Figure 11. By this method the six clutches of 6AT can be equivalent to two virtual clutches using the torque ratios of each gear, and thus the same control algorithm can be used to handle the shift processes of different gears. Therefore, the control algorithm can be simplified dramatically and thus the demand for the memory of TCU is decreased.

4. Frame of the Shift Controller

The shift controller of 6AT is designed with six parts, as shown in Figure 6. The execution sequence of them is shift schedule (SS), clutch role decision (CRD), generic control flow (GCF), virtual clutch information calculation (VCIC), oncoming virtual clutch controller (ONVCC), and offgoing virtual clutch controller (OFFVCC). In this section, the functionality of the SS, the CRD, and the GCF will be described.

The functionality of SS is to determine whether a clutch-to-clutch shift process should be executed according to the throttle and vehicle speed.

The functionality of CRD is to determine the ID of oncoming clutch (IDON) and the ID of offgoing clutch (IDOFF) according to the use of shift elements; see Table 1.

The functionality of GCF is to manage overall process flow for clutch-to-clutch shifts, and command the lower controllers, that is, ONVCC and OFFVCC, to execute related control algorithms. The GCF is designed with four phases, that is, no shift phase (NSP), shift phase 1 (SP1), shift phase 2 (SP2), and shift phase 3 (SP3), as shown in Figure 7.

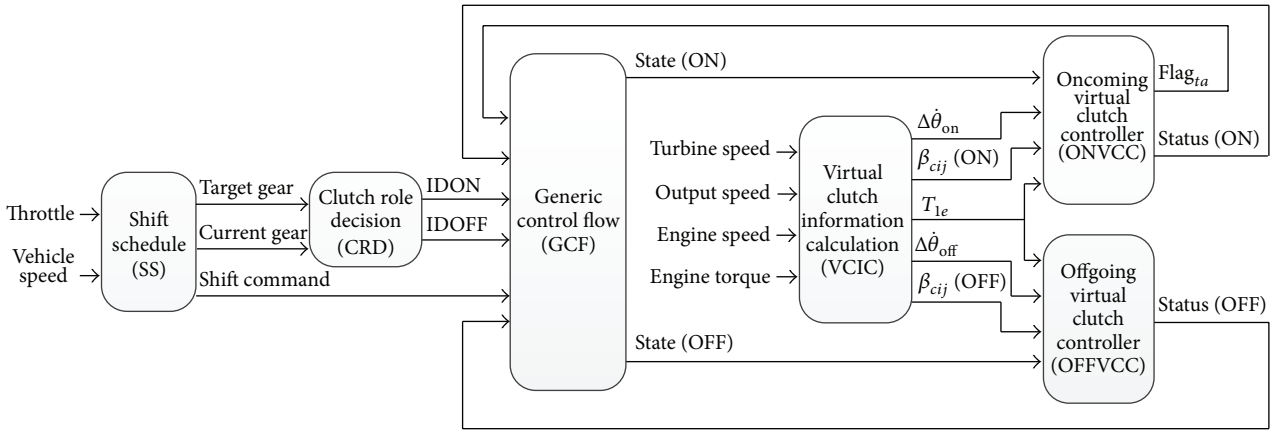

Figure 6: Frame of the shift controller of 6AT.

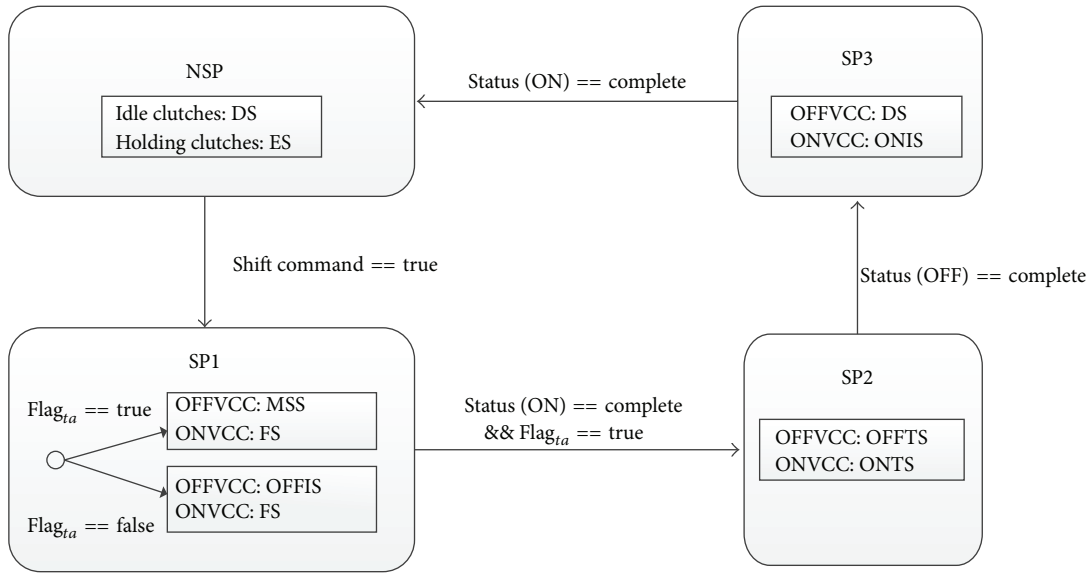

Figure 7: Schematic diagram of the generic control flow.

The functionality of VCIC is to calculate the data for the ONVCC and the OFFVCC. The slip speed of oncoming virtual clutch and offgoing virtual clutch is calculated by (12) and (13), respectively. The speed ratio of the torque converter is calculated by (14) and thus the torque ratio can be obtained according to Figure 3. The estimated input torque is calculated by (15) with the characteristics of the torque converter taken into consideration. The torque ratios of oncoming clutch and offgoing clutch can be obtained according to Table 2:

$$\Delta\dot{\theta}_{\text{off}} = \dot{\theta}_1 - \dot{\theta}_2 \cdot i_c, \tag{12}$$

$$\Delta\dot{\theta}_{\text{on}} = \dot{\theta}_1 - \dot{\theta}_2 \cdot i_t, \tag{13}$$

$$i_{\text{tc}} = \frac{\dot{\theta}_1}{\dot{\theta}_e}, \tag{14}$$

$$T_{1e} = \left(T_e - I_e\ddot{\theta}_e\right) \cdot \alpha\left(i_{\text{tc}}\right) - I_1\ddot{\theta}_1, \tag{15}$$

where $\Delta\dot{\theta}_{\text{on}}$ and $\Delta\dot{\theta}_{\text{off}}$ are the slip speed of oncoming virtual clutch and offgoing virtual clutch; i_t is the target gear ratio; i_c is the current gear ratio; i_{tc} is the speed ratio of the torque converter; $\alpha(i_{\text{tc}})$ is the torque ratio of the torque converter; T_{1e} is the estimated input torque; I_e is the engine inertia; θ_e is the rotational displacement of engine; and T_e is the engine torque.

5. Virtual Clutch Controller

In order to simplify the algorithms of the shift controller, the ONVCC is designed exactly the same with the OFFVCC, and both of them are commanded by the upper controller, that is, the GCF. The ONVCC and the OFFVCC are designed with 8 states, that is, engage state (ES), disengage state (DS), fill state (FS), microslip state (MSS), oncoming torque state (ONTS), offgoing torque state (OFFTS), oncoming inertia state (ONIS), and offgoing inertia state (OFFIS), as shown in Figure 8.

Table 3: Flow of states of the ONVCC and the OFFVCC.

Shift types	GCF	NSP	SP1	SP2	SP3	NSP
Power-on upshift and power-off downshift	ONVCC	DS	FS	ONTS	ONIS	ES
	OFFVCC	ES	MSS	OFFTS	DS	DS
Power-on downshift and power-off upshift	ONVCC	DS	FS	ONTS	ONIS	ES
	OFFVCC	ES	OFFIS	OFFTS	DS	DS

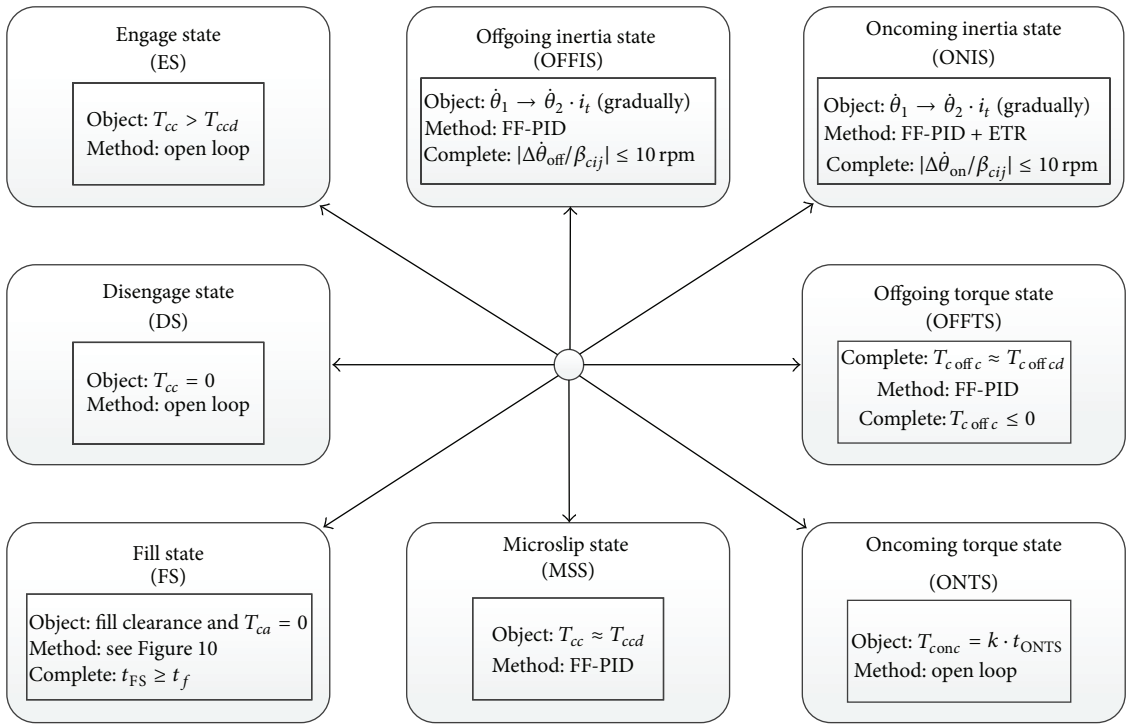

Figure 8: Virtual clutch controller.

According to the GCF, the flows of states of the ONVCC and the OFFVCC for the four types of clutch-to-clutch shifts can be summarized in Table 3.

Before the description of the control methods of the eight states, three concepts about a clutch need to be explained. The first is the "torque capacity," which is the maximum torque the clutch can transfer and be controlled by the normal force applied on the clutch plates; the second is "actual torque," which is the torque transferred by a clutch [12]; the third is "drive torque capacity," which is the torque exerted on the drive shaft of a clutch and can be calculated by (16); see Figure 9:

$$T_{ccd} = T_{\text{cin}} - I_{\text{cin}}\ddot{\theta}_{\text{cin}}, \tag{16}$$

where F_n is the nominal force; T_{cin} is the torque exerted on the input side of the clutch; I_{cin} is the inertia of the input side; $\dot{\theta}_{\text{cin}}$ is the input side speed; $\dot{\theta}_{\text{cout}}$ is the output side speed; and $\Delta\dot{\theta}_c$ is the slip speed, which equals $\dot{\theta}_{\text{cin}} - \dot{\theta}_{\text{cout}}$.

In ES, the object is to keep the torque capacity of the clutch always larger than the drive torque capacity to ensure the clutch is in stick state. The open loop control method is adopted to accomplish the task. The demand pressure for the cylinder of the clutch is set to be the line pressure, so that sufficient control current is sent to the solenoid to ensure there is no slip of the clutch.

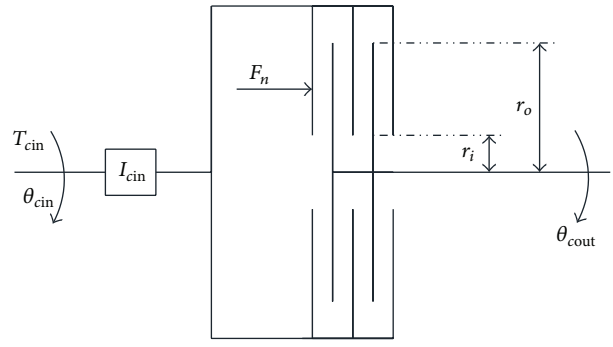

Figure 9: Sketch of a multidisc clutch.

In DS, the object is to keep the torque capacity of the clutch equivalent to zero to ensure no actual torque is

transferred by the clutch. The open loop control method is adopted. No control current is sent to the solenoid to ensure the torque capacity is zero.

In FS, the object is to make sure the clearance in the oil line of the clutch is filled up, but the actual torque of the clutch remains at zero. The open loop control method is chosen. The control current of the clutch changes following a given shape, as shown in Figure 10. Note that the fill time (t_f), fast fill time (t_{fast}), fast fill current (i_{fast}), and kiss-point current (i_{kiss}) are calibration parameters. When the duration time of FS (t_{FS}) exceeds the fill time, the status of the clutch ($\text{Status}_{\text{on}}$ or $\text{Status}_{\text{off}}$) is set to complete status; otherwise, the status is set to progress status.

In MSS, the object is to keep the torque capacity of the clutch equivalent to the drive torque capacity. However, because there are noises in the engine torque signals and input speed signals, the drive torque capacity of the virtual clutch is calculated with error. In addition, the torque capacity is also imprecise due to the variable working conditions of the hydraulic system. Therefore, a combined controller including feed-forward control (FF) and PID control is designed to achieve the control object, as shown in Figure 11. The FF torques, that is, the drive torque capacities, of the oncoming virtual clutch and the offgoing virtual clutch are calculated by (17). In MSS, the target slip of the FF-PID controller is set to a small value, that is, 10 rpm:

$$\begin{aligned} T_{c\,\text{on}\,cd} &= T_{1e} - T_{c\,\text{off}\,a}, \\ T_{c\,\text{off}\,cd} &= T_{1e} - T_{c\,\text{on}\,a}, \end{aligned} \tag{17}$$

where $T_{c\,\text{on}\,cd}$ and $T_{c\,\text{off}\,cd}$ are the FF torques of the oncoming virtual clutch and the offgoing virtual clutch; $T_{c\,\text{on}\,a}$ and $T_{c\,\text{off}\,a}$ are the actual torques of the oncoming virtual clutch and the offgoing virtual clutch.

In ONTS, the object is to increase the actual torque of oncoming clutch to follow a slope in order to take over the torque from offgoing clutch smoothly. Therefore, the open loop control method is adopted. The torque capacity of oncoming virtual clutch rises linearly, as shown in the following:

$$T_{c\,\text{on}\,c} = T_{c\,\text{on}\,a} = k \cdot t_{\text{ONTS}}, \tag{18}$$

where $T_{c\,\text{on}\,c}$ is the torque capacity of oncoming virtual clutch and t_{ONTS} is the duration time of ONTS.

In OFFTS, the object is to keep torque capacity equivalent to the drive torque capacity of offgoing clutch. The FF-PID controller is adopted in the same way with MSS. In order to avoid clutches "tie-up" phenomenon, small target slip, that is, 20 rpm, is set to the PID controller. When the torque capacity of offgoing virtual clutch reaches zero, the status of OFFVCC is set to complete status; otherwise, it is set to progress status.

In ONIS, the object is to control the turbine speed to reach the target gear speed level gradually in the inertia phase after torque phase. In order to accomplish the speed change, an inertia torque needs to be added on the oncoming clutch or be subtracted from the engine torque. The first method causes a torque "hump" in the inertia phase which reduces ride comfort. The engine torque reduction (ETR) can

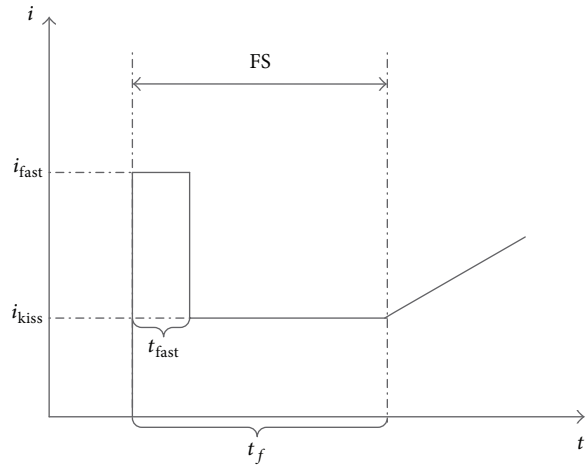

Figure 10: Control current in fill state.

avoid the torque "hump," but it cannot be used for power-off shifts and the accuracy of engine torque response is limited. Therefore, two methods are both used in this state. The engine reduction torque is calculated by (19), which considers the characteristics of the torque converter; see Figure 3. The FF-PID controller is also adopted. The target slip speed of oncoming virtual clutch decreases following the desired rate of the input speed. When the actual slip speed of oncoming virtual clutch is lower than a small slip (10 rpm), the status of ONVCC is set to complete status; otherwise, it is set to progress status:

$$T_{\text{rt}} = \frac{\ddot{\theta}_{\text{ONIS}} I_1}{\alpha\left(i_{\text{tc}}\right)} + \left(\frac{\ddot{\theta}_{\text{ONIS}}}{i_{\text{tc}}}\right) \cdot I_e, \tag{19}$$

where $\ddot{\theta}_{\text{ONIS}}$ is the desired rate of the input speed in ONIS and T_{rt} is the engine reduction torque.

In OFFIS, the object is to control the turbine speed to the target gear speed level gradually in the inertia phase before torque phase. It is different from ONIS in the way that an inertia torque (calculated by (20)) needs to be subtracted from the actual torque of offgoing virtual clutch. The FF-PID controller is also adopted, but the inertia torque is subtracted from the FF torque, as shown in (19). The target slip of offgoing clutch increases following the desired rate of the input speed. When the actual slip of oncoming clutch exceeds the small slip (10 rpm), the status of OFFVCC is set to complete status; otherwise, it is set to progress status:

$$T_{\text{OFFIS}} = \ddot{\theta}_{\text{OFFIS}} I_1 + \left(\frac{\ddot{\theta}_{\text{OFFIS}}}{i_{\text{tc}}}\right) \cdot I_e \cdot \alpha\left(i_{\text{tc}}\right) \tag{20}$$

$$T_{c\,\text{off}\,cd} = T_{1e} - T_{c\,\text{on}\,a} - T_{\text{OFFIS}}, \tag{21}$$

where $\ddot{\theta}_{\text{OFFIS}}$ is the desired rate of the input speed in OFFIS and T_{OFFIS} is the inertia torque in OFFIS.

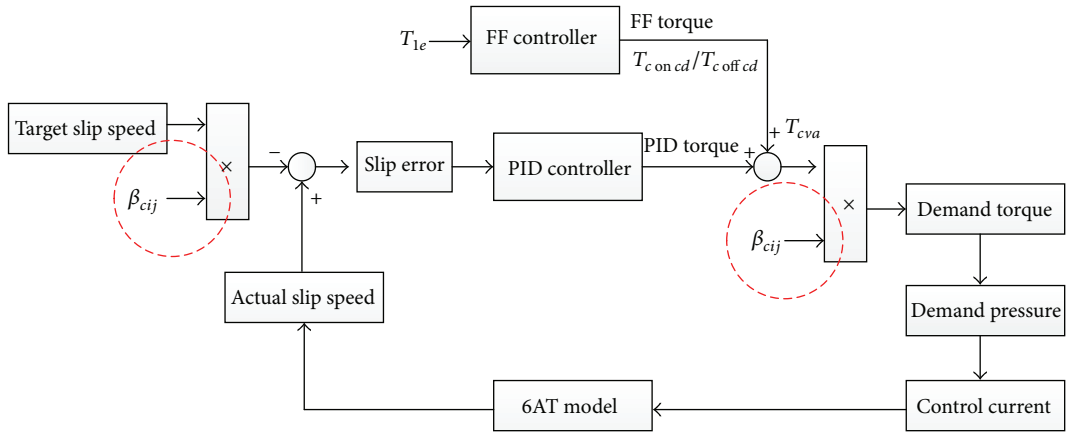

Figure 11: Principle of the FF-PID controller.

6. Shift Control Results and Analysis

6.1. Results of the Four Types of Shifts. Based on the shift controller with the ONVCC and the OFFVCC, the four types of clutch-to-clutch shifts are simulated, as shown in Figure 12. Figures 12(a), 12(b), 12(c), and 12(d) show the control current sent to the solenoids of offgoing clutch and oncoming clutch of power-on upshift, power-on downshift, power-off upshift, and power-off downshift, respectively. The four phases of the GCF and the state flows of the OFFVCC and the ONVCC are also indicated in these figures and are consistent with the designed flows; see Table 3. Figures 12(e), 12(f), 12(g), and 12(h) picture the actual torques of offgoing clutch and oncoming clutch of the four types of shifts, respectively.

Before the clutch-to-clutch shift processes, the GCF is in NSP; therefore, the holding clutches are in ES and the idle clutches are in DS. When the SS determines a shift command, the GCF enters SP1, and then the shift process begins. For the power-on upshift and the power-off downshift, the OFFVCC is in MSS and the ONVCC is in FS; for the power-on downshift and the power-off upshift, the OFFVCC is in OFFIS and the ONVCC is in FS. When the oncoming clutch and the offgoing clutch are ready for the torque phase, the GCF enters SP2; therefore, the clutch-to-clutch torque handover process takes place. For the four types of shifts, the OFFVCC is in OFFTS and the ONVCC is in ONTS. When the torque phase is over, the GCF enters SP3. For the four types of shifts, the OFFVCC is in DS and the ONVCC is in ONIS. When the slip speed of oncoming clutch approaches zero, the speed synchronization of the oncoming clutch is complete and ONVCC turns to complete status. Then the GCF gets back to NSP. The clutch-to-clutch shift process is complete in the meantime.

Based on the virtual clutch controller, the processes of torque phase and inertia phase of the four types of shifts go as expected. The torque phase takes place before the inertia phase for the power-on upshift and the power-off downshift; see Figures 12(e) and 12(h); the inertia phase takes place before the torque phase for the power-on downshift and the power-off upshift; see Figures 12(f) and 12(g).

6.2. Comparison of Different Methods in OFFTS. In the control of torque phase of clutch-to-clutch shifts, two major problems should be avoided. One is the clutch tie-up and the other is the input speed flare, but they are mutually contradictory and will not happen at the same time. Based on the frame of the shift controller, the torque phase of each shift takes place in the SP2 of the GCF. Thus The ONVCC is in ONTS and the OFFVCC is in OFFTS. The key to avoid clutch tie-up and the input speed flare is to disengage the offgoing clutch at the right time. Therefore, the control of OFFTS is worth exploring.

Figure 13 shows three simulation results of a power-on upshift under the same initial conditions. Three different control methods are used in OFFTS. Only the FF control, an open loop control method, is used in the first one; see Figures 13(a), 13(b), 13(c), and 13(d). During the torque phase, the slip speed of offgoing clutch (see Figure 13(c)) is zero because the torque capacity is higher than the drive torque capacity of offgoing clutch. The clutch tie-up occurs at the end of torque phase (dashed circle in Figure 13(a)); thus the output torque of 6AT vibrates at the beginning of the inertia phase (dashed circle in Figure 13(b)). The FF-PID controller with small gains of P term and I term is used in the second one; see Figures 13(e), 13(f), 13(g), and 13(h). Because the PID control, a close loop control method, has little effect on the torque capacity of offgoing clutch, the slip speed (see Figure 13(g)) is still zero during the torque phase. But the clutch tie-up and the output torque vibration are reduced; see Figures 13(e) and 13(f). The FF-PID controller with proper gains of P term and I term is used in the third one; see Figures 13(i), 13(j), 13(k), and 13(l). The small slip speed during the torque phase occurs; see Figure 13(k). This can represent the torque capacity which is approximately equal to the drive torque capacity of offgoing clutch. Thus the offgoing clutch can disengage at the right time when the torque phase is over. Therefore, the clutch tie-up and the output torque vibration are avoided; see Figures 13(i) and 13(j). Note that the slip power caused by the small slip speed of offgoing clutch (see Figure 13(l)) is very small compared to that of oncoming clutch.

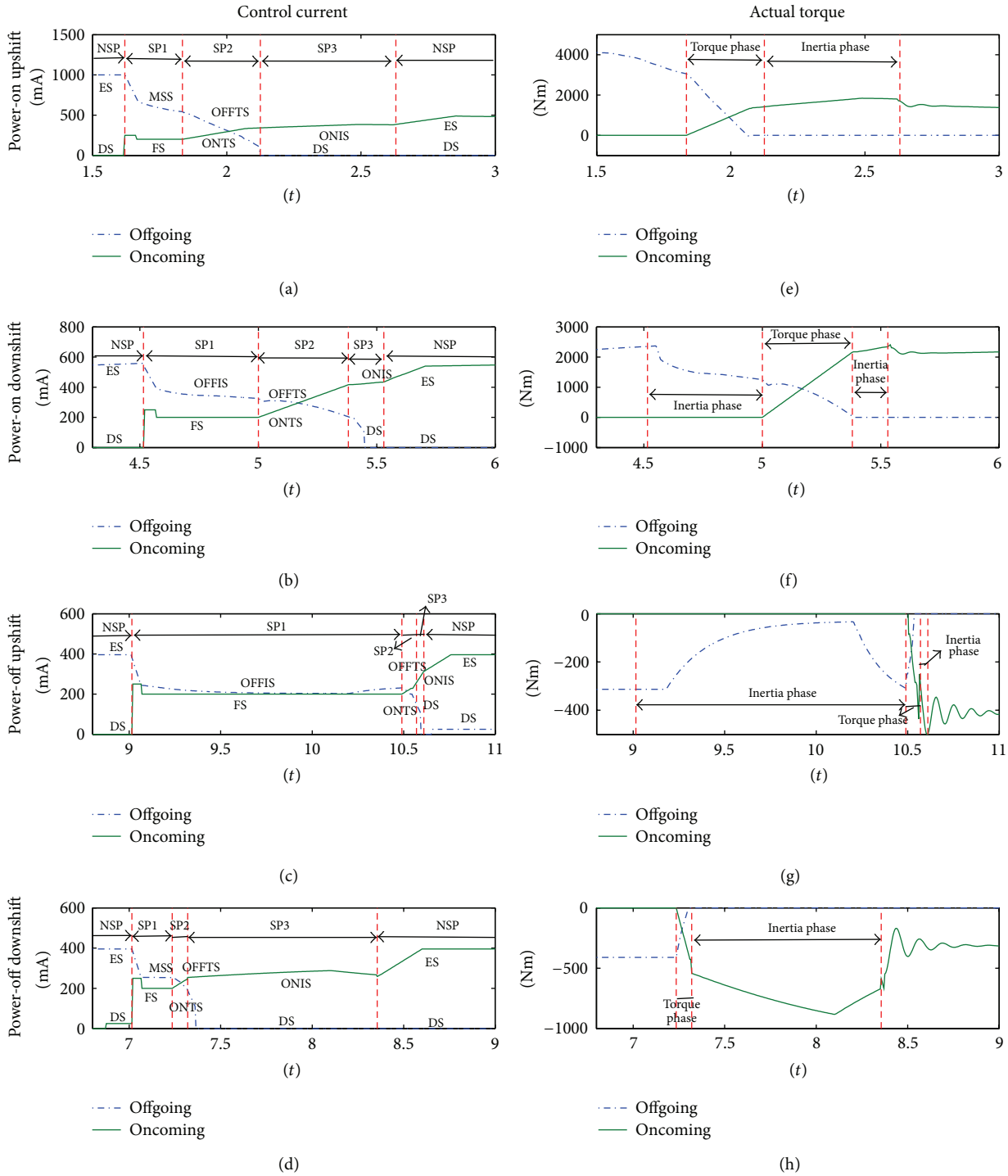

Figure 12: Simulation results of the four types of shifts.

In order to avoid clutch tie-up under different conditions, a control method, which releases the offgoing clutch quickly by open loop control when the torque capacity is smaller than a low level, is adopted in OFFTS. But the torque capacity should be calibrated properly. Figure 14 shows two simulation results of a power-on upshift with the same initial conditions. In the first one, a small speed flare (see Figure 14(c)) occurs at the end of the torque phase because the OFFTS enters the quick release control stage earlier. And a torque hole occurs in the output torque of the transmission; see Figure 14(b). The quick release control at the right time is shown in the second one; see Figures 14(d), 14(e), and 14(f). The speed flare and the torque hole are avoided.

6.3. Comparison of Different Methods in ONIS. Based on the frame of the shift controller, the inertia phase after torque

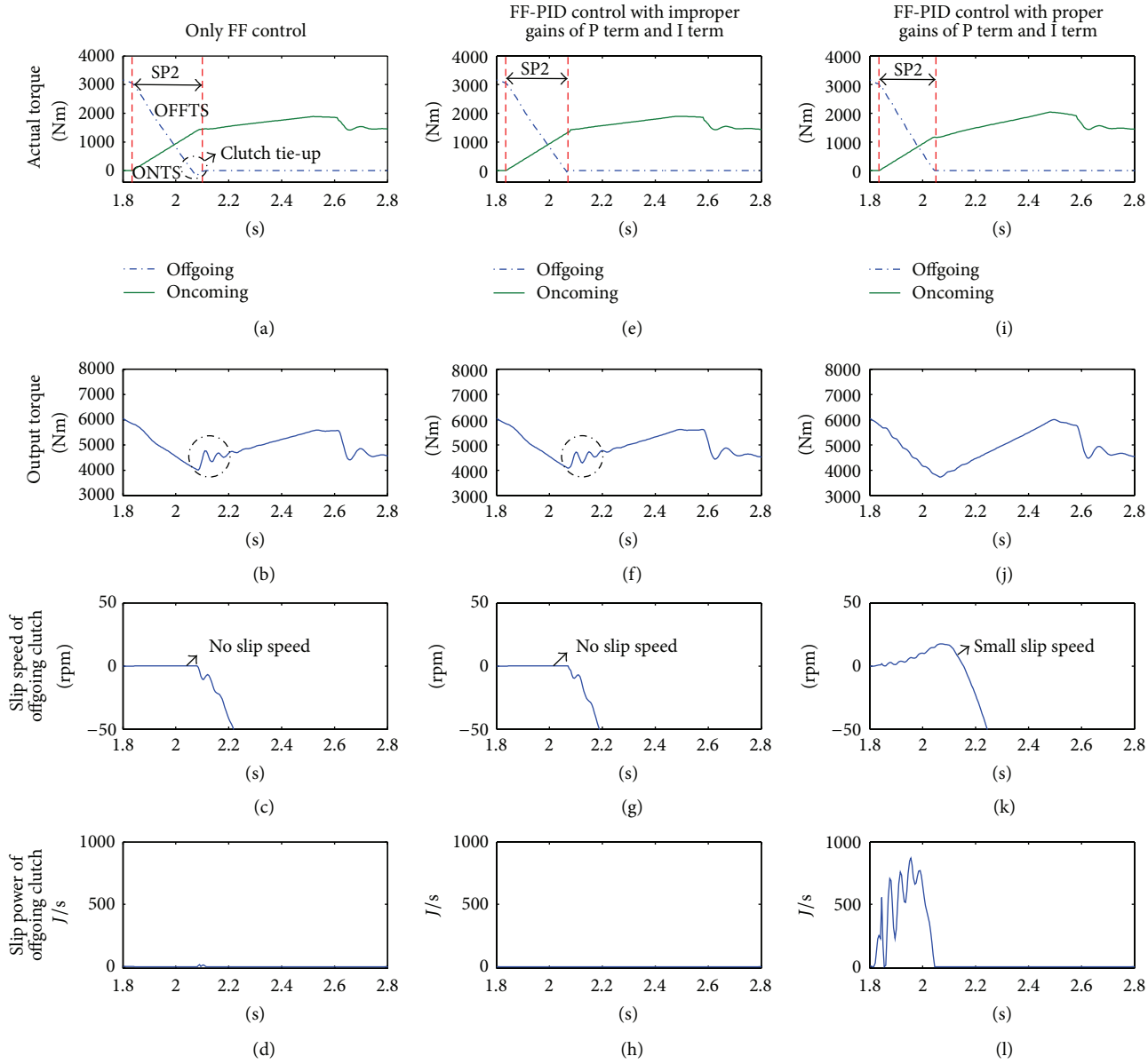

Figure 13: Method to avoid clutch tie-up.

phase takes place in the SP3 of the GCF. And thus the ONVCC is in ONIS and the OFFVCC is in DS. The object of ONIS is to control the slip speed of oncoming clutch to reach zero gradually.

Figure 15 shows three simulation results of a power-on upshift with the same initial conditions. Three different control methods are used in ONIS. Only the FF-PID control is used in the first one; see Figures 15(a), 15(b), 15(c), and 15(d). There is a torque hump in the actual torque of oncoming clutch (see Figure 15(a)) during the inertia phase because the inertia torque used for the speed change has to be added on the oncoming clutch without the engine torque reduction control. And it causes the torque hump in the output torque of 6AT; see Figure 15(c), which reduces the ride comfort. The FF-PID control with torque limitation is used in the second one; see Figures 15(e), 15(f), 15(g), and 15(h). The torque hump is reduced by mandatory torque limitation in ONIS; see Figure 15(e). Although the torque hump in the output torque (see Figure 15(g)) is reduced, the shift time increases by around 0.3 s and thus the slip power of oncoming clutch is also increased compared to Figure 15(d). The FF-PID control and the ETR control are all used in the third one; see Figures 15(i), 15(j), 15(k), and 15(l). The engine torque is reduced during the inertia phase; see Figure 15(j). The PID controller plays a supporting role for the synchronization of oncoming clutch. Therefore, the torque hump is reduced significantly and the slip power is also reduced compared to the previous results.

Figure 16 shows three simulation results of a power-on upshift with the same initial conditions. Three ETR methods

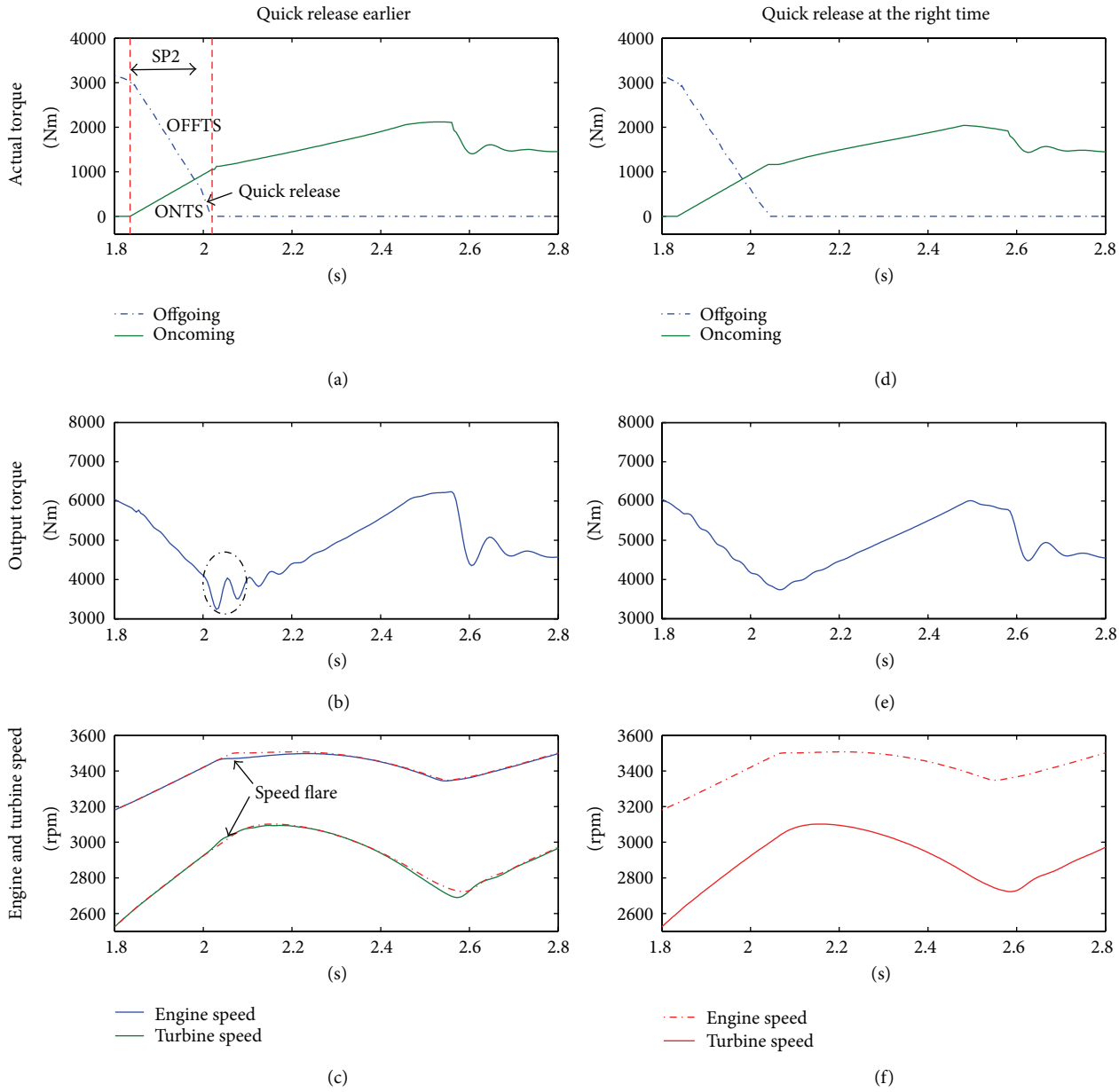

Figure 14: Method to avoid speed flare.

are used in ONIS. The ETR control with quick recovery of the engine torque at the end of the inertia phase is used in the first one; see Figures 16(a), 16(b), 16(c), and 16(d). There is a big vibration of output torque at the end of inertia phase (see Figure 16(d)) which is caused by the engagement of oncoming clutch. The ETR control with small reduction torque is used in the second one; see Figures 16(e), 16(f), 16(g), and 16(h). The engine reduction torque shown in Figure 16(f) is small comparable to Figure 16(b). And thus the stick vibration (see Figure 16(h)) is reduced, but the shift time is increased. The ETR control with slow recovery is used in the third one; see Figures 16(i), 16(j), 16(k), and 16(l). The slip speed of oncoming clutch decreases to zero gently compared to the previous result. The stick vibration is reduced significantly and the shift time has increased by just 0.05 s.

6.4. Comparison of Different PID Parameters in OFFIS. Based on the frame of the shift controller, the inertia phase before torque phase takes place in the SP1 of the GCF. And thus the ONVCC is in FS and the OFFVCC is in OFFIS. The object of OFFIS is to control the turbine speed to reach the target gear speed level gradually.

Figure 17 shows three simulation results of a power-on downshift with the same initial conditions. Three different PID parameters are used in OFFIS. The FF-PID controller

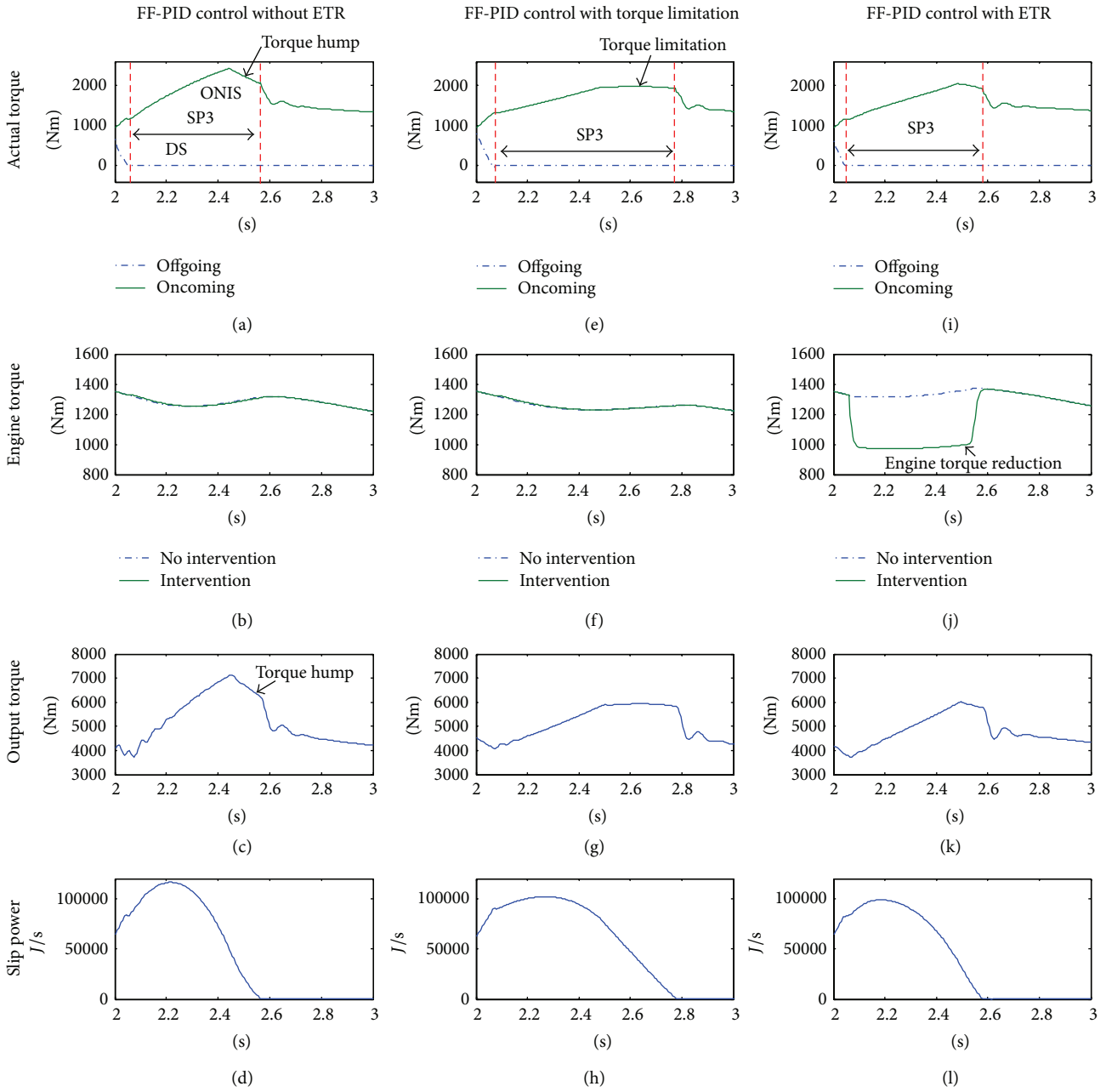

Figure 15: Inertia phase with and without engine torque reduction control.

with improper P term and I term is adopted in the first one; see Figures 17(a), 17(b), 17(c), 17(d), and 17(e). The slip speed of oncoming clutch still increases for a while after the inertia phase. Therefore, the duration time of shift is longer and the slip power of oncoming clutch is larger. The FF-PID controller with proper P term is adopted in the second one; see Figures 17(f), 17(g), 17(h), 17(i), and 17(j). The actual torque of offgoing clutch rises a little at the end of the inertia phase and the turbine speed is "caught" by the offgoing clutch. But there is a small vibration of output torque during the torque phase. The FF-PID controller with proper P term and I term is adopted in the third one; see Figures 17(k), 17(l), 17(m), 17(n), and 17(o). The turbine speed is "caught" and the slip power of oncoming clutch is reduced without the output torque vibration. The trajectory of the actual torque of offgoing clutch during the torque phase is instructive for the controller.

7. Conclusions

In this paper, an equivalent method is proposed to control an AT like a DCT. Two "virtual" clutches, that is, virtual oncoming clutch and virtual offgoing clutch, are imagined at the input side of AT by adopting the torque ratios of the corresponding clutches according to the gear. By this method

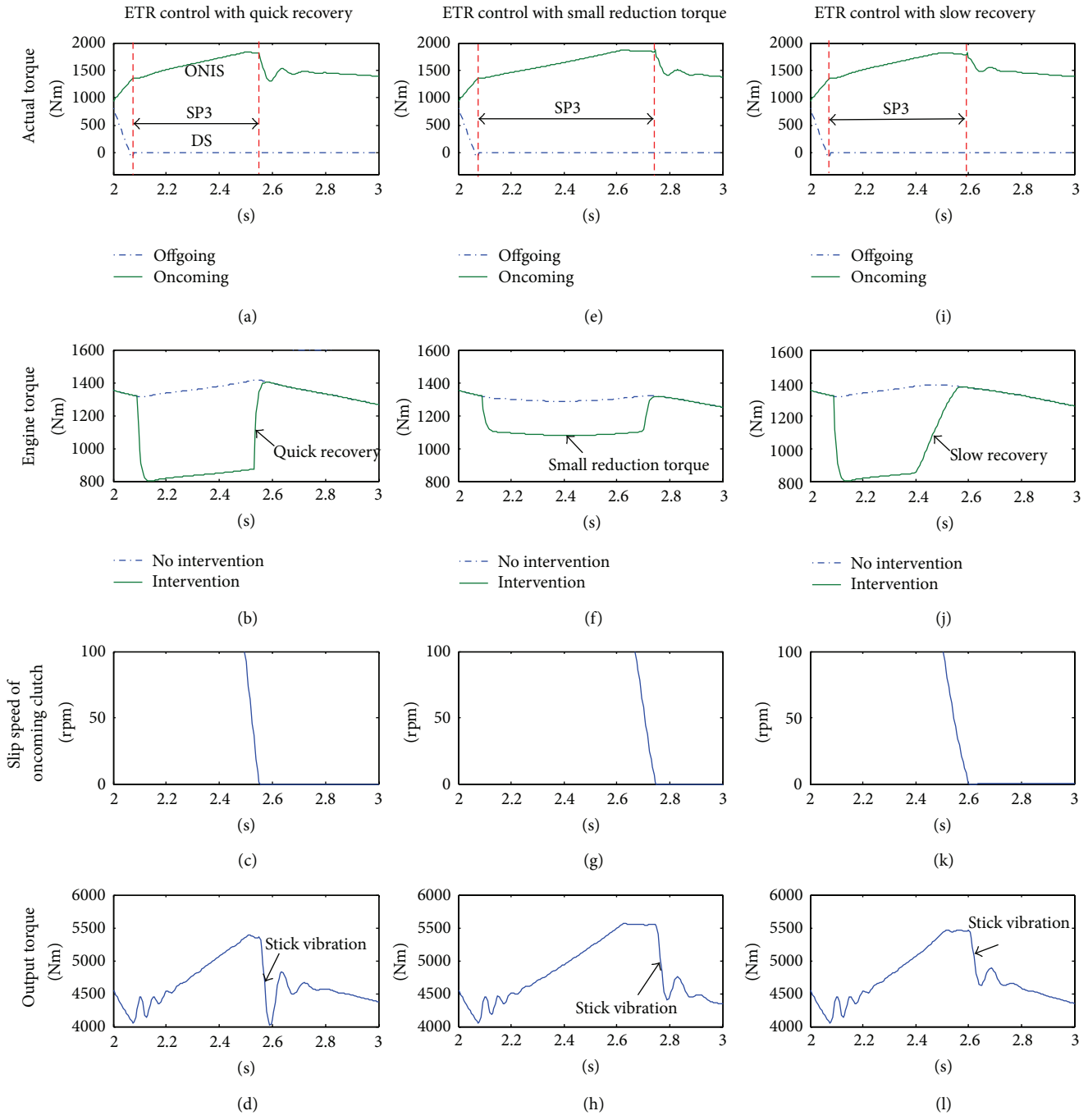

Figure 16: Engine torque reduction control considering stick vibration.

the six clutches of 6AT can be equivalent to two virtual clutches by the torque ratios of each gear, and thus the same control algorithm can be used to handle the shift processes of different gears to simplify the controller, and thus the demand for the memory of TCU is decreased.

To further simplify the algorithms of the shift controller, the virtual clutch controllers are designed with the same eight states which include all control processes for the four types of clutch-to-clutch shifts. With the powertrain model based on a truck, the virtual clutch controllers are verified by software-in-the-loop simulations. Some typical problems in the clutch-to-clutch shift control are discussed and several control methods are provided to solve these problems. Based on the virtual clutch controllers, the control methods for clutch-to-clutch shifts can be investigated conveniently and a foundation for further research is provided.

Conflict of Interests

The authors declare that there is no conflict of interests regarding the publication of this paper.

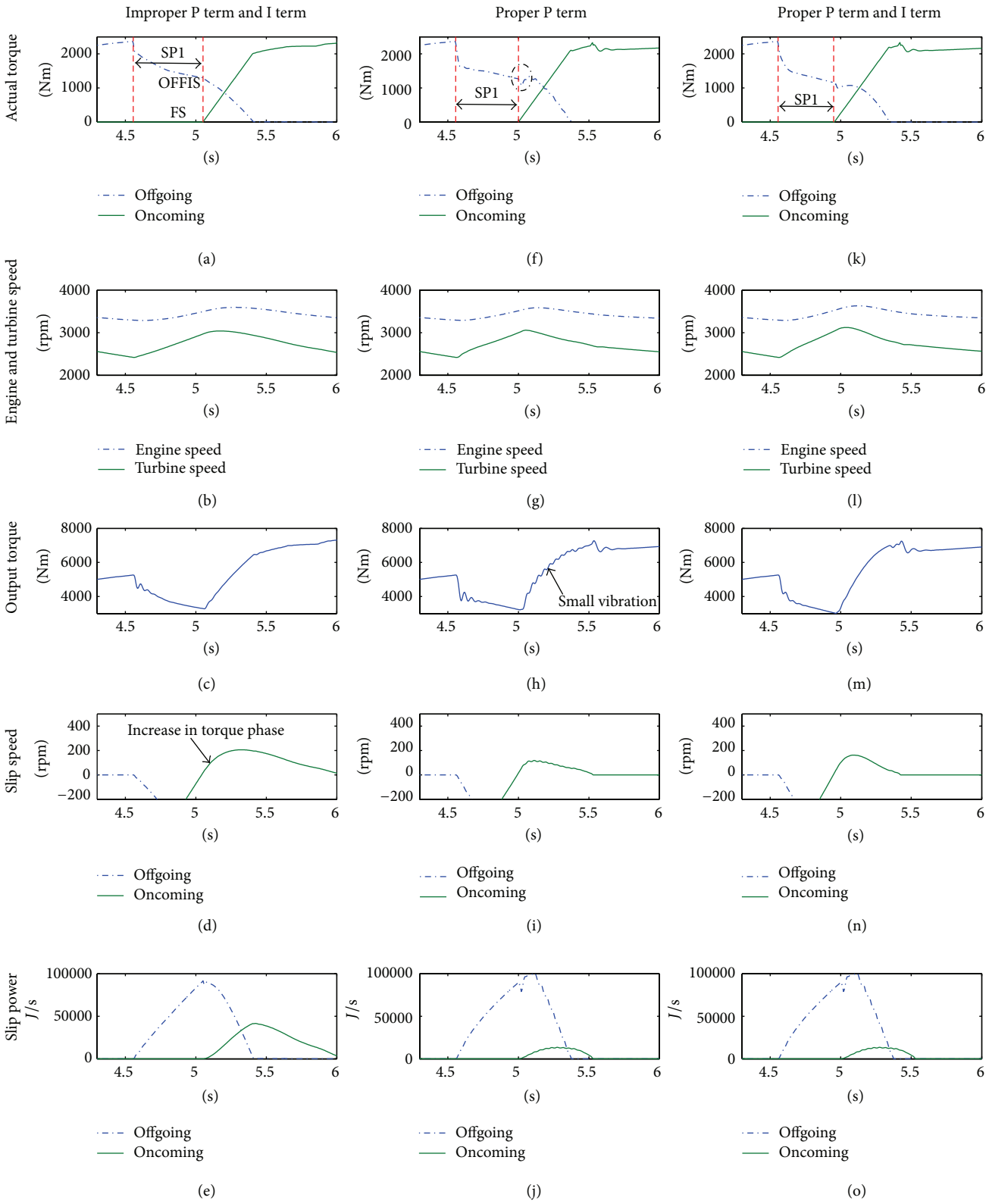

Figure 17: Results of different PID parameters in OFFIS.

Acknowledgments

This study is supported by the National Key Technology R&D Program (no. 2011BAG11B00) and the National Natural Science Foundation of China (no. 51105017).

References

[1] J. K. Runde, *Modelling and Control of an Automatic Transmission*, Massachusetts Institute of Technology, 1986.

[2] A. Haj-Fraj and F. Pfeiffer, "A model based approach for the optimization of gearshifting in automatic transmissions," *International Journal of Vehicle Design*, vol. 28, no. 1–3, pp. 171–188, 2002.

[3] D.-H. Kim, K.-J. Yang, K.-S. Hong, J.-O. Hahn, and K.-I. Lee, "Smooth shift control of automatic transmissions using a robust adaptive scheme with intelligent supervision," *International Journal of Vehicle Design*, vol. 32, no. 3-4, pp. 250–272, 2003.

[4] S. Bai and R. L. Moses, "Development of a new clutch-to-clutch shift control technology," in *Proceedings of the Transmission and Driveline Systems Symposium*, SAE paper no. 2002-01-1252, Detroit, Mich, USA, March 2002.

[5] A. Crowther, N. Zhang, D. K. Liu, and J. K. Jeyakumaran, "Analysis and simulation of clutch engagement judder and stick-slip in automotive power train systems," *Proceedings of the Institution of Mechanical Engineers, Part D*, vol. 218, no. 12, pp. 1427–1446, 2004.

[6] M. Goetz, M. C. Levesley, and D. A. Crolla, "Integrated powertrain control of gearshifts on twin clutch transmissions," in *Proceeding of Transmission & Driveline Symposium*, SAE paper 2004-01-1637, Detroit, Mich, USA, 2004.

[7] M. Goetz, M. C. Levesley, and D. A. Crolla, "Dynamics and control of gearshifts on twin-clutch transmissions," *Proceedings of the Institution of Mechanical Engineers, Part D: Journal of Automobile Engineering*, vol. 219, no. 8, pp. 951–963, 2005.

[8] Y. Liu, D. Qin, H. Jiang, and Y. Zhang, "A systematic model for dynamics and control of dual clutch transmissions," *Journal of Mechanical Design*, vol. 131, no. 6, Article ID 061012, 2009.

[9] Y. Liu, D. Qin, H. Jiang, and Y. Zhang, "Shift control strategy and experimental validation for dry dual clutch transmissions," *Mechanism and Machine Theory*, vol. 75, pp. 41–53, 2014.

[10] P. D. Walker, N. Zhang, and R. Tamba, "Control of gear shifts in dual clutch transmission powertrains," *Mechanical Systems and Signal Processing*, vol. 25, no. 6, pp. 1923–1936, 2011.

[11] P. D. Walker and N. Zhang, "Modelling of dual clutch transmission equipped powertrains for shift transient simulations," *Mechanism and Machine Theory*, vol. 60, pp. 47–59, 2013.

[12] S. Bai, J. Maguire, and H. Peng, *Dynamic Analysis and Control System Design of Automatic Transmissions*, Society of Automotive Engineers, Warrendale, Pa, USA, 2013.

[13] C. F. Xie, Q. Wang, and Y. Cheng, *Dynamics*, Higher Education Press, Beijing, China, 2004.

[14] A. Wohnhaas, D. Hötzer, and U. Sailer, *Modulares Simulationsmodell eines Kfz-Antriebsstrangs unter Berücksichtigung von Nichtlinearitäten und Kupplungsvorgängen*, VDI-Verlag, Düsseldorf, Germany, 1995.

Hindawi Publishing Corporation
Mathematical Problems in Engineering
Volume 2015, Article ID 491328, 8 pages
http://dx.doi.org/10.1155/2015/491328

Research Article

The Study of a Mathematical Model in Information Acquisition and Disclosure

Ce Huang

School of Public Finance and Taxation, Southwestern University of Finance and Economics, 555 Liutai Avenue, Wenjiang, Chengdu, Sichuan 611130, China

Correspondence should be addressed to Ce Huang; huangce@swufe.edu.cn

Received 7 October 2014; Accepted 23 November 2014

Academic Editor: Honglei Xu

Copyright © 2015 Ce Huang. This is an open access article distributed under the Creative Commons Attribution License, which permits unrestricted use, distribution, and reproduction in any medium, provided the original work is properly cited.

A mathematical model involving a decision maker and an expert is investigated. Through analyzing the model, we obtain several results on the expert's information acquisition and disclosure strategy. When withholding information is costly to the expert, in equilibrium, an expert with a higher withholding cost acquires less information but discloses more acquired information. We also examine which expert is optimal to the decision maker among a group of experts with different costs of withholding information.

1. Introduction

In many situations, a decision maker needs to make a decision but does not know which decision is the best one. For example, an investor may not know the future performance of companies in the stock market and is uncertain about which stock is the best. A patient does not have knowledge about the most cost-effective treatment for the health concern. Facing lack of information, the decision maker often looks for advice from investment consultants or doctors, who are experts and are better informed.

However, the interest of the expert is often different from that of the decision maker. In other words, the decision preferred by the expert is different from the one preferred by the decision maker. In our previous examples, an investment consultant may not be interested in picking the best stock. Instead, the consultant may want the investor to buy some particular stocks, perhaps because these stock companies will pay the consultant. Doctors often receive bonuses from expensive medical procedures, which might be unnecessary for patients with mild diseases. Due to this conflict of interests between experts and decision makers, experts often withhold information from decision makers.

We analyze a game between a decision maker (hereafter DM) and an expert (we use "she" to denote DM and "he" to denote the expert throughout this paper). DM needs to take a decision. The best decision of DM depends on an uncertain state of the world (hereafter the state). DM has no information about the state but the expert, through exerting costly effort to acquire information, can observe the state with some probability. The probability of observing the state is increasing in his effort. DM and the expert have different preferences. DM's best decision is equal to the state but the expert prefers a decision strictly higher than the state. Upon observing the state, the expert can disclose the observation to DM or withhold the information. We analyze the perfect Bayesian Nash equilibrium of the game between DM and the expert. In equilibrium, the expert decides how much effort to spend in information acquisition and what range of acquired information to disclose to DM, and DM chooses which decision to be taken when the expert does not disclose information.

We consider a situation where withholding information is costly to the expert. This is because the expert may feel guilty if he withholds information from DM. The cost of withholding information reflects the loss in the expert's utility caused by guilty feelings. An alternative explanation for the cost is that DM may discover the withholding behavior of the expert. As a result, DM will doubt the trustworthy of the expert and refuse seeking advice from the expert in the future. The cost of withholding information to the expert reflects the expert's loss in his future revenue due to losing

clients. Of course, different experts have different costs of withholding information. This is because different experts have different moral standards or have different concerns for future revenues.

We study how the expert's equilibrium information acquisition and disclosure strategy changes as the expert's withholding cost increases. We also study how the expected utility of DM changes. These questions are investigated under two different utility functions of the expert. Under both utility functions, the expert exerts less effort in acquiring information and discloses a greater proportion of collected information as withholding cost increases. If the expert prefers the decision to be as high as possible regardless of the state, the expert's effort in acquiring information quickly decreases as withholding cost increases. As a result, the likelihood that the expert can obtain information quickly decreases. Although the expert discloses a greater proportion of acquired information to DM, DM gets less information and gets worse off. Alternatively, if the ideal decision of the expert is higher than that of DM by a constant distance, the expert's effort in information acquisition slowly decreases as withholding cost increases. DM receives more information and gets better off.

This paper is related to a large literature on the strategic transmission of verifiable information between a decision maker and an expert. See Grossman [1], Grossman and Hart [2], Milgrom [3], and Milgrom and Roberts [4] for early classic studies on this topic. When information is verifiable, DM can check the truthfulness of the expert's disclosed information. Therefore, it is assumed in this literature that the expert cannot disclose information that is different from the observed state. However, the expert can withhold the information. These papers mentioned above find that the expert will not withhold information in equilibrium. To see why, suppose that the expert withholds information when some states are observed. When the expert does not disclose information, DM infers that the state is at the average value among these states. This implies that the expert should disclose the observed state that is higher than the average value, because disclosing the state induces DM to take a higher decision. The expert is better off by withholding information only when the observed state is lower than the average. Knowing this, DM adjusts her inference of the state downwards when the expert does not disclose information. Again, the expert who observes a state higher than the new inference of DM is better off by disclosing information. We can repeat the same argument and show that the expert withholds information only when he observes the lowest possible state. Knowing this, DM can infer the state when the expert does not disclose information. Therefore, there is no information withholding in equilibrium.

It is assumed in Shin [5, 6] that the expert fails to obtain information about the state with a positive probability. When the expert does not disclose information, DM takes into account the possibility that the expert does not obtain information. In equilibrium, the expert will withhold information when some states are observed.

In Che and Kartik [7], in order to obtain information about the state, the expert needs to exert costly effort. When more effort is exerted, the expert will more likely obtain the information. It is found that when the expert has a prior belief about the state different from that of DM, the expert will exert more effort in acquiring information. It is established that DM can receive a higher expected utility from consulting an expert with a slightly different prior belief about the state, compared to the utility from consulting an expert with the same prior belief. In Xu and Suen [8], a model similar to the one in Che and Kartik [7] is considered. In Xu and Suen [8], withholding information by the expert may be detected by DM and the expert will be punished. It is found that, under a larger punishment on withholding, the expert may acquire less information and disclose less acquired information to DM. The current paper studies an issue similar to the one in Xu and Suen [8]. However, the current paper considers a case where the state can take a continuum of possible values, while there are only two possible states in Xu and Suen [8]. The current paper is different from Xu and Suen [8] also in predictions. In the current paper, the expert discloses more acquired information under a larger punishment on withholding information, while, in Xu and Suen [8], the expert discloses less acquired information.

The paper is organized as follows. Section 2 builds a model of information acquisition and transmission between an expert and a decision maker. Section 3 characterizes the relationship between the expert's withholding cost and the effort in obtaining information. Also the relationship between withholding cost and the range of disclosed information is characterized. Section 4 examines which one is the best to DM in a group of experts with different costs of withholding information. Section 5 considers a model where the utility function of the expert takes a different form. Section 6 concludes and discusses future work.

2. Model

A decision maker needs to make a decision, modeled as a choice of a real number in the interval $[0, 1]$. Her utility from decision $a \in [0, 1]$ depends on a variable θ, which is called the state of the world. Assume that her utility is

$$u_{\mathrm{DM}}(a, \theta) = -(a - \theta)^2. \tag{1}$$

Apparently, DM's utility is higher when a is closer to θ. This reflects DM's desire to take a decision as close to the state as possible.

However, DM has no information about θ. We assume that θ is uniformly distributed on $[0, 1]$. In order to get more information about the state and make a better decision, DM consults an expert who can potentially observe θ.

Initially, the expert does not have any information about θ. However, the expert can exert effort to acquire information about θ, so that θ can be observed with some probability. The more effort the expert exerts, the more likely θ will be observed. Exerting effort is costly to the expert. We assume that, in order to observe θ with probability p, the expert needs to exert effort that costs him $c(p)$, where $c(p)$ strictly increases in p.

The expert's preference is different from that of DM. In the benchmark case, we assume that when the decision taken by DM is a and the state is θ, the utility of the expert is

$$u_E(a,\theta) = a. \tag{2}$$

The expert's utility only depends on the level of DM's decision and is independent of the state. Therefore, the expert is not concerned about whether the decision is appropriate for the state or not. Instead, the expert only cares about the *level* of the decision. We will consider another utility function of the expert in Section 5.

When the expert observes θ, we assume that the expert cannot lie to DM by reporting that the state is θ', which is different from the observed θ. However, the expert can say that he does not observe the state. This is because the expert does not observe the state for sure and DM does not know whether the expert observes θ or not. We call this behavior "withholding information." The expert who observes that the state is θ can report either "θ," the state he observes, or "Φ." Here Φ stands for "I do not know about the state." When the expert does not observe the state, we assume that the expert can only report "Φ." We assume that when the expert observes that the state is θ, reporting θ is costless to the expert while reporting "Φ" is costly. We assume that the cost is $x \geq 0$.

When the expert reports "Φ" (hereafter "the expert does not disclose information"), DM cannot tell whether the expert indeed does not observe the state or is just withholding information. When making a decision, DM takes into account the probability that the expert withholds information.

The equilibrium concept is perfect Bayesian Nash equilibrium (hereafter "the equilibrium"). It consists of three components: the expert's strategy in how much effort to exert in acquiring information about the state and which states to be disclosed to DM after observing the state; DM's strategy in what decision to be taken when the expert does not disclose information; and DM's belief about the state when the expert does not disclose information. To be an equilibrium, these strategies and belief are such that, given DM's strategy, the expert's strategy maximizes his expected utility, net of the expected cost and given DM's belief about the state, DM's strategy maximizes her expected utility; DM's belief is derived from the expert's strategy using Bayes' rule.

Denote the decision taken by DM by a_ϕ when the expert does not disclose information. We consider whether the expert will disclose information when the observed state is θ. If the expert discloses the information, DM believes that the state is θ and takes a decision that gives DM the highest utility, which is θ. The utility of the expert by disclosing information is θ. If the expert withholds the information, DM will take decision a_ϕ. The expert's utility, net of the cost of withholding information, is $a_\phi - x$. So the expert will disclose information when the observed state satisfies

$$\theta \geq a_\phi - x. \tag{3}$$

Now we consider how much effort the expert will exert in information acquisition, given DM's decision in the event of nondisclosure, a_ϕ, and the expert's optimal information disclosing strategy derived above. Note that when deciding how much effort to exert in acquiring information, the expert has not observed the state yet. When the expert exerts effort that costs him $c(p)$, he will observe the state with probability p and will not observe the state with probability $1-p$. In the former case, when the observed state is less than $a_\phi - x$, the expert will withhold the information from DM and receive utility (net of the withholding cost) $a_\phi - x$. When the observed state is greater than $a_\phi - x$, the expert will disclose the information to DM and receive a utility equal to the observed state. If the expert does not observe the state, he will report Φ to DM and receive utility a_ϕ. Therefore, the expert's expected utility when he exerts effort in information acquisition that costs him $c(p)$ is

$$p\left[\left(a_\phi - x\right)^2 + \left(1 - a_\phi + x\right) * \frac{\left(1 + a_\phi - x\right)}{2}\right] + (1-p)\,a_\phi - c(p), \tag{4}$$

where $(1+a_\phi - x)/2$ in the square bracket is the expected value of θ conditional on being greater than $a_\phi - x$.

In order to maximize the expected utility, the expert will exert effort in acquiring information such that the probability p that the expert obtains information satisfies

$$c'(p) = l\left(a_\phi, x\right), \tag{5}$$

where $l(a,x) \equiv [1 + (a-x)^2]/2 - a$.

Through straightforward calculation, we have the following result regarding function $l(a,x)$.

Lemma 1. *When $x \leq a \leq 1$, $l(a,x)$ strictly decreases in a and strictly decreases in x.*

Intuitively, the incentive of the expert to acquire information is from the difference between the expert's expected utility when information is successfully obtained and his expected utility when failing to obtain information. As a_ϕ increases, the difference between these two expected utilities decreases. Thus, the incentive of the expert to acquire information decreases. As x increases, the expert's expected utility when information is successfully obtained decreases while the expected utility when failing to obtain information does not change. Thus, the expert's incentive to acquire information decreases.

As the next step, we characterize DM's posterior belief about the state when the expert does not disclose information. The belief is derived from the expert's strategy in information acquisition and disclosure using Bayes' rule.

Suppose that the expert exerts effort to acquire information, and the effort exerted costs the expert $c(p)$. When information about the state is obtained, the expert withholds information if and only if the observed θ is lower than a cutoff value k (given the expert's utility function, any equilibrium strategy in information disclosure must have this "cutoff" property). Under this strategy of the expert, with probability $1-p$ the expert will fail to observe the state, and with probability pk, the expert successfully observes the state and

the observed state is less than k. In the latter case, the expert will withhold information. Conditional on that the expert does not disclose information to DM, by Bayes' rule, the probability that the expert withholds information is $pk/[(1-p)+pk]$, and the expert is genuinely uninformed about the state with the complementary probability. The state follows a uniform distribution on $[0,k]$ when the expert withholds information and follows a uniform distribution on $[0,1]$ when the expert is genuinely uninformed about the state. Therefore, when receiving no information from the expert, DM's posterior belief is that the state follows the distribution function:

$$F(\theta \mid \text{No disclosure}) = \begin{cases} \dfrac{pk}{1-p+pk}\dfrac{\theta}{k} + \dfrac{1-p}{1-p+pk}\theta, & \text{if } \theta \le k, \\ \dfrac{pk}{1-p+pk} + \dfrac{1-p}{1-p+pk}\theta, & \text{if } \theta > k. \end{cases} \quad (6)$$

Compared to DM's prior belief about the state, DM's posterior belief about the state when the expert does not disclose information features a higher probability density at $\theta \le k$ and a lower probability density at $\theta > k$. Intuitively, when the expert does not disclose information, DM thinks that the expert might withhold information from DM. Because the expert withholds information when the state is relatively low, DM thinks that the state is more likely to be low and less likely to be high.

Under the posterior belief, DM's optimal decision a_ϕ when the expert does not disclose information satisfies

$$a_\phi \in \underset{a\in[0,1]}{\operatorname{argumax}}\, E_\theta\left[-(a-\theta)^2 \mid F(\cdot \mid \text{No disclosure})\right], \quad (7)$$

from which we can solve a_ϕ as

$$a_\phi = h(p,k), \quad (8)$$

where $h(p,k) \equiv [pk^2/(1-p+pk) + (1-p)/(1-p+pk)]/2$. We have the following result regarding function $h(p,k)$.

Lemma 2. *$h(p,k)$ strictly decreases in p when $k < 1$. When k is small, $h(p,k)$ strictly decreases in k; when k is large, $h(p,k)$ strictly increases in k.*

Proof. Note that $h(p,k)$ is the average of $k/2$ and $1/2$ with the weight on $k/2$ being $pk/(1-p+pk)$. When p increases, the weight on $k/2$ increases, which implies that $h(p,k)$ decreases when $k < 1$.

To see how $h(p,k)$ changes as k increases, note that

$$\frac{\partial h(p,k)}{\partial k} = \frac{1}{2}\frac{pk}{1-p+pk}\left[1 - \frac{1-k}{k}\frac{1-p}{1-p+pk}\right]. \quad (9)$$

It can be seen that if $0 < p < 1$, there exists a cutoff value $0 < \widehat{k} < 1$ such that $\partial h(p,k)/\partial k < 0$ when $k < \widehat{k}$ and $\partial h(p,k)/\partial k > 0$ when $k > \widehat{k}$. □

Intuitively, when the probability that the expert obtains information is higher, it is more likely that the expert is withholding information when the expert does not disclose information. Given the value of the state is relatively low when the expert withholds information, DM's expectation about the state is lower. Therefore, her optimal decision $h(p,k)$ decreases.

When the cutoff value of expert's disclosing strategy increases, there are two conflicting effects. On the one hand, with a higher cutoff value and more states under which the expert will withhold information, DM thinks that the probability that the expert withholds information is higher when the expert does not disclose information. Therefore, DM's expectation of the state decreases and her optimal decision $h(p,k)$ also decreases. On the other hand, a higher cutoff value implies that the mean value of the state increases when the expert withholds information. DM's expectation of the state increases and her optimal decision $h(p,k)$ also increases. When k is small, the first effect dominates and $h(p,k)$ decreases in k. However, when k is large, the second effect dominates and $h(p,k)$ increases in k.

A perfect Bayesian Nash equilibrium can be represented as a tuple $\{a_\phi^*, p^*, k^*\}$ such that $c'(p^*) = l(a_\phi^*, x)$; $k^* = a_\phi^* - x$; $a_\phi^* = h(p^*, k^*)$. We assume that x is small enough such that, in equilibrium, the expert exerts some effort in information acquisition; that is, $p^* > 0$. Apparently, a_ϕ^*, p^*, and k^* are all functions of x. We suppress the dependence of these equilibrium variables on x in order to keep notations simple.

3. Equilibrium Characterization

In this section, we address the following question: under a greater cost of withholding information, will the expert exert more effort in information acquisition and withhold less acquired information from DM in the equilibrium? In other words, when x increases, will p^* increase and k^* decrease?

We use numerical simulation to get the relationship between x and equilibrium variables, p^*, k^*, and a_ϕ^*. As shown in Figure 1, when x increases, p^* decreases, k^* decreases, and a_ϕ^* increases. Under a greater cost of withholding information, the expert exerts less effort in information acquisition and withholds less acquired information. We have the following result.

Proposition 3. *As x increases, p^* decreases, k^* decreases, and a_ϕ^* increases.*

To see why the above relationship holds, suppose that p^* does not change when x increases. This allows us to see how a_ϕ^* and k^* change. For a fixed p^*, a_ϕ^* and k^* can be characterized as the solution to equations $k = a_\phi - x$ and $a_\phi = h(k, p^*)$. As shown in Figure 2, when x increases, the curve $k = a_\phi - x$ shifts upward and the curve $a_\phi = h(k, p^*)$ remains unchanged. Therefore, a_ϕ^* increases and k^* decreases, implying that $l(a_\phi^*, x)$ decreases. Therefore, the expert's incentive to acquire information decreases, implying that p^* decreases.

Intuitively, as x increases, the expert withholds less information from DM. k^* decreases. This implies that the

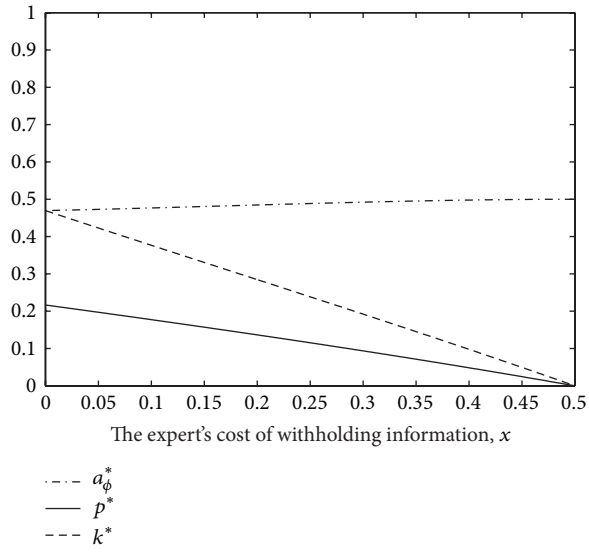

Figure 1: How equilibrium variables change as x changes.

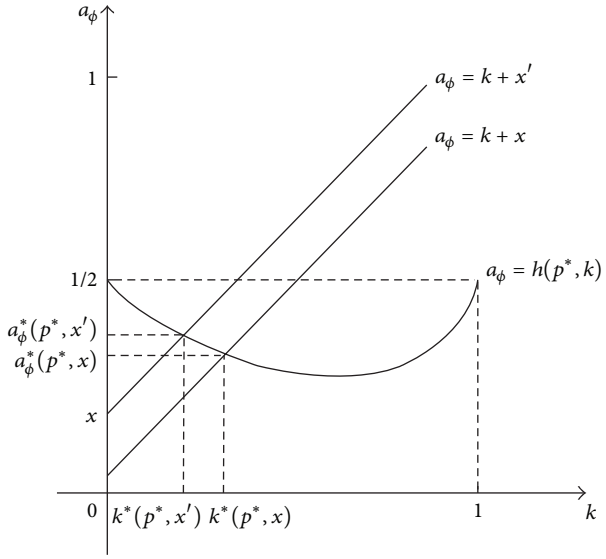

Figure 2: A higher x implies a lower k and a higher a.

likelihood that the expert withholds information decreases. As a result, DM thinks that it is more likely that the expert is uninformed about the state when the expert does not disclose information. Therefore, DM's expected state is higher and a_ϕ^* increases. The increase in a_ϕ^* and the decrease in k^* imply that the expert's incentive to acquire information decreases. Therefore, p^* decreases.

4. Optimal Expert

In this section, we consider the situation where DM faces a pool of experts, each with different cost of withholding information. We ask the following question: which expert should DM choose to acquire and report information, in order to maximize DM's expected utility? As shown in the previous section, an expert with a greater cost of withholding information has a lower likelihood of successfully obtaining information and withholds less acquired information. Therefore, it seems ambiguous whether DM can receive more information from an expert with a greater cost of withholding information and receive a higher expected utility.

To tackle this problem, we write down DM's expected utility when the equilibrium is $\{a_\phi^*, p^*, k^*\}$. There are several cases to consider. With probability p^*k^*, the expert obtains information successfully and the observed state is lower than k^*. The expert withholds the information and DM takes decision a_ϕ^*. In this case, the state follows a uniform distribution on $[0, k^*]$ and DM's expected utility is $E_\theta[-(a_\phi^* - \theta)^2 \mid \theta \le k^*]$. With probability $p^*(1 - k^*)$, the expert obtains information successfully and the observed state is higher than k^*. The expert discloses the observed state to DM and DM takes a decision equal to the state. In this case, DM's expected utility is zero. With probability $1 - p^*$, the expert does not obtain information about the state and DM takes decision a_ϕ^*. In this case, the state follows a uniform distribution on $[0, 1]$ and DM's expected utility is $E_\theta[-(a_\phi^* - \theta)^2]$.

From an ex ante point of view, the expected utility of DM when the expert has withholding cost x is

$$EU_{\mathrm{DM}}(x) \equiv p^*k^*E_\theta\left[-\left(a_\phi^* - \theta\right)^2 \mid \theta \le k^*\right] + (1 - p^*)E_\theta\left[-\left(a_\phi^* - \theta\right)^2\right], \tag{10}$$

where the right-hand side can be calculated as

$$p^*k^*\left[-\left(a_\phi^*\right)^2 + a_\phi^*k^* - \frac{(k^*)^2}{3}\right] + (1 - p^*)\left[-\left(a_\phi^*\right)^2 + a_\phi^* - \frac{1}{3}\right]. \tag{11}$$

Using numerical simulation, we can get the relationship between DM's ex ante expected utility and the expert's cost of withholding information. This is shown in Figure 3. The figure shows that the ex ante expected utility of DM reaches its highest level when the expert's cost of withholding information is zero.

5. An Alternative Utility Function of Expert

In this section, we consider an alternative utility function of the expert. In particular, we assume that when the decision is a and the state is θ, the expert's utility is

$$u_E(a, \theta) = -(a - \theta - b)^2, \tag{12}$$

where $b > 0$.

When the state is θ, the decision that leads to the highest utility of the expert is $\theta + b$. Therefore, it is no longer true that the expert always prefers a higher decision to a lower one regardless of the state. The expert may prefer a lower decision to a higher one when the state is low. This reflects that

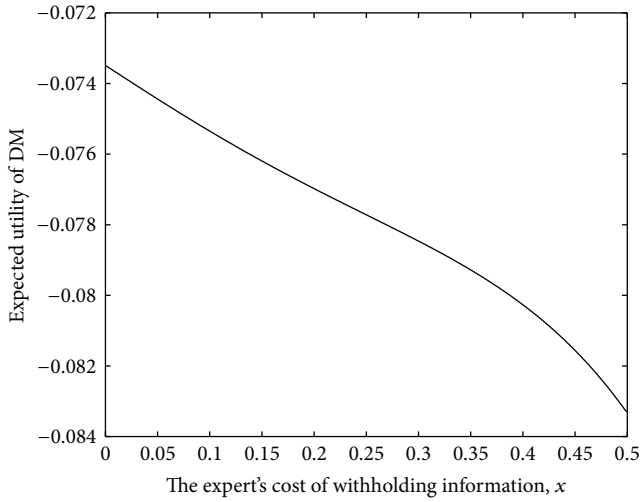

Figure 3: How the expected utility of DM changes as x changes.

the expert also has some concerns with the appropriateness of the decision to the underlying state and the conflict of interests between the expert and DM is not as large as in the benchmark case. However, given any state, the decision preferred by the expert is always higher than the one preferred by DM by a constant distance b. This reflects that the expert has a bias towards higher decisions by DM.

We characterize a perfect Bayesian Nash equilibrium between DM and the expert in a way similar to what we did before. Denote the decision taken by DM as a_ϕ when the expert does not disclose information. We consider the expert's optimal strategy in information disclosure when the observed state is θ. If the expert discloses the information, DM will take a decision equal to the disclosed state and the expert's utility is $-b^2$. If the expert withholds the information, DM will take decision a_ϕ and the expert's utility (net of withholding cost) is $-(a_\phi - \theta - b)^2 - x$. By comparing $-b^2$ with $-(a - \theta - b)^2 - x$, the expert's optimal strategy in information disclosure is to withhold information if and only if the observed state satisfies that

$$\theta \in \left[l\left(a_\phi, b, x\right), h\left(a_\phi, b, x\right) \right], \tag{13}$$

where $l(a,b,x) \equiv (a-b) - \sqrt{b^2 - x}$ and $h(a,b,x) \equiv (a-b) + \sqrt{b^2 - x}$. We restrict attention to cases where b is small enough such that $l(a_\phi, b, x) \geq 0$.

Given the expert's optimal strategy in information disclosure, when the effort exerted by the expert in information acquisition costs $c(p)$, the expert's expected utility is

$$\begin{aligned} &2p\sqrt{b^2 - x} E_\theta \left[-\left(a_\phi - \theta - b\right)^2 \right. \\ &\qquad \left. - x \mid l\left(a_\phi, b, x\right) \leq \theta \leq h\left(a_\phi, b, x\right) \right] \\ &+ p\left(1 - 2\sqrt{b^2 - x}\right)\left(-b^2\right) \\ &+ (1-p) E_\theta \left[-\left(a_\phi - \theta - b\right)^2 \right] - c(p), \end{aligned} \tag{14}$$

which can be rewritten as

$$\begin{aligned} &2p\sqrt{b^2 - x}\left[-\frac{1}{3\left(b^2 - x\right)} - x \right] \\ &+ p\left(1 - 2\sqrt{b^2 - x}\right)\left(-b^2\right) \\ &+ (1-p)\left[-\left(a_\phi - b\right)^2 + \left(a_\phi - b\right) - \frac{1}{3} \right] - c(p). \end{aligned} \tag{15}$$

The probability p that maximizes the above expected utility satisfies

$$c'(p) = f\left(a_\phi, b, x\right), \tag{16}$$

where

$$\begin{aligned} f(a,b,x) \equiv{}& 2\sqrt{b^2 - x}\left[-\frac{1}{3\left(b^2 - x\right)} - x \right] \\ &+ \left(1 - 2\sqrt{b^2 - x}\right)\left(-b^2\right) \\ &- \left[-(a-b)^2 + (a-b) - \frac{1}{3} \right]. \end{aligned} \tag{17}$$

For DM, suppose that the expert obtains information with probability p, and when successfully obtaining information, the expert withholds information if the observed state θ satisfies $k_1 \leq \theta \leq k_2$. By Bayes' rule, DM's posterior belief about the state when the expert does not disclose information is

$$\begin{aligned} &F(\theta \mid \text{No disclosure}) \\ &= \begin{cases} \dfrac{1-p}{1-p+p\left(k_2 - k_1\right)}\theta, & \text{if } 0 \leq \theta \leq k_1, \\ \dfrac{p\left(k_2 - k_1\right)}{1-p+p\left(k_2 - k_1\right)}\dfrac{\theta - k_1}{k_2 - k_1} & \\ \quad + \dfrac{1-p}{1-p+p\left(k_2 - k_1\right)}\theta, & \text{if } k_1 < \theta \leq k_2, \\ \dfrac{p\left(k_2 - k_1\right)}{1-p+p\left(k_2 - k_1\right)} & \\ \quad + \dfrac{1-p}{1-p+p\left(k_2 - k_1\right)}\theta, & \text{if } k_2 < \theta \leq 1. \end{cases} \end{aligned} \tag{18}$$

Under this belief, the optimal decision of DM when the expert does not disclose information is

$$a_\phi = E_\theta\left[\theta \mid \text{No disclosure}\right] = g\left(p, k_1, k_2\right), \tag{19}$$

where

$$\begin{aligned} g\left(p, k_1, k_2\right) \equiv{}& \frac{p\left(k_2 - k_1\right)}{1-p+p\left(k_2 - k_1\right)}\frac{k_1 + k_2}{2} \\ &+ \frac{1-p}{1-p+p\left(k_2 - k_1\right)}\frac{1}{2}. \end{aligned} \tag{20}$$

A perfect Bayesian Nash equilibrium is a tuple $\{a_\phi^*, k_1^*, k_2^*, p^*\}$ such that $a_\phi^* = g(p^*, k_1^*, k_2^*)$, $c'(p^*) = f(a_\phi^*, b, x)$, $k_1^* = l(a_\phi^*, b, x)$, and $k_2^* = h(a_\phi^*, b, x)$.

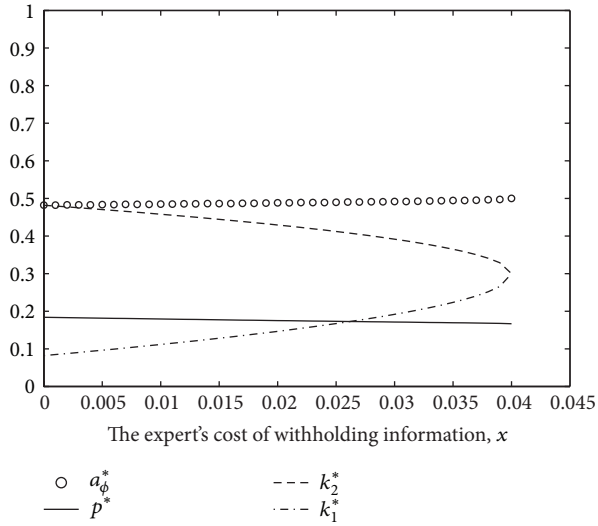

Figure 4: How equilibrium variables change as x changes ($b = 0.2$).

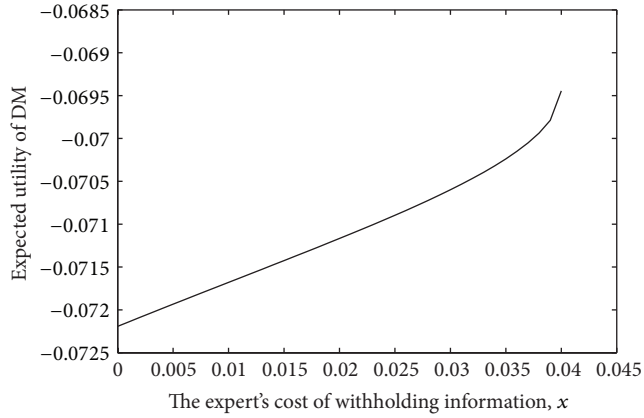

Figure 5: How the expected utility of DM changes as x changes ($b = 0.2$).

Figure 4 shows the relationship between the cost of withholding information, x, and equilibrium variables a_ϕ^*, p^*, k_1^*, and k_2^* when $b = 0.2$. From the figure, we can see that, in equilibrium, the expert's effort in acquiring information decreases as x increases. This result indicates a negative effect of the cost of withholding information on the expert's incentive to acquire information. However, the negative effect is much smaller than in the benchmark case. This can be seen from Figure 4 that the expert's effort in acquiring information approaches a positive value as x approaches b^2 from below, even though the expert discloses all information (k_2^* and k_1^* approach each other). This can also be seen from the fact that $f(a_\phi, b, x) > 0$ when $x = b^2$.

As the next step, we consider a situation where DM faces a pool of experts with different costs of withholding information. We only consider the case where the cost of withholding information is small; in particular, $x \le b^2$. This is because when $x > b^2$, the expert will disclose all information and the cost of withholding information does not affect the expert's strategy in information acquisition. From an ex ante point of view, DM's expected utility by choosing an expert with cost x of withholding information is

$$p^* \left(k_2^* - k_1^*\right) E_\theta \left[-\left(a_\phi^* - \theta\right)^2 \mid k_1^* \le \theta \le k_2^*\right] + \left(1 - p^*\right) E_\theta \left[-\left(a_\phi^* - \theta\right)^2\right], \tag{21}$$

which could be calculated as

$$-p^* \left(a_\phi^*\right)^2 \left(k_2^* - k_1^*\right) + p^* a_\phi^* \left[\left(k_2^*\right)^2 - \left(k_1^*\right)^2\right] - \frac{1}{3p^* \left[\left(k_2^*\right)^3 - \left(k_1^*\right)^3\right]} + \left(1 - p^*\right)\left[-\left(a_\phi^*\right)^2 + a_\phi^* - \frac{1}{3}\right]. \tag{22}$$

For a fixed bias b of the expert, we use numerical simulation to identify the relationship between DM's ex ante expected utility and the expert's cost of withholding information. Figure 5 shows this relationship when $b = 0.2$ and $x \le b^2$. It can be seen from the figure that DM's expected utility reaches its maximum level when the expert's withholding cost is at its largest value.

6. Conclusion

This paper studies a game between an expert and a decision maker. The expert first exerts costly effort to acquire decision-relevant information. Then the expert decides whether or not to disclose the acquired information to the decision maker. Finally, the decision maker takes a decision that affects the utilities of both the expert and the decision maker. The expert and the decision maker have different preferences about the decision. In addition, withholding information is costly to the expert. We find that an expert with a greater withholding cost exerts less effort to acquire information but discloses a greater proportion of acquired information to DM. When the expert prefers DM's decision to be as high as possible, DM's expected utility decreases when the expert's withholding cost increases. When the decision preferred by the expert is higher than that preferred by DM by a constant distance, DM's expected utility increases when the expert's withholding cost increases.

Future work involves studying similar games with other utility functions of the expert. Another direction for future studies is to analyze a model where the expert can misreport the observed state but will incur a cost when doing so. In such a model, we can investigate the relationship between the expert's cost of misreporting information and the expert's incentive to acquire information. This model is more complicated than the one we examine in this paper and is left for future research.

Conflict of Interests

The author declares that there is no conflict of interests regarding the publication of this paper.

Acknowledgment

This research is supported by the Fundamental Research Funds for the Central Universities (no. JBK140107).

References

[1] S. J. Grossman, "The informational role of warranties and private disclosure about product quality," *Journal of Law and Economics*, vol. 24, no. 3, pp. 461–483, 1981.

[2] S. J. Grossman and O. Hart, "Disclosure laws and takeover bids," *The Journal of Finance*, vol. 35, no. 2, pp. 323–334, 1980.

[3] P. Milgrom, "Good news and bad news: representation theorems and applications," *Bell Journal of Economics*, vol. 12, no. 2, pp. 380–391, 1981.

[4] P. Milgrom and J. Roberts, "Relying on the information of interested parties," *The RAND Journal of Economics*, vol. 17, no. 1, pp. 18–32, 1986.

[5] H. S. Shin, "News management and the value of firms," *The RAND Journal of Economics*, vol. 25, no. 1, pp. 58–71, 1994.

[6] H. S. Shin, "Adversarial and inquisitorial procedures in arbitration," *RAND Journal of Economics*, vol. 29, no. 2, pp. 378–405, 1998.

[7] Y.-K. Che and N. Kartik, "Opinions as incentives," *Journal of Political Economy*, vol. 117, no. 5, pp. 815–860, 2009.

[8] F. Xu and W. Suen, "Investment in concealable information," working paper, University of Hong Kong, 2012.

Hindawi Publishing Corporation
Mathematical Problems in Engineering
Volume 2015, Article ID 349781, 17 pages
http://dx.doi.org/10.1155/2015/349781

Research Article

A Multiobjective Genetic Algorithm Based on a Discrete Selection Procedure

Qiang Long,[1] Changzhi Wu,[2] Xiangyu Wang,[2,3] Lin Jiang,[4] and Jueyou Li[5]

[1]*School of Science, Southwest University of Science and Technology, Mianyang 621010, China*
[2]*Australasian Joint Research Centre for Building Information Modelling School of Built Environment, Curtin University, Perth, WA 6845, Australia*
[3]*Department of Housing and Interior Design, Kyung Hee University, Seoul 136701, Republic of Korea*
[4]*School of Mathematics, Anhui Normal University, Wuhu 430000, China*
[5]*School of Mathematics, Chongqing Normal University, Chongqing 404100, China*

Correspondence should be addressed to Changzhi Wu; changzhiwu@yahoo.com

Received 12 November 2014; Revised 15 January 2015; Accepted 20 January 2015

Academic Editor: Jianxiong Ye

Copyright © 2015 Qiang Long et al. This is an open access article distributed under the Creative Commons Attribution License, which permits unrestricted use, distribution, and reproduction in any medium, provided the original work is properly cited.

Multiobjective genetic algorithm (MOGA) is a direct search method for multiobjective optimization problems. It is based on the process of the genetic algorithm; the population-based property of the genetic algorithm is well applied in MOGAs. Comparing with the traditional multiobjective algorithm whose aim is to find a single Pareto solution, the MOGA intends to identify numbers of Pareto solutions. During the process of solving multiobjective optimization problems using genetic algorithm, one needs to consider the elitism and diversity of solutions. But, normally, there are some trade-offs between the elitism and diversity. For some multiobjective problems, elitism and diversity are conflicting with each other. Therefore, solutions obtained by applying MOGAs have to be balanced with respect to elitism and diversity. In this paper, we propose metrics to numerically measure the elitism and diversity of solutions, and the optimum order method is applied to identify these solutions with better elitism and diversity metrics. We test the proposed method by some well-known benchmarks and compare its numerical performance with other MOGAs; the result shows that the proposed method is efficient and robust.

1. Introduction

In this paper, we consider the following multiobjective optimization problem:

$$\begin{aligned} (\text{MOP}) \quad & \text{Minimize} \quad \mathbf{F}(x) \\ & \text{Subject to} \quad x \in X, \end{aligned} \tag{1}$$

where $\mathbf{F}(x) = (f_1(x), f_2(x), \ldots, f_p(x))^T$ is a multiobjective function (vector valued function), $X = \{x \in \mathbb{R}^n : l_b \leq x \leq u_b\} \subset \mathbb{R}^n$ is a box set, and l_b and u_b are lower bound and upper bound, respectively. We assume that each function in $\mathbf{F}(x)$ is Lipschitz continuous but not necessarily differentiable.

The multiobjective optimization has extensive applications in engineering and management [1–3]. Most of the optimization problems appearing in the real-world application have multiple objectives; they can be modeled as multiobjective optimization problems. However, due to the theoretical and computational challenges, it is not easy to numerically solve multiobjective optimization problems. Therefore, the multiobjective optimization attracted lots of researches over the last decades [4–8].

So far, there are two types of methods to solve multiobjective optimization problems: the indirect method and direct method. The indirect method converts multiple objectives into a single one. One strategy is to combine the multiple objective functions using the utility theory [9] or the weighted sum method [10, 11]. The difficulty for such method is the selection of the utility function or proper weights so as to satisfy the decision-maker's preference. Another indirect method is to formulate the multiple objectives, except one, as constraints. However, it is not easy to determine the upper bounds of these objectives. On the one hand, small

upper bounds could exclude some Pareto solutions; on the other hand, large upper bounds could enlarge the objective function value space which leads to some sub-Pareto solutions. Additionally, the indirect method can only obtain a single Pareto solution in each run. However, in practical applications, decision-makers often prefer a number of Pareto solutions so that they can choose one strategy according to their preferences.

Direct methods are devoted to exploring the entire set of Pareto solutions or a representative subset. However, it is extremely hard or impossible to obtain the entire set of Pareto solutions for most multiobjective optimization problems, except for some simple cases. Therefore, stepping back to a representative subset is preferred. Genetic algorithm, as a population-based algorithm, is a good choice to achieve this goal. The generic single-objective genetic algorithm can be modified to find a set of nondominated solutions in a single run [12–14]. The ability of the genetic algorithm to simultaneously search different regions of a solution space makes it possible to find a diverse set of solutions for difficult problems. The crossover and mutation operators of the genetic algorithm can be applied to various domains defined by different objectives, which in return creates new nondominated solutions in unexplored parts of the Pareto front. In addition, multiobjective genetic algorithm does not require the user to prioritize, scale, or weight objectives. Therefore, the genetic algorithm is one of the most popular metaheuristic approaches for solving multiobjective optimization problems [15–17].

The first multiobjective optimization method based on the genetic algorithm, called the vector evaluated genetic algorithm (VEGA), was proposed by Schaffer [18]. Afterwards, several multiobjective evolutionary algorithms were developed, such as multiobjective genetic algorithm (MOGA) [19], niched Pareto genetic algorithm (NPGA) [20], weight-based genetic algorithm (WBGA) [21], random weighted genetic algorithm (RWGA) [22], nondominated sorting genetic algorithm (NSGA) [23], strength Pareto evolutionary algorithm (SPEA) [24], improved SPEA (SPEA2) [25], Pareto-archived evolution strategy (PAES) [26], Pareto envelope-based selection algorithm (PESA) [27].

There are two basic criteria to measure a set of solutions for the multiobjective optimization problem [28].

(1) *Elitism*. The obtained solutions should be as close to the real Pareto solutions as possible. This can be measured by the closeness between the real Pareto frontier and the image of the obtained solutions since the image set of the real Pareto solutions is the real Pareto frontier.

(2) *Diversity*. In order to extensively describe Pareto solutions, the obtained solutions should distribute uniformly over the set of real Pareto solutions. The diversity of the obtained solutions is measured by the diversity of their images.

These two criteria of Pareto solutions are often in conflict with each other. Therefore, one has to balance the trade-off between elitism and diversity. The aim of this paper is to introduce new techniques to tackle these issues. The rest of the paper is organized as follows. In Section 2, we review some basic definitions of multiobjective optimization and the process of genetic algorithm. In Section 3, we propose an improved genetic algorithm for solving multiobjective optimization problems. In Section 4, some numerical experiments are carried out and the results are analyzed. Section 5 concludes the paper.

2. Preliminaries

In this section, we first review some definitions and theorems in the multiobjective optimization and then introduce the general procedure of genetic algorithm.

2.1. Definitions in Multiobjective Optimization. First of all, we present the following notations which are often used in vector optimization. Given two vectors

$$x = (x_1, x_2, \ldots, x_n)^T, \qquad y = (y_1, y_2, \ldots, y_n)^T \in \mathbb{R}^n, \quad (2)$$

then

(i) $x = y \Leftrightarrow x_i = y_i$ for all $i = 1, 2, \ldots, n$;

(ii) $x < y \Leftrightarrow x_i < y_i$ for all $i = 1, 2, \ldots, n$;

(iii) $x \leq y \Leftrightarrow x_i \leq y_i$ for all $i = 1, 2, \ldots, n$, and there is at least one $i \in \{1, 2, \ldots, n\}$ such that $x_i < y_i$; that is, $x \neq y$;

(iv) $x \leqq y \Leftrightarrow x_i \leq y_i$ for all $i = 1, 2, \ldots, n$.

"$>$," "$\geq$," and "$\geqq$" can be defined similarly. In this paper, we call $x \leq y$ by x dominates y or y is dominated by x (in some literatures, $x \geq y$ is called x dominates y or y is dominated by y; we reverse this definition since we are solving minimization problem in this paper).

Definition 1. Suppose that $x \subseteq \mathbb{R}^n$ and $x^* \in X$. If $x^* \leqq x$ for any $x \in X$, then x^* is called an absolute optimal point of X.

Absolute optimal point is an ideal point, but it may not exist.

Definition 2. Let $x \in \mathbb{R}^n$ and $x^* \in X$. If there is no $x \in X$ such that

$$x \leq x^* \quad (\text{or } x < x^*), \quad (3)$$

then x^* is called an *efficient point* (or *weakly efficient point*).

The sets of absolute optimal points, efficient points, and weakly efficient points of X are denoted as X_{ab}, X_{ep}, and X_{wp}, respectively. For the problem MOP, $X \subseteq \mathbb{R}^n$ is called the *decision variable space* and its image set $\mathbf{F}(X) = \{y \in \mathbb{R}^p \mid y = \mathbf{F}(x), x \in X\} \subset \mathbb{R}^p$ is called the *objective function value space*.

Definition 3. Suppose that $x^* \in X$. If

$$\mathbf{F}(x^*) \leqq \mathbf{F}(x), \quad (4)$$

for any $x \in X$, x^* is called an *absolute optimal solution* of the problem MOP. The set of absolute optimal solutions is denoted as S_{as}.

The concept of the absolute optimal solution is a direct extension of that for single-objective optimization. It is the ideal solution but may not exist for most cases.

Definition 4. Suppose that $x^* \in X$. If there is no $x \in X$ such that

$$\mathbf{F}(x) \leq \mathbf{F}(x^*) \quad (\text{or } \mathbf{F}(x) < \mathbf{F}(x^*)); \tag{5}$$

that is, $\mathbf{F}(x^*)$ is an efficient point (or weakly efficient point) of the objective function value space $\mathbf{F}(X)$, then x^* is called an *efficient solution* (or *weakly efficient solution*) of the problem MOP. The sets of efficient solutions and weakly efficient solutions are denoted as S_{es} and S_{ws}, respectively.

Another name of the efficient solution is *Pareto solution*, which was introduced by Koopmans and Reiter in 1951 [29]. The meaning of the Pareto solution is that if $x^* \in S_{\text{es}}$, then there is no feasible solution $x \in X$, such that any $f_i(x)$ of $\mathbf{F}(x)$ is not worse than that of $\mathbf{F}(x^*)$. In other words, x^* is the best solution in the sense of "$\leq$." Another intuitive interpretation of Pareto solution is that it cannot be improved with respect to any objective without worsening at least one of the other objectives. The set of Pareto solutions is denoted by $\mathscr{P}^*$. Its image set $\mathbf{F}(\mathscr{P}^*)$ is called the *Pareto frontier*, denoted by $\mathscr{PF}^*$. The following two theorems are well known.

Theorem 5 (see [6]). *For the multiobjective optimization, it holds that*

$$S_{as} \subset S_{es}(\mathscr{P}^*) \subset S_{ws} \subset X. \tag{6}$$

Theorem 6 (see [6]). *For the objective function value space* $\mathbf{F}(X)$*, if the sets of efficient points and weakly efficient points (i.e.,* F_{es} *and* F_{ws}*, resp.) are known, then, in the feasible set* X*, it holds that*

$$\begin{aligned} S_{es} &= \bigcup_{\overline{\mathbf{F}} \in F_{es}} \left\{ x \in X \mid \mathbf{F}(x) = \overline{\mathbf{F}} \right\}, \\ S_{ws} &= \bigcup_{\overline{\mathbf{F}} \in F_{ws}} \left\{ x \in X \mid \mathbf{F}(x) = \overline{\mathbf{F}} \right\}. \end{aligned} \tag{7}$$

Theorem 5 illustrates the relationship of the sets of absolute optimal solutions, efficient solutions, and weakly efficient solutions. Theorem 6 reveals that the preimage of efficient points (or weakly efficient points) in $F(X)$ is efficient solutions (or weakly efficient solutions) of the problem MOP.

2.2. Genetic Algorithm. Genetic algorithm is one of the most important evolutionary algorithms. It was introduced by Holland in the 1960s and then developed by his students and colleagues at the University of Michigan between the 1960s and 1970s [30]. Over the last two decades, the genetic algorithm was increasingly enriched by plenty of literatures, such as [31–34]. Nowadays various genetic algorithms are applied in different areas, for example, mathematical programming, combinational optimization, automatic control, and image processing.

Suppose that $P(t)$ and $O(t)$ represent parents and offspring at the tth generation, respectively. Then, the general structure of genetic algorithm can be described in the following pseudocode.

General Structure of Genetic Algorithm

(1) Initialization

  (1.1) Generate the initial population $P(0)$.
  (1.2) Set crossover rate, mutation rate, and maximal generation time.
  (1.3) Let $t \leftarrow 0$.

(2) Since the maximal generation time is not reached, do the following.

  (2.1) Crossover operator: generate $O_1(t)$.
  (2.2) Mutation operator: generate $O_2(t)$.
  (2.3) Evaluate $O_1(t)$ and $O_2(t)$: compute the fitness function.
  (2.4) Select operator: build the next population.
  (2.5) $t \leftarrow t + 1$, go to (2.1).
  End

End.

From the pseudocode, we can see that there are three important operators in a general genetic algorithm: the crossover, mutation, and selection operators. The implementation of these operators is highly dependent on the way of encoding.

3. A New Multiobjective Genetic Algorithm

In this section, we present a new multiobjective genetic algorithm for solving the problem MOP. We first propose a ranking strategy called the optimum order method and then metrics for the elitism and diversity of solutions. Finally, a new selection operator for genetic algorithm is designed using the optimum order method and the elitism and diversity metrics.

Theoretically, the terminology "solution" means the point in the decision variable space, while the corresponding point in the objective function value space is named as "image of solution." However, most of the following discussions are in the objective function value space. In order to simplify the description, we indiscriminately call the point from the decision variable space and its corresponding image from the objective function value space as the "solution," if there is no confusion to do so.

3.1. The Optimum Order Method. In numerical optimization, in order to compare the numerical performance of different solutions, it is necessary to assign a fitness value for each solution. For the single-valued function, fitness is normally assigned as its function value. However, to assign the fitness of a multiobjective function is not straightforward. So far, there are three typical approaches. The first one is weighted sum approach [22, 35], which converts the multiple objectives into a single one using normalized weight $\sum_{i=1}^{p} \lambda_i = 1$,

$\lambda_i > 0, i = 1, 2, \ldots, p$. The decision of weight parameters is not an easy task for this approach. The second one is to alter the objective functions [18, 25], which randomly divides the current population into p equal subpopulations: $P_1, P_2, \ldots, P_p$. Then, each solution in the subpopulation P_i is assigned a fitness value based on the objective function f_i. In fact, this approach is a straightforward extension of the single-objective genetic algorithm. The last one is Pareto-ranking approach [4, 23, 36], which is a direct application of the definition of Pareto solution. In the following, we present a rank strategy called the optimum order method [6].

Definition 7. Let $P = \{1, 2, \ldots, p\}$ and $N = \{1, 2, \ldots, n\}$; for any $x^i, x^j \in X$, define

$$a_{ijl} = \begin{cases} 1, & \text{if } f_l\left(x^i\right) < f_l\left(x^j\right); \\ 0.5, & \text{if } f_l\left(x^i\right) = f_l\left(x^j\right); \\ 0, & \text{if } f_l\left(x^i\right) > f_l\left(x^j\right) \text{ or } i = j. \end{cases} \tag{8}$$

Then,

$$a_{ij} = \sum_{l \in P} a_{ijl} \quad i, j \in N \tag{9}$$

is called the *optimal number* of x^i corresponding to x^j for all objectives. Furthermore, $K_i = \sum_{j \in N} a_{ij}$ is defined as *the total optimal number* of x^i corresponding to all the other solutions for all objectives.

Obviously, for a minimization problem, a larger optimal number corresponds to a better solution. Therefore, optimal numbers can be considered as criteria for ranking a set of solutions. Due to this observation, we propose the following algorithm to rank a population of solutions.

Algorithm 8 (optimum order method (OOM)). Consider the following steps.

Step 1 (input). It includes the population of solutions and their objective function values.

Step 2 (compute optimal numbers). Compute the optimal number and total optimal number of each solution; fill these numbers into Table 1 according to (8).

Step 3 (rank the solution). Rearrange the order of solutions according to the decreasing order of the total optimal numbers K_i. More precisely, denote

$$\begin{aligned} K_{\alpha_1} &= \max_{i \in N} \{K_i\}, \\ K_{\alpha_2} &= \max_{i \in N \setminus \{\alpha_1\}} \{K_i\}, \end{aligned} \tag{10}$$

and so on.

The solutions x^{α_1} and x^{α_2}, which are corresponding to K_{α_1}, K_{α_2}, and so forth, are called *the best solution*, *the second best solution*, and so forth. The new order is called the *optimal order*. It is worth mentioning that the optimum order method does not necessarily rank Pareto solutions in the frontier positions; however, those solutions who are more reasonable with respect to all objectives are more likely to be ranked in the foremost positions. This property is different from Pareto-ranking approach.

Table 1: Table of optimal numbers.

x^i	x^j						
	x^1	x^2	$\cdots$	x^j	$\cdots$	x^n	K_i
x^1	0	a_{12}	$\cdots$	a_{1j}	$\cdots$	a_{1n}	K_1
x^2	a_{21}	0	$\cdots$	a_{2j}	$\cdots$	a_{2n}	K_2
$\vdots$	$\vdots$	$\vdots$		$\vdots$		$\vdots$	$\vdots$
x^i	a_{i1}	a_{i2}	$\cdots$	a_{ij}	$\cdots$	a_{in}	K_i
$\vdots$	$\vdots$	$\vdots$		$\vdots$		$\vdots$	$\vdots$
x^n	a_{n1}	a_{n2}	$\cdots$	a_{nj}	$\cdots$	0	K_n

Lemma 9. *Suppose that $x^i, x^j \in X$. If $\mathbf{F}(x^i) \leq \mathbf{F}(x^j)$, then $a_{ij} > a_{ji}$.*

Proof. Let

$$\begin{aligned} A &= \left\{l \in P \mid f_l\left(x^i\right) < f_l\left(x^j\right)\right\}, \quad a = |A|; \\ B &= \left\{l \in P \mid f_l\left(x^i\right) = f_l\left(x^j\right)\right\}, \quad b = |B|, \end{aligned} \tag{11}$$

where $|\cdot|$ denotes the number of components in a set. Obviously, we have $a > 0, b > 0$ and $a + b = p$. Then,

$$\begin{aligned} a_{ijl} &= \begin{cases} 1, & l \in A, \\ 0.5, & l \in B, \end{cases} \\ a_{jil} &= \begin{cases} 0, & l \in A, \\ 0.5, & l \in B. \end{cases} \end{aligned} \tag{12}$$

Therefore,

$$\begin{aligned} a_{ij} &= \sum_{l \in A} a_{ijl} + \sum_{l \in B} a_{ijl} = a + 0.5b, \\ a_{ji} &= \sum_{l \in A} a_{jil} + \sum_{l \in B} a_{jil} = 0.5b. \end{aligned} \tag{13}$$

Since $a > 0$, $a_{ij} > a_{ji}$. □

Lemma 10. *Suppose that $x^i, x^j \in X$. If $\mathbf{F}(x^i) \leq \mathbf{F}(x^j)$, then, for any x^k $(k \neq i, j,\ k \in N)$, $a_{ik} > a_{jk}$.*

Proof. For any x^k $(k \neq i, j,\ k \in N)$, let

$$\begin{aligned} A &= \left\{l \in P \mid f_l\left(x^k\right) < f_l\left(x^i\right)\right\}, \quad a = |A|; \\ B &= \left\{l \in P \mid f_l\left(x^k\right) > f_l\left(x^i\right)\right\}, \quad b = |B|; \\ C &= \left\{l \in P \mid f_l\left(x^k\right) = f_l\left(x^i\right)\right\}, \quad c = |C|. \end{aligned} \tag{14}$$

Then, we have $a, b, c \geq 0$ and $a + b + c = p$.

(i) When $l \in A$. Since $\mathbf{F}(x^i) \le \mathbf{F}(x^j)$, we have

$$f_l\left(x^k\right) < f_l\left(x^i\right), \quad f_l\left(x^k\right) < f_l\left(x^j\right). \tag{15}$$

Therefore,

$$a_{ik}^1 = \sum_{l\in A} a_{ikl} = 0 \cdot a = 0, \quad a_{jk}^1 = \sum_{l\in A} a_{jkl} = 0 \cdot a = 0. \tag{16}$$

(ii) When $l \in B$. We have $f_l(x^k) > f_l(x^i)$. Thus,

$$a_{ik}^2 = \sum_{l\in B} a_{ikl} = 1 \cdot b = b. \tag{17}$$

On the other hand, let

$$\begin{aligned} M_1 &= \left\{l \in B \mid f_l\left(x^k\right) < f_l\left(x^j\right)\right\}, \quad m_1 = |M_1|; \\ M_2 &= \left\{l \in B \mid f_l\left(x^k\right) = f_l\left(x^j\right)\right\}, \quad m_2 = |M_2|; \\ M_3 &= \left\{l \in B \mid f_l\left(x^k\right) > f_l\left(x^j\right)\right\}, \quad m_3 = |M_3|. \end{aligned} \tag{18}$$

Obviously, $m_1, m_2, m_3 \ge 0$ and $m_1 + m_2 + m_3 = b$. Therefore,

$$a_{jk}^2 = m_1 \cdot 0 + m_2 \cdot 0.5 + m_3 \cdot 1 \le b. \tag{19}$$

(iii) When $l \in C$. We have

$$a_{ik}^3 = \sum_{l\in C} a_{ikl} = 0.5 \cdot c. \tag{20}$$

On the other hand, let

$$\begin{aligned} M_1 &= \left\{l \in C \mid f_l\left(x^k\right) < f_l\left(x^j\right)\right\}, \quad m_1 = |M_1|; \\ M_2 &= \left\{l \in C \mid f_l\left(x^k\right) = f_l\left(x^j\right)\right\}, \quad m_2 = |M_2|. \end{aligned} \tag{21}$$

Note that it is not possible to have $f_l(x^k) > f_l(x^j)$. Otherwise, we will have $f_l(x^i) > f_l(x^j)$, which is contrary to $\mathbf{F}(x^i) \le \mathbf{F}(x^j)$. Again, we have $m_1, m_2 \ge 0$ and $m_1 + m_2 = c$. Thus,

$$a_{jk}^3 = \sum_{l\in C} a_{jkl} = m_1 \cdot 0 + m_2 \cdot 0.5 \le 0.5c. \tag{22}$$

In light of (16)–(22), we have

$$a_{ik} = \sum_{\alpha=1}^{3} \alpha_{ik}^{\alpha} \ge a_{jk} = \sum_{\alpha=1}^{3} a_{jk}^{\alpha}. \tag{23}$$

□

Theorem 11. *If $K_e = \max_{i\in N}\{K_i\}$, then the solution x^e corresponding to K_e must be an efficient solution (Pareto solution).*

Proof. If x^e is not an efficient solution, then there exists an $x^s \in X$, such that

$$\mathbf{F}\left(x^s\right) \le \mathbf{F}\left(x^e\right). \tag{24}$$

Therefore, according to Lemma 9,

$$a_{es} < a_{se}. \tag{25}$$

Due to Lemma 10, we have, for any x^j $(j \in N, j \ne e, s)$,

$$a_{ej} \le a_{sj}. \tag{26}$$

Based on (25), (26) and $a_{ee} = a_{ss} = 0$, we have

$$K_e = \sum_{j\in N} a_{ej} < \sum_{j\in N} a_{sj} = K_s, \tag{27}$$

which is a contradiction to the assumption $k_e = \max_{i\in N}\{K_i\}$. The proof is completed. □

Based on Theorem 11, the following results are obvious.

Corollary 12. *If x^a is an absolute optimal solution, then*

$$K_a = \max_{j\in N}\left\{K_j\right\}. \tag{28}$$

Corollary 13. *If x^e is corresponding to $K_e = \max_{j\in N}\{K_j\}$ and x^s is corresponding to $K_s = \max_{j\in N\setminus\{e\}}\{K_j\}$, then x^s is an efficient solution of the population without x^e.*

Theorem 11 and Corollary 13 reveal the rationality of the optimum order method because the best solution must be an efficient solution, and the second best solution, although may not be an efficient solution, is an efficient solution without the best one. This statement is true until the solution with the smallest total optimal number (ranked as the last reasonable solution). Therefore, It is reasonable for us to choose solutions with large total optimal numbers as parents for the next generation.

3.2. The Elitism Metric. Over the last two decades, a number of different evolutionary algorithms were suggested to solve multiobjective optimization problems, such as MOGA [37], NSGA [23], NPGA [20], SPEA [24], PAES [38], and NSGA-II [4]. Among them, MOGA, NSGA, and NPGA did not introduce any elitism strategy at all. Therefore, although they were successful in finding solutions for many test problems and a number of engineering problems, researchers realized that they are still needed to be improved in the sense of obtaining better Pareto solutions [28]. Elitism is one of the main issues considered to be improved. After that, SPEA, PAES, and NSGA-II started to take into account the elitism of solutions.

SPEA introduces an external population which stores all nondominated solutions discovered so far beginning from the initial population. At each generation, a combined population based on the external population and the current population is generated firstly. Then, all the nondominated solutions in the combined population are identified and

assigned a fitness based on the number of solutions they dominate. Furthermore, the dominated solutions are assigned a fitness which is worse than the worst fitness of the nondominated solution. Then, the next generation is selected based on the fitness of each solution. This elitism strategy makes sure that the search is directed toward the nondominated solutions. Although the computational complexity of SPEA is $O(MN^3)$ (where M is the number of objectives and N is the size of the population), with proper bookkeeping, the complexity can be reduced to $O(MN^2)$.

PAES uses a single-parent single-offspring evolutionary algorithm which is similar to (1 + 1)-evolution strategy. In PAES, the elitism strategy is implemented by comparing between one parent and one offspring. If the offspring dominates the parent, the offspring is accepted as the next parent; on the other hand, if the parent dominates the offspring, the offspring is replaced by another mutated solution (a new offspring) and the comparison between the parent and offspring is made again. However, if the parent and the offspring do not dominate each other, the choice between them is made by comparing them with an archive of the best solutions found so far. More specifically, if the offspring dominates any solution stored in the archive, then the offspring is accepted by the archive and all the dominated solutions are eliminated from the archive. On the contrary, if the offspring does not dominate any solution stored in the archive, then the parent and offspring are accepted by the archive after checking the diversity. The computational complexity of PAES is calculated as $O(aMN)$, where a is the length of the archive. Since the archive size is usually chosen proportional to the population size N, the overall complexity of PAES is $O(MN^2)$.

NSGA implements the elitism strategy using naive nondominated sorting approach. For a population of solutions, the naive nondominated sorting first identifies the nondominated solutions in the population and then the nondominated solutions without considering the solutions which have already been identified. This process is repeated until all the solutions in the population have been identified. In this way, the solutions are classified into different Pareto frontiers and selected based on their Pareto ranking. The native nondominated sorting approach is based on the definition of Pareto frontier. It is easy to be implemented, but in the worst case, the task of identifying all the Pareto frontier requires a computational complexity of $O(MN^3)$. In order to reduce the complexity of NSGA, NSGA-II improved the sorting approach and presented the fast nondominated sorting approach. NSGA-II introduced two entities, domination count (n_p) and dominated count (S_p). The domination count represents the number of solutions which dominates the solution p; the dominated count represents the number of solutions which are dominated by the solutions p.

All solution in the first nondominated front will have their domination count as zero. Now, for each solution p with $n_p = 0$, we visit each member (q) of its set S_p and reduce its domination count by one. In doing so, if for any member q the domination count becomes zero, we put it in a separate list Q. These members belong to the second nondominated front. Now, the above procedure is continued with each member of Q and the third front is identified. This process continues until all frontiers are identified. It is evident to observe that the naive nondominated sorting approach and the fast nondominated sorting approach lead to the same Pareto ranking for a population of solutions. The overall computational complexity of the fast nondominated sorting approach is $O(MN^2)$.

The previous elitism strategies use the definitions of domination or Pareto ranking, but they do not quantify the elitism of solutions. In this paper, we introduce a new elitism strategy which is still based on Pareto ranking but quantifies the elitism of solutions.

Definition 14. Suppose that P_1 is a population of solutions, we define the *elitism metric* of the nondominated solutions in P_1, say F_1, as 1; define the elitism metric of the nondominated solutions in $P_2 = P_1 \setminus F_1$, say F_2, as 2; and so forth; and define the elitism metric of the nondominated solutions in $P_i = P_{i-1} \setminus F_{i-1}$, say F_i as i.

Remark 15. The process in Definition 14 is the same as the native nondominated sorting approach. And the elitism metric of each solution is actually its index of Pareto ranking.

According to Definition 14, the elitism measure of solutions can be taken as a function of the solutions, the value of the function is the elitism metric of solutions. We call this function *the elitism function*. Mathematically,

$$\theta : P_1 \longrightarrow \mathbb{Z}^+, \quad \text{where } P_1 \subset \mathbb{R}^n \text{ is a population and } \mathbb{Z}^+ \text{ is the positive integer.} \tag{29}$$

It is obvious that a small value of $\theta(x)$ means that x enjoys a good Pareto ranking. Therefore, in order to find solutions with better Pareto ranking, we should minimize function $\theta(x)$. In the following, we present a method to calculate the value of function θ.

Suppose that $P_1 = \{x_1, x_2, \ldots, x_N\}$, we calculate the value of $\alpha(x_i, x_j)$ by

$$\alpha\left(x_i, x_j\right) = \begin{cases} 1, & \text{if } x_i \text{ dominates } x_j; \\ -1, & \text{if } x_i \text{ dominated by } x_j; \\ 0, & \text{if } x_i \text{ and } x_j \text{ are not dominated by each other.} \end{cases} \tag{30}$$

Then we construct the domination table (see Table 2).

Obviously, entries of Table 2 are just −1, 0, and 1. Now we successively check every row of the table, if any row, say the ith one, whose entries are only 0 or 1; then we can claim that there is no solution dominating x_i, which means that x_i's elitism metric is 1. Then discard the rows and columns

Table 2: The domination table of P_1.

	x_1	x_2	$\cdots$	x_{N-1}	x_N
x_1	—	$\alpha(x_1, x_2)$	$\cdots$	$\alpha(x_1, x_{N-1})$	$\alpha(x_1, x_N)$
x_2	$\alpha(x_2, x_1)$	—	$\cdots$	$\alpha(x_2, x_{N-1})$	$\alpha(x_2, x_N)$
$\vdots$	$\vdots$	$\vdots$	$\ddots$	$\vdots$	$\vdots$
x_{N-1}	$\alpha(x_{N-1}, x_1)$	$\alpha(x_{N-1}, x_2)$	$\cdots$	—	$\alpha(x_{N-1}, x_N)$
x_N	$\alpha(x_N, x_1)$	$\alpha(x_N, x_2)$	$\cdots$	$\alpha(x_N, x_{N-1})$	—

in which these solutions with elitism metric of 1 locate. This means that we do not consider these solutions any more in the following process since they have already been identified. This process is repeated again and the identified solutions are assigned with elitism metric of 2 and so forth until all the solutions are identified.

In Table 2, it is evident that $\alpha(x_i, x_j) = -\alpha(x_j, x_i)$, where $1 \le i \ne j \le N$. So the computational complexity of assigning elitism metrics for the population is $O((1/2)M(N-1)^2)$. We provide the following example to illustrate the process described above.

Figure 1 illustrated a population of solutions. There are 35 solutions in this population. The numbers on the side are indexes of these solutions. Table 2 is the domination table of this population. First, we successively check rows of Table 3; rows with only 0 and 1 are 1, 2, 5, 8, 9, 10, 16, 17, 19, 20, and 28. So solutions corresponding to these rows are in the first Pareto frontier and should be assigned elitism metric 1. Then, discard the corresponding rows and columns from the domination table and do the same search again. We assign the solutions corresponding to the identified rows with elitism metric 2. This process is repeated until all the rows of the domination table are discarded. We depict the elitism metric assignment in Figure 2.

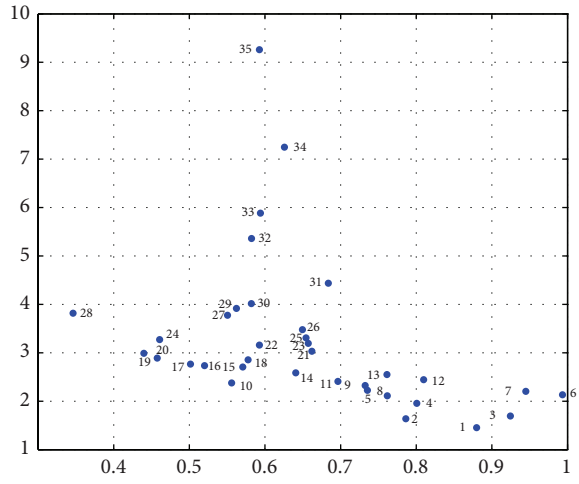

Figure 1: The population of solutions.

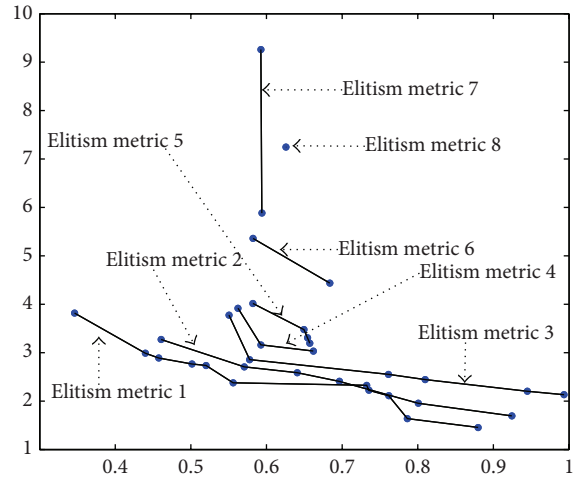

Figure 2: The elitism metric assignment for the population.

3.3. The Diversity Metric. As discussed before, diversity of solutions is another criterion for solutions obtained by the multiobjective genetic algorithm. In order to obtain uniformly distributed solutions, it is important to maintain the diversity of the population in the iteration process. Without this, solutions in the population tend to form relatively few clusters. This phenomenon is known as *genetic drift*. Several approaches have been developed to maintain the diversity of solutions. Among them, the sharing function approach [19, 39] is one of the earliest approaches. The sharing function approach degrades the objective fitness of solutions by setting a threshold θ_{share}. This threshold is still called *sharing parameter*. For a solution x_i in the current population, a *niche count* m_i is first calculated. The niche count $m_i = 1$ if there is no solution in the θ_{share}-niche (neighborhood) of x_i (i.e., there is no solution whose distance with x_i is less than θ_{share}); the niche count $m_i > 1$ if there are some solutions in the θ_{share}-niche (neighborhood) of x_i (i.e., there are some solutions whose distances with x_i) less than θ_{share}. Then, the degradation is obtained through dividing the objective fitness by the niche count, that is, f_i/m_i. This proportion is called the *shared fitness*. The original NSGA [23] used the sharing function approach to maintain the diversity of solutions. The performance of the sharing function approach terribly depends on the sharing parameter θ_{share}. However, θ_{share} is a user-decided parameter and it is difficult to choose a proper one. Since each solution must be compared with all other solutions in the population, the overall complexity of the sharing function approach is $O(MN^2)$.

Deb et al. [4] introduced the crowding distance approach to maintain the diversity of solutions. This approach calculates the density estimation of a solution by summarizing the average distance of two solutions on either side of this solution along each of the objective function. The density estimation, which is still called crowding distance, serves as an estimate of the perimeter of the cuboid formed by using the nearest neighbors as the vertices. Obviously, a solution with a smaller value of crowding distance is more crowded by other solutions. Thus, the crowding distance can be considered as a measure of the diversity of a solution. The crowding distance approach does not require any user-defined parameter.

Table 3: The domination table of P_1.

x	1	2	3	4	5	6	7	8	9	10	11	12	13	14	15	16	17	18	19	20	21	22	23	24	25	26	27	28	29	30	31	32	33	34	35
1	—	0	1	0	0	1	1	0	0	0	0	0	0	0	0	0	0	0	0	0	0	0	0	0	0	0	0	0	0	0	0	0	0	0	0
2	0	—	1	1	0	1	1	0	0	0	0	1	0	0	0	0	0	0	0	0	0	0	0	0	0	0	0	0	0	0	0	0	0	0	0
3	−1	−1	—	0	0	1	1	0	0	0	0	0	0	0	0	0	0	0	0	0	0	0	0	0	0	0	0	0	0	0	0	0	0	0	0
4	0	−1	0	—	0	1	1	0	0	0	0	1	0	0	0	0	0	0	0	0	0	0	0	0	0	0	0	0	0	0	0	0	0	0	0
5	0	0	0	0	—	1	1	0	0	0	0	1	0	0	0	0	0	0	0	0	0	0	0	0	0	0	0	0	0	0	0	0	0	0	0
6	−1	−1	−1	−1	−1	—	0	0	0	0	0	0	0	0	0	0	0	0	0	0	0	0	0	0	0	0	0	0	0	0	0	0	0	0	0
7	−1	−1	−1	−1	−1	0	—	0	0	0	0	0	0	0	0	0	0	0	0	0	0	0	0	0	0	0	0	0	0	0	0	0	0	0	0
8	0	0	0	0	0	0	0	—	0	0	0	1	1	0	0	0	0	0	0	0	0	0	0	0	0	0	0	0	0	0	0	0	0	0	0
9	0	0	0	0	0	0	0	0	—	0	0	1	1	0	0	0	0	0	0	0	0	0	0	0	0	0	0	0	0	0	0	0	0	0	0
10	0	0	0	0	0	0	0	0	0	—	1	1	1	1	1	0	0	1	0	0	1	1	1	0	1	1	0	0	1	1	1	1	1	1	1
11	0	0	0	0	0	0	0	0	0	−1	—	1	1	0	0	0	0	0	0	0	0	0	0	0	0	0	0	0	0	0	0	0	0	0	0
12	0	−1	0	−1	−1	0	0	−1	−1	−1	−1	—	0	0	0	0	0	0	0	0	0	0	0	0	0	0	0	0	0	0	0	0	0	0	0
13	0	0	0	0	0	0	0	−1	−1	−1	−1	0	—	0	0	0	0	0	0	0	0	0	0	0	0	0	0	0	0	0	0	0	0	0	0
14	0	0	0	0	0	0	0	0	0	−1	0	0	0	—	0	0	0	0	0	0	1	0	1	0	1	1	0	0	0	0	1	0	0	0	0
15	0	0	0	0	0	0	0	0	0	−1	0	0	0	0	—	0	0	1	0	0	1	1	1	0	1	1	0	0	0	1	1	1	1	1	1
16	0	0	0	0	0	0	0	0	0	0	0	0	0	0	0	—	0	1	0	0	1	1	1	0	1	1	1	0	1	1	1	1	1	1	1
17	0	0	0	0	0	0	0	0	0	0	0	0	0	0	0	0	—	1	0	0	1	1	1	0	1	1	1	0	1	1	1	1	1	1	1
18	0	0	0	0	0	0	0	0	0	−1	0	0	0	0	−1	1	−1	—	0	0	1	1	1	0	1	1	0	0	0	1	1	1	1	1	1
19	0	0	0	0	0	0	0	0	0	0	0	0	0	0	0	0	0	0	—	0	1	1	1	1	1	1	1	0	1	1	1	1	1	1	1
20	0	0	0	0	0	0	0	0	0	0	0	0	0	0	0	0	0	0	0	—	1	1	1	1	1	1	1	0	1	1	1	1	1	1	1
21	0	0	0	0	0	0	0	0	0	−1	0	0	0	−1	−1	1	−1	−1	−1	−1	—	0	0	0	0	0	0	0	0	0	1	0	0	0	0
22	0	0	0	0	0	0	0	0	0	−1	0	0	0	0	−1	1	−1	−1	−1	−1	0	—	1	0	1	1	0	0	0	0	1	0	1	1	1
23	0	0	0	0	0	0	0	0	0	−1	0	0	0	−1	−1	1	−1	−1	−1	−1	0	−1	—	0	0	0	0	0	0	0	1	0	0	0	0
24	0	0	0	0	0	0	0	0	0	0	0	0	0	0	0	0	0	0	−1	−1	0	0	0	—	1	1	1	0	1	1	1	1	1	1	1
25	0	0	0	0	0	0	0	0	0	−1	0	0	0	−1	−1	1	−1	−1	−1	−1	0	−1	0	−1	—	0	0	0	0	0	1	0	0	0	0
26	0	0	0	0	0	0	0	0	0	−1	0	0	0	−1	−1	1	−1	−1	−1	−1	0	−1	0	−1	0	—	0	0	0	0	1	0	0	0	0
27	0	0	0	0	0	0	0	0	0	0	0	0	0	0	0	1	−1	0	−1	−1	0	0	0	−1	0	0	—	0	1	1	1	1	1	1	1
28	0	0	0	0	0	0	0	0	0	0	0	0	0	0	0	0	0	0	0	0	0	0	0	0	0	0	0	—	1	1	1	1	1	1	1
29	0	0	0	0	0	0	0	0	0	−1	0	0	0	0	0	1	−1	0	−1	−1	0	0	0	−1	0	0	−1	−1	—	1	1	1	1	1	1
30	0	0	0	0	0	0	0	0	0	−1	0	0	0	0	−1	1	−1	−1	−1	−1	0	0	0	−1	0	0	−1	−1	−1	—	1	1	1	1	1
31	0	0	0	0	0	0	0	0	0	−1	0	0	0	−1	−1	1	−1	−1	−1	−1	−1	−1	−1	−1	−1	−1	−1	−1	−1	−1	—	0	0	0	0
32	0	0	0	0	0	0	0	0	0	−1	0	0	0	0	−1	1	−1	−1	−1	−1	0	0	0	−1	0	0	−1	−1	−1	−1	0	—	1	1	1
33	0	0	0	0	0	0	0	0	0	−1	0	0	0	0	−1	1	−1	−1	−1	−1	0	−1	0	−1	0	0	−1	−1	−1	−1	0	−1	—	1	0
34	0	0	0	0	0	0	0	0	0	−1	0	0	0	0	−1	1	−1	−1	−1	−1	0	−1	0	−1	0	0	−1	−1	−1	−1	0	−1	−1	—	0
35	0	0	0	0	0	0	0	0	0	−1	0	0	0	0	−1	1	−1	−1	−1	−1	0	−1	0	−1	0	0	−1	−1	−1	−1	0	−1	0	0	—

Its computational complexity is $O(MN \log N)$, which is better than the sharing function approach. However, the crowing distance just reflects the local diversity of a solution.

The cell-based density approach [6, 26, 38, 40, 41] divides the objective space into p-dimensional cells. The number of solutions in each cell is defined as the *density of the cell*, and the *density of a solution* is equal to the density of the cell in which the solution locates. An efficient approach to dynamically divide the objective function space into cells is proposed by Lu and Yen [40, 41]. The main advantage of the cell-based density approach is that a global density map of the objective function value space can be obtained. But the process of the cell-based density approach is complicated. For a single solution, in the worst case, it requires $O(LM)$ comparison to locate the solution into a proper cell, where L is the number of cells for each objective function. Thus, the total complexity of the cell-based density approach is $O(LMN)$. And furthermore, L is a user-defined parameter which is not easy to be chosen properly.

In this section, we define the metric about measuring the degree of crowdedness around a solution. Then, a specifical diversity metric is introduced.

Definition 16. Suppose that P_1 is a population, x_i and x_j are two solutions from P_1, and ϕ_i and ϕ_j are two scalars corresponding to x_i and x_j, respectively. We call ϕ_i and ϕ_j the *diversity metrics* of x_i and x_j, respectively, if $\phi_i < \phi_j$ implies that solutions around x_j are more crowded than those around x_i.

Definition 16 is just a qualitative description of the diversity metric. In the following, we introduce a specifical

definition of the diversity metric which quantitatively measures the degree of crowdedness around a solution.

Definition 17. Suppose that P_1 is a population with N solutions, x_i is a solution in P_1. We provide a function $\phi : P_1 \mapsto \mathbb{R}^+$ as

$$\phi(x_i) = \sum_{j=1, j\neq i}^{N} \beta\left(d_{ij}\right), \tag{31}$$

where $\beta : \mathbb{R}^+ \mapsto \mathbb{R}^+$ is a decrease function and d_{ij} is the Euclidean distance between solutions x_i and x_j. Then we call the value of $\phi(x_i)$ the *global diversity metric* of x_i.

It is obvious that the global diversity metric is coincident with the definition of diversity metric. One improvement of the global diversity metric is that it reflects the diversity of x_i with respect to all the other solutions since the function ϕ involves the whole population. The requirement for calculating the global diversity metric is only the Euclidean distance between any two solutions, so the computational complexity of the global diversity metric is $O((1/2)(N-1)^2)$. A proper choice of function β is

$$\beta(d) = 1 - \frac{1}{D}d, \tag{32}$$

where $D = \max_{1\leq i,j\leq N}\{d_{ij}\}$.

As an example, Figure 3 illustrates the global diversity metric of the population presented in Figure 1. From Figure 3, one can observe that these solutions which are less crowded enjoy smaller global diversity metrics, such as solutions x_{35} and x_{34} (the index of the solution can be found in Figure 1) with 7.1157 and 15.6234, respectively. On the contrary, these solutions which are more crowded have larger global diversity metrics, such as solutions x_{15}, x_{17}, and x_{21} with 19.3926, 29.3777, and 29.3826, respectively.

3.4. A New Selection Operator. As discussed before, the core criteria for multiobjective optimization are to obtain solutions with better elitism and, at the same time, maintain the diversity of solutions. If we tackle these criteria from a multiobjective optimization point of view, we need to solve a multiobjective optimization problem with two objectives: minimizing the elitism metric and the global diversity metric of the solution. Noting the definition of the elitism metric $\theta(x)$ and the global diversity metric $\phi(x)$ presented in the previous subsections, we design the following multiobjective subproblem:

$$\begin{aligned} &\text{Minimize} \quad \mathbf{H}(x) \\ &\text{Subject to} \quad x \in P_1, \end{aligned} \tag{33}$$

where $\mathbf{H}(x) = (\theta(x), \phi(x))^T$ is a multiobjective function and $P_1 \subset X$ is a population of candidate solutions. It is clear that the image of $\mathbf{H}(\cdot)$

$$H = \left\{(\theta(x), \phi(x))^T \mid x \in P_1\right\} \tag{34}$$

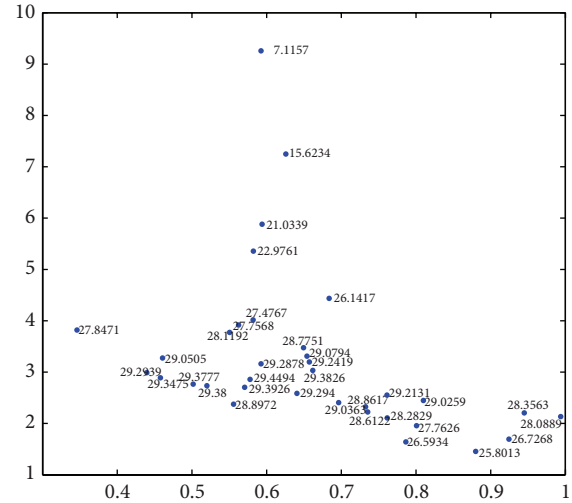

Figure 3: The global diversity metric for the population.

is a finite set whose cardinal is the same as P_1. One property of the multiobjective subproblem (33) is that its domain P_1 and image set H are finite; that is, the problem (33) is discrete. Thus, if we rank points in H by the optimum order method (Algorithm 8), it is reasonable to say that those points who have smaller optimal orders are better points; that is, solutions corresponding to these points should be maintained to the next generation. This process is summarized by the following algorithm.

Algorithm 18 (multiobjective selection operator). Consider the following steps.

Step 1. Input the selection pool P_1 and its objective function values $F(P_1) = \{\mathbf{F}(x) \mid x \in P_1\}$. Input the prefixed population size N (N is less than the cardinal of P_1).

Step 2. Calculate the elitism metric and global diversity metric of the solution in P_1 using the function (29) and (31), respectively. Let the result be

$$\begin{aligned} \Theta &= \{\theta(x) \mid x \in P_1\}, \\ \Phi &= \{\phi(x) \mid x \in P_1\}. \end{aligned} \tag{35}$$

Step 3. Construct the objective function value space of the multiobjective subproblem

$$H = \left\{(\theta_x, \phi_x)^T \mid \theta_x \in \Theta,\ \phi_x \in \Phi\right\}. \tag{36}$$

Step 4. Rank points in H by the optimum order method (Algorithm 8) and take the first N solutions according to their optimal orders as parents for the next generation.

In Table 4, we use the multiobjective selection operator to evaluate the population presented in Figure 1. In this table, θ_i, ϕ_i, K_i, and σ_i represent the elitism metric, global diversity metric, total optimal number, and optimal order of solution

Table 4: The total optimal number and optimal order without pretreatment of the diversity metric.

x_i	θ_i	ϕ_i	K_i	σ_i
x_1	1	25.8013	59.0	1
x_2	1	26.5934	57.0	2
x_3	2	26.7268	47.5	5
x_4	2	27.7626	44.5	8
x_5	1	28.2829	49.0	4
x_6	3	28.0889	36.5	10
x_7	3	28.3563	33.5	17
x_8	1	28.6122	47.0	6
x_9	1	28.8617	45.0	7
x_{10}	1	28.8972	44.0	9
x_{11}	2	29.0363	33.5	18
x_{12}	3	29.0259	28.5	26
x_{13}	3	29.2131	24.5	28
x_{14}	2	29.2940	26.5	27
x_{15}	2	29.3926	21.5	30
x_{16}	1	29.3800	32.0	25
x_{17}	1	29.3777	33.0	20
x_{18}	3	29.4494	14.5	34
x_{19}	1	29.3475	34.0	16
x_{20}	1	29.2939	36.0	11
x_{21}	4	29.3826	12.0	35
x_{22}	4	29.2878	18.0	31
x_{23}	5	29.2419	15.5	33
x_{24}	2	29.0505	32.5	22
x_{25}	5	29.0794	17.5	32
x_{26}	5	28.7751	23.5	29
x_{27}	3	28.1192	35.5	12
x_{28}	1	27.8471	52.0	3
x_{29}	4	27.7568	35.0	14
x_{30}	5	27.4767	32.5	23
x_{31}	6	26.1417	32.5	24
x_{32}	6	22.9761	34.5	15
x_{33}	7	21.0339	33.5	19
x_{34}	8	15.6234	33.0	21
x_{35}	7	7.1157	35.5	13

Table 5: The total optimal number and optimal order with pretreatment of the diversity metric.

x_i	θ_i	ϕ_i	K_i	σ_i
x_1	1	25.8013	59.0	1
x_2	1	26.5934	57.0	2
x_3	2	26.7268	47.5	4
x_4	2	27.7626	44.5	6
x_5	1	28.2829	49.0	5
x_6	3	28.0889	36.5	15
x_7	3	28.3563	33.5	17
x_8	1	28.6122	47.0	7
x_9	1	28.8617	45.0	12
x_{10}	1	28.8972	44.0	8
x_{11}	2	29.0363	33.5	21
x_{12}	3	29.0259	28.5	24
x_{13}	3	29.2131	24.5	26
x_{14}	2	29.2940	—	—
x_{15}	2	29.3926	—	—
x_{16}	1	29.3800	—	—
x_{17}	1	29.3777	33.0	19
x_{18}	3	29.4494	—	—
x_{19}	1	29.3475	34.0	18
x_{20}	1	29.2939	36.0	10
x_{21}	4	29.3826	12.0	27
x_{22}	4	29.2878	18.0	22
x_{23}	5	29.2419	15.5	25
x_{24}	2	29.0505	32.5	13
x_{25}	5	29.0794	17.5	23
x_{26}	5	28.7751	23.5	20
x_{27}	3	28.1192	35.5	9
x_{28}	1	27.8471	52.0	3
x_{29}	4	27.7568	35.0	11
x_{30}	5	27.4767	32.5	14
x_{31}	6	26.1417	32.5	16
x_{32}	6	22.9761	—	—
x_{33}	7	21.0339	—	—
x_{34}	8	15.6234	—	—
x_{35}	7	7.1157	—	—

x_i, respectively. We can observe that the multiobjective selection operator systematically considers the criteria of elitism and diversity. We select 15 solutions whose optimal orders are the smallest as parents of the next generation. They are marked as red squares in Figure 4. However, from Figure 4, distribution of the selected points is not ideal. This is because there are some irregular distributed points, such as points 33, 34, and 35. They are far away from the others, which means that they should be eliminated. But because of their very small diversity metric, they are selected by the selection operator. In order to tackle this issue, we pretreat the diversity metric before running the selection operator.

In sport matches, the statistician always eliminates the highest and the lowest marks before calculating the average. We borrow this idea to pretreat the diversity metric. We simply identify the 10% points with the highest and lowest diversity metric and eliminate them before the running of selection operator. In the example, the 10% points with the highest and lowest diversity metrics are 14, 15, 16, and 18 and 32, 33, 34, and 35, respectively. Thus, we run the selection operator without considering them.

Table 5 presents the total optimal number and optimal order with pretreatment of the diversity metric. It can be observed that points 14–16, 18, and 32–35 are excluded in the ranking process. This gives more chance to some point close to the Pareto frontier. For example, points 24 and 30 (which were ranked as 22 and 23, resp.) were not selected without pretreatment of the diversity metric, but they are selected (ranked as 13 and 14, resp.) after considering the pretreatment of the diversity metric. From Figure 5, we can see that the

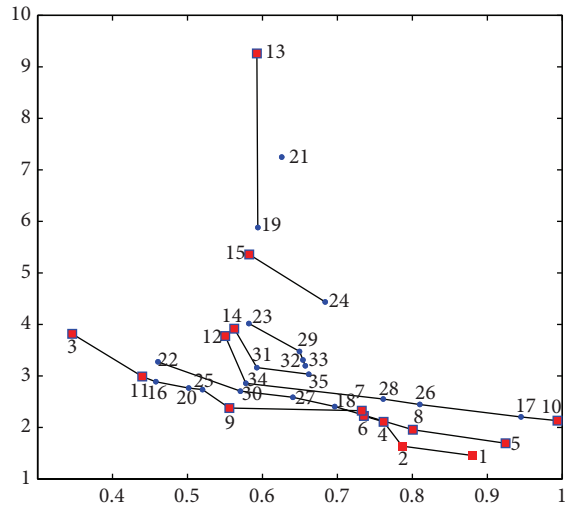

Figure 4: The selected point without pretreatment of the diversity metric.

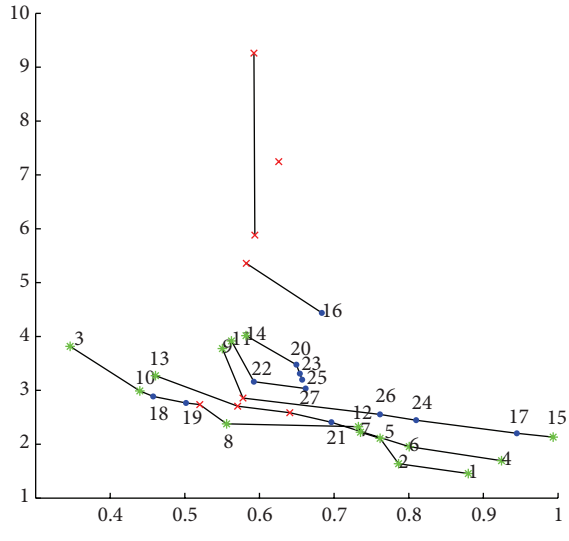

Figure 5: The selected point with pretreatment of the diversity metric.

selected points are now well distributed and closer to the Pareto frontier.

3.5. A New Multiobjective Genetic Algorithm. Given the multiobjective selection operator, we are now ready to propose a new multiobjective genetic algorithm.

Algorithm 19 (optimum order multiobjective genetic algorithm (OOMOGA)). Consider the following.

(1) Initialization

(1.1) Generate the initial population $P(0)$.

(1.2) Set the crossover rate, mutation rate, and number of maximal generations.

(1.3) Let $t \leftarrow 0$.

(2) Since the number of maximal generations has not been reached, do the following.

(2.1) Run the crossover operator: generate the offspring $O_1(t)$.

(2.2) Run the mutation operator: generate the offspring $O_2(t)$.

(2.3) Construct a selection pool $S(t)$ by combining $P(t)$, $O_1(t)$, and $O_2(t)$; that is, $S(t) = P(t) \cup O_1(t) \cup O_2(t)$. Compute their multiobjective function values; that is, $FS(t) = \{\mathbf{F}(x) \mid x \in S(t)\}$.

(2.4) Run the multiobjective selection operator (Algorithm 18) by inputting $S(t)$ and $FS(t)$; the selected solutions are maintained as the parents of the next generation, that is, $P(t+1)$.

(2.5) Let $t \leftarrow t+1$; go to (2.1).

End

End.

4. Numerical Experiments

In this section, we investigate the numerical performance of OOMOGA. In order to evaluate the numerical performance of solvers, we use the performance metric IGD proposed in [42]. Suppose that P^* is a set of uniformly distributed points along the Pareto frontier (in the objective function value space). Let A be a set of solutions obtained by a certain solver. Then, the average distance from P^* to A is defined as

$$\mathrm{IGD}\left(A, P^*\right) = \frac{\sum_{v \in P^*} d\left(v, A\right)}{|P^*|}, \tag{37}$$

where $d(v, A)$ is the minimum Euclidean distance between v and the points in A; that is,

$$d\left(v, A\right) = \min_{y \in A} \left\| v - y \right\|. \tag{38}$$

In fact, P^* represents a sample set of the real Pareto frontiers, if $|P^*|$ is large enough to approximate the Pareto frontier very well, $\mathrm{IGD}(A, P^*)$ could measure both the diversity and convergence of A in a sense. A smaller $\mathrm{IGD}(A, P^*)$ means the set A is closer to the real Pareto frontier and has better diversity.

The referential algorithms are those submitted to the special session on performance assessment of unconstrained/bound constrained multiobjective optimization algorithms at CEC'09. There are 13 algorithms submitted to the special session. They are listed as follows:

(1) MOEAD [43];

(2) GDE3 [44];

(3) MOEADGM [45];

(4) MTS [46];

(5) LiuLiAlgorithm [47];

(6) DMOEADD [48];

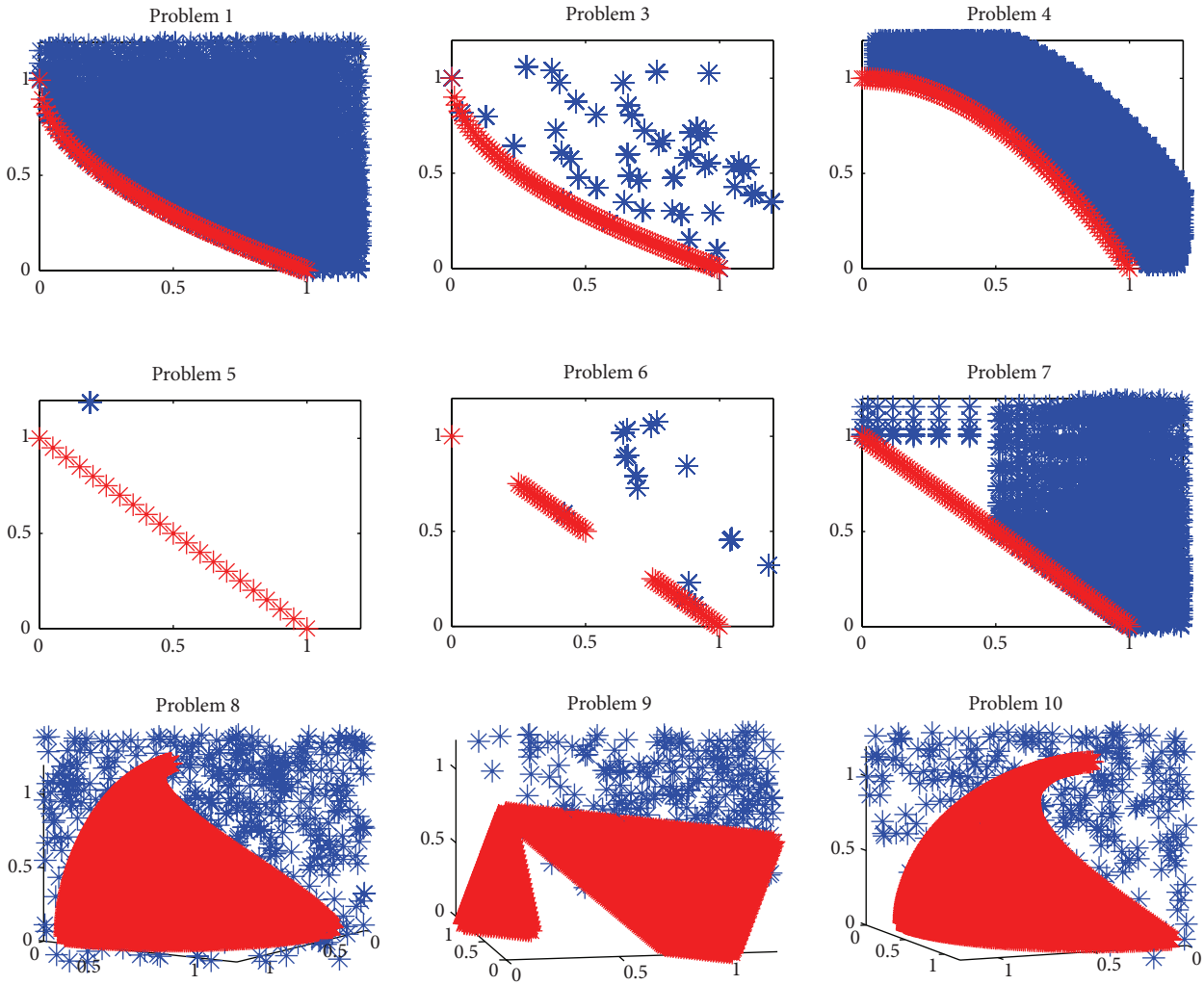

Figure 6: The objective function value space for test problems.

(7) NSGAIILS [49];

(8) OWMOSaDE [50];

(9) ClusteringMOEA [51];

(10) AMGA [52];

(11) MOEP [53];

(12) DECMOSA-SQP [54];

(13) OMOEAII [55].

The benchmarks are taken from [42] which are still used in CEC'09. Figure 6 illustrates the objective function value space of these test problems (the figure of test problem 2 is ignored here since it is similar to that of the test problem 1); the red curve/surface represents their Pareto frontiers. Among these test problems, Problems 1–7 have two objective functions, whereas Problems 8–10 have three objective functions. The Pareto solutions of Problems 5, 6, and 9 are disconnected, while the others are connected.

In order to keep consistency with the final report of CEC'09 [56], in the implementation of OOMOGA, we set the population size as 100 for problems with two objectives and 150 for problems with three objectives; the number of function evaluations is less than 300,000. For each test instance, we run OOMOGA independently for 30 times. The numerical performance evaluated by IGD is illustrated in Table 6.

From Table 6, the proposed solver OOMOGA performs the best at solving the test problem 2; its IGD evaluation is 0.00527, which is better than all the other solvers. In solving the test Problem 9, OOMOGA (whose IGD evaluation is 0.0601) performs only worse than DMOEADD (whose IGD evaluation is 0.4896) but better than all the other solvers. In solving the test Problem 3, the IGD evaluation of OOMOGA (0.0331) is ranked in the third position, worse than MOEAD (0.0072) and LiuLiAlgorithm (0.01497). In solving the test Problem 4, the IGD evaluation of OOMOGA (0.0347) is ranked in the fourth one, worse than MTS (0.02356), GDE3 (0.0265), and DECMOSA-SQP (0.03392). The numerical performance of OOMOGA is moderate in solving test Problems 1, 6, and 8; the IGD ranks are 8, 9, and 9, respectively. For test Problems 5 and 10, the numerical performance of the solver

Table 6: The numerical performance evaluated by IGD.

Rank	UF1		UF2		UF3	
1	MOEAD	0.00435	**OOMOGA**	**0.00527**	MOEAD	0.00742
2	GDE3	0.00534	MTS	0.00615	LiuLiAlgorithm	0.01497
3	MOEADGM	0.0062	MOEADGM	0.0064	**OOMOGA**	**0.0331**
4	MTS	0.00646	DMOEADD	0.00679	DMOEADD	0.03337
5	LiuLiAlgorithm	0.00785	MOEAD	0.00679	MOEADGM	0.049
6	DMOEADD	0.01038	OWMOSaDE	0.0081	MTS	0.0531
7	NSGAIILS	0.01153	GDE3	0.01195	ClusteringMOEA	0.0549
8	**OOMOGA**	**0.0118**	LiuLiAlgorithm	0.0123	AMGA	0.06998
9	OWMOSaDE	0.0122	NSGAIILS	0.01237	DECMOSA-SQP	0.0935
10	ClusteringMOEA	0.0299	AMGA	0.01623	MOEP	0.099
11	AMGA	0.03588	MOEP	0.0189	OWMOSaDE	0.103
12	MOEP	0.0596	ClusteringMOEA	0.0228	NSGAIILS	0.10603
13	DECMOSA-SQP	0.07702	DECMOSA-SQP	0.02834	GDE3	0.10639
14	OMOEAII	0.08564	OMOEAII	0.03057	OMOEAII	0.27141
Rank	UF4		UF5		UF6	
1	MTS	0.02356	MTS	0.01489	MOEAD	0.00587
2	GDE3	0.0265	GDE3	0.03928	MTS	0.05917
3	DECMOSA-SQP	0.03392	AMGA	0.09405	DMOEADD	0.06673
4	**OOMOGA**	**0.0347**	LiuLiAlgorithm	0.16186	OMOEAII	0.07338
5	AMGA	0.04062	DECMOSA-SQP	0.16713	ClusteringMOEA	0.0871
6	DMOEADD	0.04268	OMOEAII	0.1692	MOEP	0.1031
7	MOEP	0.0427	MOEAD	0.18071	DECMOSA-SQP	0.12604
8	LiuLiAlgorithm	0.0435	MOEP	0.2245	AMGA	0.12942
9	OMOEAII	0.04624	ClusteringMOEA	0.2473	**OOMOGA**	**0.1411**
10	MOEADGM	0.0476	DMOEADD	0.31454	LiuLiAlgorithm	0.17555
11	OWMOSaDE	0.0513	OWMOSaDE	0.4303	OWMOSaDE	0.1918
12	NSGAIILS	0.0584	NSGAIILS	0.5657	GDE3	0.25091
13	ClusteringMOEA	0.0585	**OOMOGA**	**0.7695**	NSGAIILS	0.31032
14	MOEAD	0.06385	MOEADGM	1.7919	MOEADGM	0.5563
Rank	UF7		UF8		UF9	
1	MOEAD	0.00444	MOEAD	0.0584	DMOEADD	0.04896
2	LiuLiAlgorithm	0.0073	DMOEADD	0.06841	**OOMOGA**	**0.0601**
3	MOEADGM	0.0076	LiuLiAlgorithm	0.08235	NSGAIILS	0.0719
4	DMOEADD	0.01032	NSGAIILS	0.0863	MOEAD	0.07896
5	MOEP	0.0197	OWMOSaDE	0.0945	GDE3	0.08248
6	NSGAIILS	0.02132	MTS	0.11251	LiuLiAlgorithm	0.09391
7	ClusteringMOEA	0.0223	AMGA	0.17125	OWMOSaDE	0.0983
8	DECMOSA-SQP	0.02416	OMOEAII	0.192	MTS	0.11442
9	GDE3	0.02522	**OOMOGA**	**0.2137**	DECMOSA-SQP	0.14111
10	OMOEAII	0.03354	DECMOSA-SQP	0.21583	MOEADGM	0.1878
11	MTS	0.04079	ClusteringMOEA	0.2383	AMGA	0.18861
12	AMGA	0.05707	MOEADGM	0.2446	OMOEAII	0.23179
13	OWMOSaDE	0.0585	GDE3	0.24855	ClusteringMOEA	0.2934
14	**OOMOGA**	**0.1267**	MOEP	0.423	MOEP	0.342
Rank	UF10					
1	MTS	0.15306				
2	DMOEADD	0.32211				
3	AMGA	0.32418				
4	MOEP	0.3621				
5	DECMOSA-SQP	0.36985				
6	ClusteringMOEA	0.4111				
7	GDE3	0.43326				
8	LiuLiAlgorithm	0.44691				
9	MOEAD	0.47415				
10	MOEADGM	0.5646				
11	OMOEAII	0.62754				
12	**OOMOGA**	**0.7269**				
13	OWMOSaDE	0.743				
14	NSGAIILS	0.84468				

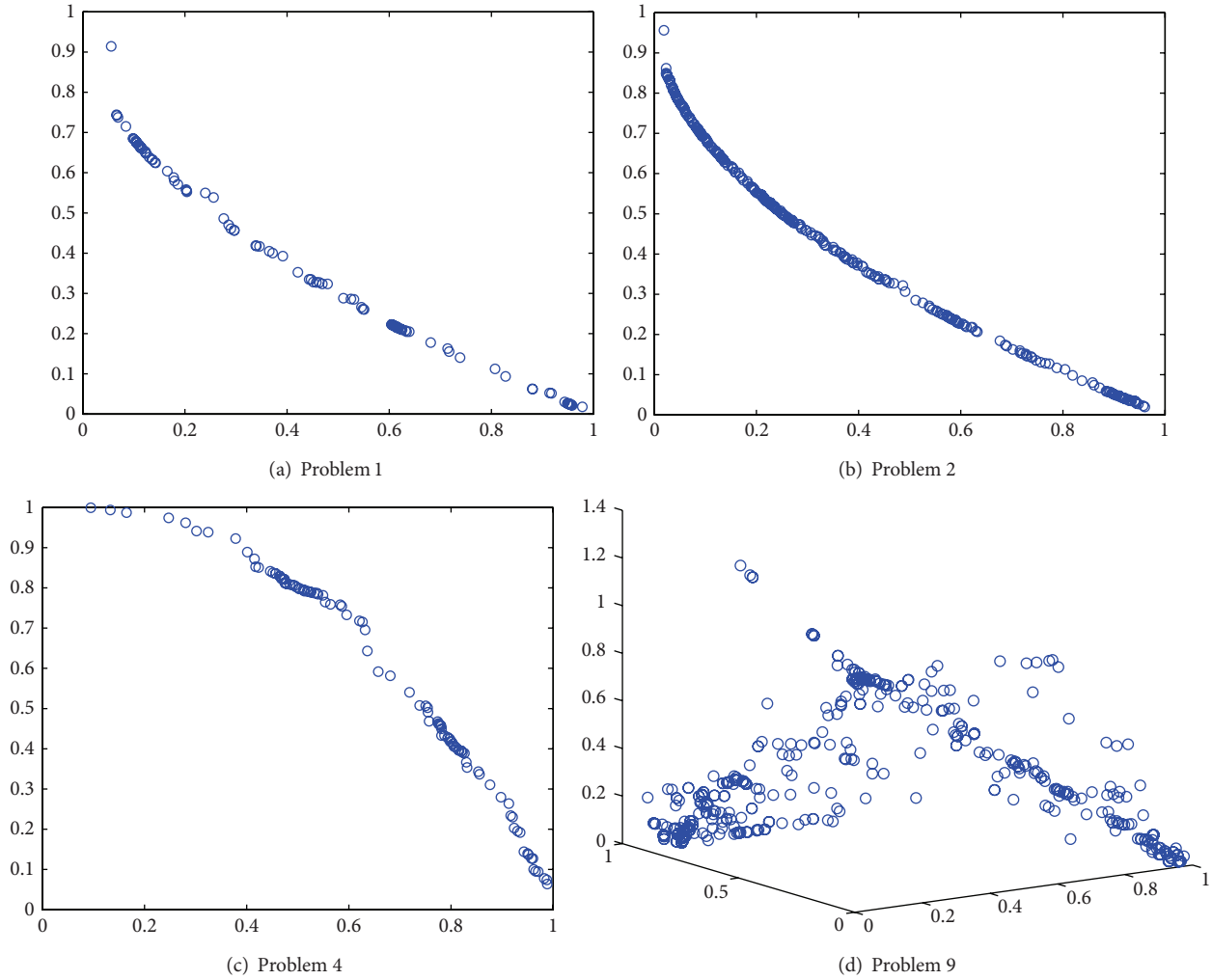

Figure 7: The approximated Pareto frontier of Problems 1, 2, 4, and 9.

OOMOGA is not so good, ranking in 13 and 12, respectively. The worst performance of OOMOGA appears in solving the test Problem 7; the IGD evaluation is 0.1267, which is worse than all the other solvers.

It is not uncommon that the numerical performance of the proposed solver OOMOGA is unstable among different test problems because the numerical results are not only affected by the performance of solvers, but also impacted by the linearity and structure of objective function themselves. Furthermore, the crossover and mutation operators are also affected by the distribution of points in the objective function value space. Generally speaking, if a new point generated by the crossover or mutation operators has a higher probability of locating around the Pareto frontier, then the Pareto frontier can be well approximated by the solver, for example, the test Problems 2, 3, and 4. On the contrary, if it is hard for the crossover or mutation operators to generate new point around the Pareto frontier, then the problem is difficult to be solved by MOGAs, for instance, the test Problems 5, 6, and 7. In fact, this instability still appears in the other solvers, such as MOEAD which is reported to be the best solver in [56]. The IGD evaluation of MOEAD in solving the test Problems 4, 5, and 10 is not very good, ranking in 14, 7, and 9, respectively.

Figure 7 demonstrates Pareto frontiers of test Problems 1, 2, 4, and 9, respectively. From Figures 7(a) and 7(b), we can observe that, for the test Problems 1 and 2, the proposed solver obtained very good representations of their Pareto frontiers. Results for the test Problem 4 (see Figure 7(c)) is not very uniformly distributed, which may affect the performance of IGD evaluation. Figure 7(d) illustrates the approximate Pareto frontier of the test Problem 9; we can see that the structure is more or less an approximation of the real Pareto frontier.

5. Conclusion

This paper proposed a solver based on genetic algorithm for multiobjective optimization. In the process of using genetic algorithm to solve multiobjective optimization, the evolutionary procedure prefers to select individuals with better elitism and diversity. Therefore, in the algorithm, we

have to consider the trade-off between elitism and diversity. To tackle this issue, we first developed strategies to measure the elitism and diversity of populations. Then we used the proposed elitism and diversity metrics to construct a discrete multiobjective subproblem. Finally, the new selection operator is designed by applying the optimum order method to solve the multiobjective subproblem. We tested the proposed solver by the test instances used in CEC'09 and compared the numerical result with the referential solvers proposed in CEC'09. The numerical performance analysis shows that the proposed solver is good at solving problems whose objective function value space is high density around the Pareto frontier.

We will further study this topic from the following two points of view.

(i) Improving the performance of crossover and mutation operators of the genetic algorithm: the crossover and mutation operators are very important for the diversity of solutions. However, the distribution of new individuals generated by the current crossover and mutation operators is coincident with the distribution of parents. This leads the excessive search of the "rich" area, but insufficient search of the "poor" area.

(ii) Introducing some more reasonable diversity metrics: it is very important to maintain the diversity of population in the evolutionary process of genetic algorithm. However, measuring diversity is not an easy task. The global diversity metric proposed in this paper is a proper diversity metric, but it is far from perfect.

Conflict of Interests

The authors declare that there is no conflict of interests regarding the publication of this paper.

Acknowledgments

Changzhi Wu was partially supported by Australian Research Council Linkage Program LP140100873, Natural Science Foundation of China (61473326), and Natural Science Foundation of Chongqing (cstc2013jcyjA00029 and cstc2013jjB0149).

References

[1] C. J. Li, C. D. Li, X. F. Liao, and T. W. Huang, "Impulsive effects on stability of high-order BAM neural networks with time delays," *Neurocomputing*, vol. 74, no. 10, pp. 1541–1550, 2011.

[2] C. J. Li, W. W. Yu, and T. W. Huang, "Impulsive synchronization schemes of stochastic complex networks with switching topology: average time approach," *Neural Networks*, vol. 54, pp. 85–94, 2014.

[3] C. J. Li, D. Y. Gao, C. Liu, and G. Chen, "Impulsive control for synchronizing delayed discrete complex networks with switching topology," *Neural Computing and Applications*, vol. 24, no. 1, pp. 59–68, 2014.

[4] K. Deb, A. Pratap, S. Agarwal, and T. Meyarivan, "A fast and elitist multiobjective genetic algorithm: NSGA-II," *IEEE Transactions on Evolutionary Computation*, vol. 6, no. 2, pp. 182–197, 2002.

[5] M. Ehrgott, J. Ide, and A. Schöbel, "Minmax robustness for multi-objective optimization problems," *European Journal of Operational Research*, vol. 239, no. 1, pp. 17–31, 2014.

[6] Q. Long, "A constraint handling technique for constrained multi-objective genetic algorithm," *Swarm and Evolutionary Computation*, vol. 15, pp. 66–79, 2014.

[7] G. Mavrotas, O. Pechak, E. Siskos, H. Doukas, and J. Psarras, "Robustness analysis in Multi-Objective Mathematical Programming using Monte Carlo simulation," *European Journal of Operational Research*, vol. 240, no. 1, pp. 193–201, 2015.

[8] Y. T. Qi, X. L. Ma, F. Liu, L. C. Jiao, J. Y. Sun, and J. S. Wu, "MOEA/D with adaptive weight adjustment," *Evolutionary Computation*, vol. 22, no. 2, pp. 231–264, 2014.

[9] P. C. Fishburn, "Utility theory for decision making," DTIC Document, 1970.

[10] I. Y. Kim and O. L. De Weck, "Adaptive weighted-sum method for bi-objective optimization: pareto front generation," *Structural and Multidisciplinary Optimization*, vol. 29, no. 2, pp. 149–158, 2005.

[11] R. T. Marler and J. S. Arora, "The weighted sum method for multi-objective optimization: new insights," *Structural and Multidisciplinary Optimization*, vol. 41, no. 6, pp. 853–862, 2010.

[12] J. J. Liu, C. Z. Wu, G. Wu, and X. Y. Wang, "A novel differential search algorithm and applications for structure design," Submitted.

[13] Q. Long and C. Z. Wu, "A hybrid method combining genetic algorithm and Hooke-Jeeves method for constrained global optimization," *Journal of Industrial and Management Optimization*, vol. 10, no. 4, pp. 1279–1296, 2014.

[14] Q. Long, C. Z. Wu, T. W. Huang, and X. Y. Wang, "A genetic algorithm for unconstrained multi-objective optimization," *Swarm and Evolutionary Computation*, 2015.

[15] D. F. Jones, S. K. Mirrazavi, and M. Tamiz, "Multi-objective meta-heuristics: an overview of the current state-of-the-art," *European Journal of Operational Research*, vol. 137, no. 1, pp. 1–9, 2002.

[16] P. Kumar, D. Gospodaric, and P. Bauer, "Improved genetic algorithm inspired by biological evolution," *Soft Computing*, vol. 11, no. 10, pp. 923–941, 2007.

[17] K. Sindhya, S. Ruuska, T. Haanpää, and K. Miettinen, "A new hybrid mutation operator for multiobjective optimization with differential evolution," *Soft Computing*, vol. 15, no. 10, pp. 2041–2055, 2011.

[18] J. D. Schaffer, "Multiple objective optimization with vector evaluated genetic algorithms," in *Proceedings of the 1st international Conference on Genetic Algorithms*, pp. 93–100, L. Erlbaum Associates, 1985.

[19] C. M. Fonseca and P. J. Fleming, "Multiobjective genetic algorithms," in *Proceedings of the IEE Colloquium on Genetic Algorithms for Control Systems Engineering*, pp. 6/1–6/5, IET, London, UK, May 1993.

[20] J. Horn, N. Nafpliotis, and D. E. Goldberg, "A niched Pareto genetic algorithm for multiobjective optimization," in *Proceedings of the 1st IEEE Conference on Evolutionary Computation, IEEE World Congress on Computational Intelligence*, vol. 1, pp. 82–87, IEEE, Orlando, Fla, USA, June 1994.

[21] P. Hajela and C.-Y. Lin, "Genetic search strategies in multicriterion optimal design," *Structural Optimization*, vol. 4, no. 2, pp. 99–107, 1992.

[22] T. Murata and H. Ishibuchi, "MOGA: multi-objective genetic algorithms," in *Proceedings of the IEEE International Conference on Evolutionary Computation*, vol. 1, pp. 289–294, IEEE, December 1995.

[23] N. Srinivas and K. Deb, "Muiltiobjective optimization using nondominated sorting in genetic algorithms," *Evolutionary Computation*, vol. 2, no. 3, pp. 221–248, 1994.

[24] E. Zitzler and L. Thiele, "Multiobjective evolutionary algorithms: a comparative case study and the strength Pareto approach," *IEEE Transactions on Evolutionary Computation*, vol. 3, no. 4, pp. 257–271, 1999.

[25] E. Zitzler, M. Laumanns, and L. Thiele, "SPEA2: improving the strength Pareto evolutionary algorithm," Tech. Rep., Eidgenössische Technische Hochschule Zurich (ETH) Institut fur Technische Informatik und Kommunikationsnetze (TIK), 2001.

[26] J. D. Knowles and D. W. Corne, "Approximating the nondominated front using the pareto archived evolution strategy," *Evolutionary computation*, vol. 8, no. 2, pp. 149–172, 2000.

[27] D. W. Corne, J. D. Knowles, and M. J. Oates, "The Pareto envelope-based selection algorithm for multiobjective optimization," in *Parallel Problem Solving from Nature PPSN VI*, vol. 1917 of *Lecture Notes in Computer Science*, pp. 839–848, Springer, Berlin, Germany, 2000.

[28] E. Zitzler, K. Deb, and L. Thiele, "Comparison of multiobjective evolutionary algorithms: empirical results," *Evolutionary computation*, vol. 8, no. 2, pp. 173–195, 2000.

[29] T. C. Koopmans and S. Reiter, "A model of transportation," in *Activity Analysis of Production and Allocation*, p. 222, John Wiley & Sons, New York, NY, USA, 1951.

[30] J. H. Holland, *Adaptation in Natural and Artificial Systems*, vol. 53, University of Michigan Press, Ann Arbor, Mich, USA, 1975.

[31] D. E. Goldberg, "A note on Boltzmann tournament selection for genetic algorithms and population-oriented simulated annealing," *Complex Systems*, vol. 4, no. 4, pp. 445–460, 1990.

[32] D. E. Goldberg, B. Korb, and K. Deb, "Messy genetic algorithms: motivation, analysis, and first results," *Complex Systems*, vol. 3, no. 5, pp. 493–530, 1989.

[33] J. J. Grefenstette, "Optimization of control parameters for genetic algorithms," *IEEE Transactions on Systems, Man and Cybernetics*, vol. 16, no. 1, pp. 122–128, 1986.

[34] H. Kitano, "Neurogenetic learning: an integrated method of designing and training neural networks using genetic algorithms," *Physica D: Nonlinear Phenomena*, vol. 75, no. 1–3, pp. 225–238, 1994.

[35] T. Murata, H. Ishibuchi, and H. Tanaka, "Multi-objective genetic algorithm and its applications to flowshop scheduling," *Computers and Industrial Engineering*, vol. 30, no. 4, pp. 957–968, 1996.

[36] D. E. Goldberg, *Genetic Algorithms in Search, Optimization, and Machine Learning*, Addison-Wesley, Reading, Mass, USA, 1989.

[37] C. M. Fonseca and P. J. Fleming, "Genetic algorithms for multiobjective optimization: formulation discussion and generalization," in *Proceedings of the 5th International Conference on Genetic Algorithms (ICGA '93)*, pp. 416–423, 1993.

[38] J. Knowles and D. Corne, "The pareto archived evolution strategy: a new baseline algorithm for Pareto multiobjective optimisation," in *Proceedings of the Congress on Evolutionary Computation (CEC '99)*, vol. 1, pp. 98–105, July 1999.

[39] D. E. Goldberg and J. Richardson, "Genetic algorithms with sharing for multimodal function optimization," in *Proceedings of the 2nd International Conference on Genetic Algorithms and Their Applications*, pp. 41–49, Lawrence Erlbaum Associates, 1987.

[40] H. Lu and G. G. Yen, "Rank-density-based multiobjective genetic algorithm and benchmark test function study," *IEEE Transactions on Evolutionary Computation*, vol. 7, no. 4, pp. 325–343, 2003.

[41] G. G. Yen and H. Lu, "Dynamic multiobjective evolutionary algorithm: adaptive cell-based rank and density estimation," *IEEE Transactions on Evolutionary Computation*, vol. 7, no. 3, pp. 253–274, 2003.

[42] Q. F. Zhang, A. Zhou, S. Z. Zhao, P. N. Suganthan, W. D. Liu, and S. Tiwari, "Multiobjective optimization test instances for the CEC 2009 special session and competition," Tech. Rep. CES-487, University of Essex and Nanyang Technological University, 2009.

[43] Q. F. Zhang, W. D. Liu, and H. Li, "The performance of a new version of MOEA/D on CEC09 unconstrained MOP test instances," in *Proceedings of the IEEE Congress on Evolutionary Computation (CEC '09)*, pp. 203–208, IEEE, May 2009.

[44] S. Kukkonen and J. Lampinen, "Performance assessment of Generalized Differential Evolution 3 (GDE3) with a given set of problems," in *Proceedings of the IEEE Congress on Evolutionary Computation (CEC '07)*, pp. 3593–3600, IEEE, September 2007.

[45] C.-M. Chen, Y.-P. Chen, and Q. F. Zhang, "Enhancing MOEA/D with guided mutation and priority update for multi-objective optimization," in *Proceedings of the IEEE Congress on Evolutionary Computation (CEC '09)*, pp. 209–216, May 2009.

[46] L.-Y. Tseng and C. Chen, "Multiple trajectory search for unconstrained/constrained multi-objective optimization," in *Proceedings of the IEEE Congress on Evolutionary Computation (CEC '09)*, pp. 1951–1958, IEEE, May 2009.

[47] H.-L. Liu and X. Q. Li, "The multiobjective evolutionary algorithm based on determined weight and sub-regional search," in *Proceedings of the IEEE Congress on Evolutionary Computation (CEC '09)*, pp. 1928–1934, IEEE, May 2009.

[48] M. H. Liu, X. F. Zou, C. Yu, and Z. J. Wu, "Performance assessment of DMOEA-DD with CEC 2009 MOEA competition test instances," in *Proceedings of the IEEE Congress on Evolutionary Computation (CEC '09)*, pp. 2913–2918, IEEE, Trondheim, Norway, May 2009.

[49] K. Sindhya, A. Sinha, K. Deb, and K. Miettinen, "Optimization algorithm for constrained and unconstrained problems," in *Proceedings of the IEEE Congress on Evolutionary Computation (CEC '09)*, pp. 2919–2926, May 2009.

[50] V. L. Huang, S. Z. Zhao, R. Mallipeddi, and P. N. Suganthan, "Multi-objective optimization using self-adaptive differential evolution algorithm," in *Proceedings of the IEEE Congress on Evolutionary Computation (CEC '09)*, pp. 190–194, May 2009.

[51] Y. P. Wang, C. Y. Dang, H. C. Li, L. X. Han, and J. X. Wei, "A clustering multi-objective evolutionary algorithm based on orthogonal and uniform design," in *Proceedings of the IEEE Congress on Evolutionary Computation (CEC '09)*, pp. 2927–2933, IEEE, Trondheim, Norway, May 2009.

[52] S. Tiwari, G. Fadel, P. Koch, and K. Deb, "Performance assessment of the hybrid archive-based micro genetic algorithm (AMGA) on the CEC09 test problems," in *Proceedings of the IEEE Congress on Evolutionary Computation (CEC '09)*, pp. 1935–1942, IEEE, Trondheim, Norway, May 2009.

[53] B. Y. Qu and P. N. Suganthan, "Multi-objective evolutionary programming without non-domination sorting is up to twenty times faster," in *Proceedings of the 11th Conference on Congress on Evolutionary Computation (CEC '09)*, pp. 2934–2939, IEEE, 2009.

[54] A. Zamuda, J. Brest, B. Bošković, and V. Žumer, "Differential evolution with self-adaptation and local search for Constrained multiobjective optimization," in *Proceedings of the IEEE Congress on Evolutionary Computation (CEC '09)*, pp. 195–202, May 2009.

[55] S. Gao, S. Y. Zeng, B. Xiao et al., "An orthogonal multi-objective evolutionary algorithm with lower-dimensional crossover," in *Proceedings of the IEEE Congress on Evolutionary Computation (CEC '09)*, pp. 1959–1964, IEEE, May 2009.

[56] Q. F. Zhang and P. N. Suganthan, "Final report on CEC'09 MOEA competition," in *IEEE Congress on Evolutionary Computation (CEC '09)*, Piscataway, NJ, USA, 2009.

Hindawi Publishing Corporation
Mathematical Problems in Engineering
Volume 2015, Article ID 905761, 15 pages
http://dx.doi.org/10.1155/2015/905761

Research Article

A Lower Extremity Exoskeleton: Human-Machine Coupled Modeling, Robust Control Design, Simulation, and Overload-Carrying Experiment

Qing Guo,[1] Songjing Li,[2] and Dan Jiang[3]

[1]*School of Aeronautics and Astronautics, University of Electronic Science and Technology of China, Chengdu 611731, China*
[2]*Department of Fluid Control & Automation, Harbin Institute of Technology, Harbin 150001, China*
[3]*School of Mechatronics Engineering, University of Electronic Science and Technology of China, Chengdu 611731, China*

Correspondence should be addressed to Qing Guo; guoqinguestc@163.com

Received 4 November 2014; Revised 8 May 2015; Accepted 10 May 2015

Academic Editor: Stanisław Migorski

Copyright © 2015 Qing Guo et al. This is an open access article distributed under the Creative Commons Attribution License, which permits unrestricted use, distribution, and reproduction in any medium, provided the original work is properly cited.

A robust H_∞ control method and switched control algorithm for hydraulic actuator presents in human-machine coordinated motion to solve the motion delay of lower extremity exoskeleton. After the characteristic parameters synthesis of human limb and exoskeleton linkage, the human-machine coupled motion model is constructed to estimate the appropriate hydraulic pressure, which is considered as a structural uncertainty in hydraulic model. Then the robust controller is designed to improve the robust stability and performance under the structural and parametric uncertainty disturbances. Simulation results show that, in walking mode, this robust controller can achieve a better dynamic response and aid-force efficiency than PID controller. Then, according to gait divisions of person's limb motion, the switched control algorithm is designed to reduce the delay of exoskeleton tracking person. Finally, the experimental results show that the human-machine coordinated walk with bearing 60 kg load and squat action with no external load are realized effectively by this proposed method.

1. Introduction

Lower extremity exoskeleton is a humanoid mechanical equipment. Since the exoskeleton can help a person bear many loads and track a person's motion, the soldier's load capacity and flexibility can be significantly improved. The exoskeleton is a complex system including 4 subsystems: mechanical structure, gait sensing, hydraulic control, and power supply. Recently lower extremity exoskeleton can bear the maximum load 200 lbs and realize typical action such as walk, running, up and down hill or stairs, squatting, and trotting [1]. Since 2000, DARPA and U. C. Berkeley have done many researches on exoskeleton and developed the prototypes called "XOS" and "BLEEX" [2–4], respectively. Lockheed has simplified the hydraulic actuator amount of BLEEX and renamed "Human Universal Load Carrier" (HULC) [1]. Other countries like Japan and France have developed commercial or military exoskeleton called "HAL" or "Hercule" [5]. In 2000, Atkeson et al. [6] made conclusions on the characteristics of humanoid robot: sometimes the motion of machine is guided by person, sometimes just the opposite, especially sometimes the boundary is not clearly divided between the two. Due to the person's participation, the traditional robotic program control method will cause the motional delay of exoskeleton tracking person [7].

Since 2004, the exoskeleton technology is developed in China [8]. A motor-driven exoskeleton with no external load is designed by Naval Aeronautical Engineering Institute [9]. In addition, the aid-force exoskeleton with hydraulic-driven actuator is designed to realize walk, up and down stairs [10]. However, the human-machine coordinated motion is not presented in aforementioned references; if person's gait characteristic is ignored in exoskeleton control, person's comfort and the aid-force effect are reduced. In this paper, a human-machine coupled model is constructed to analyze the dynamic external load. This external load describes the aid-force efficiency of exoskeleton in the case of person's safety and should be compensated by exoskeleton controller.

Due to the demands of high load efficiency and fast response, lower extremity exoskeleton is driven by the electrohydraulic servo system (EHSS). However, EHSS has some model uncertainties such as parametric disturbances, structural uncertainties, which are consequences of hydraulic physical characteristics, oil leakage, oil temperature variations, and characteristics of valves near null [11]. The classical control method of EHSS is PID [12]. Due to lower order and constant gains, PID control is easy to be realized in engineering. So the variable parameters of PID controller are presented to suit the hydraulic dynamic characteristic [13, 14]. Some advanced control methods such as adaptive sliding mode [15–17] and backstepping controllers [18, 19] are used in EHSS and get some good performance. In addition, the robust controllers [20–22] of EHSS are presented with parameter uncertainty disturbance, which are converted to H_∞ control problem solved by conventional robust analysis or linear matrix inequality. The mixed sensitivity H_∞ control method [23] of EHSS is presented to balance to the robust stability and response performance. But the external load of hydraulic control model is only considered as a disturbance, not to be quantitatively analyzed and described in robust uncertainty model. In this paper, by referring to H_∞ control method aforementioned references, a robust H_∞ controller is designed to suppress structural uncertainty and parametric uncertainties, which are caused by the external load and parametric disturbances. Furthermore, combined with the switched control algorithm of hydraulic actuator, this H_∞ controller can reduce the delay of exoskeleton tracking person. Simulation and experimental results validate this proposed controller.

2. Human-Machine Coupled Model Construction

Since human fast conscious is ahead of exoskeleton, the only mechanical motion model is not insufficient to analyze the systematic dynamics. So the coupled motion model needs to be constructed to estimate the dynamic loads and the supply power.

2.1. Characteristic Parameters Synthesis. Some characteristic parameters like mass and moment of inertia are different between human limb and exoskeleton linkage. So the characteristic parameters need be synthetic to balance 2 motion responses activated by person and exoskeleton. It means that human-constraint is relieved but not vanished through equivalent multibody motion. The human-constraint is a small value in the thigh bandage, which can not exceed the human tolerance.

If the sagittal motion is considered only, the rotational motion around the knee is shown in Figure 1. Here components B_1, B_2, B_3, B_4, and B_5 represent, respectively, human calf, mechanical calf, sensing shoes, human thigh, and mechanical thigh.

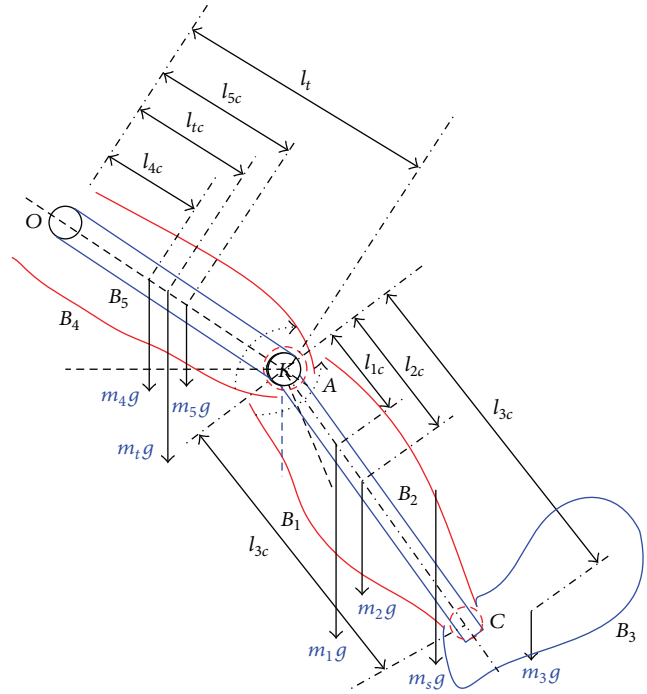

Figure 1: The rotational motion around the knee of human-machine synthetic model.

The centers of synthetic calf and thigh for human-machine coordinated motion [24] are shown as

$$l_{sc} = \frac{m_1 l_{1c} + m_2 l_{2c} + m_3 l_{3c}}{m_1 + m_2 + m_3} = \frac{m_1 l_{1c} + m_2 l_{2c} + m_3 l_{3c}}{m_s}, \quad (1a)$$

$$l_{tc} = \frac{m_4 l_{4c} + m_5 l_{5c}}{m_4 + m_5} = \frac{m_4 l_{4c} + m_5 l_{5c}}{m_t}. \quad (1b)$$

According to the moment of inertia of the parallel axis theorem, the moment of inertia of synthetic calf and thigh around respective center of mass is shown as

$$I_{sc} = \left[I_{1c} + m_1 \left(l_{sc} - l_{1c}\right)^2\right] + \left[I_{2c} + m_2 \left(l_{sc} - l_{2c}\right)^2\right] + \left[I_{3c} + m_3 \left(l_{sc} - l_{3c}\right)^2\right], \quad (2a)$$

$$I_{tc} = \left[I_{4c} + m_4 \left(l_{tc} - l_{4c}\right)^2\right] + \left[I_{5c} + m_5 \left(l_{tc} - l_{5c}\right)^2\right], \quad (2b)$$

where m_i is the ith component mass. m_s and m_t are the total masses of equivalent calf and thigh, l_{1c}, l_{2c}, and l_{3c} are the distances from center of mass to knee, respectively, l_{4c}, l_{5c} are the distances from center of mass to hip, respectively, and I_{ic} is the ith moment of inertia around respective center of mass.

2.2. Human-Machine Coupled Motion Model. In human-machine coordinated motion, the exoskeleton linkages should compensate the load when human foot contacts the ground. So in the stance phase of walk or squat, the hydraulic actuator not only realizes the exoskeleton knee rotation tracking human limb rotation but also balances the variable load. In order to estimate the dynamic load on the hydraulic

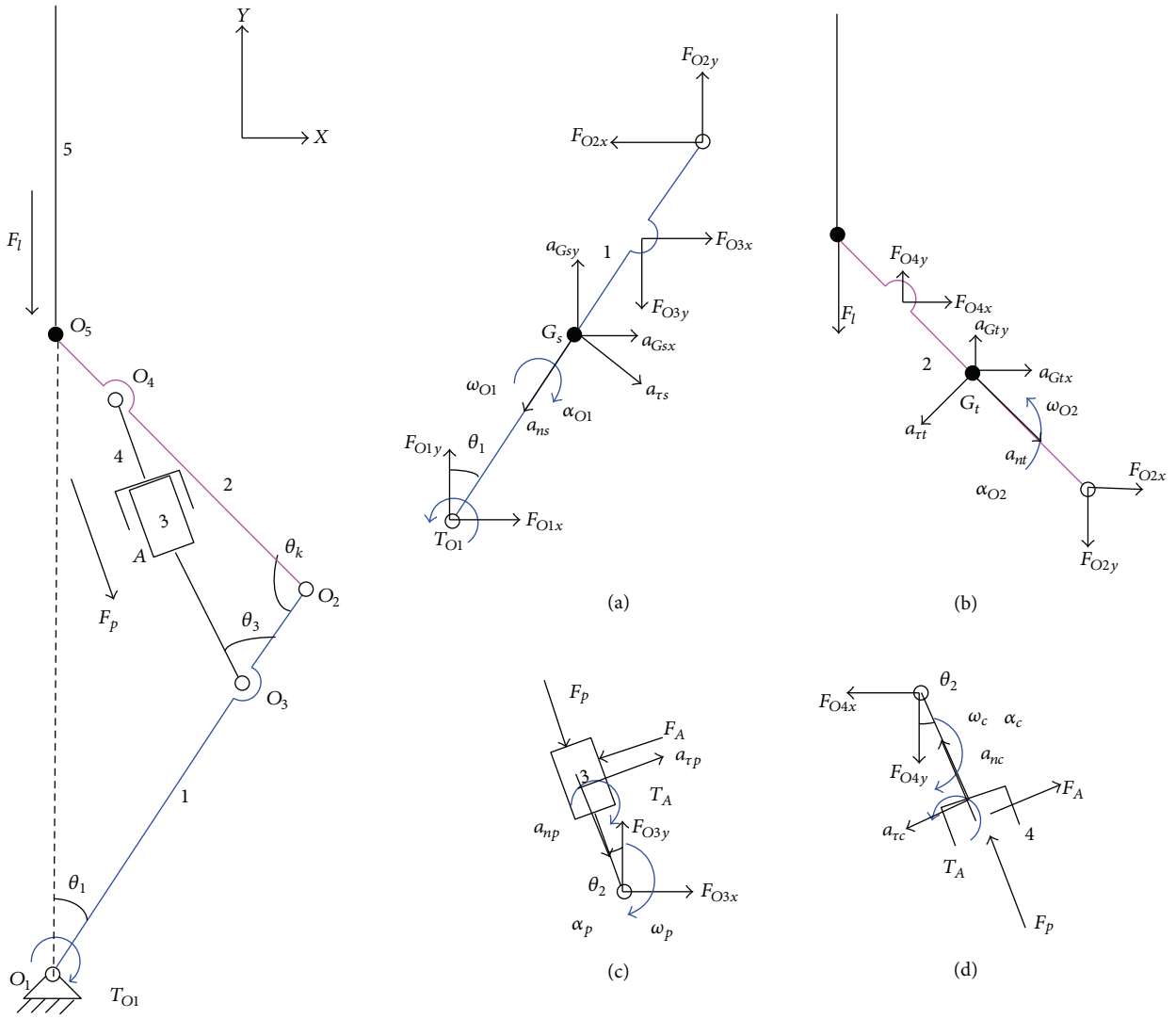

FIGURE 2: The synthetic model of human-machine coupled motion (linkages 1 and 2 represented the synthetic calf and thigh).

actuator, the human-machine coupled motion model needs to be constructed in Figure 2. The link point "O_5" between mechanical back frame and thigh is the hip joint. The ankle joint "O_1" is equivalent to a hinge when human foot contacts the ground. The external load "F_l" including the exoskeleton mass and effective load hung at the back frame. The force "F_p" provided by hydraulic actuator compensates the load on the exoskeleton.

The force and moment equilibrium equations of 1# linkage (synthetic calf) are shown as

$$F_{O1x} - F_{O2x} + F_{O3x} = m_{sc} a_{Gsx}, \tag{3a}$$

$$F_{O1y} + F_{O2y} - F_{O3y} - m_{sc} g = m_s a_{Gsy}, \tag{3b}$$

$$\begin{aligned} &T_{O1} + F_{O2x} l_{sc} \cos\theta_1 + F_{O2y} l_{sc} \sin\theta_1 \\ &\quad - F_{O3x} (l_{sc} - l_1) \cos\theta_1 - F_{O3y} (l_{sc} - l_1) \sin\theta_1 \\ &\quad - m_{sc} g l_{gs} \sin\theta_1 = - I_{sc} \alpha_{O1}, \end{aligned} \tag{3c}$$

$$\begin{aligned} a_{Gsx} &= a_{O1x} - a_{ns} \cdot \cos\theta_1 + a_{\tau s} \cdot \sin\theta_1, \\ a_{Gsy} &= a_{O1y} - a_{ns} \cdot \sin\theta_1 - a_{\tau s} \cdot \cos\theta_1, \end{aligned} \tag{3d}$$

where $a_{ns} = l_{gs} \cdot \omega_{O1}^2$, $a_{\tau s} = l_{gs} \cdot \alpha_{O1}$, $a_{O1x} = a_{O1y} = 0$.

Similarly, the 2# linkage (synthetic thigh), 3# linkage (piston), and 4# linkage (cylinder) can also be analyzed as follows:

$$F_{O2x} + F_{O4x} = m_t a_{Gtx}, \tag{4a}$$

$$F_{O4y} - F_{O2y} - m_{tc} g - F_{\text{load}} = m_t a_{Gty}, \tag{4b}$$

$$\begin{aligned} &- F_l l_{tc} \cos(\theta_k + \theta_1) + F_{O4x} l_2 \cos(\theta_k + \theta_1) \\ &\quad - F_{O4y} l_2 \sin(\theta_k + \theta_1) + m_t g l_{gt} \sin\theta_k = I_{tc} \alpha_{O2}, \end{aligned} \tag{4c}$$

$$F_p \sin\theta_2 - F_A \cos\theta_2 + F_{O3x} = m_p a_{Gpx}, \tag{5a}$$

$$-F_p\cos\theta_2 - F_A\sin\theta_2 + F_{O3y} = m_p a_{Gpy}, \tag{5b}$$

$$-F_A l_r + T_A = I_p\alpha_p, \tag{5c}$$

$$-F_p\sin\theta_2 + F_A\cos\theta_2 - F_{O4x} = m_c a_{Gcx}, \tag{6a}$$

$$F_p\cos\theta_2 + F_A\sin\theta_2 - F_{O4y} = m_c a_{Gcy}, \tag{6b}$$

$$-F_A\left(l_h - l_r\right) - T_A = I_c\alpha_c. \tag{6c}$$

Some angle and angular velocity relations in Figure 2 are as follows:

$$\sin\theta_1 = \frac{l_2\sin\theta_k}{\sqrt{l_1^2 + l_2^2 - 2l_1l_2\cos\theta_k}}, \tag{7a}$$

$$\sin\theta_3 = \frac{(l_2 - l_{tc})\sin\theta_k}{\sqrt{l_{sc}^2 + (l_2 - l_{tc})^2 - 2l_{sc}(l_2 - l_{tc})\cos\theta_k}}, \tag{7b}$$

$$\theta_2 = \theta_3 - \theta_1, \tag{7c}$$

$$\omega_p = \omega_{O1} - \frac{l_2\cos\theta_k\omega_k + l_2\sin\theta_k\left(l_1l_2\sin\theta_k\omega_k/\sqrt{l_1^2 + l_2^2 - 2l_1l_2\cos\theta_k}\right)}{\cos\theta_3\left(l_1^2 + l_2^2 - 2l_1l_2\cos\theta_k\right)}, \tag{8a}$$

$$\omega_c = \omega_{O2} - \frac{l_1\cos\theta_k\omega_k + l_1\sin\theta_k\left(l_1l_2\sin\theta_k\omega_k/\sqrt{l_1^2 + l_2^2 - 2l_1l_2\cos\theta_k}\right)}{\cos(\pi - \theta_k - \theta_3)\left(l_1^2 + l_2^2 - 2l_1l_2\cos\theta_k\right)}, \tag{8b}$$

$$\omega_{O2} = \omega_k + \omega_{O1}. \tag{8c}$$

In above equations, some parameters are defined as follows.

Description of Some Motion and Geometry Parameter. Consider the following:

F_{O1x}, F_{O1y}: force from hinge O_1 to linkage 1,

F_{O2x}, F_{O2y}: force from linkage 1 to linkage 2,

F_{O3x}, F_{O3y}: force from linkage 1 to linkage 3,

F_{O4x}, F_{O4y}: force from linkage 2 to linkage 4,

a_{Gsx}, a_{Gsy}: calf acceleration at the center of gravity,

a_{Gtx}, a_{Gty}: thigh acceleration at the center of gravity,

$a_{\tau s}$, a_{ns}: tangential and normal acceleration of calf acceleration,

$a_{\tau t}$, a_{nt}: tangential and normal acceleration of thigh,

$a_{\tau p}$, a_{np}: tangential and normal acceleration of piston,

$a_{\tau c}$, a_{nc}: tangential and normal acceleration of cylinder,

l_{gs}: length between the center of gravity calf and the ankle,

l_{gt}: length between the center of gravity thigh and the knee,

l_1, l_2: distance between hydraulic cylinder calf, thigh connections, and knee,

ω_{O1}, α_{O1}: angular velocity and angular acceleration of calf around the ankle,

ω_{O2}, α_{O2}: angular velocity and angular acceleration of thigh around the knee,

ω_k: knee angular velocity,

I_p: moment of inertia of piston around the leg connection point,

T_{O1}: torque from point O_1,

ω_p, α_p: angular velocity and angular acceleration of piston,

ω_c, α_c: angular velocity and angular acceleration of cylinder,

F_p: radial force along the piston,

F_A: normal force perpendicular to cylinder,

T_A: torque from point O_3,

θ_1: angle between linkage 1 and vertical line,

θ_2: angle between piston and vertical line,

θ_3: angle between piston and linkage 1,

θ_k: knee angle,

m_p, m_c: piston and cylinder mass,

l_h: total length of hydraulic actuator,

l_r: length of piston.

If knee angle θ_k and angular velocity ω_k are given, (1a)–(8c) can get the analytical solution "F_p." So load pressure "P_l" of the hydraulic actuator can be computed by

$$P_l = \frac{F_p}{\pi r_p^2}, \tag{9}$$

where "r_p" is hydraulic cylinder diameter.

Now the person can realize 2 typical actions: walk and squat after wearing the exoskeleton. The motional range of knee angle is from 85° to 155° in the gait duration of these actions. In addition, the maximum external load on the back frame of exoskeleton is 60 kg. Substituting some known parameters into (3a)–(9), the load pressure P_l can be computed digital simulation method shown in Figure 3. So if the external Load "F_l" does not exceed 90 kg, the load pressure P_l will not be more than 8 MPa. It means that the hydraulic supply pressure "P_s" can be set as 8 MPa to appropriately compensate the external load 60 kg. If the person wears the exoskeleton with no effective load, the supply pressure is chosen as 4 MPa to balance the exoskeleton mass.

2.3. Hydraulic Model. The electrohydraulic servo control system is also fixed on the exoskeleton. It has 2 different characteristics: the asymmetric hydraulic cylinder and the single-rod actuator. The dynamics of servo valve can be described as follows:

$$\frac{x_v}{u} = \frac{K_{sv}\omega_{sv}^2}{s^2 + 2\zeta_{sv}\omega_{sv}s + \omega_{sv}^2}, \tag{10}$$

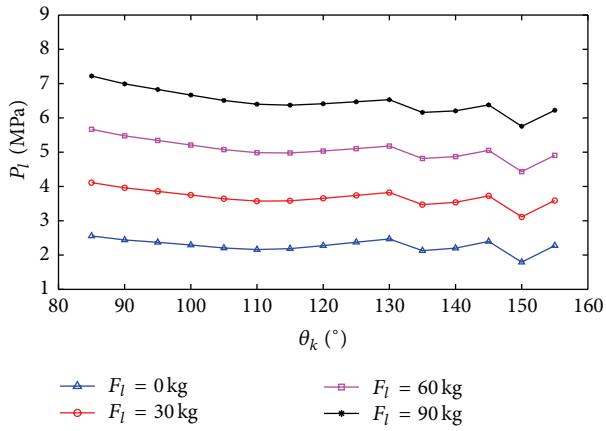

FIGURE 3: The load pressure P_l in the gait duration of walk and squat varying load and knee angle.

where ζ_{sv} is the damping ratio, ω_{sv} is natural frequency, and K_{sv} is the servo valve gain.

The flow equations can be linearized as follows [25]:

$$Q_a = K_q^1 x_v - K_c^1 p_a, \tag{11a}$$

$$Q_b = K_q^2 x_v + K_c^2 p_b, \tag{11b}$$

$$K_q^1 = C_d w \sqrt{\frac{2\Delta p_p}{\rho}}, \quad K_q^2 = C_d w \sqrt{\frac{2\Delta p_R}{\rho}}, \tag{12a}$$

$$K_c^1 = \left| \frac{C_d w x_v}{\sqrt{2\rho \Delta p_p}} \right|, \quad K_c^2 = \left| \frac{C_d w x_v}{\sqrt{2\rho \Delta p_R}} \right|, \tag{12b}$$

$$\Delta p_p = \begin{cases} |p_s - p_a| & x_v \geq 0 \\ |p_a - p_r| & x_v < 0, \end{cases} \tag{13a}$$

$$\Delta p_R = \begin{cases} |p_b - p_r| & x_v \geq 0 \\ |p_s - p_b| & x_v < 0, \end{cases} \tag{13b}$$

where Q_a, Q_b are 2 sides of cylinder flow, p_a, p_b are the cylinder chamber pressures, p_s, p_r are supply and return pressures, C_d is the valve coefficient of discharge, w is the valve orifice area gradient, ρ is the oil density, and x_v is the spool valve position. $K_q^1(K_q^2)$ and $K_c^1(K_c^2)$ are flow gains of the servo valve and flow-pressure coefficient.

If the internal and external leakages are neglected, the flow-pressure continuous equation of cylinder is shown as follows:

$$\dot{p}_a = \frac{\beta_e}{V_{01} + A_a y} \left(Q_a - A_a \dot{y} \right), \tag{14a}$$

$$\dot{p}_b = \frac{\beta_e}{V_{02} - A_b y} \left(-Q_b + A_b \dot{y} \right), \tag{14b}$$

$$V_{01} = V_{02} = \frac{V_t}{2} = \frac{A_a l_h}{2}, \tag{15}$$

where β_e is the fluid bulk modulus, A_a and A_b are the annulus areas of 2 sides of the cylinder, V_{01}, V_{02} are half-volume of the cylinder, and y is the cylinder position.

The mechanical dynamic equation is shown as follows:

$$m\ddot{y} = \left(p_a A_a - p_b A_b - F_f - F_p \right), \tag{16}$$

where F_f is the stick-slip friction caused by the viscous damp of oil and F_p is the variable load on the hydraulic actuator.

If the knee angle is known, the linear position of cylinder y can be correspondingly computed by geometric relationship as follows:

$$y(\theta_k) = \sqrt{l_1^2 + l_2^2 - 2 \times l_1 \times l_2 \times \cos \theta_k}. \tag{17}$$

According to the analytical computation method of the load pressure P_l by (9), the linear expression between F_p and y can be constructed as follows:

$$F_p(\theta_k, F_L) = K_{F_p}(\theta_k)\, y(\theta_k), \tag{18}$$

where K_{F_p} represents a variable bounded scale with load and knee angle.

The stick-slip friction often includes 2 items: a stick phase $F_{f\text{static}}$ which occurs when velocity is within a small critical velocity range and a slip friction $F_{f\text{slip}}$ which is the same as Coulomb friction model [26]. Here the slip friction can be estimated by simplified parameter identification method. Here the stick item is neglected, so the stick-slip friction F_f can be approximately described as follows:

$$F_f \approx b\dot{y}, \tag{19}$$

where b is the viscous damping coefficient of oil.

The slip friction $F_{f\text{slip}}$ should be constructed in the simulation model to identify the parameters b. The maximum stroke of cylinder is controlled by one best PID control parameters to track the square demand. The comparison results are shown in Figure 4. The simulation result of hydraulic position is similar to the experiment when parameters b are 100, especially the dynamic response is better than other conditions. So the nominal value of b can be approximately identified to be used in the parametric uncertainty model in Section 3.

3. Robust Controller Design

Lower extremity exoskeleton provides two features: high load bearing and fast motion. So exoskeleton should have fast

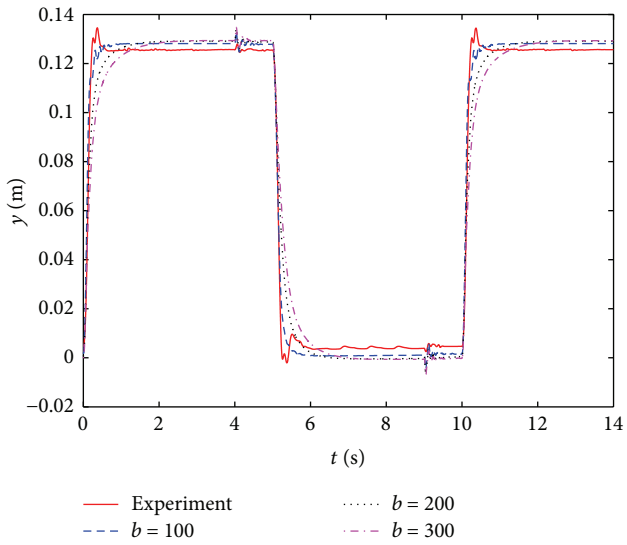

FIGURE 4: The square response of experiment and simulation varying the viscous damping coefficient b.

responses but should not hinder the wearer. In this section, a robust controller is designed to improve the dynamic response. The knee angle will be servo controlled to realize the human-machine coordinated motion. Because this EHSS has parametric disturbances and structural uncertainties, the robust H_∞ control method is presented to satisfy the requirement of close-loop stability and robust performance. After the uncertainty model of the EHSS is constructed, the robust controller is designed to find the H_∞ suboptimal controller.

3.1. Uncertainty Model Construction. This EHSS has some parametric uncertainties: the flow gains of servo valve K_q^i $(i = 1, 2)$, the viscous damping coefficient b, the effective bulk modulus β and variable volume of 2 sides cylinder $(V_{01} + A_a y, V_{02} - A_b y)$, and a structural uncertainty K_{F_p} from external load. These uncertainties parameters K_q, E, b, and K_{F_p} are described by upper Linear Fractional Transformation [27, 28] as follows:

$$M_{K_q} = \begin{bmatrix} 0 & \overline{K}_q \\ p_{K_q} & \overline{K}_q \end{bmatrix},$$

$$M_E = \begin{bmatrix} -p_E & \dfrac{1}{\overline{E}} \\ -p_E & \dfrac{1}{\overline{E}} \end{bmatrix},$$

$$M_b = \begin{bmatrix} 0 & \overline{b} \\ p_b & \overline{b} \end{bmatrix}, \tag{20}$$

$$M_{K_{Fp}} = \begin{bmatrix} 0 & 1 \\ p_{K_{Fp}} & \overline{K}_{F_p} \end{bmatrix},$$

$$K_q = \overline{K}_q \left(1 + p_{K_q} \delta_{K_q}\right), \quad -1 \le \delta_{K_q} \le 1, \tag{21a}$$

$$E = \overline{E}\left(1 + p_E \delta_E\right), \quad -1 \le \delta_E \le 1, \tag{21b}$$

$$b = \overline{b}\left(1 + p_b \delta_b\right), \quad -1 \le \delta_b \le 1, \tag{21c}$$

$$K_{F_p} = \overline{K}_{F_p} + p_{K_{Fp}} \delta_{K_{Fp}}, \tag{21d}$$

where $E = V_t/2\beta$, $\overline{K}_q$, $\overline{E}$, and $\overline{b}$ are the nominal values, δ_{K_q}, δ_E, and δ_b are relative variation, respectively, and the maximum relative uncertainties p_{K_q}, p_E, and p_b can be estimated varying some hydraulic parameters [20].

If these vectors are defined, the state vector $X = [x_1, x_2, x_3, x_4, x_5, x_6]^T = [x_v, \dot{x}_v, p_a, p_b, y, \dot{y}]^T$, the control input $u(t)$, which is the current of servo valve, the vector of exogenous inputs $w(t) = [w_1, w_2, w_3, w_4, w_5]^T$, the output cylinder position $y(t)$ measured by encoder, and the regulated output vector $z(t) = [z_1, z_2, z_3, z_4, z_5, z_6]^T$, then the uncertain state-space model is constructed as follows:

$$\dot{X}(t) = AX(t) + B_1 W(t) + B_2 u(t), \tag{22a}$$

$$Z(t) = C_1 X(t) + D_{11} W(t), \tag{22b}$$

$$Y(t) = C_2 X(t), \tag{22c}$$

where

$$A = \begin{bmatrix} 0 & 1 & 0 & 0 & 0 & 0 \\ -\omega_v^2 & -2\zeta_v\omega_v & 0 & 0 & 0 & 0 \\ \dfrac{\overline{K}_q}{\overline{E}} & 0 & -\dfrac{K_c}{\overline{E}} & 0 & 0 & -\dfrac{A_a}{\overline{E}} \\ -\dfrac{\overline{K}_q}{\overline{E}} & 0 & 0 & -\dfrac{K_c}{\overline{E}} & 0 & \dfrac{A_2}{\overline{E}} \\ 0 & 0 & 0 & 0 & 0 & 1 \\ 0 & 0 & \dfrac{A_a}{m} & -\dfrac{A_b}{m} & -\dfrac{\overline{K}_{F_p}}{m} & \dfrac{\overline{b}}{m} \end{bmatrix}, \tag{23a}$$

$$B_1 = \begin{bmatrix} 0 & 0 & 0 & 0 & 0 \\ 0 & 0 & 0 & 0 & 0 \\ \dfrac{p_{K_q}}{\overline{E}} & -p_E & 0 & 0 & 0 \\ -\dfrac{p_{K_q}}{\overline{E}} & 0 & -p_E & 0 & 0 \\ 0 & 0 & 0 & 0 & 0 \\ 0 & 0 & 0 & -\dfrac{p_b}{m} & -\dfrac{p_{K_{Fp}}}{m} \end{bmatrix}, \tag{23b}$$

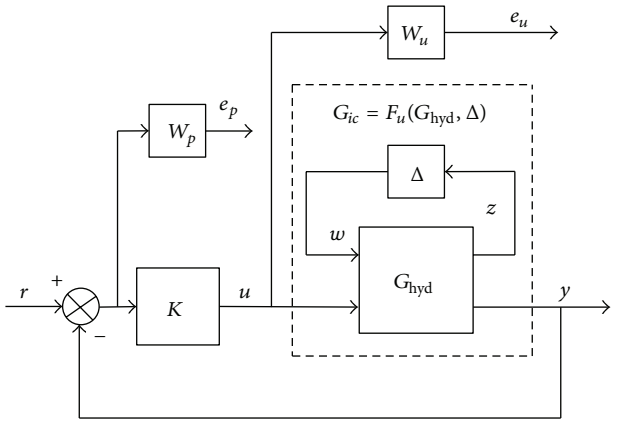

FIGURE 5: The block diagram of the closed-loop system with robust stability and performance requirements.

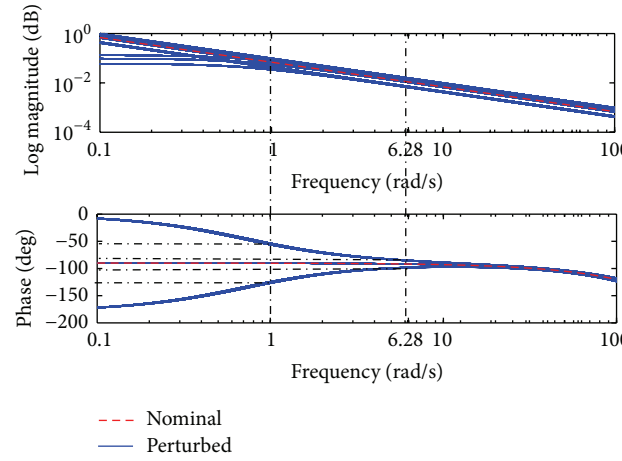

FIGURE 6: The frequency response of the open-loop system with varying uncertainty parameters K_q, E, b, and K_{F_p}.

$$B_2 = \begin{bmatrix} 0 & K_{sv}\omega_v^2 & 0 & 0 & 0 & 0 \end{bmatrix}^T, \tag{23c}$$

$$C_1 = \begin{bmatrix} \overline{K}_q & 0 & 0 & 0 & 0 & 0 \\ \dfrac{\overline{K}_q}{\overline{E}} & 0 & -\dfrac{K_c}{\overline{E}} & 0 & 0 & -\dfrac{A_a}{\overline{E}} \\ -\dfrac{\overline{K}_q}{\overline{E}} & 0 & 0 & -\dfrac{K_c}{\overline{E}} & 0 & \dfrac{A_b}{\overline{E}} \\ 0 & 0 & 0 & 0 & 0 & \overline{b} \\ 0 & 0 & 0 & 0 & 1 & 0 \end{bmatrix}, \tag{23d}$$

$$D_{11} = \begin{bmatrix} 0 & 0 & 0 & 0 & 0 \\ \dfrac{p_{K_q}}{\overline{E}} & -p_E & 0 & 0 & 0 \\ -\dfrac{p_{K_q}}{\overline{E}} & 0 & -p_E & 0 & 0 \\ 0 & 0 & 0 & 0 & 0 \\ 0 & 0 & 0 & 0 & 0 \end{bmatrix}, \tag{23e}$$

$$C_2 = \begin{bmatrix} 0 & 0 & 0 & 0 & 1 & 0 \end{bmatrix}. \tag{23f}$$

The robust stability and performance requirements of the closed-loop system are shown in Figure 5.

In Figure 5, the weighting functions W_p and W_u are used to reflect the relative significance of the performance requirement. The robust controller K needs to be designed to optimize the robust performance e_p and e_u. The nominal model G_{hyd} and the interconnection model G_{ic} represent the robust uncertainty model shown in (22a), (22b), and (22c). The demand and actual cylinder position r, y are the input and output of this EHSS.

3.2. Robust Controller Design. The frequency response of the open-loop system with model uncertainties is shown in Figure 6. The phase margins are obviously different between perturbed model and nominal model, which is caused by the uncertainty parameter K_{F_p}. Due to the presence of K_{F_p}, the stable phase of open-loop system will lead or lag approximately 50 degrees in middle frequency stage (1~6.28 rad/s).

The weight functions W_p and W_u are iteratively designed according to robust performance requirement and control constraint shown as follows [29]:

$$W_p = 0.95 \times \frac{s^2 + 1.8s + 5}{s^2 + 8s + 0.01}, \tag{24a}$$

$$W_u = 5 \times 10^{-4}. \tag{24b}$$

The singular values of the weight function W_p and the sensitivity function of close-loop G_s^n should satisfy $\|W_p G_s^n\|_\infty \le \mu(W_p)\mu(G_s^n) < 1$, which has guaranteed the basic control performance.

The robust controller will guarantee robust stability and robust performance requirement which can be described in Figure 5 [30, 31].

(1) H_∞ suboptimal control problem: to design a controller K satisfying the following condition:

$$\left\| F_l\left(G_{ic}, K\right)\right\|_\infty = \left\| F_l\left(F_u\left(G_{hyd}, \Delta\right), K\right)\right\|_\infty < \gamma, \tag{25}$$

where $\gamma > \gamma_0$, γ_0 is the minimum value of $\|F_l(G_{ic}, K)\|_\infty$ under K is a stable controller.

(2) Robust performance requirement: the close-loop system composed of G_{ic} and K should satisfy

$$\left\| \begin{bmatrix} W_p\left(I + G_{ic}K\right)^{-1} \\ W_u K\left(I + G_{ic}K\right)^{-1} \end{bmatrix} \right\|_\infty < 1. \tag{26}$$

If the relative uncertainty Δ is from $-I$ to $\Delta = I$, the singular value of close-loop perturbed is 0.28, which is less than 1 shown in Figure 7. The close-loop system G_c is stable and its relative uncertainties Δ can be extended to 1/0.28.

In Figure 8, the maximum singular value μ of close-loop shows that the robust performance requirement is 1.4, which

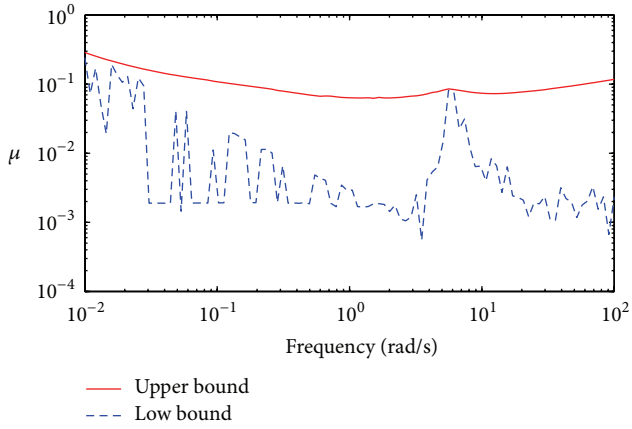

Figure 7: The maximum robust stability bound with varying uncertainty parameters K_q, E, b, and K_{F_p}.

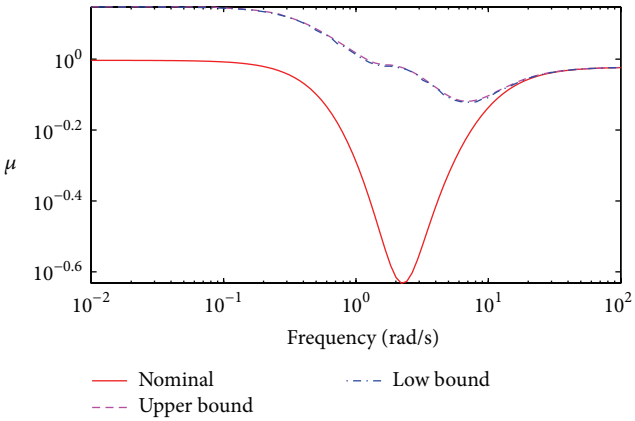

Figure 8: The maximum robust performance bound with varying uncertainty parameters K_q, E, b, and K_{F_p}.

means that the steady tracking accuracy may not be excellent. But in middle and high frequency stage from 4 to 100 rad/s, the dynamic tracking performance and robustness margin meet the requirement [32].

After iterative design, the robust controller is 7 orders. Taking the actual project into account, the controller should be reduced into lower order by Balanced Truncation Method [33]. So the controller is simplified to 4 orders as follows:

$$\begin{aligned} u_{\text{extension}} &= K(s)(\tilde{y} - y) \\ &= \frac{n_4 s^4 + n_3 s^3 + n_2 s^2 + n_1 s + n_0}{d_4 s^4 + d_3 s^3 + d_2 s^2 + d_1 s + d_0}(\tilde{y} - y), \end{aligned} \tag{27}$$

where n_i $(i = 0, \ldots, 4)$, d_i $(i = 0, \ldots, 4)$ are numerator and denominator constant, $\tilde{y}$ is demand input, and y is output.

4. Gait Divisions of Coordinated Motion

In this section, the gait phase divisions of 2 typical action modes are analyzed and designed. According to the gait identification, the switched control is realized to reduce the delay of exoskeleton tracking person and improve the human-machine coupling effect.

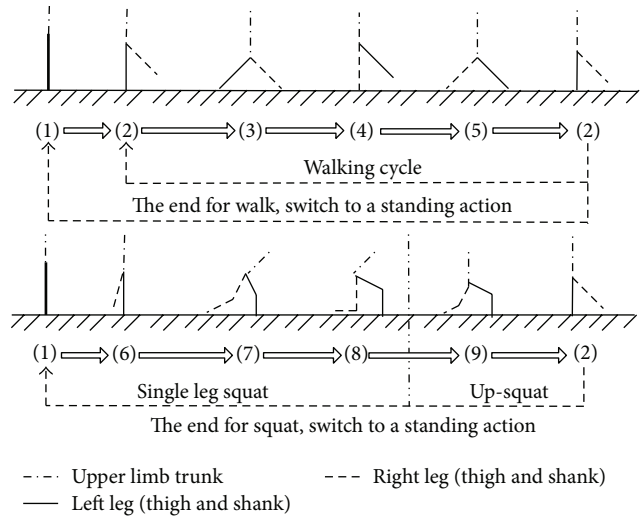

Figure 9: The gait subphases division of walk and squat action in human-machine coordinated motion.

4.1. Walk Mode. The walking gait law of human-machine coordinate motion can be divided into 5 subphases shown in Figure 9. These subphases are (1) double standing; (2) right leg swing, left leg stance; (3) double stance with right leg front and left leg back; (4) right leg stance and left leg swing; and (5) double stance with left leg front and right leg back.

In order to improve the exoskeleton tracking person's motion, 2 subphases (3) and (4) are merged. That means if the subphases (3) are identified, make the hydraulic cylinder of left leg retract in advance. This operation realizes the exoskeleton ahead of person, which helps person regulate the center of system gravity easily in overload carrying condition. After the subphase (4) is identified by exoskeleton, the center of system gravity is steadily regulated by person. Simultaneously, the exoskeleton continuously realizes the right stance leg and the left swing leg. The subphases (5) and (2) are similar to subphases (3) and (4). So the switched control algorithm is described in Table 1.

In Table 1, u_l and u_r are control current of the of left and right servo valve, $u_{\max} = \pm 40$ mA, which is the maximum current of servo.

4.2. Squat Mode. The squat gait law is divided into 6 subphases: (1) double standing; (6) left leg stance and right leg uplift for preparation; (7) left leg retraction gradually and right leg swing; (8) left leg reached the minimum position of cylinder and right knee contacting the ground, which means the single leg squat action ends; (9) left leg extension gradually and right leg swing; and (2) left leg stance and right leg swing, which means the up-squat action ends and switch to the walking mode. So the switched control algorithm is described in Table 2.

In gait (7), the left knee angle is retracted by fader control. The symbol $k = 2$ and t is fader time.

Table 1: The duty of exoskeleton and person in walking gait subphases by different switched controller form.

Gait	Controller	Exoskeleton	Person
(1)	$u_l = u_{\text{extension}}$ $u_r = u_{\text{extension}}$	Control double knee angle	Adapt to exoskeleton
(2)	$u_l = u_{\text{extension}}$ $u_r = -u_{\max}$	Control left knee angle and retract right leg	Adapt to exoskeleton
(3)	$u_l = -u_{\max}$ $u_r = u_{\text{extension}}$	Adapt to person and retract left leg in advance	Regulate the center of gravity
(4)	$u_l = -u_{\max}$ $u_r = u_{\text{extension}}$	Control right knee angle and retract left leg	Adapt to exoskeleton
(5)	$u_l = u_{\text{extension}}$ $u_r = -u_{\max}$	Adapt to person and retract right leg in advance	Regulate the center of gravity

Table 2: The duty of exoskeleton and person in squat gait subphases by different switched controller form.

Gait	Controller	Exoskeleton	Person
(6)	$u_l = u_{\text{extension}}$ $u_r = -u_{\max}$	Control left knee angle and retract right leg	Squat preparation
(7)	$u_l = u_{\max}(1 - e^{-kt})$ $u_r = -u_{\max}$	Retract left knee angle gradually	Adapt to exoskeleton
(8)	$u_l = -u_{\max}$ $u_r = -u_{\max}$	Adapt to person and hold in the prescript posture	Regulate the center of gravity
(9)	$u_l = u_{\text{extension}}$ $u_r = u_{\text{extension}}$	Control 2 knee angles and extend 2 legs	Adapt to exoskeleton

To ensure the safety of person, the squat preparation time need to be set as 2 or 3 sec. The subphase (8) is identified by a pressure force sensor on the right knee. The transition from subphase (8) to subphase (9) needs a mode switch button and gait identification algorithm which is not described in this section.

5. Simulation Results

The hydraulic model is simulated with the external load 60 kg. The hydraulic parameters for simulation are shown in Table 3. In order to verify the effectiveness of the proposed method, the natural walking gait law is considered as the command input with 0.5 Hz frequency. The fore-half duration is stance phase for one leg with the range of knee angle from 15° to 30°. The afterwards duration is swing phase with range of knee angle from 15° to 73°.

According to the above analysis of the load pressure P_l, the hydraulic supply pressure P_s is 8 MPa and the external load is 60 kg in simulation. Some hydraulic parameters are shown in Table 3. The maximum relative uncertainties $p_{K_q} = 0.25$, $p_E = 0.7$, $p_b = 1$, and $p_{K_{Fp}} = 300$. Here 2 control methods are used to make the exoskeleton track the person in the walking mode simulation. The PID control parameters are designed as the best group, which satisfy the frequency domain margin. The robust H_∞ control method is realized by (27).

Table 3: The hydraulic parameters for simulation.

Name	Value	Unit
Damping ratio ξ_{sv}	0.7	—
Natural frequency ω_n	628	rad/s
Servo valve gain K_{sv}	0.0125	m/A
Fluid bulk modulus β_e	7000	bar
Mass of hydraulic actuator m	2.5	kg
Annulus areas of no-rod cylinder A_a	1.77×10^{-4}	m^2
Annulus areas of rod cylinder A_b	1.13×10^{-4}	m^2
Distance between hydraulic cylinder calf connections and knee l_1	0.322	m
Distance between hydraulic cylinder thigh connections and knee l_2	0.065	m
Return pressures p_r	1	bar
Piston stroke L_r	0.16	m
Flow-pressure coefficient $K_c^1 \approx K_c^2$	$5.18e-12$	$m^3/s/Pa$
Nominal value of $\overline{K}_q$	0.188	m^2/s
Nominal value of $\overline{b}$	100	Ns/m
Nominal value of $\overline{E}$	$1.98e-14$	m^3/pa
Nominal value of $\overline{K}_{F_p}$	1200	N/m

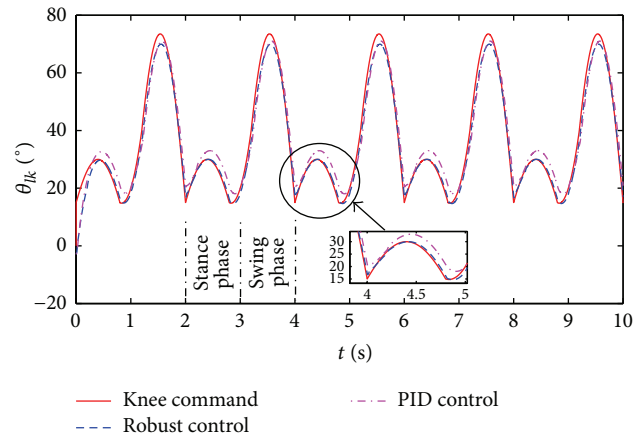

Figure 10: The left knee angle response of walking gait.

The left knee angle response of exoskeleton is shown in Figure 10. In swing phase, the dynamic characteristic of PID control is same as the robust H_∞ control because there is no external load on the hydraulic actuator. But, in stance phase, the dynamic performance of robust control is better than PID control due to the variable compensation force F_p provided by hydraulic actuator on the exoskeleton. This external force disturbance results in the parametric uncertainty of K_q, E, which reduce the stabile margin of PID control. Importantly, the control current needs to balance the compensation force F_p and stick-slip friction F_f in the case

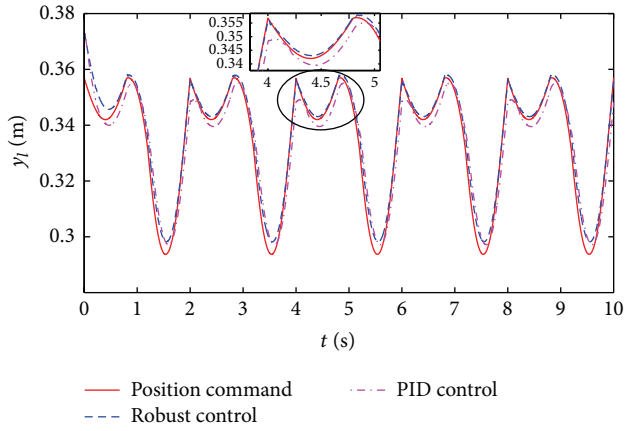

Figure 11: The position response of left hydraulic cylinder of walking gait.

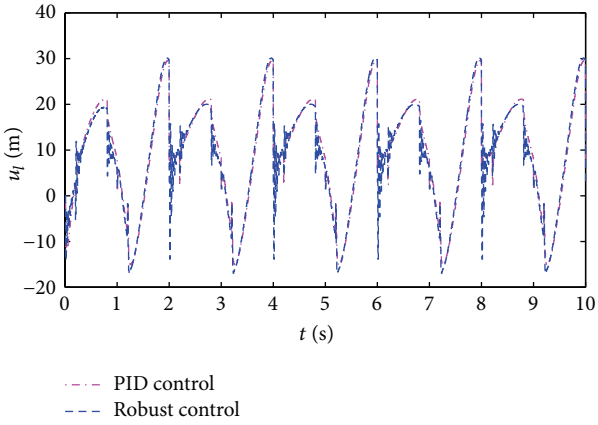

Figure 12: The left servo valve control current of walking gait.

of positional error suppression. In addition, the asymmetric cylinder affects the dynamic characteristic of hydraulic model when cylinder extension switches into retraction, especially in stance phase. The parametric uncertainty of K_q, E, and b and structural uncertainty F_p are considered in the system model construction, so the robust controller can guarantee the dynamic performance in the whole duration of walking mode.

The dynamic cylinder position of left hydraulic actuator on exoskeleton is shown in Figure 11. It is computed by (17) after the knee angle is measured by encoder. The available displacement of cylinder is 0.07 m in waking mode, which is less than the maximal stroke 0.16 m of cylinder. It means that only half stroke is useful in human-machine coordinated walk. But the maximal stroke of cylinder needs to satisfy the squat mode, which requires enough length of cylinder.

The control current of left servo valve is shown in Figure 12. The general trend of control current is same using 2 control methods. But the robust controller $u_{\text{extension}}$ is more intense than PID control, especially in stance phase. Because the controller involves the high order item, the robust controller can reduce the tracking error quickly in the case of model uncertainty. The maximal amplitude of control current is 30 mA, which does not exceed the maximal servo valve control current $\pm u_{\max}$.

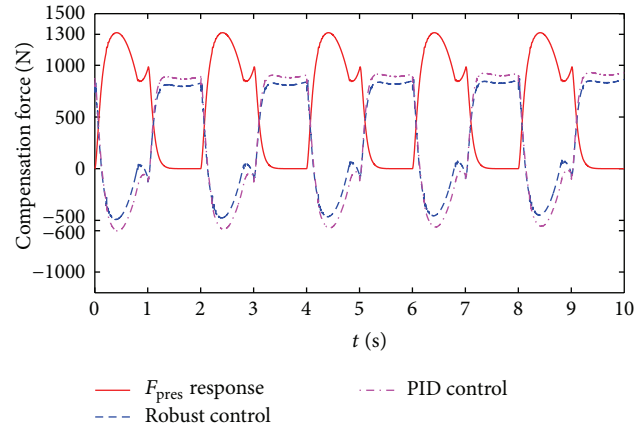

Figure 13: The aid-force effect of exoskeleton by left hydraulic actuator.

The aid-force effect of exoskeleton by left hydraulic actuator is shown in Figure 13. Here the demand compensation force F_{pres} is constructed by

$$F_{\text{pres}} = \begin{cases} \dfrac{F_p}{(T_\alpha s + 1)^2} & \text{stance phase} \\ \left(1 - \dfrac{1}{(T_\alpha s + 1)^2}\right) F_p & \text{swing phase,} \end{cases} \tag{28}$$

where $T_\alpha = 0.05$ s is defined as the transition response time of external load F_l.

In Figure 13, the compensation force error means the error between F_{pres} and the hydraulic output actual force F_{act}. In stance phase of left leg, the compensation force error does not exceed 500 N by the robust controller. The demand compensation force F_{pres} is 1300 N approximately. It means that the load bearing efficiency is great than 60% in stance phase of left leg. Because 2 legs are alternative in walking gait, the left hydraulic actuator needs not to compensate F_{pres} in its swing phase, while the hydraulic actuator on right leg of exoskeleton is in charge of this load bearing task. Therefore, the aid-force effect of simulation result can not include the hydraulic output actual force in swing phase in this figure.

6. Experimental Results

The human-machine coordinated motion is realized by a tester wearing the exoskeleton prototype. The gait can be identified by 4 force sensors in the sensor shoes. The 2 knee angles of exoskeleton are measured by 2 encoders. The hydraulic control system includes a motor, a fixed pump, 2 servo valves, 2 cylinders, and an embedded controller on the mechanical brace. The net weight of prototype is 30 kg. In walking mode, the tester can bear no more than 60 kg external load. In squat mode, the tester can realize the basic gait with no external load due to the safety of

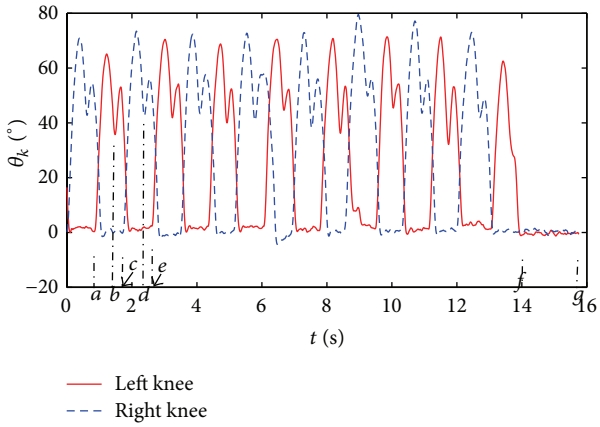

FIGURE 14: The knee angles of 2 legs in walking mode.

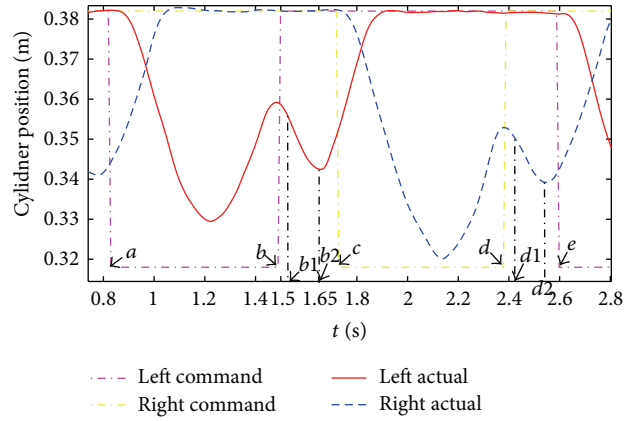

FIGURE 15: The cylinder positions of 2 hydraulic actuators in one cycle of walking mode.

tester. The hydraulic actuators are controlled by the robust control method and the control algorithm will be switched in different gait.

6.1. Walking Mode with Overloading. In walking mode, the extension and retraction of 2 legs are alternatively realized by hydraulic actuator. The walking frequency is 0.5 Hz bearing with 60 kg load.

The dynamic characteristics of 2 knee angles are shown in Figure 14, which includes 5 subphases of walking gait. In gait (4), described by time slice $a\sim b$ (0.8 s~1.5 s), the left leg is retracted by the tester himself and the control current of left leg is $-u_{\max}$ shown in Figure 20. In gait (5), described by time slice $b\sim c$ (1.5 s~1.7 s), the left leg is extended by feedback control and the right leg begins to retract in advance to help the tester regulate the center of gravity. This ahead of control can make the tester move easily. In gait (2), described by time slice $c\sim d$ (1.7 s~2.4 s), the right leg is retracted by the tester himself like as gait (4). In gait (3), described by time slice $d\sim e$ (2.4 s~2.6 s), the right leg is extended by feedback control like gait (5). These 4 subphases are switched frequently in walking mode. If the walking mode ends, the double stance phase gait (1) will arise, described by time slice $f\sim g$ (14 s~15.6 s). In gait (1), 2 legs are controlled by feedback control. The external load is compensated by 2 hydraulic actuators on the exoskeleton only in stance phase. In swing phase, the exoskeleton should help the tester switch the center of gravity from one leg to the other leg. Otherwise, the human-machine coupled effect is reduced significantly and the tester may be at loss of balance.

The cylinder positions of 2 hydraulic actuators in one cycle of walking mode are shown in Figure 15. Here the extended position commands are designed as a rising step. The servo feedback control phase of left leg is described as time slice $b\sim e$ (1.5 s~2.6 s). But, in time slice $b1\sim b2$ (1.55 s~1.65 s), the cylinder position is still retracted after the positive control current output. This response delay is caused by the bandwidth limitation of the whole hydraulic control system. The pressure of cylinder is constructed with time-consuming 0.8 s from 0 to stable value 8 MPa. So the available position response of left cylinder is time slice $b2\sim e$ (1.65 s~2.6 s),

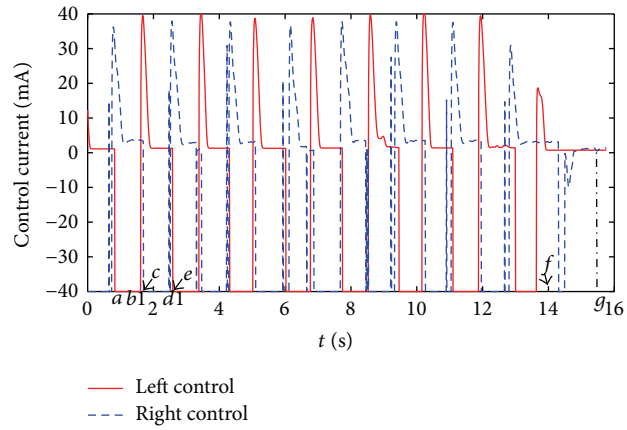

FIGURE 16: The control current of 2 servo valves in walking mode.

where the actual position of cylinder tracks the extended position commands. In time slice $a\sim b$, the retracted position commands of left leg is designed as a fall step. It is not a servo control phase for left leg. So the control current of servo valve is minus maximal value $-u_{\max}$ directly in order to help the tester retract the cylinder quickly. The dynamic characteristic of right cylinder positions is similar to the left cylinder.

The switched control currents correspond to 5 subphases shown in Figure 16. The servo control phase of left leg is time slice $b1\sim e$ (1.55 s~2.6 s) in one cycle. Similarly, the servo control phase of right leg is starting at time $d1$. In double stance phase, described by time slice $f\sim g$, the servo control value is near 0 after 2 knee angles reach the tester's stance posture. The dynamic pressures of 2 hydraulic actuators are shown in Figure 17. In stance phase, the pressure is constructed from 0 to 8 MPa with approximately 0.8 s time consumed due to bearing heavy load. In swing phase, the fast time-consuming is 0.4 s for pressure from 8 MPa to 0. It reveals that person's active control can be faster than the control response of exoskeleton if the walking speed is possible. So the switched control algorithm shown in Table 1 is suitable for human-machine coordinated walk.

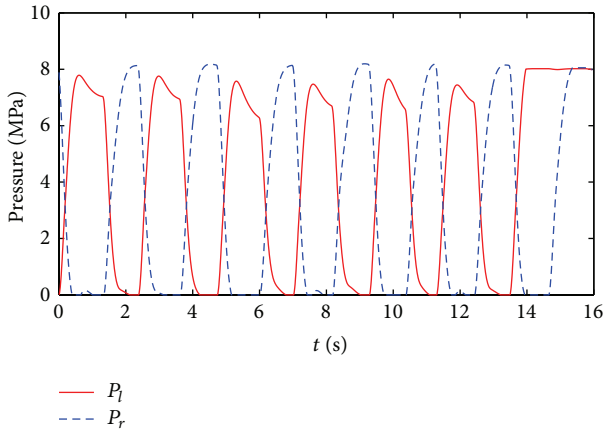

Figure 17: The pressures of 2 hydraulic actuators in walking mode.

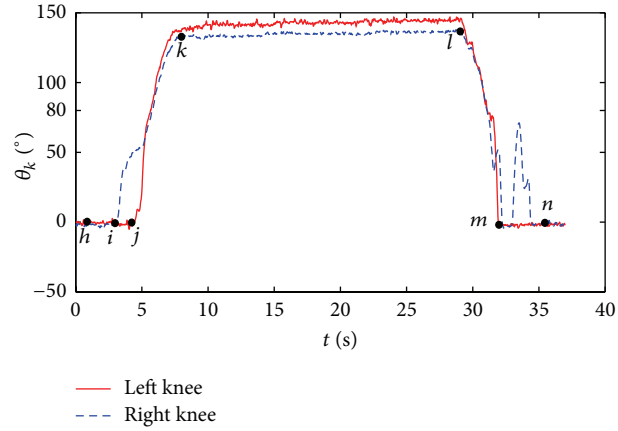

Figure 18: The knee angles of 2 legs in squat mode.

6.2. Squat Mode Test. According to Figure 9, 6 gait subphases of squat mode are realized by switched control algorithm shown in Table 2. The dynamic characteristics of 2 knee angles in squat mode are shown in Figure 18. The gait subphases are described by time slice $h \sim i$ (0 s~2 s), $i \sim j$ (2 s~4 s), $j \sim k$ (4 s~7 s), $k \sim l$ (7 s~29 s), $l \sim m$ (29 s~32 s), and $m \sim n$ (32 s~35 s), respectively. In gait (5), described as time slice $h \sim i$, the double stance phase should be passed before the squat mode begins. The cylinder positions are controlled to reach the tester's stance posture shown in Figure 19. In gait (6), described as time slice $i \sim j$, the right leg swings to prepare the squat action and the tester regulates the center of gravity at this moment. In gait (7), described as time slice $j \sim k$, the left cylinder is retracted gradually by exponential fader control shown in Table 2. So the left leg bends gradually before the right knee contacts the ground. The control current is reduced from 0 to $-u_{\max}$ in 3 sec shown in Figure 20. In gait (8), described as time slice $k \sim l$, 2 control currents are minus maximal value. The exoskeleton can not compensate its mass by 2 hydraulic actuators at this phase. The tester can bear the load himself through regulating the center of gravity to reduce the backward torque caused by exoskeleton mass and hold in the prescript posture. In gait (9), described as time slice $l \sim m$, 2 cylinders are extended to realize the up-squat action in 3 sec (Figure 21). The cylinder positions of 2 legs are controlled by robust control algorithm to reach the suitable positions where gait (9) is switched into gait (2). After up-squat phase ends, the squat mode will return to the walking mode.

6.3. Experimental Scene. The experimental scenes of human-machine coordinated motion are shown in Figures 22 and 23. In walking mode, the tester can bear the external load 60 kg hung on the back frame of exoskeleton. When the waking gait is switched, the tester will bear a little more load himself due to the regulation of center of gravity. In the stable stance phases, such as double standing or single leg stance, the exoskeleton can guarantee the aid-force effect by the proposed robust controller. Also, the comfortable effect of tester is improved by the switched control algorithm.

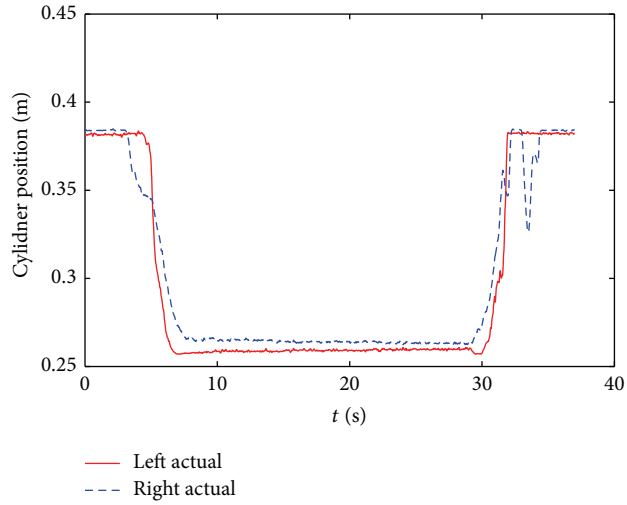

Figure 19: The cylinder position of 2 hydraulic actuators in squat mode.

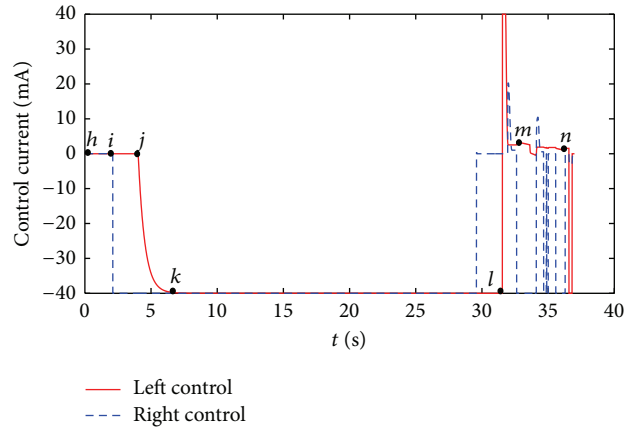

Figure 20: The control current of 2 servo valves in squat mode.

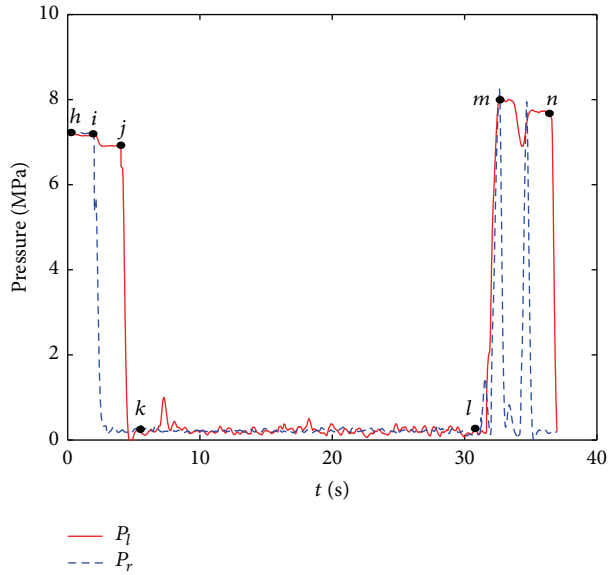

Figure 21: The pressures of 2 hydraulic actuators in squat mode.

(a) Gait (1) (b) Gait (2) (c) Gait (3)

(d) Gait (4) (e) Gait (5)

Figure 22: The walking gait subphases experiment.

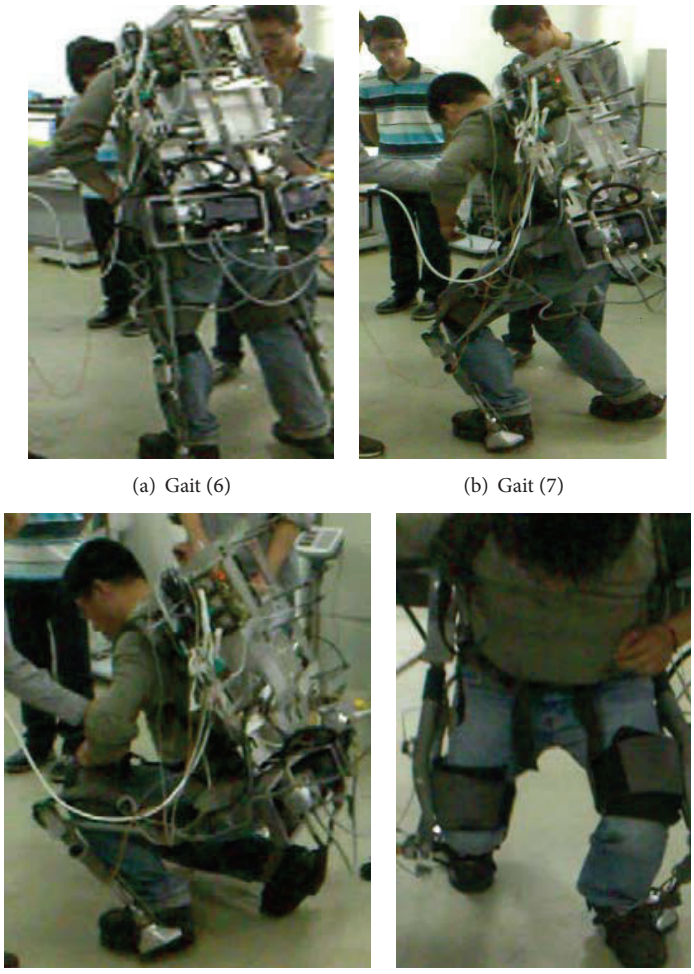

(a) Gait (6) (b) Gait (7)

(c) Gait (8) (d) Gait (9)

Figure 23: The squat gait subphases experiment.

In squat mode, the tester only bears the exoskeleton mass because of the safety of system at the present stage. The tester can realize the basic gait of squat action under the help of another person's arm, especially in gait (7) and gait (9).

7. Conclusion

In this paper, a human-machined coordinated motion control method is presented to realize the aid-force of lower extremity exoskeleton. This proposed method improves the robust performance under the structural and parametric uncertainty disturbance. The positions of 2 hydraulic actuators are controlled to make exoskeleton track person's motion by output feedback control. Compared with conventional PID control method in simulation, the proposed method can achieve a better dynamic response performance and aid-force effect in stance phase of walking gait. According to the gait divisions of human-machined coordinated motion, the switched control algorithm is designed to reduce the delay of exoskeleton tracking person. The experimental results of 2 motion modes validate the effectiveness of this proposed method and gait switched control algorithm.

Conflict of Interests

The authors declare that there is no conflict of interests regarding the publication of this paper.

Acknowledgments

This research was supported by project of National Natural Science Foundation of China (no. 61305092 and no. 51205045) and project of China Postdoctoral Science Foundation (no. 2013M542487). The authors would like to thank anonymous reviewers for their valuable comments and suggestions.

References

[1] S. Ackerman, *The Report of Production Display for "HULC" Made in Lockheed Martin*, Montgomery County, Md, USA, 2010, http://www.lockheedmartin.com.

[2] Z. X. Wang, "Raytheon launched XOS2 second-generation exoskeleton device," *Light Weapons*, pp. 24–44, 2010.

[3] J. R. Steger, *A design and control methodology for human exoskeletons [Ph.D. dissertation]*, Department of Mechanical Engineering, University of California, Berkeley, Calif, USA, 2006.

[4] J. F. Veneman, R. Ekkelenkamp, R. Kruidhof, F. C. T. van der Helm, and H. van der Kooij, "Design of a series elastic- and Bowden cable-based actuation system for use as torque-actuator in exoskeleton-type training," in *Proceedings of the IEEE 9th International Conference on Rehabilitation Robotics (ICORR '05)*, pp. 496–499, Chicago, Ill, USA, July 2005.

[5] Verge, "The report of 'Hercule exoskeleton can help a regular human carry up to 220 pounds,'" 2012, http://www.theverge.com/2012/2/22/2815704/hercule-exoskeleton-human-carry-220-pounds.

[6] C. G. Atkeson, J. G. Hale, F. Pollick et al., "Using humanoid robots to study human behavior," *IEEE Intelligent Systems and Their Applications*, vol. 15, no. 4, pp. 46–55, 2000.

[7] Q. Guo, H. Zhou, and D. Jiang, "Coordinated control method of the lower extremity exoskeleton based on human electromechanical coupling," in *Social Robotics: 4th International Conference, ICSR 2012, Chengdu, China, October 29–31, 2012. Proceedings*, vol. 7621 of *Lecture Notes in Computer Science*, pp. 650–659, Springer, Berlin, Germany, 2012.

[8] Q. Li, M. Kong, Z. Du, L. Sun, and D. Wang, "Interactive rehabilitation exercise control strategy for 5-DOF upper limb rehabilitation arm," *Chinese Journal of Mechanical Engineering*, vol. 44, no. 9, pp. 169–176, 2008.

[9] Z. Y. Yang, Y. S. Zhang, W. J. Gu et al., "Bone clothing sensitivity amplification control," *Computer Simulation*, vol. 27, no. 1, pp. 177–180, 2010.

[10] H. Cao, X. W. Meng, Z. Y. Ling et al., "Two-legged robot exoskeleton plantar pressure measurement system," *Journ of Sensors and Actuators*, vol. 23, no. 3, pp. 326–330, 2010.

[11] R. Fales and A. Kelkar, "Robust control design for a wheel loader using H_∞ and feedback linearization based methods," *ISA Transactions*, vol. 48, no. 3, pp. 312–320, 2009.

[12] G. P. Liu and S. Daley, "Optimal-tuning PID controller design in the frequency domain with application to a rotary hydraulic system," *Control Engineering Practice*, vol. 7, no. 7, pp. 821–830, 1999.

[13] I. Boiko, "Variable-structure PID controller for level process," *Control Engineering Practice*, vol. 21, no. 5, pp. 700–707, 2013.

[14] M. Moradi, "Self-tuning PID controller to three-axis stabilization of a satellite with unknown parameters," *International Journal of Non-Linear Mechanics*, vol. 49, pp. 50–56, 2013.

[15] O. Cerman and P. Hušek, "Adaptive fuzzy sliding mode control for electro-hydraulic servo mechanism," *Expert Systems with Applications*, vol. 39, no. 11, pp. 10269–10277, 2012.

[16] C. Guan and S. X. Pan, "Adaptive sliding mode control of electro-hydraulic system with nonlinear unknown parameters," *Control Engineering Practice*, vol. 16, no. 11, pp. 1275–1284, 2008.

[17] D. H. Sha, V. B. Bajic, and H. Y. Yang, "New model and sliding mode control of hydraulic elevator velocity tracking system," *Simulation Practice and Theory*, vol. 9, no. 6–8, pp. 365–385, 2002.

[18] C. W. Wang, Z. X. Jiao, S. Wu, and Y. X. Shang, "Nonlinear adaptive torque control of electro-hydraulic load system with external active motion disturbance," *Mechatronics*, vol. 24, no. 1, pp. 32–40, 2014.

[19] I. Ursu, A. Toader, A. Halanay, and S. Balea, "New stabilization and tracking control laws for electrohydraulic servomechanisms," *European Journal of Control*, vol. 19, no. 1, pp. 65–80, 2013.

[20] V. Milić, Ž. Ŝitum, and M. Essert, "Robust H_∞ position control synthesis of an electro-hydraulic servo system," *ISA Transactions*, vol. 49, no. 4, pp. 535–542, 2010.

[21] F. L. Weng, Y. C. Ding, and M. K. Tang, "LPV model-based robust controller design of electro-hydraulic servo systems," *Procedia Engineering*, vol. 15, pp. 421–425, 2011.

[22] X. Song, Y. Wang, and Z. Sun, "Robust stabilizer design for linear time-varying internal model based output regulation and its application to an electrohydraulic system," *Automatica*, vol. 50, no. 4, pp. 1128–1134, 2014.

[23] R. Fales and A. Kelkar, "Robust control design for a wheel loader using mixed sensitivity H-infinity and feedback linearization based methods," in *Proceedings of the American Control Conference (ACC '05)*, pp. 4381–4386, Portland, Ore, USA, June 2005.

[24] S. Kawamura and M. Svinin, *Advances in Robot Control: From Everyday Physics to Human-like Movements*, Springer, Berlin, Germany, 2006.

[25] A. Akers, M. Gassman, and R. Smith, *Hydraulic Power System Analysis*, Taylor & Francis Group, 2006.

[26] A. Alleyne and R. Liu, "A simplified approach to force control for electro-hydraulic systems," *Control Engineering Practice*, vol. 8, no. 12, pp. 1347–1356, 2000.

[27] W.-M. Lu, K. M. Zhou, and J. C. Doyle, "Stabilization of uncertain linear systems: an LFT approach," *IEEE Transactions on Automatic Control*, vol. 41, no. 1, pp. 50–65, 1996.

[28] M. K. H. Fan, A. L. Tits, and J. C. Doyle, "Robustness in the presence of mixed parametric uncertainty and unmodeled dynamics," *IEEE Transactions on Automatic Control*, vol. 36, no. 1, pp. 25–38, 1991.

[29] D. W. Gu, P. H. Petkov, and M. M. Konstantinov, *Robust control design with MATLAB*, Springer Press, 2005.

[30] J. C. Doyle, K. Glover, P. P. Khargonekar, and B. A. Francis, "State-space solutions to standard H_2 and H_∞ control problems," *IEEE Transactions on Automatic Control*, vol. 34, no. 8, pp. 831–847, 1989.

[31] G. J. Balas and J. C. Doyle, "Robustness and performance trade-offs in control design for flexible structures," *IEEE Transactions on Control Systems Technology*, vol. 2, no. 4, pp. 352–361, 1994.

[32] A. Packard, M. K. H. Fan, and J. C. Doyle, "A power method for the structured singular value," in *Proceedings of the 27th IEEE Conference on Decision and Control*, pp. 2132–2137, Chicago, Ill, USA, December 1988.

[33] W. Gawronski, "Balanced systems and structures: reduction, assignment, and perturbations," in *Control and Dynamic Systems*, vol. 54, pp. 373–415, 1992.